

MODELING AND EXPERIMENTAL INVESTIGATION OF TRANSPORT PROCESSES IN THE POROUS CATHODE OF AQUEOUS LI-AIR BATTERIES

Von der Fakultät Energie-, Verfahrens- und Biotechnik der Universität
Stuttgart zur Erlangung der Würde eines Doktor-Ingenieurs (Dr.-Ing.)
genehmigte Abhandlung

Vorgelegt von

Timo DANNER

aus Göppingen

Hauptberichter:	Prof. Dr. Wolfgang G. BESSLER
1. Mitberichter:	Prof. Dr. K. Andreas FRIEDRICH
2. Mitberichter:	Prof. Dr. Helmut EHRENBERG

Tag der mündlichen Prüfung: 31.03.2015

Institut für Thermodynamik und Wärmetechnik
der Universität Stuttgart

2015

Contents

1. Introduction and motivation	1
1.1. Introduction	1
1.1.1. Political situation	1
1.1.2. State-of-the-art battery technology	2
1.2. Li-air batteries	5
1.2.1. Non-aqueous Li-O ₂ batteries	6
1.2.2. Aqueous Li-O ₂ batteries	11
1.3. Numerical modeling	15
1.4. Approach and scope	18
2. Experimental work	21
2.1. Background	21
2.1.1. Thermodynamics and kinetics of charge-transfer reactions	22
2.1.2. Double-layer structure and capacitance	27
2.1.3. The Ag O ₂ system in alkaline media	29
2.2. Methodology	32
2.2.1. Structural characterization of Ag/Ag ₂ O Gas Diffusion Electrodes	33
2.2.2. Electrochemical characterization of electrodes	39
2.3. Results and discussion	42
2.3.1. Structural characterization of Ag/Ag ₂ O Gas Diffusion Electrodes	42
2.3.2. Electrochemical characterization of Ag/Ag ₂ O Gas Diffusion Electrodes	48
2.4. Conclusions	62

3. Lattice-Boltzmann modeling and simulation	65
3.1. Background	65
3.1.1. The Boltzmann equation	66
3.1.2. The Lattice Boltzmann Method	67
3.1.3. Lattice Boltzmann multiphase models	70
3.1.4. Boundary conditions	73
3.2. Methodology	74
3.2.1. Model description and parametrization	74
3.2.2. Structure generation	80
3.2.3. Initial conditions	82
3.2.4. Simulation of Ag/Ag ₂ O electrodes	83
3.3. Results and discussion	88
3.3.1. Numerical tests	88
3.3.2. Simulation of $p_c - s$ curves	92
3.3.3. Determination of transport parameters and active surface area	97
3.4. Conclusions	101
4. Continuum modeling and simulation	105
4.1. Background	106
4.2. Methodology	114
4.2.1. Half-cell model	114
4.2.2. Full-cell model	120
4.2.3. Simulation methodology	124
4.3. Results and discussion	125
4.3.1. Model parametrization	125
4.3.2. Model validation	137
4.3.3. Electrode design	143
4.3.4. Full cell simulations	153
4.4. Conclusions	164
5. Summary and outlook	167
5.1. Summary	167
5.2. Outlook	172
Bibliography	175

Appendices	195
A. Pitzer formalism	197

List of Abbreviations

$p_c - s$	Capillary pressure-saturation curves, page 65
AFC	Alkaline fuel cell, page 13
APL	Anode protective layer, page 6
BET	Brunauer, Emmett, Teller method, page 42
BEV	Battery-powered electric vehicle, page 2
BGK	Bhatnagar-Gross-Krook single phase collision operator, page 70
BMBF	German Ministry of Education and Research, page 2
CFD	Computational fluid dynamics, page 17
CNG	Classical theory of nucleation and growth, page 121
CST	Concentrated solution theory, page 10
CTR	Charge-transfer reaction, page 22
CV	Cyclic voltammetry, page 18
D2Q9	Two-dimensional lattice with 9 discrete velocities, page 68
D3Q19	Three-dimensional lattice with 19 discrete velocities, page 69
DENIS	Detailed Electrochemistry and Numerical Impedance Spectroscopy, page 164
DFT	Density functional theory, page 10
DME	Dimethyl ether, page 9
DMSO	Dimethyl sulfoxide, page 9
DOD	Depth of discharge, page 154

EC	Ethylene carbonate, page 9
EIS	Electrochemical impedance spectroscopy, page 18
FE	Finite element discretization method, page 17
FEM	Free-energy multiphase model, page 71
FIB	Focused ion beam, page 18
FV	Finite volume discretization method, page 17
GDE	Gas diffusion electrode, page 11
GDL	Gas diffusion layer, page 6
HEV	Hybrid electric vehicle, page 4
IHP	Inner Helmholtz plane, page 28
IV	Characteristic current - voltage curve, page 26
LBM	Lattice-Boltzmann method, page 17
LiTFSI	Lithium Bis (Trifluoromethanesulfonyl) Imide, page 8
MC	Monte carlo simulations, page 16
MD	Molecular dynamics simulations, page 16
MIP	Mercury intrusion porosimetry, page 37
MPL	Micro-porous layer, page 39
OCP	Open circuit potential, page 22
OER	Oxygen evolution reaction, page 7
OHP	Outer Helmholtz plane, page 28
ORR	Oxygen reduction reaction, page 7
PC	Propylene carbonate, page 8
PEMFC	Polymer electrolyte membrane fuel cell, page 6
PSD	Pore size distribution, page 37
RHE	Reversible hydrogen electrode, page 23
RK	Rothman-Keller multiphase model, page 66
SC	Shan-Chen multiphase model, page 71
SEI	Solid electrolyte interphase, page 5

SEM	Scanning electron microscopy, page 18
SHE	Standard hydrogen electrode, page 23
SRT	Single relaxation time, page 70
TEGDME	Tetraethylene glycol dimethyl ether, page 9

List of Symbols

Symbol	Unit	Meaning	Eq.
A	m^2	Cross-sectional area	(4.40)
A_k	kg s^{-1}	Parameter determining surface tension	(3.29)
a	m^2	Surface area	(2.27)
a	m	Length scale of nucleus	(4.48)
a_i		Activity of species i	(2.3)
a_m^v	$\text{m}^2 \text{m}^{-3}$	Specific surface area of reaction m	(4.27)
B_k	m^2	Permeability of phase k	(2.42)
B_i		Parameter of the perturbation operator	(3.29)
c	m s^{-1}	Lattice velocity	(3.8)
c_s	m s^{-1}	Speed of sound	(3.26)
c_i	mol m^{-3}	Concentration of species i	(2.1)
$c_{p,i}$	$\text{J mol}^{-1} \text{K}^{-1}$	Heat capacity of species i	(2.4)
C_{dl}	F m^{-3}	Double-layer capacitance	(2.29)
c_{dl}	F m^{-2}	Area-specific double-layer capacitance	(2.29)
D_i	$\text{m}^2 \text{s}^{-1}$	Diffusion coefficient of species i	(2.38)
D_i^{migr}	$\text{m}^2 \text{s}^{-1}$	Migration coefficient of species i	(4.15)
d_p	m	Particle diameter i	(2.44)
E	V	Cell / half-cell voltage	(2.9)
E_m^a	J mol^{-1}	Activation energy of chemical reaction m	(4.8)
\mathbf{e}	m s^{-1}	Discrete lattice velocities	(3.7)
\mathbf{F}	N	External force	(3.1)
f		Probability distribution	(3.2)

Symbol	Unit	Meaning	Eq.
G	J	Free Gibbs Energy	(2.1)
ΔG	J mol ⁻¹	Gibbs free energy of the reaction	(2.12)
h_i	J mol ⁻¹	Molar enthalpy of species i	(2.4)
i	A m ⁻²	Current density	(2.50)
i_F	A m ⁻³	Faradaic current density	(2.18)
i_{dl}	A m ⁻³	Double-layer current density	(2.30)
$J(s)$		Leverett function	(3.48)
\vec{j}_i	mol m ⁻² s ⁻¹	Flux of species i	(2.38)
k_f, k_r		Forward and backward rate constant (units depend on the stoichiometry of the reaction)	(2.11)
k^0		Pre-exponential factor of rate constant	(2.12)
L	m	Length	(2.46)
l	m	Characteristic length	(3.42)
MW_i	kg mol ⁻¹	Molecular weight of species i	(4.38)
\overline{MW}_k	kg mol ⁻¹	Mean molecular weight of phase k	(4.38)
m_i	mol kg ⁻¹	Molality of substance i	(4.56)
N_i	mol	Amount of species i	(2.2)
N_0		Number of nucleation sites	(4.49)
n		Number of electrons in charge-transfer step	(2.5)
nv		Number of discrete velocities of the LB lattice	(3.5)
p_k	Pa	Pressure of phase k	(2.1)
Q	C	Charge	(2.27)
q	C m ⁻³	Charge density	(2.27)
\bar{r}	m	Pore radius	(2.45)
R	Ω m ²	Resistance	(2.46)
S		Supersaturation of the solution	(4.47)
s		Saturation of porous electrode	(2.44)
s_i	J mol ⁻¹ K ⁻¹	Molar entropy of species i	(2.4)
\dot{s}_i	mol m ⁻² s ⁻¹	Chemical source term of species i	(4.4)
t	s	Time	(2.29)
t_{\pm}		Transference number	(4.20)

Symbol	Unit	Meaning	Eq.
T	K	Temperature	(2.1)
V	m^3	Volume	(4.3)
V_i	$\text{m}^3 \text{mol}^{-1}$	Partial molar volume of species i	(4.39)
\bar{V}_k	$\text{m}^3 \text{mol}^{-1}$	Mean molar volume of phase k	(4.46)
\mathbf{v}	m s^{-1}	Velocity	(2.42)
w_i		Weights of the equilibrium distribution	(3.21)
X_i		Mole fraction of species i	(4.31)
Z		Zeldovich factor	(4.49)
Z	$\Omega \text{ cm}^2$	Impedance	(2.45)
z_i		Charge number of species i	(2.3)

Greek symbols

α_k		Parameter for compressibility of phase k	(3.24)
β_m		Symmetry factor of charge-transfer reaction m	(2.14)
β		Bruggeman coefficient	(2.41)
γ		Density ratio	(3.27)
γ	$^\circ$	Angle	(4.2)
γ_A	J m^{-2}	Surface energy	(4.47)
γ_i		Activity coefficient of species i	(4.68)
δ	m	Thickness of layer	(2.28)
ϵ		Relative permittivity	(2.28)
ϵ_k		Volume fraction of phase k	(2.39)
ϵ_0		Porosity	(3.50)
ζ_i		Directions in the D2Q25 pseudo-lattice	(3.32)
ζ_m	mol	Extent of reaction m	(2.2)
ζ		Parameters in the sensitivity analysis	(4.70)
η	V	Overpotential	(2.10)
η^{aggl}		Effectiveness factor of the agglomerate	(4.41)
Θ	$^\circ$	Contact angle	(3.41)
θ	$^\circ$	Angle between color gradient and velocity	(3.38)

Symbol	Unit	Meaning	Eq.
κ_i	$\text{m}^3 \text{mol}^{-1} \text{Pa}^{-1}$	Partial molar compressibility of species i	(4.39)
λ	m	Penetration depth of AC signal	(2.45)
μ_k	$\text{kg m}^{-1} \text{s}^{-1}$	Dynamic viscosity of phase k	(2.42)
μ_i	J mol^{-1}	Chemical potential of species i	(2.4)
$\bar{\mu}_i$	J mol^{-1}	Electrochemical potential of species i	(2.3)
ν_k		Kinematic viscosity of phase k	(3.19)
ν_i		Stoichiometric coefficient of species i	(2.2)
ν_{\pm}		Dissociation number of electrolyte	(4.20)
ρ_k	kg m^{-3}	Density of phase k	(3.5)
σ_k	S m^{-1}	Ionic or electronic conductivity of phase k	(2.43)
σ_D	C m^{-1}	Diffusional conductivity	(4.23)
σ	N m^{-1}	Surface tension	(3.30)
$\bar{\tau}$		Tortuosity factor	(2.39)
$\bar{\tau}$		Density average relaxation time	(3.30)
τ		Relaxation time	(3.18)
ϕ_k	V	Electric or ionic potential of phase k	(2.1)
ϕ_i		Parameter of the equilibrium distribution	(3.21)
$\Delta\phi$	V	Potential difference	(2.7)
ψ		Color field	(3.28)
Ω		Collision operator	(3.10)
ω_i		Weights of the 2D color gradient	(3.31)

Indices

a	Anodic	(2.11)
aggl	Agglomerate	(4.41)
c	Cathodic	(2.11)
dl	Double layer	(2.27)
ct	Charge-transfer	(2.48)
crit	Critical (radius or enthalpy)	(4.48)
cryst	Crystal phase	(4.50)

Symbol	Unit	Meaning	Eq.
elyte		Electrolyte phase	(2.6)
elode		Electrode phase	(2.6)
eq		Thermodynamic / Fluid mechanical equilibrium	(2.7)
i		Index of species or discrete velocities	(2.2)
j		Index of species	(4.18)
k		Index of phases	(3.13)
m		Index of chemical reactions and interfaces	(4.7)
O		Oxidized	(2.11)
pore		Pore space	(2.49)
R		Reduced	(2.11)
solid		Solid phase	(3.40)
tot		Total (resistance)	(2.50)
x, y, z	m	Spatial coordinates	(2.38)

Physical constants

ϵ^0	F m ⁻¹	Permittivity of vacuum - $8.854 \cdot 10^{-12}$	(2.28)
k_B	kg m ² s ⁻² K ⁻¹	Boltzmann constant - $1.3806488 \cdot 10^{-23}$	(4.47)
F	C mol ⁻¹	Faraday constant - 96485.34	(2.3)
N_A	mol ⁻¹	Avogadro number - $6.0221367 \cdot 10^{23}$	(2.28)
p^\ominus	Pa	Standard pressure - 101 325	(4.39)
R	J K ⁻¹ mol ⁻¹	Ideal gas constant - 8.314	(2.3)
T^\ominus	K	Reference temperature - 298.15	(2.4)

Dimensionless numbers

Bo		Bond number	(3.42)
Ca		Capillary number	(3.43)
Re		Reynolds number	(3.44)
Φ_1		Inner Thiele modulus	(4.42)
Φ_2		Outer Thiele modulus	(4.43)

Symbol	Unit	Meaning	Eq.
<i>Sh</i>		Sherwood number	(4.44)

Abstract

Lithium-air batteries are promising candidates as power sources for next-generation battery electric vehicles. Due to their high theoretical capacity they might allow driving ranges which are impossible to realize with state-of-the-art Li-ion technology. Mainly two types of Li-O₂ batteries are in the focus of intensive research at the moment, namely, batteries employing aprotic or aqueous electrolytes. Most of the publications are reported on the aprotic Li-O₂ battery, however, the stability of the solvent proved to be a major issue of this system. Moreover, the formation of solid, insulating discharge products limits the capacity of the battery.

The aqueous Li-O₂ battery is an interesting alternative. Offering a similar theoretical capacity it has a stable electrolyte and better rate-capability due to the applicability of so-called gas diffusion electrodes (GDE). In this type of electrode hydrophobic binders ensure the coexistence of gas and liquid phase, thereby, offering fast transport of O₂ in the gas phase. Similar to the aprotic system the formation of solid LiOH·H₂O limits the capacity of the battery. The interplay of transport, electrochemistry, and precipitation is very complex and hard to study experimentally.

In this work a multiscale modeling framework for the investigation of transport processes in porous GDEs for application in Li-O₂ batteries was developed. First, electrochemical measurements in a half-cell setup were conducted to access the electrochemical properties of Ag/Ag₂O model electrodes. In a following step 3D reconstructions of the electrode were used for Lattice-Boltzmann multiphase simulations on the micro-structure of the GDE. The simulations allow the determination of pore space saturation and corresponding effective transport parameters.

The results of experiments and micro-structure simulations were used for the parametrization of a detailed continuum model. Simulations of the half-cell setup are in good agreement to the experimental data over a large range of conditions and demonstrate the validity of the model. The validated model allows the determination and optimization of important design parameters and is able to guide the development of future electrodes for application in Li-O₂ batteries.

Moreover, the GDE model was inserted into a virtual battery cell. This allows conclusive insights in the operation of aqueous Li-O₂ batteries and reveals the limitations of different battery designs. The model gives the unique opportunity for the assessment of battery

power and energy which already in this early stage of research allows a comparison to other battery chemistries.

Kurzfassung

Die Lithium-Luft-Batterie ist eine vielversprechende neue Technologie, welche in den Elektrofahrzeugen der Zukunft zum Einsatz kommen könnte. Durch ihre hohe theoretische Kapazität könnte sie Reichweiten ermöglichen, die mit konventionellen Li-Ionen Akkumulatoren undenkbar sind. Lithium-Luft Batterien können entweder mit organischen oder wässrigen Elektrolyten betrieben werden. Der Fokus der internationalen Batterieforschung liegt momentan bei den aprotischen Systemen. Allerdings stellt die Stabilität dieser Elektrolyte sowie die Bildung isolierender Entladeprodukte eine große Herausforderung dar.

Die wässrige Li-O₂-Batterie erreicht eine vergleichbare Kapazität und bietet darüber hinaus aber eine reversible Elektrochemie und eine Entladung bei höheren Strömen. Dies wird erreicht durch den Einsatz von Gasdiffusionselektroden. Hydrophobe Binder ermöglichen die Koexistenz von Gas- und Flüssigphase im Porenraum der Elektrode, wodurch der Transport von Sauerstoff erheblich verbessert wird. Auch im wässrigen System wird die Kapazität begrenzt durch den Ausfall des festen Entladeprodukts LiOH·H₂O. Das Zusammenspiel von Transport, Elektrochemie und Ausfallreaktionen in der porösen Elektrode ist äußerst komplex und experimentell nur schwer zugänglich.

In dieser Arbeit wurde ein skalenübergreifendes Modell zur Untersuchung der Transportvorgänge in der porösen Gasdiffusionselektrode einer Li-O₂ Batterie entwickelt. Zunächst wurde eine experimentelle elektrochemische Charakterisierung von Ag/Ag₂O Modellelektroden in einer Halbzellen-Anordnung durchgeführt. Die Messungen dienen der Bestimmung von kinetischen Parametern und bieten die Basis zur Validierung des späteren Elektrodenmodells. Im nächsten Schritt wurden Mehrphasensimulationen beruhend auf einem Gitter-Boltzmann-Verfahren dazu verwendet, das Sättigungs- und Transportverhalten der porösen Elektroden zu untersuchen. Als Grundlage diente hierzu eine dreidimensionale Rekonstruktion der realen Mikrostruktur. Die Ergebnisse der Messungen und Mikrostruktur-Simulationen fließen direkt in ein detailliertes makroskopisches Kontinuumsmodell ein. Simulationen der Halbzell-Anordnung sind in guter Übereinstimmung mit den experimentellen Daten und demonstrieren die Aussagekraft des erstellten Modells. Dies ermöglicht die Bestimmung und Optimierung wichtiger struktureller Parameter, wodurch mögliche Maßnahmen für die Entwicklung besserer Gasdiffusionselektroden abgeleitet werden können.

Darüber hinaus wurde das Modell der Gasdiffusionselektrode in eine virtuelle Batteriezelle

eingesetzt. Diese Vorgehensweise ermöglicht einen detaillierten Einblick in den Betrieb wässriger Li-O₂ Batterien und gibt Aufschluss über limitierende Prozesse und Designkonzepte. So kann durch das Modell die wahrscheinliche Energie- und Leistungsdichte des Systems vorhergesagt werden, wodurch ein direkter Vergleich mit anderen Speichertechnologien ermöglicht wird.

1. Introduction and motivation

1.1. Introduction

1.1.1. Political situation

The global consumption of energy increased tremendously over the past decades. In recent years, this development was especially driven by the rapidly growing economies in South and East Asia.

At the moment almost 85 % of the world energy are produced from fossil fuels [1] like oil, gas and coal. The fear of expected shortages of these sources and the more and more visible effects of a global climate change led to an increased awareness of a sustainable handling of our natural resources.

The second pillar of today's energy supply is nuclear power. Major problem of this technology is the secure disposal of radio-active waste. Already in the early 1970s first protest movements tried to call the public attention to this issue and attempted to enforce a nuclear phaseout. However, it was only for the terrible accident in the nuclear power plant in Fukushima (Japan) that this discussion reached the center of our society.

As a result of this accident, the German government enacted the so called law of 'Energiewende' in June 2011[2]. The main goals are a step-wise phaseout from nuclear energy until the end of 2022 and a reduction of energy consumption and greenhouse gases until 2020 by 20 and 40%, respectively. The former is supposed to be achieved with an increase in the share of renewable energies up to 18% in gross final energy consumption [3].

While the efforts of the 'Energiewende' comprise the sectors electricity, heat and transportation, the electricity sector recently received the most attention. An increase in the share of electricity produced from renewable sources requires an extension of the power

grid in combination with a storage of surplus energy. These steps are necessary in order to guarantee the future electricity supply and to balance load and production fluctuations. In the transportation sector the topic of electromobility will become increasingly important. Until 2020 the German government would like to bring one million electric cars on German roads [4]. At the current state this number will be hard to attain since at the beginning of 2014 an overall number of only 12,156 electric vehicles were registered in Germany [5]. In the electricity as well as the transportation sector electrochemical devices will play a key role to reach these ambitious goals. Fuel and electrolyzer cells can be used for local and centralized energy supply and storage. Moreover, fuel cell technology might also become more important for the automotive sector. Still, a special focus is here on the development of battery-powered electric vehicles (BEV). However, at the moment this technology is not competitive with the internal combustion engine. Considerable progress in science and engineering has to be made in order to produce batteries with higher capacities at lower costs.

It is foreseeable that a mere development of the existing Li-ion battery technology will eventually not be enough to achieve this target. Research on novel battery materials and design concepts will be absolutely mandatory. Therefore, the German government granted substantial funding (2 billion €) [4] for numerous projects in order to make Germany a key player in the market of electromobility. The present work is part of the BMBF (German Ministry of Education and Research) funded project 'Strom aus Luft und Li(thium)' (LuLi) [6] which started during this initiative.

1.1.2. State-of-the-art battery technology

Since the invention of the 'electric pile' by Alessandro Volta around 1800 it was a long road of developments to the modern batteries we know today. Still, the underlying principle is the same. In general the different battery types can be divided in two main groups, namely primary and secondary or rechargeable batteries. Figure 1.1 shows a schematic of the working principle of a generic battery.

During discharge electrons flow from the negative electrode (anode) to the positive electrode (cathode). In this process the participating materials at the cathode and anode get reduced and oxidized, respectively. The electrolyte is needed for the transport of dissolved charge carriers (ions) between the two electrodes. In rechargeable batteries this process is reversed upon charging. Now, the oxidation takes place at the positive electrode

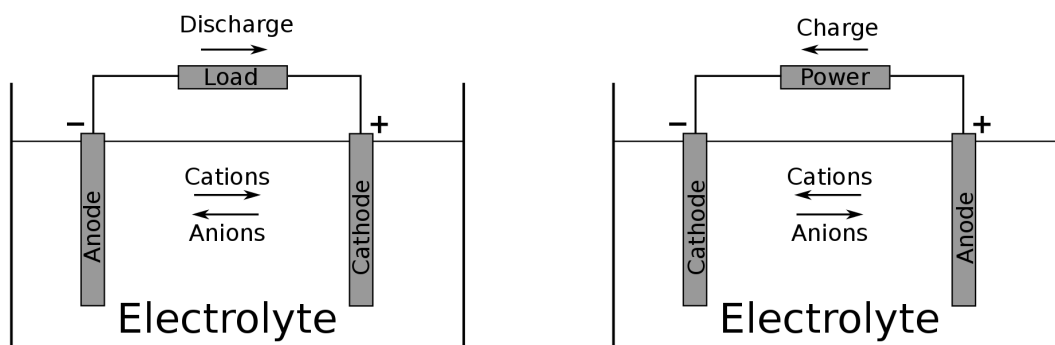


Figure 1.1.: Schematic figure of a battery cell during discharge (left) and charge (right).

and the reduction occurs at the negative electrode.

Although formally not correct, it is common in the battery community to name the electrodes according to their electrochemistry during discharge. This convention is adhered here, so the positive electrode is named cathode and the negative electrode is named anode.

The choice of materials determines the cell voltage, capacity and specific energy of the battery. The latter is especially important for batteries in mobile applications, where high specific energy densities are desirable. In principle it is possible to combine a large number of different materials in a battery cell. However, not all of these couples offer a reversible (electro)chemistry. A comprehensive review of primary and secondary batteries can be found in 'Linden's Handbook of batteries' [7]. In this context the discussion is limited to the most common rechargeable battery types.

Figure 1.2 shows specific energy densities of the battery concepts discussed in this section. The theoretical energy densities are calculated for the pure electrochemically active materials. Energy densities of practical cells are typically much lower due to other cell components, like the battery housing etc.. For the established technologies the practical values can be easily obtained from the manufacturers. Li-sulfur and Li-air batteries are still under development and future practical energy densities are hard to predict. As a rule of thumb about 25 % of the theoretical energy density can be reached in practice. The left-hand side of Figure 1.2 shows the specific energy density of the **lead-acid battery**. This battery was already invented in 1860 by Gaston Planté. Owing to its application as starter battery in vehicles with internal combustion engine, it is still the most produced type of battery. The low cost and high reliability make it also very interesting for stationary and

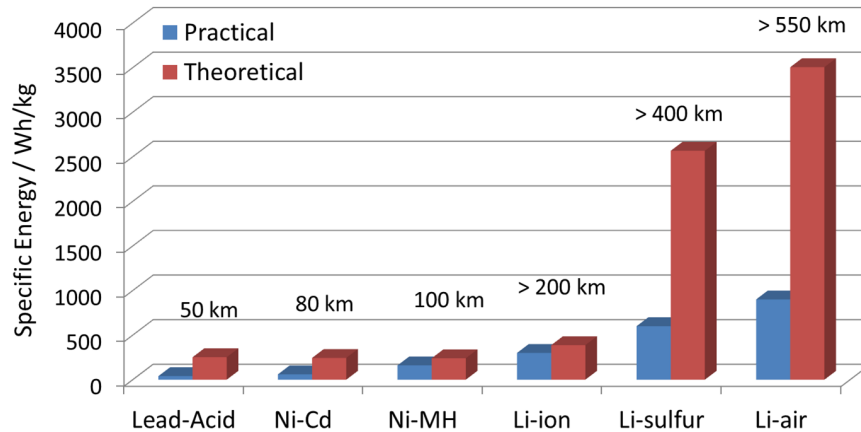


Figure 1.2.: Specific energies for common rechargeable battery types. The theoretical specific energies are calculated based on the pure components. Practical specific energies for Li-S and Li-air batteries are estimates based on the experience that around 25 % of the theoretical energy density can be reached in practice [8, 9]. The given driving ranges are calculated based on practical energy densities for electric vehicles comparable to a Nissan Leaf [10].

emergency power supply. Main drawback of this type of battery is the low specific energy. **Nickel-cadmium** and **nickel-metal hydride batteries** offer higher capacities and an excellent cycle life. This makes them suitable candidates for application in consumer electronics and portable devices. Due to their high reliability and comparably low cost they are also used in modern Hybrid Electric Vehicles (HEV), like the Toyota Prius [11]. Developments in the market of laptop computers and smartphones drove the research in the battery community to systems with higher energy densities. **Lithium-ion** technology offers at the moment the highest energy density of all commercially available rechargeable battery systems [12, 13]. In its most common configuration the battery consists of a graphite anode, a transition metal as lithium source (LiCoO_2) and a solution of a lithium salt (LiPF_6) in a carbonate solvent as electrolyte. This design is often referred to as a 'rocking chair' battery. During charge/discharge the Li ions are de/intercalated at one electrode and then 'rock' to the other electrode to get intercalated again.

At the cathode several intercalation materials are under investigation which offer lower cost and less safety issues (e.g. LiFePO_4) or a higher operational voltage (e.g. $\text{Li}_{0.5}\text{NiMnO}_4$) [14]. At the anode, lithium metal alloys (Li-Si, Li-Sn) could contribute to improving the energy density of future Li-ion batteries. Eventually, it is desirable to use pure Li metal as anode material. However, the high reactivity of lithium prevented a successful application

in commercial batteries. In contact with the electrolyte a passivating film quickly forms on the Li surface, the so called Solid Electrolyte Interphase (SEI). The SEI is permeable for lithium ions but a non-uniform plating can produce the growth of dendrites. These dendrites in turn can cause internal shorts which might lead to thermal runaway and explosion of the battery. The dendrite growth is a serious problem which all Li metal based battery types have in common.

Still, the use of lithium metal electrodes is necessary to reach energy densities which are needed for practical driving ranges of BEVs (see Figure 1.2). The focus in lithium battery research in recent years turned to '**beyond Li-ion technology**'. This class mainly comprises Li-sulfur and Li-air conversion batteries. First prototypes of Li-sulfur batteries are already available (Sion power) on the market. However, a commercialization of Li-air batteries is still far away into the future. The enormous perspective of this battery with its very high theoretical energy density attracted a lot of attention. This kind of battery might even offer the opportunity to attain driving ranges which exceed 550 km (Figure 1.2). A detailed description of the Li-air system can be found in Section 1.2. Despite these great perspectives, the fear of a depletion of Li already stimulated research on other battery chemistries based on, e.g., Mg, Al, Na, or Si [15–19]. Some of these systems offer only slightly lower or even comparable specific energy densities but the raw materials are much more abundant.

1.2. Li-air batteries

Due to their high theoretical specific energy Li-air batteries have the potential to become a serious competitor to fossil fuels in the automotive sector. On the realistic assumption that only 25% of the theoretical energy density can be reached in practice, the expected driving range is still more than 500 km (Figure 1.2).

The terminology of Li-air suggests that this battery operates on ambient air at the positive electrode. This is just a part of the truth, as only the O_2 in the air is reduced during discharge. Other components like CO_2 or moisture are in fact detrimental for the cycle life of the battery and will need to be filtered by special membranes. In most studies, including this work, the authors use purified oxygen in their experimental setup in order to avoid side reactions. Therefore, the terminology 'Li- O_2 ' battery will be used in this work.

At the anode a Li metal electrode is employed which is necessary to reach the highest possible specific energy. The typical problems of Li metal electrodes have already been discussed in the previous Section 1.1.2 for Li-ion batteries. In Li-O₂ batteries an additional Anode Protective Layer (APL) will be necessary in order to prevent contact of the Li metal with O₂, CO₂ and most importantly H₂O. In some respect Li-O₂ batteries can be regarded as fuel cells with a Li metal anode, unfortunately combining all major problems of the two systems. But this similarity can also be exploited as a guide for new developments of Li-O₂ cell components.

In the literature mainly four different types of Li-O₂ batteries are discussed. They differ by the choice of electrolyte, which can either be aprotic, aqueous or a solid polymer. The fourth design consists of an aqueous electrolyte at the cathode and an aprotic electrolyte at the anode and is typically called the 'mixed' design. An overview of the the different types can be found in one of the numerous reviews on Li-O₂ batteries [8, 20–28].

The two most common types use aprotic or aqueous electrolytes and will be discussed in Section 1.2.1 and 1.2.2, respectively.

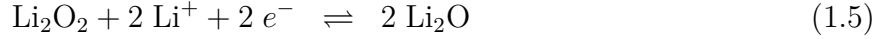
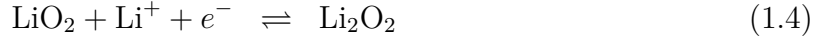
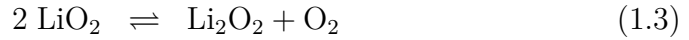
1.2.1. Non-aqueous Li-O₂ batteries

Intense research on this type of battery started in 1996 when Abraham *et al.* [29] demonstrated the use of organic electrolytes for Li-O₂ batteries. Since then the aprotic system attracted the most attention in the community and the majority of published work was done on this type of battery.

Working principle

Figure 1.3 shows the typical design and working principle of an aprotic Li-O₂ battery. The cathode usually consists of a porous carbon material. Various types of carbon materials with different grain sizes and specific surface areas were studied in the literature as possible electrode material [30, 31]. Small amounts of binder material are added to improve the stability of the layer. Some groups also propose Gas Diffusion Layers (GDL) of Polymer Electrolyte Membrane Fuel Cells (PEMFC) as additional support for an improved mechanical stability [32]. In PEMFCs the hydrophobic binders have the additional task to prevent flooding of the pore space with water. This is important because the transport

of reactants (e.g. O_2) in the gas phase is much faster than in the liquid phase. For the non-polar aprotic solvents it can be assumed that the whole pore space is flooded with electrolyte. O_2 enters the cell on the left hand side, dissolves in the electrolyte and then diffuses to the active sites on the electrode surface. During discharge O_2 is reduced in the Oxygen Reduction Reaction (ORR). The current understanding of the reaction mechanism is shown in Equations 1.1 - 1.5 [12].



First the O_2 molecule is reduced to the superoxide (Eq. (1.1)). This intermediate species is highly reactive and rapidly reacts with Li^+ to form LiO_2 (Eq. (1.2)). In most electrolytes this lithium superoxide is not very stable and reacts according to reactions (1.3) or (1.4) to the more stable reaction product Li_2O_2 . In the literature the lithium peroxide is reported as most common discharge product. A further reduction to Li_2O (Eq. (1.5)) has indeed been observed in cyclic voltammetry studies [33, 34] but not for full Li- O_2 cells [12]. However, the exact mechanism of the ORR in organic solvents is still a topic of active research in the Li- O_2 community. The discharge product Li_2O_2 has a low solubility and immediately precipitates as solid material in the porous structure of the cathode.

The mechanism of the Oxygen Evolution Reaction (OER) received less attention compared to the ORR. Stability problems of the electrolyte during discharge made systematic studies very challenging [12, 34]. It was shown that among the possible discharge products only an oxidation of Li_2O_2 is possible in the battery cell [35]. The proposed mechanism [36] suggests a formation of LiO_2 like species on the surface



which disproportionate according to



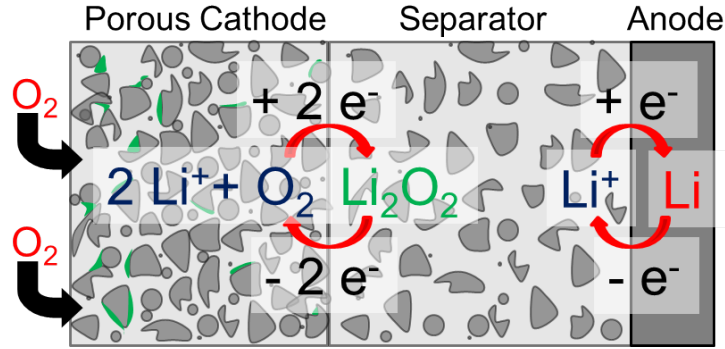


Figure 1.3.: Schematic drawing of an aprotic Li-O₂ battery. Oxygen enters the porous electrode from the left and dissolves in the liquid electrolyte. During discharge O₂ is reduced in the cathode and Li is oxidized at the anode.

to evolve O₂. The total oxidation step follows as



The two electrodes are separated by a porous separator which is typically soaked with the electrolyte solution. At the anode Li metal is oxidized and the Li ions dissolve in the liquid electrolyte according to



The global reaction of an aprotic Li-O₂ cell is given by



Challenges and problems

The search for a suitable liquid electrolyte is one of the largest challenges of the non-aqueous Li-O₂ battery. Several organic solvents have been proposed for use in Li-O₂ batteries [37–41]. Typical electrolyte salts are LiTFSI and LiPF₆ which are known from Li-ion batteries. However, most of these electrolyte solutions proved to be unstable during the operation of the cell. It was found that the carbonate- and ether-based solvents (PC,

EC, DME, etc.) which are often employed in Li-ion batteries decompose during discharge [36, 42–44]. Probable reason is a nucleophilic attack of the highly reactive intermediate reaction product O_2^- (Eq. (1.1)) on the solvent chain [45]. After this discovery several organic solvents were screened as possible candidates for Li- O_2 batteries. DMSO [46] and TEGDME [32, 40] showed an improved stability and are commonly used in present studies. However, also with these solvents it was not possible to demonstrate a stable operation over a large number of cycles [32, 36]. An alternative might be the class of room-temperature ionic liquids [47, 48]. These compounds seem to be stable, reasonably conductive, inflammable and have a low volatility. An issue is the often low solubility and diffusivity of O_2 . The transport of O_2 in the liquid electrolyte of the flooded electrode might be the limiting factor for high discharge currents [49, 50].

Also, the stability of the carbon electrode proved to be a problem itself [36]. Sample electrodes which were prepared from C^{13} carbon showed a formation of C^{13}O_2 during charge which is a strong indication for their instability. Coated or even carbon-free electrodes might be practical alternatives for this problem. These electrodes could for example be based on an inexpensive catalyst.

Several catalyst materials were studied for Li- O_2 batteries. Apart from noble metal catalysts [32, 51, 52] also several oxide materials [24, 53–55], like $\alpha\text{-MnO}_2$, showed a good performance. The catalyst reduces the voltage gap between discharge and charge and thus, improves the cycling efficiency of the system. However, a detailed investigation of the catalytic mechanism remains difficult with the parallel side reactions mentioned above [36]. At the moment it is even questionable if a catalyst does not merely accelerate the degradation of the battery cell.

Even if all the fundamental stability issues can be resolved some important challenges remain. As briefly mentioned above, the transport of oxygen occurs by diffusion in the liquid electrolyte. As the transport of O_2 in the liquid phase is comparatively slow it will most likely determine the maximum discharge current [49]. This problem is alleviated by the solid product Li_2O_2 which forms in the porous structure of the cathode during discharge (Eq. (1.3)). On the one hand the transport pathways for O_2 and Li^+ ions are blocked and on the other hand active surfaces are passivated. Li_2O_2 is also known to have a poor electronic conductivity [56–58] and even small amounts might be enough to shut down the surface completely. Recent studies show that the surface conductivity might be higher compared to the conductivity of the bulk material [36]. This gives hope that nonetheless reasonable capacities can be attained. Detailed theoretical and experimental

studies will be necessary to clarify this issue. This will also help to explain the different growth modes and particle formations of the discharge product, like toroids etc, which have been reported in the literature [36, 59].

Continuum modeling

The first continuum model of a non-aqueous Li-O₂ battery was presented by Sandhu *et al.* [50] in 2007. It includes the dissolution, transport and reduction of O₂ in the liquid electrolyte of the porous cathode. The model demonstrates the influence of pore-clogging on the discharge performance. Following publications of Andrei *et al.* [60] and Albertus *et al.* [61] also include the transport of Li ions using Concentrated Solution Theory (CST) [62]. In addition to the clogging of the pore space they take into account a passivation of the surface [60, 61] and a limited conductivity of the discharge products [61]. A more detailed study of passivation effects can also be found in [63].

Figure 1.4 shows simulated spatial profiles of porosity and O₂ concentration during discharge of an aprotic Li-O₂ battery [64] following the modeling work of Andrei *et al.* [60]. The model takes into account a passivation of the active surface and an increase in transport resistance due to the solid discharge products. A limiting electric conductivity of the product film on the surface of the electrode is not included in this study. The oxygen enters the cell at $y=0$. The simulations show that due to a diffusion limitation of O₂ the ORR mainly proceeds close to the O₂ inlet. The discharge products enhance the transport problem and at the end of discharge the inlet is totally blocked.

These first modeling studies were parametrized for carbonate solvents because the severe stability problems were not known at the time. The simulation results will change due to different O₂ solubilities and diffusivities in other electrolyte solutions [65]. Still, the simulations demonstrate the major transport and design problems which remain even if a stable system can be found. Recent publications also include side reactions and a degradation of the organic electrolyte [66–68]. Continuum models in general are not able to predict the stability of different electrolyte systems or to make suggestions for more suitable solvents. These questions will need to be addressed in DFT studies [41, 69]. However, they allow to study the effects of solvent degradation on the cell or electrode performance.

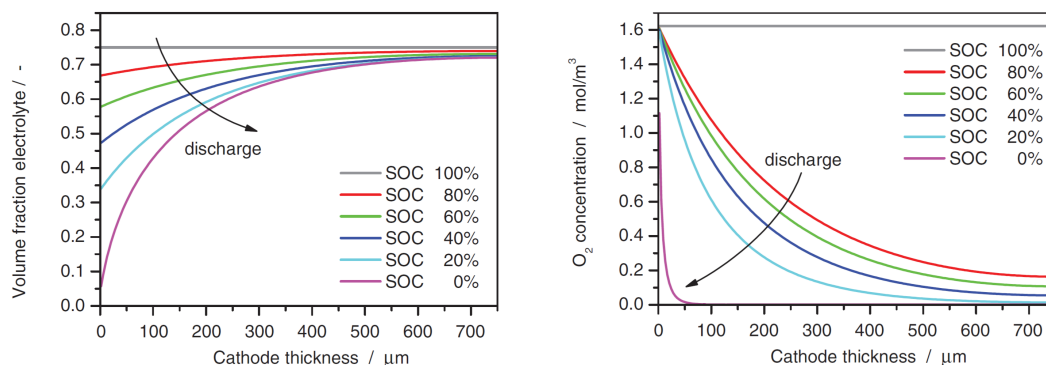


Figure 1.4.: Spatial profiles of electrolyte volume fraction (left) and O_2 concentration (right) during discharge of a non-aqueous Li- O_2 battery at 1 A/m^2 [64]. At the end of discharge the solid discharge products block the inlet due to a slow transport of O_2 in the liquid electrolyte.

1.2.2. Aqueous Li- O_2 batteries

Although aqueous Li- O_2 batteries have slightly smaller theoretical capacities [22], they are an interesting alternative to the aprotic system [70–72]. Aqueous LiOH solution is the most common electrolyte for this battery type. It offers the advantage of a high ionic conductivity and a large stability window to operate the cell.

Working principle

Figure 1.5 shows the schematic image of a possible design for an aqueous Li- O_2 battery. Similar to the aprotic system it has a porous cathode where O_2 is reduced during discharge. However, in the aqueous system the concept of Gas Diffusion Electrodes (GDE) can be used [73]. GDEs were originally developed for fuel cells and also find application in chemical reactors for, e.g., chlor-alkali electrolysis [74]. In GDEs hydrophobic binder materials ensure the coexistence of gas and liquid phase. Their design offers the advantage of a fast transport of reacting species in the gas phase. This allows for high current densities without any visible mass transport limitations. The mechanism of the ORR in alkaline media has been the subject of intensive research over the past decades [75, 76]. Section 2.1.3 gives an overview of ORR and OER on noble metal catalysts in alkaline media. It is important to note that the discharge in aqueous Li- O_2 batteries is a two-stage process. Oxygen enters the electrode in the gas phase and subsequently dissolves in the

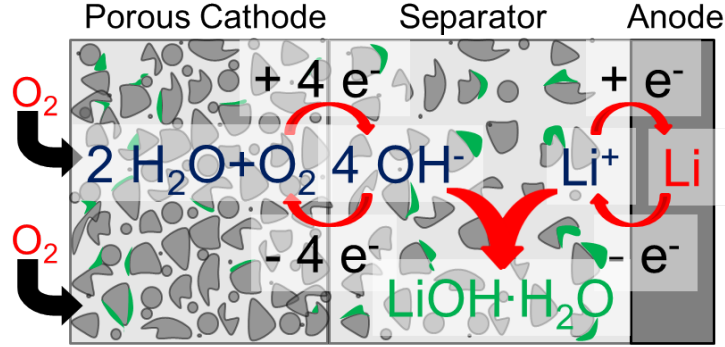
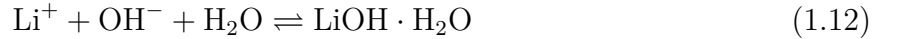


Figure 1.5.: Schematic drawing of an aqueous Li-O₂ battery. Oxygen enters the porous electrode from the left and dissolves in the liquid electrolyte. During discharge O₂ is reduced in the cathode and Li is oxidized at the anode.

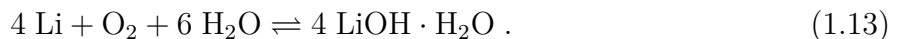
liquid electrolyte. The dissolved O₂ is reduced in the ORR to form hydroxide ions which are still dissolved in the liquid electrolyte



The concentration of LiOH in the liquid electrolyte rises until the solubility limit is reached ($c_s = 5.3 \text{ mol/l}$, 25 °C). Beyond this point LiOH·H₂O starts to precipitate according to



and the Li ion concentration stays approximately constant. The precipitation can either start on nucleation sites on the surface of the porous cathode and separator or on impurities of the electrolyte solution. The transference number of Li ions in aqueous solutions is pretty small ($t_+ \approx 0.16$). Simulations and experiment show that due to this effect the precipitation of solid discharge products mainly occurs in the separator region close to the anode [77, 78]. Lithium metal reacts vigorously with water and needs to be protected from contact with the aqueous electrolyte by an APL. Typically Li ion conducting glass ceramics are used for this task [71, 79]. The Li metal is either in direct contact with the glass or surrounded by an organic electrolyte which might also be embedded in a polymer matrix. The global cell reaction is given by



Challenges and problems

The APL with its Li ion conducting glass ceramic will be most likely one of the largest hurdles for a commercial aqueous Li-O₂ battery. The ionic conductivity of these glasses is typically several orders of magnitude smaller compared to the aqueous electrolyte solution. Thus, they have to be manufactured as thin as possible but still need to be stable against the Li metal anode and the strongly alkaline electrolyte solution. Several groups [77, 79–82] dedicated their efforts to this task and already demonstrated a stable operation over a reasonable number of cycles. It was also proposed to use highly concentrated solutions of LiCl in order to prevent a degradation of the ceramic glass [83]. An overview of possible materials can be found in [84].

A lot of research has been done on the ORR in alkaline media [75, 85]. The efforts have been mainly driven by research on Alkaline Fuel Cells (AFC). Comparatively little is known about the exact mechanism of oxygen evolution. For the development of high-energy Li-O₂ batteries it is essential to find bi-functional catalysts which catalyze both ORR and OER [76]. Several materials were proposed as catalyst for Li-O₂ batteries, ranging from noble metals to metal oxides [86]. The noble metals show a superior catalytic activity. Au and Pt are probably the best catalysts for oxygen reduction and Ru and Ir show superb performance in the OER [86]. However, these materials are too expensive for commercial systems. Oxide materials like MnO₂ or Co₃O₄ are interesting alternatives [87–89]. They do not offer the high reaction rates of noble metals but their cost is much lower. Typically the catalysts are coated or distributed on a carbon support. It is well established that carbon materials dissolve at the potentials of oxygen evolution [90–93]. Graphite materials and carbon nanotubes exhibit a higher stability but are probably also not suitable for applications which require a long cycle life [86]. Another challenge for the stability of the electrodes is the evolution of gas bubbles in the porous structure during charge. At high currents the resulting pressure might cause a mechanical degradation of the electrode. Some authors propose the use of a second metal electrode for OER [77]. This approach reduces the risk of carbon corrosion at the ORR electrode. However, it will also substantially reduce possible energy densities. Another suggestion is to manufacture the GDEs based on pure metal oxide catalysts mixed with a metal as conductive agent (e.g. Ag). This promising approach has the advantage that the serious problem of carbon corrosion can be avoided and additionally Ag is an excellent catalyst for the ORR in alkaline media [94, 95].

Suitable membranes at the O_2 inlet are especially important for the aqueous system. On the one hand $LiOH$ solution is known to be one of the best absorbers of CO_2 . The resulting lithium carbonate is insoluble and cannot be oxidized during charge. On the other hand the membranes have to impede the evaporation of water in order to prevent the cell from drying out. This difficult yet possible task is demonstrated by the developments made for Zn-air batteries.

The solid product $LiOH \cdot H_2O$ precipitates in the cell during discharge. This also influences the transport of reactants and eventually limits the capacity of the cell. However, in the aqueous system the reduction of oxygen and precipitation of $LiOH \cdot H_2O$ is a two-stage process (Eq. (1.11) and (1.12)). This gives an additional degree of freedom for an engineering of the battery design. Stevens *et al.* [77] and Horstmann *et al.* [78] demonstrated that a bulk separator is able to improve the capacity of the battery. In their approach the APL is coated with a polymer in order to prevent a blockage of transport pathways of the Li ions. The precipitate accumulates on the bottom of the separator which in this case also serves as a reservoir for $LiOH \cdot H_2O$.

Continuum modeling

Compared to the work done on the aprotic system, models of aqueous $Li-O_2$ batteries are scarce. In this respect the present work closes a gap in the modeling of Li-air batteries with aqueous electrolyte. Andrei *et al.* [96] simulate a battery with aqueous electrolyte but model the reduction of O_2 to $LiOH \cdot H_2O$ in a single reaction step. As a result most of the discharge product forms at the O_2 inlet. Horstmann *et al.* [78] explicitly take into account reduction and precipitation as a two stage process. In agreement with experimental observations they predict a formation of solid discharge products close to the anode.

At this point the similarity to fuel cells, especially to the AFC, can be exploited [55, 73, 97, 98]. First transport models of AFCs were developed on the assumption of thin electrolyte films on the surface of electrode particles [99]. This model was later on extended for flooded agglomerates [100] where a good agreement with experiments could be reported [74]. A special challenge is the correct description of the saturation management in the heterogeneous structure (hydrophilic electrode, hydrophobic binder) of the GDE. This is a crucial point as the saturation determines the transport in the porous structure. Special methods for volume-averaged 1D models were developed for PEMFCs [98, 101] and can be transferred to the present case of GDEs in $Li-O_2$ batteries. Central to this approach

is the idea of a semi-empirical correlation which describes the saturation as function of the capillary pressure, the so called 'Leverett function'. This function has to be measured or calculated for each electrode as it is specific to the respective material and structure [102–108]. Lattice-Boltzmann simulations proved to be a useful tool for solving the Navier-Stokes equations on the nano and micrometer scale. As a result the characteristic pressure-saturation curves and effective transport parameters can be obtained [109–111].

1.3. Numerical modeling

The Nobel prize in Chemistry was in 2013 awarded to Karplus, Levitt and Warshel "for the development of multiscale models for complex chemical systems" [112]. This impressively underlines the importance of modeling and simulation for the understanding of complex systems. Numerical simulations give the unique possibility to study and understand systems which are inaccessible or hard to address experimentally. In this sense numerical simulations have to be understood as additional tool to study physical, chemical, biological or engineering problems. In every discipline simulation tools were developed which are specific to the questions which need to be answered. While in the natural sciences the focus is often on the atomic and molecular scale, the problems in engineering disciplines range up to hundreds of meters. Every simulation tool offers unique possibilities but also has its limitations. It is up to the user to choose the right tool which is specific to his problem.

Figure 1.6 gives an overview of modeling techniques which are used for battery-related applications on the different length and time scales. Methods on the upper left have a high level of detail and require no or only few input parameters but are computationally very demanding. The computational cost decreases towards the lower right corner on the expense of the level of detail. Therefore, the number of required input parameters, e.g. material properties, increases. In a multiscale modeling approach the different simulation tools bridge across the length and time scales in order to increase the predictivity of the model.

Ab-initio and Density Functional Theory (DFT) methods are able to give insights on the electronic structure on an atomistic scale by solving the Schrödinger equation [114]. Although continuous developments make the DFT method increasingly efficient, the calculations are limited to a small number of molecules. However, DFT is a well-accepted

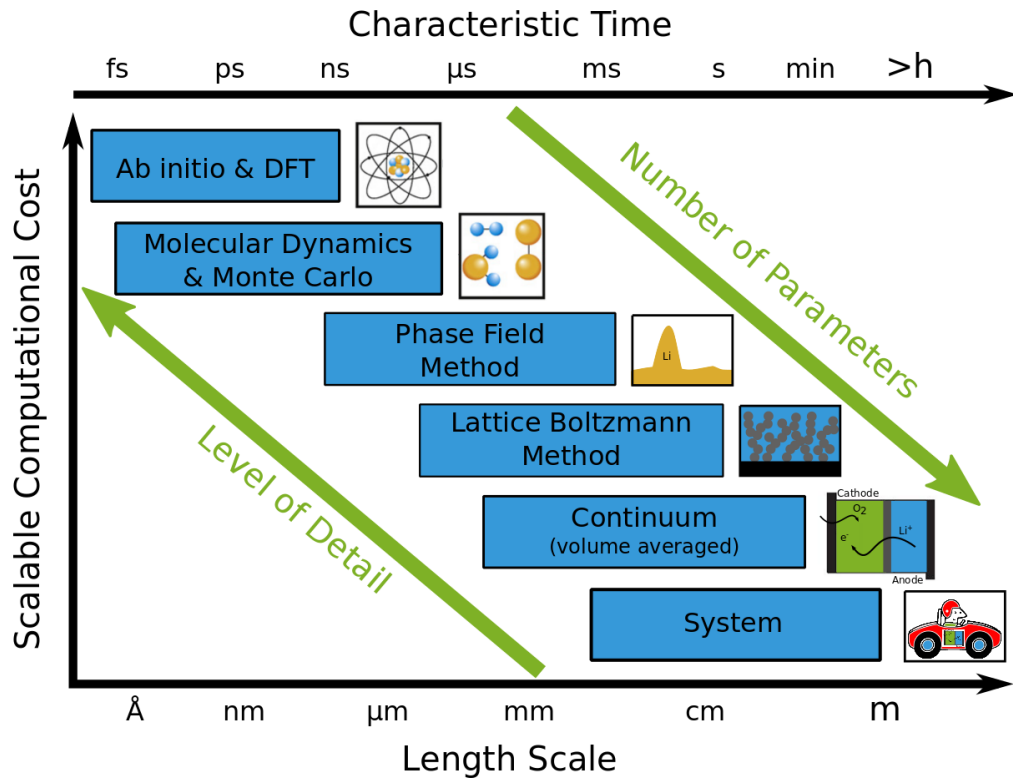


Figure 1.6.: Multiscale modeling on different length and time scales for battery-related applications. In the style of [113]

tool in the electrochemical community. DFT studies allow the calculation of reaction pathways and corresponding activation energies [115]. The method is able to predict the stability and catalytic activity of electrode materials [116] as well as their electric conductivity [58].

While in ab-initio molecular dynamics simulations the force field of interacting particles is updated in ab-initio calculations, the classical **Molecular Dynamics** and **Monte Carlo** methods use a fixed parametrization [117]. This reduces the computational load tremendously and allows the treatment of a considerably larger system of molecules. Classical statistical mechanics help to translate the simulation results into thermodynamic and transport properties [118]. Possible applications are the determination of diffusion coefficients and kinetic parameters (MD) or properties of phase equilibrium like surface tension and vapor pressure (MC) [119]. Another active field of research is the study of protein folding and resulting enzymatic activity which was awarded with the above-mentioned Nobel prize .

Phase-field methods can be used to study the formation and evolution of phases on a micro-structure scale [120]. The processes are already on the brink to the continuum level and result from the non-equilibrium thermodynamics of the system. In Li-O₂ batteries the method can be used to study the formation of the discharge products Li₂O₂ [121] and LiOH·H₂O. On the anode side the method might give answers to the serious problem of dendritic growth.

The transport in these discrete micro-structures can in turn be treated in methods which are based on the solution of the Boltzmann equation. These **Lattice-Boltzmann-Methods** (LBM) are typically formulated to recover the Navier-Stokes equations in the macroscopic limit [122]. It is a relatively novel method in Computational Fluid Dynamics (CFD) and especially advantageous for the calculation of multiphase flow problems with a free surface and flow in complex geometries. In this context it was applied for the calculation of pressure-saturation relationships in porous electrodes [110].

Traditional **continuum modeling** methods rely on the conservation equations for mass, momentum and total energy [123]. These methods are typically discretized using a finite element (FE) or finite volume (FV) approach. For CFD applications usually the FV method is preferred as it is intrinsically conservative. The range of applications is almost limitless. Typical examples in the engineering sector are chemical reactors, filter media or whole combustion engines [124]. The meshing of complex geometries is a common problem of the method and volume-averaged representations of geometries and phases are often used which are also computationally more efficient [125]. Continuum simulations can be utilized to study transport and reaction mechanisms in electrochemical systems [62] like batteries and fuel cells [64, 78].

These methods are already much less demanding in terms of computational load compared to ab-initio calculations. However, a further reduction of detail is often required for system simulations or even management systems in e.g. combustion engines or battery packs [126].

In this work the focus is on the electrode and cell level simulation of aqueous Li-O₂ batteries. The typical length scale comprises several microns up to several cm. Therefore, this work is situated in the length scale of continuum modeling. LBM simulations are used for a detailed understanding of transport processes in the porous structure of the GDE and are supplemental to the traditional continuum modeling approach on the cell level.

1.4. Approach and scope

Li-O₂ technology might play a key role in the development of batteries for electric vehicles [8, 9]. However, as shown in Section 1.2, there are many fundamental issues which need to be addressed. Theoretical models are helpful in creating an improved understanding of the system and relevant processes therein. Therefore, they can guide the technical progress in this field.

Aim of this work is the development of a detailed continuum model for reaction and transport in aqueous Li-O₂ batteries. The model can be used to study different design options of cell components and full battery systems.

An important step towards a validated model is the reliable parametrization of relevant physical properties. Thermodynamic parameters of the LiOH solution can be obtained from the comprehensive literature on aqueous electrolytes. Structural and kinetic parameters of the GDE are specific to the catalyst system and have to be obtained from experiments. Therefore, Cyclic Voltammetry (CV) and Electrochemical Impedance Spectroscopy (EIS) measurements on Ag model GDEs are performed in order to determine the electrochemical properties of the system. Additionally, the electrodes are studied by project partners with Focused Ion Beam - Scanning Electron Microscopy (FIB-SEM). The images allow to generate a three-dimensional reconstruction of the GDE micro-structure which can be used for a detailed structural characterization. An overview of the experimental activities is given in Chapter 2.

Structural parameters of the GDE also have a strong influence on the transport of reactants in the porous media. In compact porous media the transport pathways may be tortuous and thus effective transport properties many times smaller than in the respective bulk phase. This effect is enhanced if a second phase (e.g. gas or solid discharge products) is present in the pore space. In this case the saturation of the GDE with liquid electrolyte determines the transport of reactants in the porous network. However, it is cumbersome to study the saturation behavior of porous media experimentally. Lattice-Boltzmann simulations on the reconstructed micro-structure of the model GDEs are helpful to clarify the behavior. A Lattice-Boltzmann multiphase model, which has been developed for the simulation of an air-water system in porous media is introduced in Chapter 3. The model is validated on simple flow problems, such as a steady bubble or capillary wetting. Subsequent 2D and 3D simulations are used to determine the saturation behavior and effective transport properties of the reconstructed model electrodes.

The experimental data (Chapter 2) and the Lattice-Boltzmann simulations (Chapter 3) provide the basis for the parametrization and validation of the detailed continuum model which is derived in Chapter 4. The model includes a multiphase description of the cathode GDE, where solid, liquid, and gaseous phases coexist. It takes into account oxygen dissolution in the electrolyte, oxygen reduction and lithium oxidation at the two electrodes, and precipitation of solid $\text{LiOH}\cdot\text{H}_2\text{O}$. The validated model allows for interesting insights on the operation of GDEs and Li-O_2 single-cells. A sensitivity analysis and parameter variations are conducted to identify the most important parameters for electrode and cell design.

The most important aspects and findings are summarized at the end of each chapter. Finally, Chapter 5 concludes this thesis and gives an outlook on possible future activities.

2. Experimental work

This chapter presents the experimental work on Ag/Ag₂O GDEs. The electrodes are provided by Bayer Material Science [127] and were developed as depolarized electrodes for chlor-alkali synthesis. The electrodes are prepared in a dry mixing and pressing process [127]. The substrate of the electrode mainly consists of Ag₂O and small amounts of Ag which are added to improve the electrical conductivity. A hydrophobic binder material improves the stability of the catalyst layer and ensures the coexistence of gas and liquid phase during operation. The substrate is pressed on a Nickel mesh which serves as a current collector and guarantees the mechanical stability of the GDE. A cross-cut of the electrode can also be seen in Figure 2.14. Two different batches of the Ag/Ag₂O electrode were received from Bayer Material Science, which were prepared with the same composition but at a different pressure load in the production process. The electrodes were characterized structurally as well as electrochemically. Aim of these studies is the development of a basic understanding of relevant electrochemical processes and, above all, a sound experimental basis for the parametrization and validation of the continuum model presented in Chapter 4.

2.1. Background

This section gives a short introduction to the fundamental characteristics of charge-transfer reactions in liquid electrolytes [128, 129]. The discussion also includes an overview of O₂ electrochemistry on Ag catalysts in alkaline systems.

2.1.1. Thermodynamics and kinetics of charge-transfer reactions

Chemical reactions where a transfer of electrons across an electrode-electrolyte interface is involved are called charge-transfer reactions (CTR). The resulting electrical current is named Faradaic current i_F . In a system in thermodynamic equilibrium the Faradaic current $i_F = 0$. The corresponding potential is called the open circuit potential OCP and is characteristic for the electrochemical couple involved in the CTR.

Thermodynamically, the condition for equilibrium is given by a (local) minimum in the free Gibbs energy

$$dG(T, p, c, \phi) = 0 . \quad (2.1)$$

At constant pressure p and temperature T this condition simplifies to

$$\frac{\partial G}{\partial \zeta}_{T,p} = \sum_i \nu_i \bar{\mu}_i = 0 , \quad (2.2)$$

where ζ is the extent of the reaction in moles, $\bar{\mu}_i$ the electrochemical potential and ν_i the stoichiometric coefficient of species i . The index i runs over all species participating in the CTR. The electrochemical potential is defined as

$$\bar{\mu}_i(T, p, c, \phi) = \mu_i^0(T, p) + RT \ln(a_i) + z_i F \phi , \quad (2.3)$$

where $\mu_i^0(T, p)$ is the chemical potential at temperature T and pressure p , R the ideal gas constant, F Faraday's constant, and a_i and z_i the activity and charge of species i , respectively. The first two terms describe the chemical potential of pure species i and contributions of the mixture/solution due to interactions with other components. The chemical potential of pure species i at standard pressure p^\ominus can be calculated according to

$$\begin{aligned} \mu_i^0(T, p^\ominus) &= h_i^0(T, p^\ominus) - T s_i^0(T, p^\ominus) \\ &= \left(h^\ominus(T^\ominus, p^\ominus) + \int_{T^\ominus}^T c_{p,i} dT \right) - T \left(s^\ominus(T^\ominus, p^\ominus) + \int_{T^\ominus}^T \frac{c_{p,i}}{T} dT \right) , \end{aligned} \quad (2.4)$$

where h is the enthalpy, s the entropy, c_p the heat capacity at constant pressure and T^\ominus the reference temperature for the enthalpy and entropy of formation (h^\ominus, s^\ominus). The

reference temperature is typically 298.15 K. A deviation from standard pressure p^\ominus is not included in the discussion.

Evaluation of Eq. (2.2) for a general reaction of the form



gives

$$0 = \nu_R (\mu_R^0 + RT \ln a_R + z_R F \phi_{\text{elyte}}) - \nu_O (\mu_O^0 + RT \ln a_O + z_O F \phi_{\text{elyte}}) - n F \phi_{\text{elode}}, \quad (2.6)$$

taking into account charge conservation $\nu_R - \nu_O = n$ this can be rearranged to

$$\Delta \phi^{\text{eq}} = \phi_{\text{elode}} - \phi_{\text{elyte}} = \frac{\Delta \mu^0}{nF} + \frac{RT}{nF} \ln \left(\frac{a_R^{\nu_R}}{a_O^{\nu_O}} \right). \quad (2.7)$$

In a more general form Eq. (2.7) can be written as

$$\Delta \phi^{\text{eq}} = \Delta \phi^0 - \frac{RT}{nF} \ln \prod_i a_i^{\nu_i}, \quad (2.8)$$

which is commonly known as the Nernst equation. $\Delta \phi^{\text{eq}}$ is the half-cell potential of the reaction and $\Delta \phi^0$ the standard potential of the reference. The literature value for $\Delta \phi_{\text{SHE}}^0$ of the ORR in alkaline media (Eq. (1.11)) is 0.4 V against a standard hydrogen electrode (SHE). In the measurements described in this work a reversible hydrogen electrode (RHE) is employed directly in the electrolyte solution and the potential has to be corrected accordingly. In 1 M LiOH solution at 25 °C the theoretical potential $\Delta \phi_{\text{RHE}}^0$ of the ORR is 1.23 V.

The cell voltage E of an electrochemical cell follows from the half-cell potentials as

$$E = \Delta \phi_{\text{cathode}} - \Delta \phi_{\text{anode}}. \quad (2.9)$$

If the half-cell potential $\Delta \phi$ differs from $\Delta \phi^{\text{eq}}$ a Faradaic current is observed. The deviation of $\Delta \phi$ from $\Delta \phi^{\text{eq}}$ is called overpotential η with

$$\eta = \Delta \phi - \Delta \phi^{\text{eq}}. \quad (2.10)$$

Per definition positive values of η produce a positive current, which is called *anodic* and negative currents are called *cathodic*. The relationship between η and the Faradaic current

2. Experimental work

i_{F} is central to the studies of the kinetics of CTRs.

A general form of the relationship between overpotential and current can be derived from transition state theory [130]. According to the law of mass action the Faradaic currents of the general reaction in Eq. (2.5) have the form

$$\begin{aligned} i_a &= nFk_a c_{\text{R}} \\ i_c &= nFk_c c_{\text{O}} \end{aligned} \quad (2.11)$$

for forward (anodic) and backward (cathodic) reaction, respectively. Many experiments showed that k has a typical form, which is generally known as the Arrhenius equation

$$k = k^0 e^{\left(-\frac{\Delta G^\ddagger}{RT}\right)}, \quad (2.12)$$

where k^0 is the so-called frequency factor or standard rate constant of the reaction and ΔG^\ddagger the difference in free energy between the educt and transition state. As shown before (see Eqs. (2.2) and (2.3)), the free energy landscape of electrochemical reactions additionally depends on the applied potential ϕ

$$\Delta G^\ddagger(\phi) = \Delta G^0(\phi^0) + \Delta G'(\Delta\phi), \quad (2.13)$$

where $\Delta\phi$ is the difference between ϕ and the potential of the reference electrode ϕ^0 (e.g. a SHE). The contribution of the potential to the free energy is given by

$$\begin{aligned} \Delta G'_c(\phi) &= -\beta nF\Delta\phi \\ \Delta G'_a(\phi) &= (1 - \beta)nF\Delta\phi \end{aligned} \quad (2.14)$$

for the cathodic and anodic reaction, respectively. The coefficient β is the so-called symmetry factor of the CTR and describes the position of the transition state with respect to potential. The total free energy difference follows as

$$\begin{aligned} \Delta G_c^\ddagger(\phi) &= \Delta G_c^0(\phi^0) - \beta nF\Delta\phi \\ \Delta G_a^\ddagger(\phi) &= \Delta G_a^0(\phi^0) + (1 - \beta)nF\Delta\phi. \end{aligned} \quad (2.15)$$

The Faradaic currents for reduction and oxidation (Eqs. (2.11)) are by convention

$$\begin{aligned} i_c &= -nF c_O k_c e^{\left(-\frac{\beta nF}{RT} \Delta\phi\right)} \\ i_a &= nF c_R k_a e^{\left(\frac{(1-\beta)nF}{RT} \Delta\phi\right)}, \end{aligned} \quad (2.16)$$

where k_c and k_a are the rate constants at the reference potential

$$\begin{aligned} k_c &= k_c^0 e^{-\frac{\Delta G_c^0(\phi^0)}{RT}} \\ k_a &= k_a^0 e^{-\frac{\Delta G_a^0(\phi^0)}{RT}}. \end{aligned} \quad (2.17)$$

The net resulting Faradaic current is then given by

$$i_F = i_a + i_c = nF \left[k_a^0 c_R e^{\left(\frac{(1-\beta)nF}{RT} \Delta\phi\right)} - k_c^0 c_O e^{\left(-\frac{\beta nF}{RT} \Delta\phi\right)} \right]. \quad (2.18)$$

At the equilibrium potential $\Delta\phi^{eq}$ the net resulting current $i_F = 0$ and the exchange current densities follow as

$$\begin{aligned} i_c(\Delta\phi^{eq}) &= -i_0 = -nF c_O k_c^0 e^{\left(-\frac{\beta nF}{RT} \Delta\phi^{eq}\right)} \\ i_a(\Delta\phi^{eq}) &= i_0 = nF c_R k_a^0 e^{\left(\frac{(1-\beta)nF}{RT} \Delta\phi^{eq}\right)} \end{aligned} \quad (2.19)$$

Finally, inserting Eq. (2.19) in Eq. (2.18) and setting $\Delta\phi = \Delta\phi^{eq} + \eta$ results in the well-known Butler-Volmer equation

$$i_F = i_0 \left[e^{\left(\frac{(1-\beta)nF}{RT} \eta\right)} - e^{\left(-\frac{\beta nF}{RT} \eta\right)} \right]. \quad (2.20)$$

The general form of the Butler-Volmer equation can be seen in Figure 2.1 a), where contributions of the anodic and cathodic currents to the total current (green) are shown in red and blue, respectively. By introducing the Nernst equation (2.8) in Eq. (2.19) it can be shown [130] that at the equilibrium potential

$$nF k_a^0 e^{\left(\frac{(1-\beta)nF}{RT} \Delta\phi^{eq}\right)} = nF k_c^0 e^{\left(-\frac{\beta nF}{RT} \Delta\phi^{eq}\right)} = nF k^0. \quad (2.21)$$

Therefore,

$$i_0 = nF k^0 c_O^{(1-\beta)} c_R^\beta \quad (2.22)$$

2. Experimental work

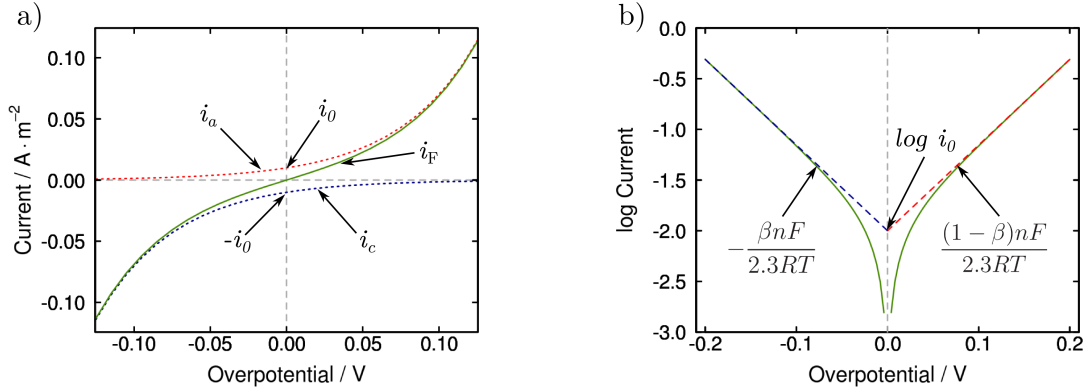


Figure 2.1.: Butler-Volmer equation (left) and Tafel plot (right) for an exemplary one electron transfer ($n=1$) reaction with $(1 - \beta)=0.5$ and $i_0=10^{-2}$ A/m².

gives a relation for the dependence of i_0 on the concentrations in the electrolyte solution. In the case of small or high overpotentials Eq. (2.20) can be rewritten in simpler forms. This is especially helpful in the analysis of experimental data. At small overpotentials the exponential e^x can be approximated by $1 + x$ and Eq. (2.20) takes a linear form

$$i_F = i_0 \frac{nF}{RT} \eta . \quad (2.23)$$

At high negative or positive overpotentials the anodic or cathodic contribution to the Butler-Volmer equation can be neglected, respectively. It follows the so-called Tafel equation which is for cathodic currents given by

$$i_F = i_0 e^{\left(-\frac{\beta n F}{RT} \eta\right)} . \quad (2.24)$$

In its logarithmic form

$$\log(i_F) = \log(i_0) - \left(\frac{\beta n F}{2.3 R T}\right) \eta \quad (2.25)$$

it is a valuable tool for a graphical analysis (see Figure 2.1 b)) of IV curves. An expression for high positive overpotentials can be derived in the same fashion. Note, that the overpotential has to be sufficiently large for this simplification but at the same time mass transport effects might influence the measurements at high current densities. In some cases this gives only a small room for analysis.

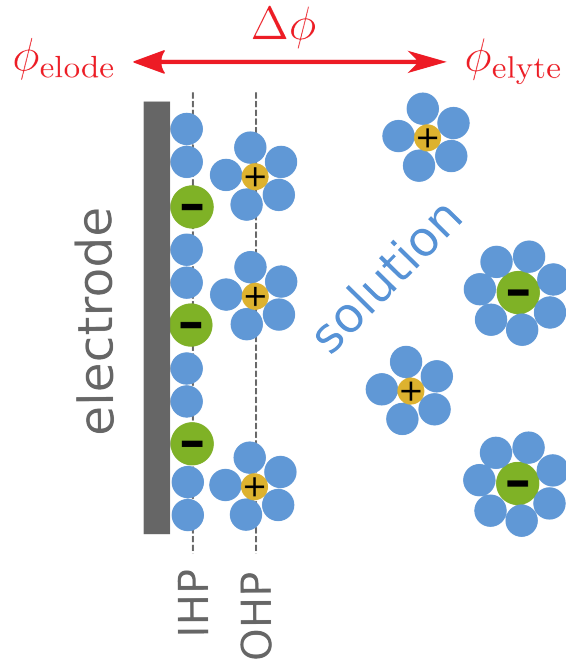


Figure 2.2.: Model of the electric double-layer at the electrode-solution interface. The solvent molecules are marked as blue circles. Anions (green) are specifically adsorbed on the electrode surface (gray) and form the so-called compact layer. Cations (yellow) and anions in the diffuse layer are surrounded by a solvation shell.

For a global description of more complex multi-step kinetics the deduction of an expression is not straightforward. Often, phenomenological expressions of the form

$$i_F = nFk^0 \left[\prod_{educts} c_i^{-\nu_i} e^{\left(-\frac{\beta nF}{RT} \eta\right)} - \prod_{products} c_i^{\nu_i} e^{\left(\frac{(1-\beta)nF}{RT} \eta\right)} \right] \quad (2.26)$$

are used to capture the experimentally observed behavior.

2.1.2. Double-layer structure and capacitance

The situation at the interface of two phases is always special. The interactions of molecules at the interface differ from their interactions in the bulk as at one side they are in contact with molecules of the neighboring phase. Thus, the properties at the interface will change under the influence of the other phase. For an electrode in contact with an electrolyte

2. Experimental work

solution a capacitive behavior is observed. The reason is the formation of an electric double-layer. The bulk of the solution can be safely assumed to be electroneutral, meaning that the sum of negative and positive charges (anions and cations) is zero (neutral). However, if a potential step $\Delta\phi$ is applied at the electrode-electrolyte interface, the ions accumulate close to the surface, balancing the charge of the electrode ($Q_{\text{elode}} = -Q_{\text{elyte}}$). The overall interface region is again electroneutral.

Figure 2.2 shows a common model of the electrode-solution interface. In the inner or compact layer the ions are thought to be specifically adsorbed on the electrode surface. The position of their electrical centers is named the inner Helmholtz plane (IHP). The charge density $q^i = Q^i/V^i$ of the inner layer depends on the ions and solvent molecules which are involved. Solvated ions are not able to approach the surface and the position of the electrical centers of ions closest to the surface is called outer Helmholtz plane (OHP). The ions beyond the OHP contribute to the charge density q^o in the outer or diffuse layer. The thickness of this layer decreases with increasing electrolyte concentration and polarization. The total charge density in the solution is given by $q_{\text{elyte}} = q^i + q^o = -q_{\text{elode}}$. The double-layer structure also has a strong effect on the potential distribution close to the surface. This is particularly important as the potential step $\Delta\phi = \phi_{\text{elode}} - \phi_{\text{elyte}}$ is also driving the charge-transfer reaction (see previous Section).

The charge density q which is stored in the electrical double-layer can be approximated by the equation for an electric capacitor

$$q_{\text{dl}} = C_{\text{dl}}\Delta\phi = a_{\text{dl}}^v c_{\text{dl}}\Delta\phi, \quad (2.27)$$

where c_{dl} is the area specific capacitance of the double-layer with specific surface area a_{dl}^v . For a parallel-plate capacitor the capacitance can be calculated according to

$$c_{\text{dl}} = \frac{\epsilon^0 \epsilon}{\delta_{\text{dl}}}, \quad (2.28)$$

where ϵ^0 is the permittivity of vacuum, ϵ the relative permittivity of the medium and δ_{dl} the thickness of the double-layer. This approximation typically gives a good estimate for the charge density in the inner layer q_i . Weak point of this theory is that the charge density does not depend on the applied potential. There are several descriptions of the diffuse layer in the literature [128] where temperature, concentration of the electrolyte and polarization are taken into account (Gouy-Chapman and Stern models). However, for a first approximation and at high overpotentials it is often sufficient to take into account

only the contribution of a compact layer.

A change in the potential across the surface results in a response in the current signal. Differentiation of Eq. (2.27) with respect to time yields

$$\frac{\partial q_{\text{dl}}}{\partial t} = \frac{\partial}{\partial t} (C_{\text{dl}} \Delta \phi) = C_{\text{dl}} \frac{\partial \Delta \phi}{\partial t} + \Delta \phi \frac{\partial C_{\text{dl}}}{\partial t}, \quad (2.29)$$

where $\frac{\partial q_{\text{dl}}}{\partial t}$ is the double-layer current i_{dl} . A change in the capacitance is often negligible and Eq. (2.29) results in

$$i_{\text{dl}} = C_{\text{dl}} \frac{\partial \Delta \phi}{\partial t} = a_{\text{dl}}^v c_{\text{dl}} \frac{\partial \Delta \phi}{\partial t}. \quad (2.30)$$

2.1.3. The Ag|O₂ system in alkaline media

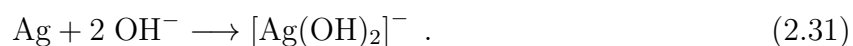
The chemistry of Ag and O₂ in alkaline media has been intensively studied in the literature. However, most of the work has been done in aqueous solutions of KOH or NaOH and only very few authors use aqueous solutions of LiOH as electrolyte [131]. A report of Ag electrochemistry or oxygen reduction and evolution on Ag in LiOH solution could not be found in the literature.

Ag chemistry in alkaline media

The Ag/Ag₂O system has been widely studied in the literature as it is of technical interest for Ag-Zn batteries [132–135]. In the potential range of O₂ reduction and evolution Ag exhibits several oxidation states.

Figure 2.3 shows a typical CV of a polycrystalline Ag electrode in alkaline media (1 M NaOH solution) recorded by Abd el Rehim *et al.* [132] in the absence of O₂. The potentials in the graph are given relative to a saturated calomel electrode (≈ -1.07 V vs. RHE). This corresponds to a potential range between -0.6 V and 2.0 V vs. RHE. In the presence of O₂ the ORR starts at potentials around 700 mV vs. RHE. O₂ evolution in the presented system occurs at potentials above 1.8 V vs. RHE.

The first anodic peak (A1) might be attributed to an oxidation of Ag according to



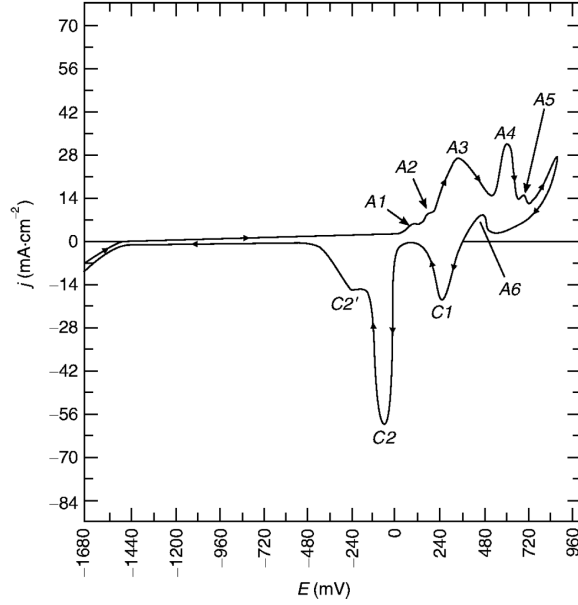
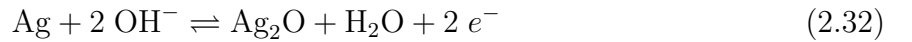
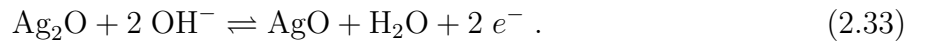


Figure 2.3.: Typical CV of a polycrystalline Ag electrode in alkaline media (1M NaOH solution) recorded at a scan rate of 100 mV/s in the absence of O_2 . Anodic and cathodic peaks are marked by A and C, respectively. Potentials are given relative to a saturated calomel electrode (≈ -1.07 V vs. RHE). Reprinted with permission from [132].

The soluble $[Ag(OH)_2]^-$ is able to diffuse into the bulk of the solution which might lead to a degradation of the electrode. However, some studies show that during a complete cycle anodic and cathodic charges are identical. This indicates that the oxidation products stay on or at least close the electrode surface. The peak A2 might be an indication for the precipitation of Ag_2O from the supersaturated solution close to the surface. The two main steps in the oxidation process of Ag are the formation of Ag_2O (A3)



and AgO (A4)



The small peak (A5) right before O_2 evolution potential might indicate the formation of higher oxides of Ag. The last anodic peak (A6) on the reverse scan is not observed in all studies. Abd el Rehim *et al.* [132] state that it might be assigned to a continuous

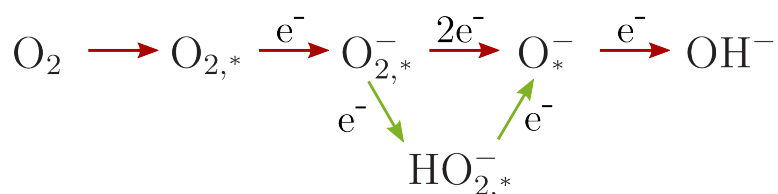


Figure 2.4.: Simplified reaction mechanism for the reduction of O_2 in alkaline media [75]. Red arrows indicate the direct 4e^- pathway and the green arrows indicate the indirect $2+2\text{e}^-$ pathway via a HO_2^- intermediate species. The asterisk marks adsorbed species on the electrode surface.

formation of Ag_2O from Ag substrate. The cathodic peaks on the backward scan can be linked with the reductions to Ag_2O (C1) and Ag (C2), respectively.

Oxygen reduction in alkaline media

The ORR in alkaline media is of great industrial importance as it is used in alkaline fuel cells, chlor-alkali electrolysis and metal-air batteries. Several catalyst systems are proposed in the literature for this reaction [86]. The most prominent one is Pt due to its high stability and outstanding performance. Major problem of Pt-based catalyst systems is their high cost. Ag electrodes are an interesting alternative in alkaline media as Ag has a comparable kinetic activity at a much lower price.

The global reaction for O_2 reduction in alkaline media is given by Eq. 1.11. The detailed kinetic mechanism of the reaction is, however, quite complicated [75]. Figure 2.4 gives a simplified overview of the mechanism. There are two possible pathways in alkaline media, the direct 4e^- step and a consecutive $2+2\text{e}^-$ step involving a HO_2^- intermediate species. It is in common agreement that on Ag the dominant pathway is the direct 4-electron reduction [75]. Traces of HO_2^- indicate that also the indirect pathway is contributing to the overall reduction of O_2 . The reaction rate is found to be first order in O_2 concentration and the catalytic activity of Ag increases with pH in highly alkaline media. Sepa *et al.* observe a change in the apparent Tafel slope at high potentials [75, 136]. Similar to Pt [131], the increase in Tafel slope might be explained by a change in the adsorption isotherms of intermediate species [74].

Oxygen evolution in alkaline media

The OER in alkaline media is less studied compared to O₂ reduction. An important application is the alkaline water electrolysis for the production of hydrogen. In this context several oxide catalysts were studied regarding their activity towards O₂ evolution. RhO₂ and IrO₂ show the best performance but are, like Pt, very expensive. Besides Ni [137] and Co [88, 138] based catalyst systems, oxides of the spinel and perovskite type are proposed as possible alternatives. Among these Co₃O₄ is one of the most promising candidates for O₂ evolution in alkaline media. Work on Ag/AgO electrodes is not reported in the literature, probably due to the observed dissolution of Ag at potentials of O₂ evolution [76].

The reaction mechanism of O₂ evolution is rather complex and several reaction routes are proposed for the different materials [137–140]. The most common mechanism for the oxides of Co and Ni is suggested by Krasil'shchikov [88]. The asterisk indicates adsorbed species on the electrode surface.



2.2. Methodology

In this section the methodology for the structural and electrochemical characterization of the Ag/Ag₂O electrodes is explained in detail. The microscopy and image manipulation work described here was done by the project partners at the University of Ulm in the Electron Microscopy Group of Materials Science [141]. The electrochemical characterization of the electrodes and determination of structural and transport parameters is part of this work.

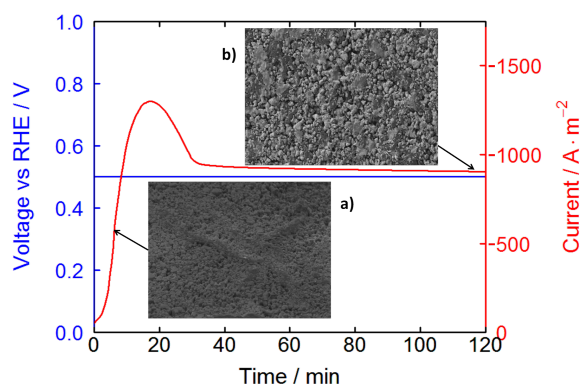


Figure 2.5.: Reduction process of the Ag-GDE under O_2 atmosphere in 1 M LiOH solution: a) pristine state and b) reduced state [141].

2.2.1. Structural characterization of Ag/Ag₂O Gas Diffusion Electrodes

Overview

The structure of the Ag/Ag₂O-GDE has been studied in two different oxidation states. The pristine electrode as received from Bayer Material Science [127] mainly consists of Ag₂O. In order to study the electrode under the conditions of prolonged oxygen reduction, the GDE is reduced electrochemically in O_2 atmosphere. During the reduction process Ag₂O is converted to Ag (see Section 2.1.3). Figure 2.5 shows the current signal over time during the reduction process. Electron microscopy images [141] of the pristine and reduced state are also included as insets a) and b), respectively. First, the current rises due to the facile reduction of Ag₂O. After a short time the amount of Ag₂O becomes limited and one can see the resulting peak in the current signal at ~ 20 minutes. Towards longer reduction time the current approaches a constant value, which originates from the ORR at the pure Ag electrode. The color of the pristine Ag₂O electrode is almost black and the microscope image reveals a grainy structure with particle sizes of 2-3 microns. The size of the Ag particles in the reduced state is approximately the same but the color of the particles is much lighter.

The porous structure of the GDE offers a high surface area and an improved transport of reactants. Pore diameters typically range from a couple of microns down to only a few nanometers. The micro-structure of the electrode determines the transport behavior and performance of the GDE. Simulations on the micro-structure can give conclusive insights

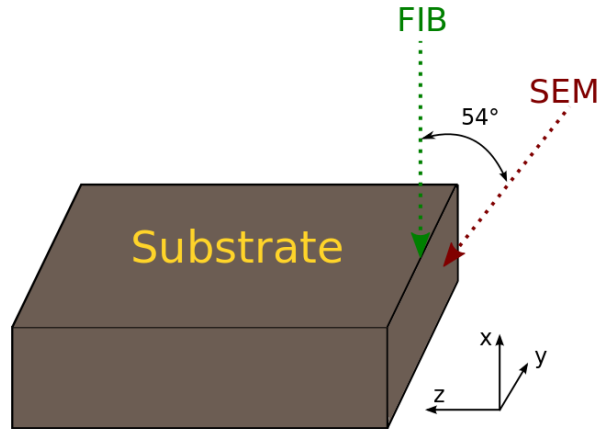


Figure 2.6.: Operation of the FIB-SEM instrument. A Ga^+ ion beam is used to cut slices of the electrode while the electron beam takes images of the GDE clipping at predefined intervals in time.

on the operation of the electrode. For this purpose the electrode structure can either be created by a virtual packing of geometric particles or by tomography of real electrodes. In this work Focused Ion Beam (FIB) and Scanning Electron Microscopy (SEM) techniques are used to create a series of images from a representative cutout of the GDE. In a following step the images can be used to reconstruct the three-dimensional structure. This reconstruction approach allows on the one hand to gain geometrical information of the GDE. On the other hand, CFD simulations on the micro-structure can be used to obtain effective transport properties.

FIB-SEM and binarization

The imaging techniques described in this section were developed by the project partners at the University of Ulm [141]. The method is explained here in detail as some technical aspects do have a strong influence on the evaluation of structural and transport parameters which are determined from the reconstruction.

A dual-beam ZEISS N-Vision 40 FIB-SEM instrument is employed to collect electron microscope images of the Ag electrode micro-structure. The SEM has a field-emission electron gun with an acceleration voltage between 5 and 30 kV and a vertical electron-optic axis. The FIB is based on a Ga^+ primary ion beam with a 30 kV acceleration voltage. The ion-beam is at an angle of 54° to the electron-optic axis. The standard vacuum levels for the electron gun and the sample chamber are 10^{-9} and 10^{-5} mbar, respectively. The

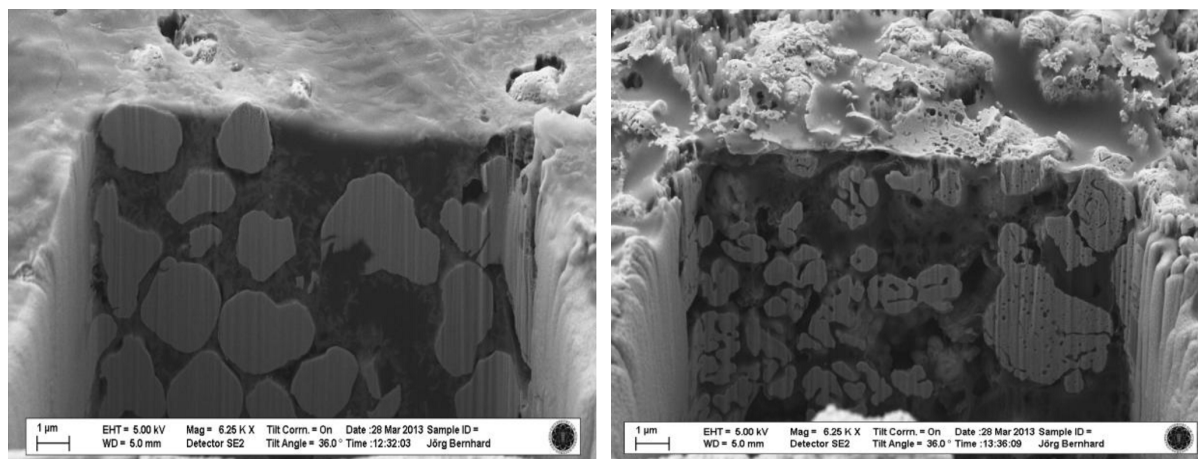


Figure 2.7.: SEM images of GDE samples filled with epoxy resin. Left: Pristine electrode Right: Reduced electrode [141].

sectioning of the sample is achieved using the FIB and the images are acquired using the SEM at specified intervals. The number of images and the interval length determine the spatial resolution of the reconstruction perpendicular to the imaging plane (z -direction). Before the SEM imaging of the sample begins, it must be ensured that the SEM and FIB windows correspond to the same region-of-interest of the sample. A trench is cut into the sample in the vicinity of the region-of-interest with a relatively harsh ion-beam current of 6.5 nA such that the cross-sectional plane becomes visible. The plane is then polished with an ion-beam current of 300 pA. Subsequently, the total region of 3D tomography is scanned by the ion and electron beam.

Prior to the imaging step the electrode samples are filled with a low-viscosity epoxy resin in order to improve the contrast of the images. This is an important step to facilitate the binarization process. Figure 2.7 shows SEM images of the pristine (left) and reduced (right) electrode. Note, that the resin rather well impregnates the pore space of the GDE. The size of the Ag₂O particles in the pristine electrode is around 2-3 μm. The morphology of these particles looks very smooth. In the reduced state the formation of intrinsic pore space and inclusions on a smaller length scale can be observed. Possible explanation is the evolution of molecular oxygen during the reduction of the electrode. These inclusions do not change the accessible pore space of the GDE and are assigned to the electrode phase in the reconstruction step.

The images of the different slices are aligned to account for the sample-drift during imaging. The perspective correction and pixel-size adjustments are done in the software package

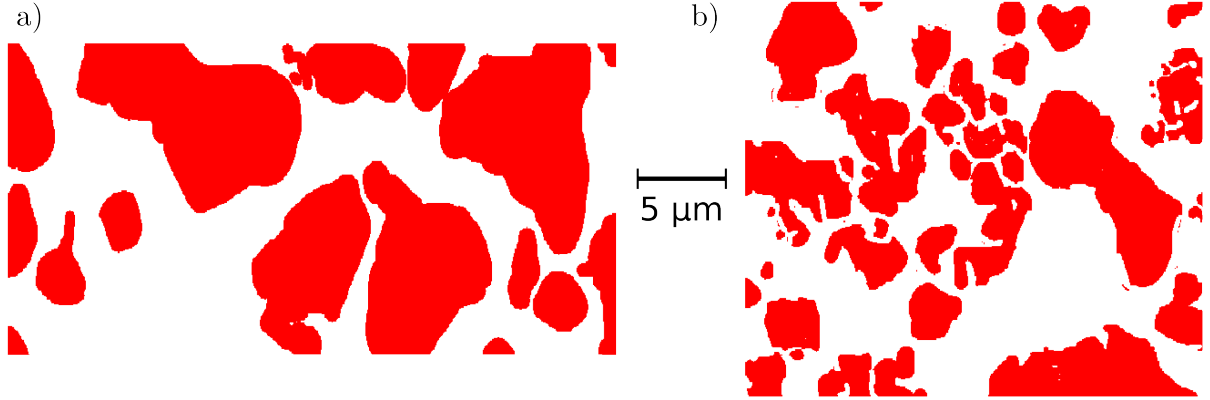


Figure 2.8.: Binarized images of a representative crosscut. The solid structure of the GDE is shown in red. Left: Pristine GDE, right: Reduced GDE [141].

IMOD [142]. The epoxy resin improves the contrast in the images and helps to identify the solid particles. In spots where the impregnation of the electrode is incomplete the contrast is adjusted manually. A color threshold is set to determine if a voxel is electrode or pore volume. This seemingly simple step is very important for the quality of the reconstruction. While the influence on porosity is small in most cases the effect on the specific surface area can be quite substantial. Figure 2.8 shows binarized images of the pristine (left) and reduced electrode (right). The solid particles of the electrode structure are shown in red color. The horizontal and vertical dimension are named x and y , respectively. The direction perpendicular to the x - y plane is denoted by z and represents the direction of the FIB cut. Note, that (x, y) dimensions of the voxels are related by the relation $y = x/\sin(54^\circ)$, where the value of x is determined by the magnification of the image and the 54° origin from the tilt of the sample. The dimensions of reconstructed samples are summarized in Table 2.1.

	Dimensions / μm			Voxel size / nm				
	x	y	z	x	y	z	GeoDict	LBM
Pristine Ag_2O -GDE	36.1	18.4	10.0	54	67.5	3.8	54	216
Reduced Ag -GDE	27.8	23.9	10.0	55.3	69	119	55.3	221
High pressure (Ag_2O -GDE)	12.03	8.25	5.00	22.3	27.5	19	19	76

Table 2.1.: Dimensions and resolution of electrode samples in x, y, z direction. The reconstructed electrodes in GeoDict and for the lattice Boltzmann simulations (Chapter 3) are based on cubic voxels. A coarsening of the structure is necessary to reduce the computational load in the LBM simulations.

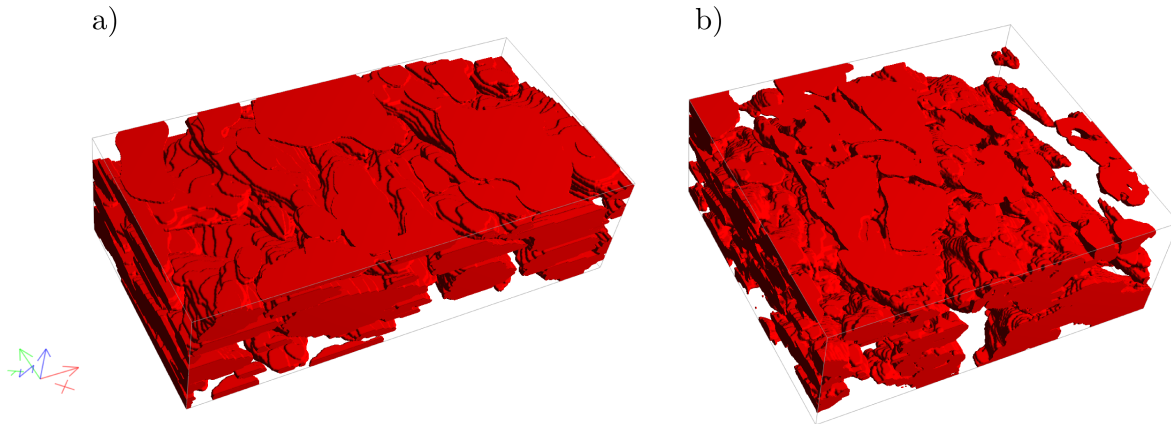


Figure 2.9.: 3D representation of reconstructed sample electrodes. Left: Pristine electrode. Right: Reduced electrode.

Structural and effective transport parameters

The reconstruction of electrode samples and determination of structural and effective parameters is an inherent part of this work. For this task the commercial software package GeoDict [143] is used. The structure is imported from the binarized images and rescaled according to the dimensions given in Table 2.1. The 3D representations of the reconstructed electrodes are shown in Figure 2.9. GeoDict offers multiple tools for the structural characterization and determination of transport parameters of porous media. The porosity and specific surface area are calculated in a voxel based analysis of the reconstruction. Additionally, GeoDict can predict pore size distributions (PSD) by simulating a mercury intrusion porosimetry measurement (MIP). Effective transport properties of the porous electrode are calculated based on CFD simulations in the reconstruction of the GDE.

The tortuosity is a measure for the diffusion length in a porous structure. In GeoDict it is calculated by applying a concentration gradient in one direction. The diffusive flux \vec{j}_i follows from the simulation and is evaluated in the, e.g., x -direction by

$$\vec{j}_{x,i} = -D_{x,i}^{\text{eff}} \frac{\Delta c_i}{\Delta x}, \quad (2.38)$$

2. Experimental work

where c_i is the concentration of species i and $D_{x,i}^{\text{eff}}$ the effective diffusion coefficient in x -direction. In a macro-scale porous electrode model the effective transport properties are often calculated according to [125]

$$D_i^{\text{eff}} = \frac{\varepsilon}{\bar{\tau}} \cdot D_i^0, \quad (2.39)$$

where ε is the volume fraction of the phase, $\bar{\tau}$ the tortuosity factor of the electrode, and D^0 the bulk diffusion coefficient. In the case of $\bar{\tau} = 1/\sqrt{\varepsilon}$ follows the standard Bruggeman correlation

$$D_i^{\text{eff}} = \varepsilon^{1.5} \cdot D_i^0. \quad (2.40)$$

In a more general form it can be written as

$$D_i^{\text{eff}} = \varepsilon^\beta \cdot D_i^0, \quad (2.41)$$

where β is the so-called Bruggeman coefficient.

Similarly, the permeability can be calculated by applying a pressure gradient in one direction. The pressure gradients are restricted to small values in order to preserve Stokes flow ($Re \ll 1$) in the porous media. The permeability B can be calculated from the simulated flow field \mathbf{v} by the Darcy equation [144]

$$\mathbf{v}_x = -\frac{B_x \Delta p}{\mu \Delta x}, \quad (2.42)$$

where μ is the dynamic viscosity of the fluid.

The effective electrical conductivity of the solid electrode is calculated in the same manner as the tortuosity and permeability of the pore space. If a potential gradient is applied on the electrode structure, an electric current starts to flow. The stationary current density distribution \vec{j}_{el} is calculated by solving the Poisson equation numerically. The effective conductivity $\sigma_{\text{el}}^{\text{eff}}$ in e.g., x -direction can be evaluated from Ohm's law

$$\vec{j}_{x,\text{el}} = -\sigma_{\text{el}}^{\text{eff}} \frac{\Delta\phi}{\Delta x}, \quad (2.43)$$

where $\Delta\phi$ is the potential step across the solid electrode.

The structural parameters of a pristine Ag_2O electrode are additionally also investigated experimentally. Mercury intrusion porosimetry (MIP) and krypton adsorption measure-

ments are conducted in order to determine the porosity, mean pore diameter and specific surface area [145]. The experimental measurements serve as a reference for the accuracy of the FIB-SEM method outlined above.

2.2.2. Electrochemical characterization of electrodes

The electrochemical characterization of Ag/Ag₂O GDEs is one of the key parts of this thesis. The experimental data was generated during the first part of this PhD work in the department of Electrochemical Energy Technology at the Institute of Technical Thermodynamics of the German Aerospace Center [145].

Experimental setup

Two different experimental setups are used for the electrochemical characterization of Ag/Ag₂O electrodes. Schematic drawings of the setups can be seen in Figure 2.10. The left panel shows the 'standard' cell which is commonly used in the characterization of GDEs. It consists of an electrolyte bath which is placed in a water bath for temperature-controlled measurements. The right panel of Figure 2.10 shows the setup of a second cell which allows to set the pressure in the electrolyte by adjusting the height of the solution in an ascending pipe. For the standard measurements the pressure difference between the electrolyte bath and the gas channel is approximately set to zero.

Both experimental arrangements have the typical configuration of a three-electrode setup [94, 128]. The working electrode is mounted in a sample holder of acrylic glass. The gas phase is fed to the electrode from the current collector side. Electrical contact is made by a gold-coated Ni mesh. The coating is necessary to avoid corrosion of the mesh where it is in contact with the electrolyte solution. As Ni is known to be electrochemically active in alkaline media, the gold film additionally reduces the catalytic activity. A SIGRACET® GDL 35DC (SGL) with a micro-porous layer (MPL) is positioned between the electric contact and the working electrode. Its purpose is to prevent flooding of the gas supply with liquid electrolyte. The measurements are controlled by a Zahner IM-6 Electrochemical Workstation which is accessed by the in-house software Thales installed on a personal computer. The voltage of the half-cell is measured between the working electrode and a reversible hydrogen electrode (Gaskatel) in direct contact with the electrolyte solution.

2. Experimental work

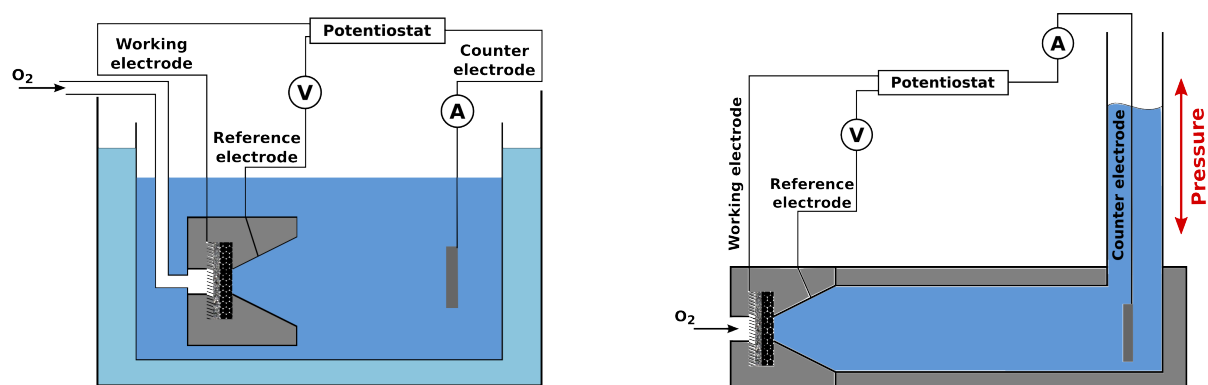


Figure 2.10.: Experimental setups for half-cell measurements. Left: Classical setup including water bath for temperature-controlled measurements. Right: Setup for measurements at various pressures in the liquid phase. The pressure is set by adjusting the height of the meniscus in the ascending pipe.

The position of the reference electrode is ~ 5 mm in front of the working electrode surface. The cross-sectional area of the sample holder increases towards the electrolyte bath with an angle of 30° . This circumvents an accumulation of gas bubbles in front of the electrode. A thin Pt sheet serves as counter electrode at the opposite side of the electrolyte bath. The distance between the working electrode and the counter electrode is around 10 cm. The large size of the electrolyte bath ensures an approximately constant concentration of the LiOH solution. The electrolyte is prepared from commercially available LiOH \cdot H₂O (98 % purity, Alpha Aesar) and demineralized water. All measurements are performed with purified oxygen.

Electrochemical measurements

In this work mainly two different experimental techniques are applied for the electrochemical characterization of GDEs. Cyclic Voltammetry (CV) measurements [146] are employed to study the characteristic I-V behavior of the electrodes in the time domain. Electrochemical Impedance Spectroscopy (EIS) [147, 148] in turn is used to resolve the different physical and chemical processes depending on their characteristic time scales in the frequency domain.

The measurements are recorded at varying concentration (0.1, 0.2, 0.5, 1, 2 mol l⁻¹) and temperature (25, 40, 55°C) of the electrolyte solution in order to study the effect on

transport and kinetics. All measurements are repeated twice as a check of reproducibility. At each concentration a pristine electrode of the same batch is used. The procedure for the temperature dependent measurements at each concentration is described below and measurements at other temperatures follow the same routine. As initial step the pristine Ag_2O electrode is reduced (500 mV vs. RHE) under O_2 atmosphere in the LiOH solution at 55 °C (see Figure 2.5). After the reduction the electrolyte solution is cooled down to 25 °C. During rest times and between measurements the electrode is kept at potentials slightly below OCP in order to prevent a major oxidation of the electrode surface.

The first measurements in the procedure are CVs of O_2 reduction. The potential is swept linearly between 1.1 and 0.5 V vs. RHE with scan rates of 1, 10, and 100 mV/s. At the lowest scan rate the system is assumed to be close to equilibrium and the data can be used for kinetic analysis. In the following step impedance spectra are recorded at various overpotentials. Starting at 900 mV vs. RHE the half-cell voltage is decreased successively in steps of 100 mV. Between the measurements the system is kept for 5 minutes at the potential of the upcoming measurement. The minimum applied potential is 500 mV vs. RHE. The amplitude of the sinusoidal excitation is 5 mV with frequencies ranging from 10 kHz to 100 mHz. In order to decrease the measurement time only 6 points/decade are recorded at frequencies below 10 Hz, whereas the number of measurement points/decade at higher frequencies is 10. After the last EIS measurement the temperature of the water bath is increased and the measurement protocol is repeated at 40 and 55 °C.

For the measurements of O_2 evolution the electrode is oxidized at 1800 mV vs. RHE until the current signal stabilizes at a constant value. In compliance with the measurements for O_2 reduction CVs are recorded at each temperature. The potential interval of the measurements is 1.4 to 1.95 V vs. RHE. EIS measurements are not recorded for O_2 evolution as a noisy signal of the current response obviates an analysis of the experimental data. After the anodic cycle the AgO GDE is again reduced and the measurements of O_2 reduction at 55 °C are repeated in order to test the electrode for possible degradation (see Section 2.1.3).

Equivalent circuit models are a valuable tool for the analysis of electrochemical impedance spectra. An equivalent circuit is an electric circuit which represents an electrochemical system and each element of the circuit is equivalent to a physical or electrochemical process in the real system. The parameters of the equivalent circuit are fitted to the experimental data using a complex non-linear least squares algorithm [149]. This allows a quantitative analysis of the experimental data. The accuracy of the fit gives a first hint if

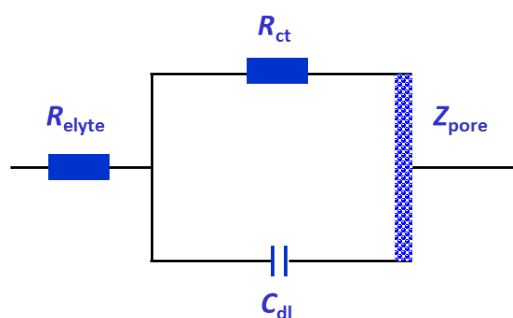


Figure 2.11.: Equivalent circuit of the porous Ag electrode. R_{elyte} is the resistance of the electrolyte and is in series with an RC element representing the CTR and double-layer on the electrode surface. Z_{pore} is a transmission line element following Göhr *et al.* [147].

the equivalent circuit model is able to capture all relevant processes.

Figure 2.11 shows the equivalent circuit which is used in this work to model the Ag/Ag₂O GDE. R_{elyte} is the resistance of the electrolyte solution between GDE and reference electrode. It is in series with an RC element which represents the electrochemical reaction and double-layer at the electrode surface. Z_{pore} is a so-called transmission line element which reflects the porous structure of the GDE [147, 150]. The number of elements in the present model is kept relatively small. More complex models are proposed in the literature which give an optimal fit to the experimental data. However, if the number of parameters is too large the system might be overdetermined and an unambiguous assignment of parameters is difficult.

2.3. Results and discussion

2.3.1. Structural characterization of Ag/Ag₂O Gas Diffusion Electrodes

Structural parameters

Porosity and specific surface area are the most important structural parameters of porous GDEs. In the case of the pristine Ag₂O GDE they are in addition to the FIB-SEM method also determined by MIP and krypton adsorption measurements (BET) [145]. The

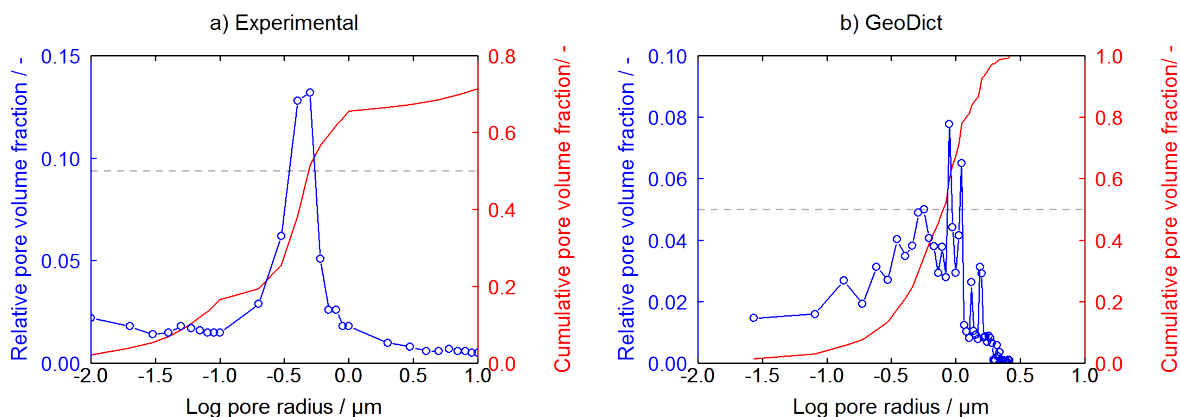


Figure 2.12.: Pore Size Distributions (PSD) from mercury intrusion porosimetry at the pristine Ag_2O electrode. Left: Experimental, Right: Simulations in GeoDict.

measurements will serve as a reference for the accuracy of the FIB-SEM approach. The resulting PSDs of the MIP measurement (left) and simulation (right) are shown in Figure 2.12. In general, simulation and experiment show a favorable qualitative agreement. Both techniques give a mono-modal distribution of pore diameters. The mean pore diameter d_{50} is in the order of $\sim 1 \mu\text{m}$ and the relative volume of pores smaller than d_{50} is a bit higher compared to the volume of larger pores. MIP on Ag electrodes is very difficult as Ag in contact with Hg is known to form amalgams. This might introduce a small error, especially, at small pore sizes where the pressure for the intrusion is the highest. The increase in relative pore volume at small diameters might be attributed to this effect. The simulated curve of relative pore volume in turn looks quite noisy. Reason is the relatively small size of the reconstructed sample and a corresponding lower statistical significance. A survey of structural parameters of the pristine and reduced electrodes is given in Table 2.2. The overall porosity of the reconstruction agrees fairly well with the MIP measurements. It is a bit higher for the reduced electrodes compared to the pristine electrodes. This is explained by a shrinkage of the particles during the reduction process. The porosity scales almost exactly according to a change in density from Ag_2O to Ag. However, the reconstructed sample is small and might not be representative for the whole electrode. A larger number of samples will need to be studied for a final conclusion. The structure of the Ag_2O electrode prepared at a high pressure load ('low-porosity electrode') is denser than the electrode prepared at low pressure ('high-porosity electrode'). Surface areas determined by the reconstruction method can be expected to be smaller

2. Experimental work

than the real surface area as some information on the morphology of the surface is lost in the milling and reconstruction process. Additionally, the values of surface area are prone to systematic errors due to an inaccurate threshold during binarization. Nevertheless, the simulated surface areas are in reasonable accordance to the values determined in the experiment (BET) (see Table 2.2). The electrode prepared at higher pressure load does exhibit a larger specific surface area compared to the high-porosity electrode which is also expected due to its denser structure.

The good agreement of reconstruction and measurement data demonstrates that the proposed method can be applied for quantitative studies on porous electrodes.

Effective transport parameters

Diffusivity, permeability and electric conductivity of the pristine and reduced electrode can be calculated according to the equations presented in Section 2.2. Concentration and velocity fields from stationary CFD simulations on the reduced electrode are depicted exemplary in Figure 2.13. The simulations are used for the calculation of relative diffusivity and permeability, respectively. The images show representative slices of the electrode in the y - z plane. The y -direction is important for the analysis of the transport behavior as it is the main direction of transport in the GDE during operation. In the experimental setup the electrode is in contact with the electrolyte reservoir on the left and the gas channel on the right. In the simulations the concentration and pressure gradients are applied in horizontal direction, accordingly.

The concentration on the right hand side of the reconstruction is higher than on the left

Method	Pristine Ag ₂ O		Reduced Ag	Low-porosity Ag ₂ O
	BET/MIP	FIB-SEM	FIB-SEM	FIB-SEM
Porosity / -	0.479	0.495	0.617	0.307
Pore radius / μm	0.51	0.82	0.87	0.21
Surface area / m^{-1}	$3.3 \cdot 10^6$	$1.1 \cdot 10^6$	$1.3 \cdot 10^6$	$2.3 \cdot 10^6$
Thickness / μm	560	-	560	475

Table 2.2.: Structural parameters of the pristine and reduced Ag/Ag₂O electrodes. For the pristine Ag₂O electrode data of BET and MIP measurements are included. The low-porosity case corresponds to an electrode which is prepared with a high pressure load in the production process.

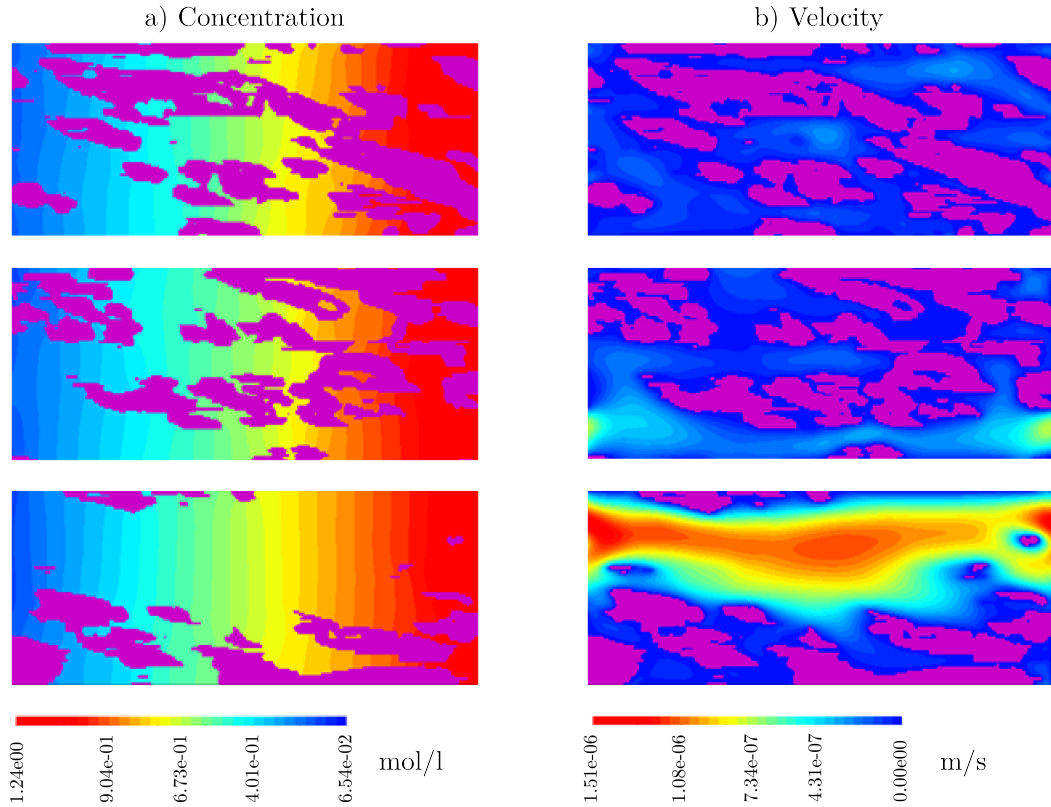


Figure 2.13.: Stationary concentration (left) and velocity (right) distributions for representative slices of the reduced GDE in the y - z plane.

hand side which induces a diffusive transport in the electrode from right to left. In the velocity distribution the areas of red color indicate a high local velocity. In dense areas the convection is rather small owing to an increased pressure drop due to friction on the surfaces. The velocity distribution at the bottom of Figure 2.13 b) shows a band of high velocity stretching across the whole length of the reconstruction. This indicates a preferred transport pathway which will cause a higher permeability (see Table 2.3).

The resulting transport parameters of the electrodes prepared at low and high pressure load are given in Tables 2.3 and 2.4, respectively. The geometry of the reduced low-porosity case has unfortunately not been reconstructed by the FIB-SEM method. Instead, it is obtained by rescaling the particle sizes of the pristine case according to the change in density during the reduction from Ag_2O to Ag . In general, the diffusivity and permeability in x and y direction show similar values. Parameters in the z -direction are slightly lower which normally indicates an increased transport resistance in this direction. However, the SEM pictures show a more or less homogenous structure which in turn would suggest an

2. Experimental work

isotropic transport behavior. Thus, the higher values in z -direction might be an artifact of the reconstruction process. In the imaging process the x - y plane is recorded with the high resolution of the SEM (see 2.1). The z -direction corresponds to the milling direction of the FIB. Here, the resolution is given by the SEM sampling frequency and is typically less than the resolution of the image. During the reconstruction process the software interpolates between neighboring slices which essentially results in a loss of information (see also discussion of specific surface area). Due to this uncertainty the z -direction will not be included in the following discussion.

The resulting effective diffusivities D_i^{eff}/D_i^0 are generally higher for the reduced electrodes and the electrodes produced at low pressure load. This agrees favorably with the prediction of Eq. (2.39) that the diffusivity is proportional to the porosity of the electrode. In the case of the reduced low-porosity electrode the porosity is approximately the same as for the pristine high-porosity electrode and also the resulting diffusivity is similar. Bruggeman coefficients for both the pristine and the reduced electrodes are around the standard value of 1.5. This is in good agreement with other theoretical work [151] and a further hint for the validity of the method. The Bruggeman coefficients of the reduced low-porosity electrode are slightly lower. This might indicate that a mere scaling of particle sizes according to the density ratio of Ag/Ag₂O results in an overestimation of effective transport parameters.

Values of the permeability are around $5 \cdot 10^{-14} \text{ m}^2$ and $1 \cdot 10^{-15} \text{ m}^2$ for the pristine electrodes with high and low porosity, respectively. The corresponding permeability of the reduced state is about an order of magnitude higher. The value of permeability in the y -direction of the reduced high-porosity electrode is exceptionally high. This is in line with the observed band of high velocity which can be seen in Figure 2.13 b).

The Kozeny-Carman relationship [144] gives an estimate of the permeability of porous media under the assumption of a packing of spherical particles

$$B = \frac{\varepsilon_0^3 d_p^2}{72 \bar{\tau} (1 - \varepsilon_0)^2}, \quad (2.44)$$

where d_p is the electrode particle diameter. The Kozeny-Carman permeability of the pristine high-porosity electrode is $7 \cdot 10^{-14} \text{ m}^2$ which is in reasonable agreement with the values calculated by GeoDict (Tables 2.3 and 2.4).

The effective electric conductivity of the electrode structure is also included in Tables 2.3 and 2.4. For these calculations the pore space is assumed to be insulating ($\sigma_{\text{el}} = 0$). The

High-porosity electrode	Pristine Ag ₂ O electrode			Reduced Ag electrode		
	<i>x</i>	<i>y</i>	<i>z</i>	<i>x</i>	<i>y</i>	<i>z</i>
Diffusivity / -	0.355	0.394	0.123	0.446	0.499	0.279
Tortuosity factor / -	1.393	1.256	4.012	1.385	1.237	2.213
Bruggeman coefficient / -	1.473	1.929	4.340	1.672	1.440	2.644
Permeability / m ²	3.1·10 ⁻¹⁴	5.2·10 ⁻¹⁴	1.0·10 ⁻¹⁴	5.1·10 ⁻¹⁴	1.1·10 ⁻¹³	3.6·10 ⁻¹⁴
Conductivity / S m ⁻¹	1.2·10 ⁻⁷	2.1·10 ⁻⁷	2.3·10 ⁻⁸	2.7·10 ⁶	6.7·10 ⁶	1.8·10 ⁶

Table 2.3.: Effective transport properties of the Ag/Ag₂O GDE fabricated with low pressure. Values are a result of the calculations in GeoDict.

Low-porosity electrode	Pristine Ag ₂ O electrode			Reduced Ag electrode		
	<i>x</i>	<i>y</i>	<i>z</i>	<i>x</i>	<i>y</i>	<i>z</i>
Diffusivity / -	0.155	0.159	0.080	0.355	0.375	0.264
Tortuosity factor / -	1.987	1.930	3.833	1.272	1.206	1.712
Bruggeman coefficient / -	1.582	1.558	2.140	1.303	1.236	1.677
Permeability / m ²	1.0·10 ⁻¹⁵	1.0·10 ⁻¹⁵	4.7·10 ⁻¹⁶	1.1·10 ⁻¹⁴	1.1·10 ⁻¹⁴	6.5·10 ⁻¹⁵
Conductivity / S m ⁻¹	4.2·10 ⁻⁷	3.8·10 ⁻⁷	3.0·10 ⁻⁷	7.4·10 ⁶	5.2·10 ⁶	2.8·10 ⁶

Table 2.4.: Effective transport properties of the Ag/Ag₂O GDE fabricated with high pressure. The structure of the reduced Ag electrode is obtained by rescaling the particle sizes of the pristine case according to the change in density during the reduction from Ag₂O to Ag.

conductivity of metallic Ag is very high [152] compared to the conductivity of Ag₂O [135]. In both cases the resulting effective conductivity is about an order of magnitude smaller than the bulk conductivity.

Distribution of hydrophobic binder material

Figure 2.14 shows an electron microscope image of a cross section of the Ag₂O gas diffusion electrode fabricated at low pressure (high-porosity electrode). At the bottom of the image one can see the wires of the nickel mesh which serves as support and current collector for the catalyst layer. The picture gives a good impression of the porosity of the material. The inset shows a close-up image of the micro-structure of the catalyst layer. Smaller particles are connected by thin filaments which originate from the hydrophobic binder. The binder fibers are finely dispersed in the whole electrode volume and have a diameter of around 50 nm. The binder preferentially spans across the surface of agglomerates and at some spots an almost dense surface of hydrophobic material is formed. The distribution

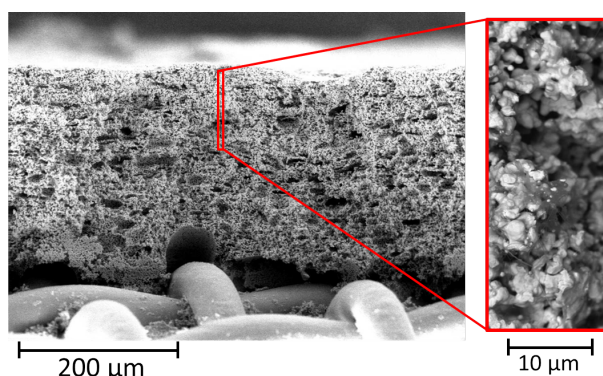


Figure 2.14.: Electron microscope image of an Ag_2O gas diffusion electrode fabricated at low pressure ('high-porosity case'). The inset shows a close-up image of the micro-structure of the catalyst layer. Smaller particles are connected by thin filaments forming larger agglomerates. The thin filaments originate from the hydrophobic binder [145].

of the binder fibers is not resolved in the reconstruction process. On the one hand the fiber structure is damaged by the ion beam in the milling process. On the other hand it is covered by the epoxy resin which is hard to distinguish from the binder material in the microscope image.

However, the hydrophobic binder is important for the operation of the GDE as it ensures the coexistence of gas and liquid phase in the pore network. The saturation of the pore space with liquid electrolyte determines the transport of reactants in the gas as well as in the liquid phase. This issue will be discussed in more detail in Chapter 3.

2.3.2. Electrochemical characterization of $\text{Ag}/\text{Ag}_2\text{O}$ Gas Diffusion Electrodes

Electrochemical Impedance Spectroscopy

Electrochemical impedance spectra are often displayed in so-called complex plane or Nyquist plots. In this type of graph the real and negative imaginary part of the complex impedance are plotted on the abscissa and ordinate, respectively. The lowest impedance in the complex plane diagram corresponds to the highest frequency of the sinusoidal excitation.

The impedance of a flat electrode in the absence of mass transport effects is given by a

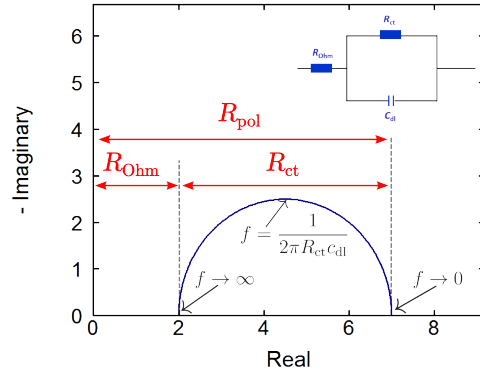


Figure 2.15.: Schematic Nyquist plot of the equivalent circuit depicted in the upper right-hand corner. The circuit consists of an element describing the contribution of the ohmic resistance (R_{Ohm}) in line with a RC-element representing the CTR and double-layer at the electrode-electrolyte interface.

semi-circle in the complex plane. It can be modeled by the equivalent circuit depicted in the upper right-hand corner of Figure 2.15. In this simple case it is possible to graphically extract some important parameters of the electrochemical system. The first element of the equivalent circuit represents the contribution of the ohmic resistance R_{Ohm} . In the Nyquist plot the ohmic resistance can be taken from the high-frequency crossing with the real axis. The charge-transfer resistance R_{ct} in turn is given by the diameter of the semi-circle. The sum of ohmic and charge-transfer resistance is called the polarization resistance of the electrode R_{pol} . The double-layer capacitance c_{dl} can be evaluated at the frequency where the semi-circle reaches its maximum.

Contributions to the impedance due to slow diffusion in the electrolyte or active particle (e.g. Li-ion batteries) are typically described by a so-called Warburg element [147]. It is modeled in line with the charge-transfer resistance at the electrode surface ('Randles circuit') [147]. Similarly, mass transport effects in the porous structure of the GDE cause a deviation of the impedance spectra from the perfect semi-circle. In the equivalent circuit model employed in this work a transmission line element for porous electrodes proposed by Göhr *et al.* [149] is included (see Figure 2.11). A fitting procedure to the experimental data is used to quantify relevant physical and electrochemical processes.

Figure 2.16 shows Nyquist plots of impedance spectra of the Ag electrode during O_2 reduction. Under oxygen evolution conditions, the formation of gas bubbles on the electrode surface deteriorates the measurement signal (cf. noise in Figure 2.22) and

2. Experimental work

impedance spectra are not reported here. The symbols represent data points of the measurements and the solid lines are the result of the fit to the equivalent circuit model. The recorded spectra show features typical for porous electrodes [147, 148]. At high frequencies the imaginary part linearly increases at an angle of approximately 45° with the real axis and a depressed semi-circle is attached to this linear region. As explained above the resistance in the limit of infinite frequencies corresponds to the combined ohmic resistance of the electrode and liquid electrolyte. The conductivity of silver, however, is very high and the contribution of the electrode can be neglected [152]. A linear increase of the imaginary part can be observed if the signal of the excitation is not penetrating the whole pore space of the GDE [148]. This typically occurs if the penetration depth λ is much smaller than the characteristic length scale of the pore network. In the present case the characteristic length is approximately given by the thickness of the electrode $L_{\text{GDE}} = 560 \mu\text{m}$. The penetration depth follows as [148]

$$\lambda = \sqrt{0.5\bar{r}Z_{\text{elode}}\sigma_{\text{elyte}}} . \quad (2.45)$$

Here Z_{elode} is the impedance of the electrode, \bar{r} the mean pore radius and σ_{elyte} the conductivity of the electrolyte solution. At a frequency of 1 kHz λ is around $3 \mu\text{m}$ for the measurements shown in Figure 2.16. The impedance of the electrode and the penetration depth increase [153] towards lower frequencies. At 1 Hz λ is already around $20 \mu\text{m}$ and the ac signal is able to penetrate the whole pore space. In this case, the impedance is comparable to one of a flat electrode.

Figure 2.16 shows the influence of a) overpotential, b) temperature, and c) LiOH concentration on oxygen reduction at the porous Ag electrode. In Figure 2.16 a) the impedance spectra are given at different potentials vs. RHE in 1 M LiOH solution at 25°C . The high-frequency crossing of the spectra with the real axis stays approximately the same for all potentials. However, the diameter of the semi-circle changes with the applied potential. For a small overpotential it is large and at low frequencies the plot does not reach down to the real axis in the frequency range studied here. Towards higher overpotentials the diameter of the semi-circle decreases. These observations suggest that the applied potential does not influence the conductivity of the electrolyte but it does have a positive effect on the kinetics of the charge-transfer reaction. Figure 2.16 b) shows impedance spectra in 1 M LiOH solution at a fixed potential of 700 mV vs. RHE. The varying parameter in this case is the temperature of the electrolyte bath. For a rise in temperature the high-frequency crossing of the real axis as well as the diameter of the semi-circle

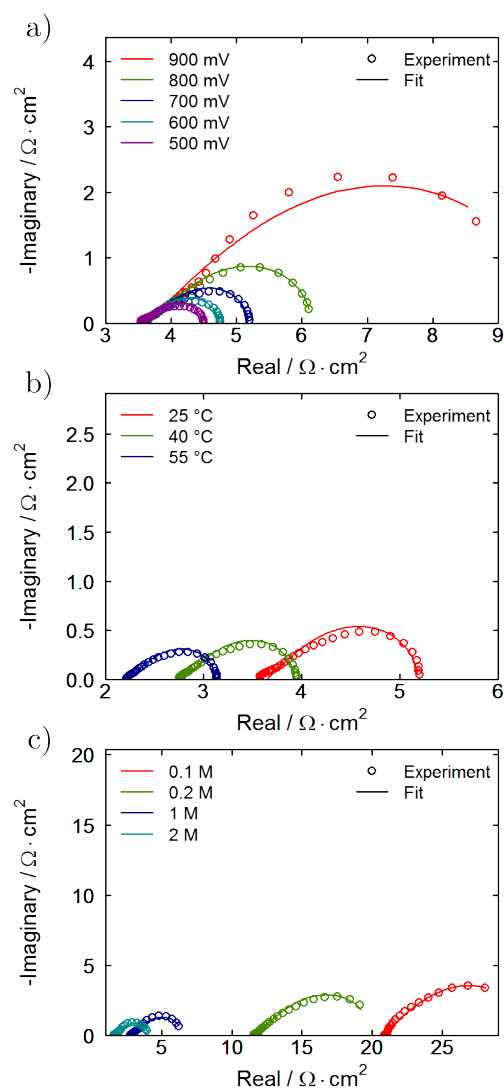


Figure 2.16.: Nyquist plot (100 mHz to 10 kHz, 6 and 10 measurement points per decade at frequencies below and above 10 Hz, respectively) of impedance spectra recorded during O_2 reduction. Symbols represent experimental data and lines show results of the fit to the equivalent circuit model (see Figure 2.11). a) Impedance spectra in 1 M LiOH at 25 °C, b) Impedance spectra in 1 M LiOH at 700 mV vs. RHE, c) Impedance spectra at 40 °C and 900 mV vs. RHE.

2. Experimental work

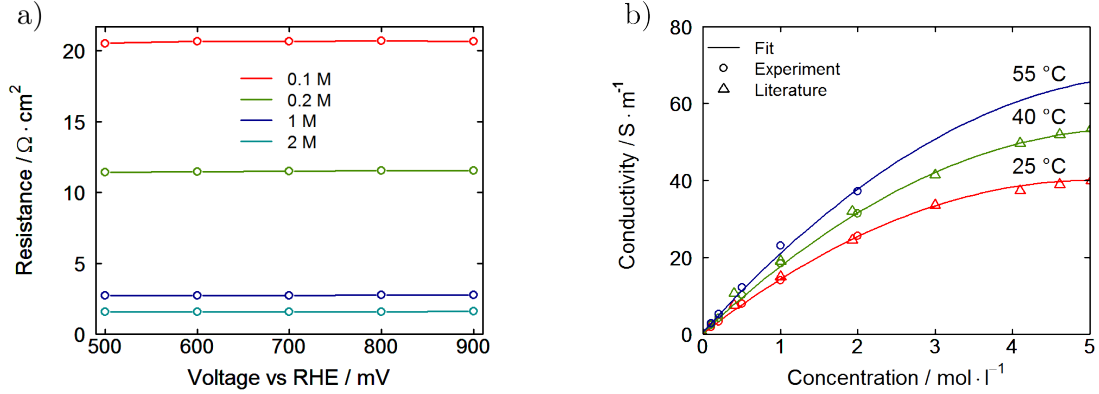


Figure 2.17.: a) Electrolyte resistance as function of potential at 40 °C in 0.1, 0.2, 1, and 2 M LiOH solution. b) Corresponding specific electrolyte conductivity as function of concentration at 25, 40, and 55 °C. Open circles represent results of the measurements and open triangles are included from the literature [154]. The solid line is a result of the fit to the combined set of data (Eq. (4.58)).

decrease. This demonstrates more facile kinetics of the CTR and an improved conductivity and transport of reactants at elevated temperatures. Similar effects can be seen for the impedance spectra with varying LiOH concentration. They are depicted in Figure 2.16 c) at a fixed temperature (40 °C) and potential (900 mV vs. RHE). The high-frequency crossing of the real axis reduces significantly by going to higher concentrations and also the diameter of the semi-circle decreases.

The qualitative observations of Figure 2.16 are in line with the theoretical considerations of Section 2.1. Analysis of the data with the aid of the equivalent circuit model described in Section 2.2.2 is able to give quantitative information on the processes discussed above. The error of the fit to the experimental data is in all cases less than 3%. In general, the fit to the measurements at high concentrations is slightly better compared to the measurements in 0.1 M. This good agreement demonstrates that the relatively simple equivalent circuit is able to represent all relevant processes.

Figure 2.17 a) shows the **electrolyte resistance** R_{elyte} as function of potential at 40 °C in 0.1, 0.2, 1, and 2 M LiOH solution. The horizontal lines confirm the observation that the electrolyte resistance does not depend on overpotential. The resistance can be converted to a conductivity by

$$\sigma_{\text{elyte}} = \frac{1}{R_{\text{elyte}}} L_{\text{ref}}, \quad (2.46)$$

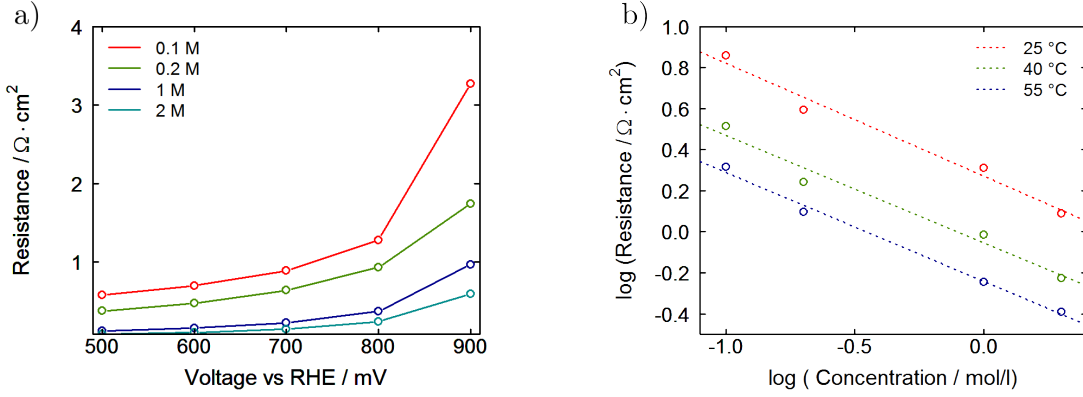


Figure 2.18.: a) Charge-transfer resistance R_{ct} as function of potential at 40 °C in 0.1, 0.2, 1, and 2 M LiOH solution. b) Plot of R_{ct} as function of LiOH concentration in double logarithmic form at a potential of 900 mV vs. RHE. The dotted line represents a linear fit to the data points at 25, 40, and 55 °C, respectively.

where $L_{\text{ref}} = 5$ mm is the distance between the electrode surface and the position of the reference electrode in the electrolyte bath. The resulting conductivities are included as open circles in Figure 2.17 b). Open triangles represent values of conductivity from the literature [154]. The solid line is the result of fit to the combined set of data (see Eq. (4.58)). The plot demonstrates a good agreement of the measurements with the literature and reflects the effect of concentration and temperature observed in the Nyquist plots.

Figure 2.18 a) shows the **charge-transfer resistance** R_{ct} as function of potential and concentration at 40 °C. As expected from the Nyquist plot, the resistance decreases with rising overpotential and concentration. The Faradaic current in the linear regime is given by (Eq. (2.23))

$$i_F = i_0 \frac{nF}{RT} \eta, \quad (2.47)$$

where η/i_F corresponds to the charge-transfer resistance R_{ct} . According to Eq. (2.22) i_0 is proportional to c_R^β and thus

$$R_{ct} \sim \frac{1}{c_R^\beta}. \quad (2.48)$$

This is consistent to the trend of Figure 2.18 a). In a double-logarithmic plot of $\log R_{ct}$ vs. $\log c_{\text{LiOH}}$ (Figure 2.18) the measured values at each temperature fall on a single line

2. Experimental work

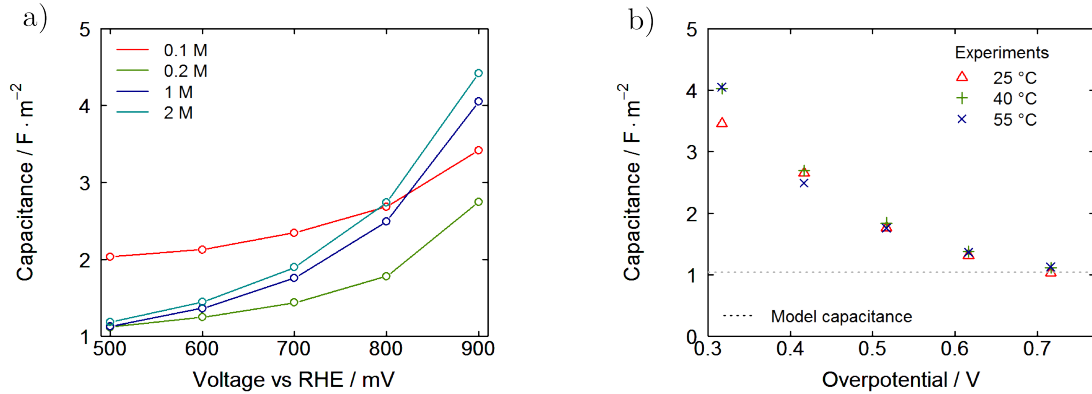


Figure 2.19.: a) Values of double-layer capacitance c_{dl} as function of potential in 0.1, 0.2, 1, and 2 M LiOH solution at a temperature of 40 °C. b) Capacitance as function of cathodic overpotential in 1 M LiOH at 25, 40, and 55 °C. The dotted line represents the model capacitance of a compact layer at low potentials.

with a slope of $-\beta$. This is shown in Figure 2.18 b) for a potential of 900 mV vs. RHE and at temperatures of 25, 40, and 55 °C. The dotted lines represent a linear fit to the measurements yielding an estimate of $\beta_{\text{Cathode}} = 0.133$.

Figure 2.19 a) shows a graph of the **double-layer capacitance** c_{dl} as function of potential at a temperature of 40 °C. As a general trend one can see a reduction of capacitance with growing overpotential and decreasing concentration. At high overpotentials the values for the capacitance approach a constant value regardless of electrolyte concentration. There are probably two independent effects contributing to the observed trend with potential. At high overpotentials the diffuse layer moves closer to the electrode surface. As a result the double-layer becomes more compact and the contribution of the diffuse layer vanishes. Additionally, ad- and desorption processes on the surface of the electrode might contribute to the capacitance. This agrees with the change in Tafel slope at high overpotentials which is observed in the literature [75]. The measurements in 0.1 M solution do not follow the overall trend with concentration. A possible reason is the lower accuracy of the fit of the equivalent circuit model.

Figure 2.19 b) shows the double-layer capacitance in 1 M LiOH solution. The graphs at different temperatures almost collapse on a single line. This indicates a small influence of temperature compared to the applied potential. At high overpotentials the double-layer is compact and the capacitance can be modeled by assuming a parallel-plate capacitor. The dotted line in Figure 2.19 b) represents the capacitance of the model. More details on

the modeling of the electric double-layer are given in Section 4.3.1 in the course of the parametrization of the continuum model.

The last remaining parameter of the equivalent circuit model is the **pore transport impedance** Z_{pore} . Figure 2.20 shows the values of the impedance over potential (left) and concentration (right). The impedance decreases towards higher concentrations, temperatures and overpotentials. Although the model for Z_{pore} is complex [149] it can be assumed, analogous to R_{elyte} (see Eq. (2.46)), that in a first approximation (constant ionic current)

$$Z_{\text{pore}} \sim \frac{1}{\sigma_{\text{elyte}}} L' , \quad (2.49)$$

where L' is a characteristic length for ionic conduction in the pore space of the electrode. The decrease in resistance at higher concentration and temperatures can be explained by an increase in electrolyte conductivity as discussed above (Figure 2.17 b)). The observed trend with potential is less intuitive. Eq. (2.49) suggests a dependence of the characteristic length on potential. However, the transport in porous media is complex and other effects might contribute to this behavior. One explanation is an increase of the local concentration of LiOH at high overpotential due to mass transport limitations in the pore space. This causes an increase in electrolyte conductivity and a corresponding drop in the effective pore transport resistance. The continuum model described in Chapter 4 can be used as an effective tool to elucidate this topic.

Cyclic Voltammetry

As mentioned in Section 2.2, cyclic voltammograms are recorded separately in the ORR and OER regime. The potential range covered is 1100 mV - 500 mV (ORR) and 1400 mV - 1950 mV (OER), respectively.

The cyclic voltammograms for both regimes are shown together in Figure 2.21 a). After an initial drop at the beginning of the ORR measurements, the cathodic current stabilizes at a small value. At even lower potential the current linearly increases with overpotential during the forward scan. A rise in temperature leads to steeper slopes in the linear region. The maximum current is drawn at the turning point of the potential scan. Below potentials of 1 V the forward and the backward sweep collapse onto a single line for all studied scan rates. The initial drop in current can be attributed to a reduction of

2. Experimental work

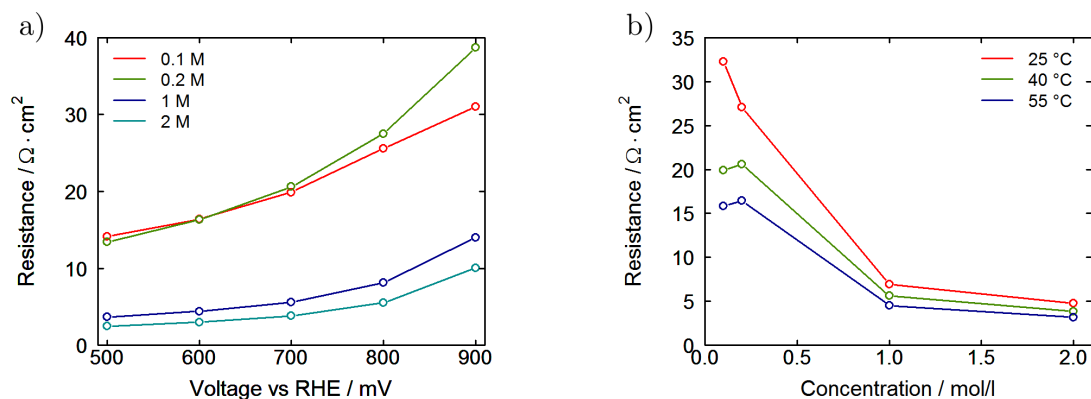


Figure 2.20.: a) Pore transport impedance Z_{pore} as function of potential at 40 °C in 0.1, 0.2, 1, and 2 M LiOH solution. b) Pore transport impedance Z_{pore} as function of concentration at 700 mV vs. RHE. Curves are shown at temperatures of 25, 40, and 55 °C.

remaining amounts of silver oxides. Surface layers of Ag_2O start to form at potentials close to the equilibrium potential of silver oxide reduction (1173 mV vs. RHE). At higher overpotentials Ag_2O is fully consumed and the current is produced by the continuous reduction of oxygen alone. The porous structure of the GDE allows good transport of reactants and causes a linear increase of current towards higher overpotentials. Even at potentials as low as 100 mV no limiting current can be observed. This demonstrates a good supply of oxygen to the active sites of the GDE. Thus, the peak performance of the electrode is not determined by mass or charge transport processes. The facile kinetics show an increase of ORR activity at elevated temperatures. A dashed line in Figure 2.21 a) represents the repetition of the CV measurements after operating the electrode under oxygen evolution conditions. It shows the same features as the pristine electrode. The lower current, however, is a clear indication for a degradation of the electrode during oxygen evolution. Possible degradation mechanisms are discussed below.

Cyclic voltammograms of oxygen evolution (OER) are shown above 1.4 V in Figure 2.21 a). At low overpotentials, a small and constant anodic current can be measured. After a small dip, the current continuously increases towards higher potentials. A gap of around 0.01 A cm^{-2} exists between the forward and the backward scan. At high currents the measurement signal shows a significant noise. This coincides with the observation of gas bubble formation on the GDE surface [86]. These bubbles obstruct the transport of reactants in the porous electrode and block parts of the catalytically active surface. The

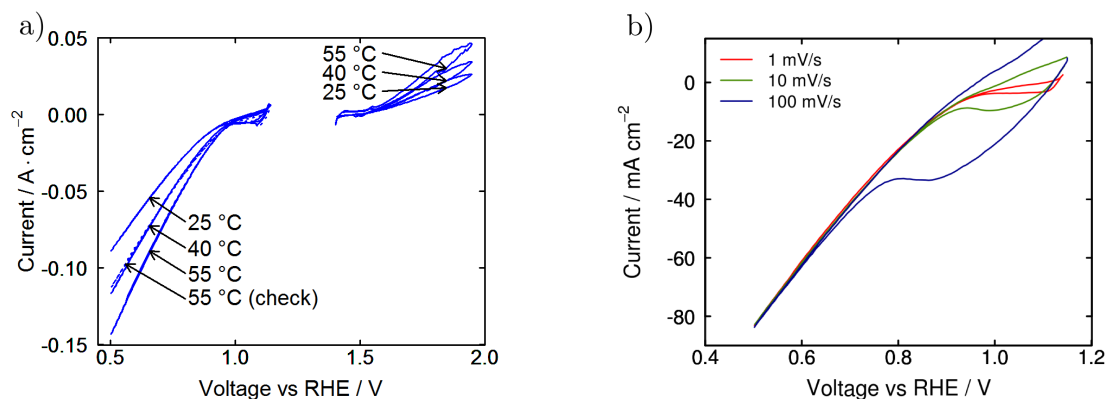


Figure 2.21.: a) CVs of O₂ reduction (1.1 V - 0.5 V) and evolution (1.4 V - 1.95 V) in 1 M LiOH solution. The scan rate of the measurements is 1 mV/s. b) CVs of O₂ reduction at 25 °C and scan rates of 1, 10, 100 mV/s.

statistical process of bubble nucleation generates noise which can be seen in the current signal. A visible mechanical damage of the electrode is not observed. In the potential range studied, silver exhibits several oxidation states (see Figure 2.3 [132]). The small dips in the forward and backward scan arise from corresponding changes therein. Some of these states are reported to dissolve in alkaline electrolytes [155, 156]. The resulting changes in the surface morphology in turn might lead to the observed degradation of GDE performance.

In contrast to the negative potential sweep there is a gap between forward and backward scan. Possible reason is the aforementioned degradation of the electrode or a change in surface properties due to an adsorption of strongly binding species. Another possibility might be a depletion of hydroxide ions in the liquid electrolyte due to transport limitations. This is, however, unlikely as mass transport limitations are not observed at higher currents during oxygen reduction.

Figure 2.21 b) shows the negative sweep at different scan rates. The cathodic peak at the beginning of the forward scan is more pronounced at higher scan rates. After the peak the current signals of the different scan rates collapse on a single line. A significant contribution of the double-layer current is not observed. As explained above, the cathodic peak on the forward scan can be assigned to a consumption of remaining Ag₂O on the electrode surface. At higher scan rate Ag₂O is consumed at higher overpotentials and the resulting Faradaic currents are also higher, accordingly.

The negligible influence of the scan rate indicates that the electrodes are very likely in

2. Experimental work

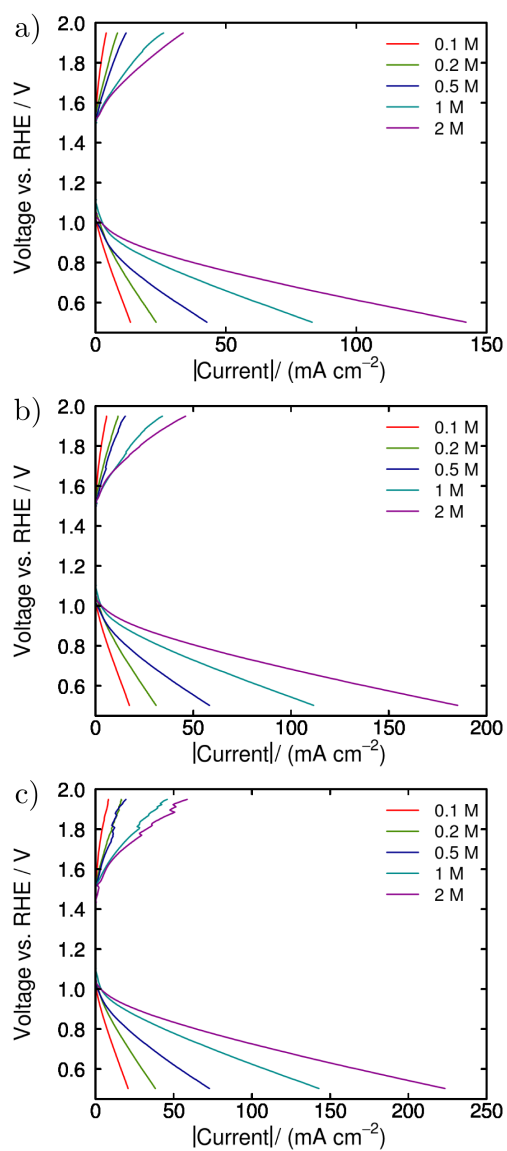


Figure 2.22.: IV curves of the Ag electrode in 0.1 M, 0.2 M, 0.5 M, 1 M, and 2 M at temperatures of a) 25°C, b) 40°C, c) 55°C. The curves are deduced from the backward sweep of the CV measurements at a scan rate of 1 mV/s.

quasi-equilibrium at the lowest scan rate of 1 mV/s. This allows to interpret the backward scan as characteristic IV curve of the GDE. Figure 2.22 shows IV curves of the Ag GDE at different concentrations and temperatures. The trends are consistent to the observations made by electrochemical impedance spectroscopy. Generally speaking, the performance of the GDE improves towards higher concentrations and temperatures.

Furthermore, the IV curves can be used to determine the kinetics of the Ag electrode by Tafel analysis. The noisy signal during O₂ evolution makes an exact analysis of OER kinetics very difficult. Additionally, the observed degradation adds to the insecurity in this parameter. Therefore, the focus in the analysis is here on O₂ reduction.

The Tafel analysis outlined below is performed at a LiOH concentration of 1 M. This concentration also serves as standard case for the parametrization of the continuum model. In a first step the potential of the measurements is corrected for overpotentials due to mass and charge transport effects in the porous electrode and electrolyte bath. The activation overpotential η_{act} is given by

$$\eta_{\text{act}} = \eta - R_{\text{tot}}i \quad , \quad (2.50)$$

where $R_{\text{tot}}=R_{\text{elyte}}+Z_{\text{pore}}$ is the total mass transport resistance. R_{elyte} and Z_{pore} are determined from the equivalent circuit model. The Tafel plot with corrected overpotentials is shown in Figure 2.23. A straight line is fitted to the Tafel regime between $\eta_{\text{act}}=150$ mV and 200 mV. Although the values are corrected for mass transport effects, a significant deviation from linear behavior can be observed at higher overpotentials. This might be an artifact of the iR -correction. Therefore, the values at higher potentials are not included in the Tafel fits. The Tafel slope of ~ 100 mV/decade gives a symmetry factor β_{Cathode} of ~ 0.145 [128]. This value is slightly higher compared to the one determined from the charge-transfer resistance ($\beta_{\text{Cathode}} = 0.133$). However, it is in good agreement with the data reported for Ag in alkaline electrolytes in the literature [75]. The exchange current densities at the three different temperatures follow from the intercept of the Tafel line with the line of zero overpotential (see Table 2.5). The kinetic data obtained by the Tafel analysis is important for the parametrization of the rate equation of the continuum model (Section 4.3.1).

2. Experimental work

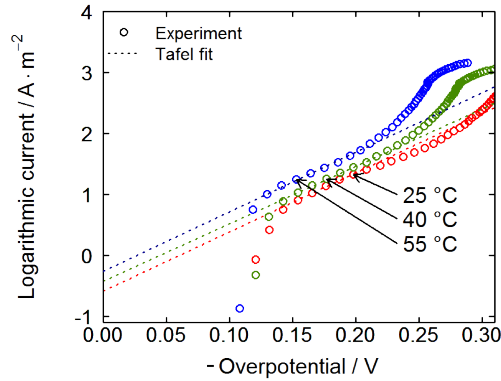


Figure 2.23.: Tafel analysis for the ORR in 1 M LiOH solution at temperatures of 25, 40 and 55 °C. Experimental data of CV measurements is indicated by open circles. The data is corrected for mass transport effects according to Eq. (2.50). The dashed lines represent the best Tafel fit at overpotentials between $\eta_{\text{act}} = 150$ mV and 200 mV.

Effect of electrode structure and pressure in the liquid phase

Two different batches of Ag electrodes which were prepared with the same composition but at different compression levels are investigated in this work (cf. introduction to Chapter 2 [127]). The production process has a considerable effect on the GDE structure and the resulting porosities in the pristine state are 31% and 48%, respectively (Table 2.2). This has an impact on the transport behavior of the electrodes and effective transport parameters were found to be considerably smaller in the electrodes with lower porosity (see Table 2.4).

The transport in the porous structure has a direct influence on the performance of the GDE. Figure 2.24 a) shows IV curves of the electrodes prepared at low and high pressure load at 25 and 50 °C in 1 M LiOH solution [145]. At the same overpotential the resulting currents are smaller in the electrode with lower porosity. Here, the transport pathways in

Temperature / °C	Exchange current density i_0 / A/m ²	Symmetry factor β_{cathode} / -
25	0.262	0.143
40	0.376	0.146
55	0.547	0.158

Table 2.5.: Exchange current density and symmetry factor determined in Tafel analysis in 1 M LiOH solution at 25, 40, 55 °C.

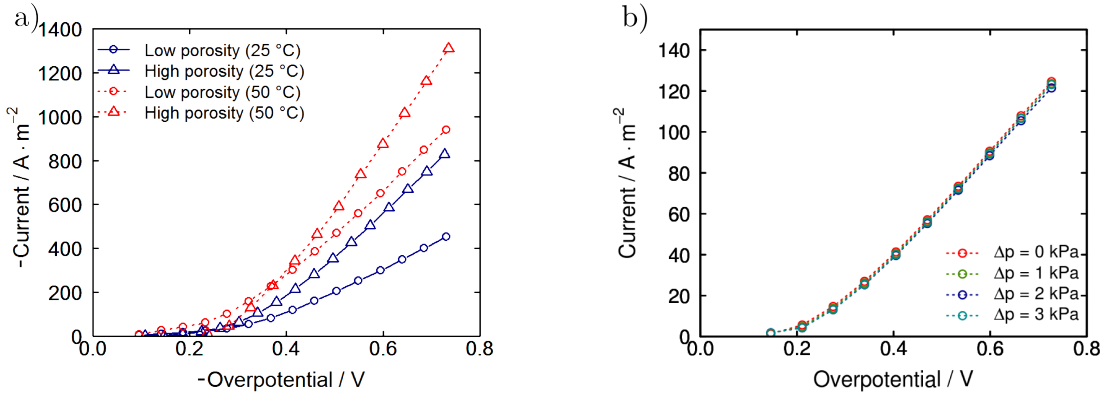


Figure 2.24.: IV curves of O₂ reduction deduced from CV measurements at a scan rate of 1 mV/s. a) Effect of electrode porosity at 25 (blue) and 50 °C (red). The LiOH concentration is 1 M. b) Effect of pressure in the electrolyte bath at 25 °C and a concentration of 0.1 M.

the liquid electrolyte are more tortuous and, hence, longer compared to the electrode with higher porosity. Therefore, the transport resistance in the low-porosity GDE is higher which causes a higher ohmic loss. These losses which are essentially due to charge transport in the liquid electrolyte mainly determine the slope of the IV curves at high overpotentials and, thus, the performance of the GDE. At elevated temperatures qualitatively the same effect is observed. The graph demonstrates that almost a doubling in temperature is needed to compensate the detrimental effect of the lower porosity.

Another parameter which has an influence on the transport in the pore space is the pressure in the electrolyte bath. At elevated pressures the saturation of the porous electrode with liquid electrolyte increases. According to Eq. (2.39) this leads to an improved transport in the liquid phase. This in turn reduces the losses due to concentration overpotentials and results in a better performance of the electrode. Figure 2.24 b) shows results of measurements which are recorded in the 'pressure cell' (Figure 2.10) at an electrolyte concentration of 0.1 M. For the standard measurements the pressure difference between the electrolyte bath and the gas channel is approximately zero. After increasing the pressure by adding electrolyte to the ascending pipe the system is given 30 minutes to attain fluid mechanical equilibrium. However, in the parameter range studied here, the electrolyte pressure does not affect the performance of the Ag electrode. The differences in the maximum current are not systematic and could also be caused by inaccuracies in the measurements. One reason might be that the pressure loads which are applied in this

study are not sufficient to change the saturation of the pore space.

The influence of electrode structure and pressure in the liquid electrolyte on transport and performance will be discussed in more detail in the following chapters.

2.4. Conclusions

Chapter 2 gives an overview of the experimental activities on Ag/Ag₂O electrodes. The electrodes were characterized structurally as well as electrochemically.

For the structural characterization a FIB-SEM based tomography technique was used by the project partners at the University of Ulm [141] to obtain a three-dimensional reconstruction of pristine (Ag₂O) and reduced (Ag) samples. The reconstruction was imported in the software GeoDict for the determination of structural and effective transport parameters. It was found that the reduction process has a strong influence on the structural properties. The porosity in the reduced samples was much higher compared to the pristine ones. The difference between the pristine and reduced porosity approximately corresponded to a change in density from Ag₂O to Ag. The porosity had a direct influence on the effective transport in the porous structure. Samples with different porosity have been studied for their effective diffusivity, permeability and electric conductivity. Diffusivity and permeability were generally higher in electrodes with a high porosity. The resulting Bruggeman coefficient, however, was in all cases around the standard value of 1.5.

For the electrochemical characterization cyclic voltammetry and electrochemical impedance spectroscopy were employed to study the performance of the electrode under different conditions. A focus in the characterization was on the oxygen reduction reaction (ORR) as the measurements of O₂ evolution (OER) showed a noisy signal and degradation of the electrode. In general, the performance of the electrode improved towards higher electrolyte concentration, temperature and overpotential. The final performance was eventually determined by the mass and charge transport in the porous structure. However, a limiting current due to an insufficient supply of O₂ was not observed even at currents as high as 225 mA cm⁻².

The measured impedance spectra showed the typical features known for porous electrodes. An equivalent circuit model was used to extract quantitative information on the contribution of different processes to the total impedance. Main findings were the specific

conductivity of the electrolyte and the capacitance of the electric double-layer. The data from cyclic voltammetry in turn offered information on the kinetics of the system. The Tafel slope in 1 M LiOH solution was around 100 mV/decade. Measurements on GDEs with varying porosity demonstrated the significant influence of structure on electrode performance. An influence of liquid electrolyte pressure could not be observed in the measurements.

The measurements give a good insight on the operation of GDEs in LiOH solution. Primary goal of the measurements, however, is to gain a solid basis for parametrization and validation of the continuum model described in Chapter 4.

3. Lattice-Boltzmann modeling and simulation

In recent years the Lattice-Boltzmann Method (LBM) became a popular tool for the simulation of flow problems in complex geometries [157]. The applications range from blood flow in arteries [158] to multiphase flow in gas diffusion layers of PEMFCs [109–111, 159]. Advantages of the method are a relatively simple implementation and an excellent parallelization capability. Still, the computational cost of the method is high and 3D simulations of large geometries are tedious.

This chapter gives an overview of LBM and discusses in detail the multiphase model employed in this work. The model allows to obtain steady-state liquid-phase distributions in the pore space of the reconstructed GDEs (Chapter 2). This gives the opportunity to calculate characteristic capillary pressure-saturation curves $p_c - s$ curves, effective transport parameters, and active surface areas.

The Lattice-Boltzmann model presented here was developed in collaboration with Prof. Arnulf Latz from the Helmholtz Institute Ulm for electrochemical energy storage [160].

3.1. Background

This section gives a short introduction to the fundamentals of the Lattice-Boltzmann method [122]. As a first step the Boltzmann equation is derived which is of course the basis of all LBM models (Section 3.1.1). In a following step the Lattice-Boltzmann method for single-phase flow is introduced (Section 3.1.2) and, finally, models for multiphase flow are discussed (Section 3.1.3). The focus is here on the color gradient or Rothmann-Keller

(RK) type model which is used in this study. A detailed description of the model including all relevant parameters is given in Section 3.2.1.

3.1.1. The Boltzmann equation

The Boltzmann equation describes the behavior of fluids on a microscopic scale and is based on the kinetic theory of gases pioneered by Ludwig Boltzmann. In this approach a gas is regarded as a system composed of many interacting particles. In general, a system consisting of N molecules is fully determined if the position, velocity, and mass of all particles is known. The state of the system can be described at every point in time t by a distribution function $f^{(N)}(\mathbf{x}, \mathbf{v}, t)$ which keeps track of all particle positions \mathbf{x} and velocities \mathbf{v} . In this case classical mechanics and suitable collision rules allow the prediction of all future states of the system. This basically corresponds to the approach taken in MD simulations.

However, at standard conditions one liter of gas already consists of $\sim 2.7 \cdot 10^{22}$ molecules. Due to this huge number an efficient calculation of large systems is not feasible because of computational limitations and a statistical treatment of the problem is inevitable. Therefore, a distribution function $f^{(1)}(\mathbf{x}, \mathbf{v}, t)$ is introduced which only gives the probability of finding a molecule at position \mathbf{x} and time t with velocity \mathbf{v} . Still, all relevant macroscopic properties of the system, such as, density, velocity, or pressure can be determined from the statistical moments of the distribution function. In statistical mechanics [118] this approach is called ensemble averaging and is based on the assumption that the N molecules are indistinguishable.

An MD-like approach is not possible within this theoretical framework and other concepts need to be derived to calculate the distribution function of the system for future states $f^{(1)}(\mathbf{x} + d\mathbf{x}, \mathbf{v} + d\mathbf{v}, t + dt)$. Consider a system of molecules residing in state space at position \mathbf{x} and velocity \mathbf{v} . The total number of molecules in the interval $\mathbf{x} \pm d\mathbf{x}$ and $\mathbf{v} \pm d\mathbf{v}$ is given by $f^{(1)}(\mathbf{x}, \mathbf{v}, t)d\mathbf{x}d\mathbf{v}$. If the system is exposed to an external force \mathbf{F} , the positions and velocities at a new time-step $t^1 = t^0 + dt$ are given by

$$\begin{aligned} \mathbf{x}^1 &= \mathbf{x}^0 + d\mathbf{x} = \mathbf{x}^0 + \mathbf{v}dt \\ \mathbf{v}^1 &= \mathbf{v}^0 + d\mathbf{v} = \mathbf{v}^0 + \frac{\mathbf{F}}{m}dt, \end{aligned} \quad (3.1)$$

where m is the mass of the fluid. In these considerations interactions between molecules, meaning particle collisions, are not yet included. Two different scenarios are possible if collisions are taken into account:

- Due to particle collisions not all molecules heading for position \mathbf{x} will arrive at their new position (Ω^-)
- Some molecules not heading for position \mathbf{x} will end up at that position due to a collision process (Ω^+)

In a mathematical form this can be expressed as

$$f^{(1)}(\mathbf{x} + d\mathbf{x}, \mathbf{v} + d\mathbf{v}, t + dt)d\mathbf{x}d\mathbf{v} = f^{(1)}(\mathbf{x}, \mathbf{v}, t)d\mathbf{x}d\mathbf{v} + [\Omega^+ - \Omega^-] d\mathbf{x}d\mathbf{v}dt . \quad (3.2)$$

By using a first order Taylor series expansion for the left-hand side of Eq. (3.2)

$$f^{(1)}(\mathbf{x} + d\mathbf{x}, \mathbf{v} + d\mathbf{v}, t + dt) = f^{(1)}(\mathbf{x}, \mathbf{v}, t) + \nabla_{\mathbf{x}}f^{(1)}d\mathbf{x} + \nabla_{\mathbf{v}}f^{(1)}d\mathbf{v} + \frac{\partial f^{(1)}}{\partial t}dt \quad (3.3)$$

and by division through $d\mathbf{x}d\mathbf{v}dt$ finally follows the Boltzmann equation

$$\frac{\partial f}{\partial t} + \mathbf{v}\nabla_{\mathbf{x}}f + \frac{\mathbf{F}}{m}\nabla_{\mathbf{v}}f = \Omega . \quad (3.4)$$

The first and second term describe the advection of the probability distribution and the third term takes into account the effect of the external force \mathbf{F} . The term on the right-hand side of the equation is called the collision integral Ω . Its nature is complex and the resulting Boltzmann equation has a complicated integro-differential form. It should be noted that in the derivation above it is assumed that particle collisions are not correlated, meaning, that the time between two collision processes is much larger than the time of the collision itself.

3.1.2. The Lattice Boltzmann Method

The Boltzmann equation as written in Eq. (3.4) shows some formal similarity to the conservation equations of mass, momentum, and energy. In fact it is possible to derive the Navier-Stokes equations from the Boltzmann equation by a Chapman-Enskog expansion

3. Lattice-Boltzmann modeling and simulation

[161]. In this respect LBM can be seen as 'just another' work-horse for solving the Navier-Stokes equations. The method was proposed by McNamara *et al.* as an extension to the existing lattice gas automata [162]. Its main advantage is the absence of statistical noise which is quite a challenge in lattice gas simulations. Although the Boltzmann equation is based on the kinetic theory of gases LBM is not limited to this case. It has been successfully applied to the simulation of multiphase fluid flow and even heat transport [163].

In LBM the Boltzmann equation is discretized in space on a lattice which represents the simulated geometry. Figure 3.1 a) shows a schematic illustration of a generic porous structure in which each dot represents a node of the lattice. Nodes of the fluid and solid phase are marked in blue and gray color, respectively. The spacing between two nodes in horizontal or vertical direction is one lattice unit (lu). Red dots represent nodes at the interface between the fluid and solid phase and require a special treatment which is discussed in Section 3.1.4 on boundary conditions. In order to further simplify the calculations only a discrete number of velocities is allowed at each node. The velocity discretization of a D2Q9 lattice (two dimensions, nine velocities [164]) is shown in Figure 3.1 b). The probabilities of the discrete velocity directions are marked by f_0 to f_8 . The green area represents the probable fluid momentum at the lattice node and indicates that the fluid will have the tendency to flow in the direction of discrete velocity number 5. The macroscopic properties at each node are given by the lower moments of the probability distribution. The density ρ is given by the 0th order moment which is simply the sum of the probabilities in all possible lattice directions nv

$$\rho = \sum_i^{nv} f_i. \quad (3.5)$$

The fluid velocity \mathbf{v} follows as the first order moment of the distribution which can be regarded as average of the discrete velocities \mathbf{e} weighted by their probability

$$\mathbf{v} = \frac{1}{\rho} \sum_i^{nv} \mathbf{e}_i f_i. \quad (3.6)$$

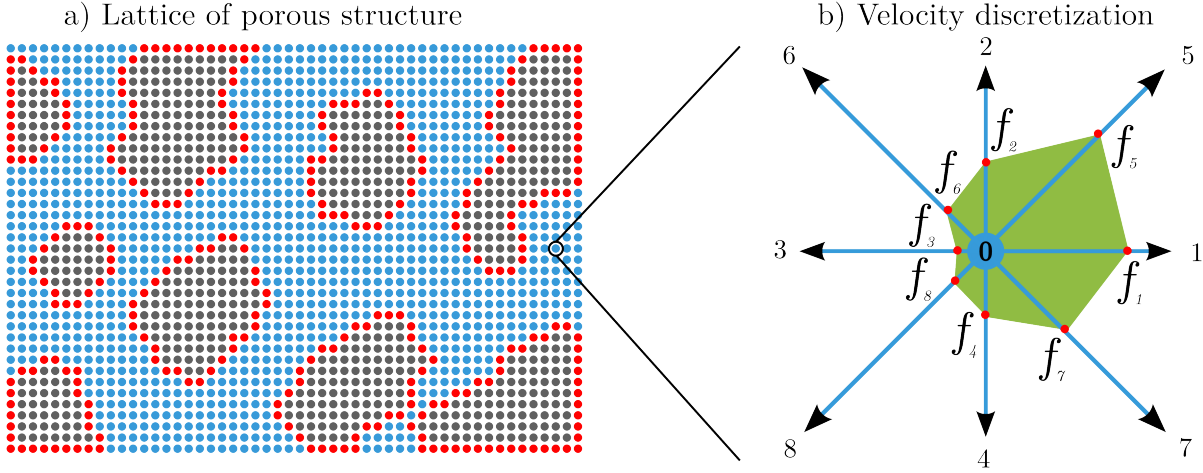


Figure 3.1.: Left: Two-dimensional lattice of a porous structure. Colored dots indicate the nodes of the computational lattice. Blue and gray colors represent lattice nodes of fluid and solid phase, respectively. The red dots represent nodes at the fluid-solid interface. Right: Velocity discretization for the D2Q9 lattice. Probabilities in the 9 lattice directions are marked by f_0 to f_8 .

This mathematical formulation is in line with the qualitative observations made in Figure 3.1 b) (cf. green area of fluid momentum). The discrete velocities \mathbf{e} of a D2Q9 [164] lattice in Cartesian coordinates are given by

$$\mathbf{e} = c \begin{pmatrix} 0 & 1 & 0 & -1 & 0 & 1 & -1 & 1 & -1 \\ 0 & 0 & 1 & 0 & -1 & 1 & 1 & -1 & -1 \end{pmatrix}, \quad (3.7)$$

where $c = \Delta x / \Delta t$ is a free constant that determines the basic speed on the lattice. Several other velocity discretizations are proposed in the literature [122, 164]. For the three-dimensional simulations presented in this work a D3Q19 lattice is employed [161].

$$\mathbf{e} = c \begin{pmatrix} 0 & 1 & -1 & 0 & 0 & 0 & 0 & 1 & -1 & 1 & -1 & 1 & -1 & 0 & 0 & 0 & 0 \\ 0 & 0 & 0 & 1 & -1 & 0 & 0 & 1 & -1 & -1 & 1 & 0 & 0 & 0 & 0 & 1 & -1 & 1 & -1 \\ 0 & 0 & 0 & 0 & 0 & 1 & -1 & 0 & 0 & 0 & 0 & 1 & -1 & -1 & 1 & 1 & -1 & -1 & 1 \end{pmatrix}, \quad (3.8)$$

For the discretization of the Boltzmann equation (Eq. (3.4)) a simple finite-difference scheme can be used and the discretized Boltzmann equations are given by

$$\frac{f_i(\mathbf{x}, t + \Delta t) - f_i(\mathbf{x}, t)}{\Delta t} + c \frac{f_i(\mathbf{x} + \mathbf{e}_i \Delta t, t + \Delta t) - f_i(\mathbf{x}, t + \Delta t)}{\Delta \mathbf{x}} = \Omega_i. \quad (3.9)$$

3. Lattice-Boltzmann modeling and simulation

In the present work external forces are neglected and the time step Δt is chosen such that $c = 1$ ($\Delta x = \Delta t$). In this case follow the so-called lattice Boltzmann equations as

$$f_i(\mathbf{x} + \mathbf{e}_i \Delta t, t + \Delta t) = f_i(\mathbf{x}, t) + \Delta t \Omega_i . \quad (3.10)$$

The left part of the equation describes the advection or streaming step which is a linear operation on the probability distribution. Ω_i is the collision operator introduced in the previous section. The collision process is a central idea in the kinetic theory of gases, however, it took some time before a suitable approximation was found. A simple version for Ω was proposed by Bhatnagar, Gross and Krook (BGK) (Eq. (3.13) [165]). It essentially describes that the collision process brings the system closer to the state of (local) fluid dynamical equilibrium. In their approach all collision processes do have the same relaxation time. Therefore, this class of LBM models is also referred to as single relaxation time BGK (SRT-BGK). At low fluid viscosity and in a turbulent flow regime this might cause numerical instabilities. In the literature more complex models are proposed which use a scheme developed for multiple relaxation times [166].

One advantage of LBM is that the streaming step is linear and operators can be applied subsequently to the probability distribution. In an algorithm the streaming operator is typically applied after the collision rules:

1. Collision

$$f_i(\mathbf{x}, t^*) = \Omega_i (f_i(\mathbf{x}, t)) \quad (3.11)$$

2. Streaming

$$f_i(\mathbf{x} + \mathbf{e}_i, t + 1) = f_i(\mathbf{x}, t^*) \quad (3.12)$$

3.1.3. Lattice Boltzmann multiphase models

Multiphase simulation of immiscible fluids is one of the largest challenges for CFD simulations. This problem is hard to handle in conventional CFD techniques (e.g. volume-of-fluid method [123, 167]), especially, if the flow geometries are complex. The efficient calculation of multiphase flow in complex geometries is one of the most prominent advantages of the Lattice-Boltzmann method.

Several models for multiphase flow in the framework of LBM were proposed in the literature. The most prominent ones are the Shan-Chen (SC) model, the free-energy (FEM) model, and the color gradient or RK model. The at the moment most popular model was proposed by Shan and Chen in 1993 [168, 169]. Central to the approach is an interaction force which mimics long-range interactions between the molecules and also allows to simulate phase separation. A shortcoming of the method is that physical parameters like surface tension and density and/or viscosity ratios cannot be adjusted independently. Furthermore, some model parameters have to be determined in numerical experiments [170]. In the free energy model proposed by Swift *et al.* [171, 172] a free energy functional is employed to track the evolution of the interface by solving the Cahn-Hilliard equation on the lattice [173]. Suitable collision rules ensure that the system evolves towards a minimum of the free energy functional.

The model presented in this work is based on the concepts developed by Rothman and Keller for lattice gases [174] and was extended to the simulation of immiscible fluids by Gunstensen *et al.* [175, 176]. In this type of model the two fluids are distinguished by their color (red and blue) and each phase is described by its own distribution function $f^k(\mathbf{x}, t)$. In the bulk of the fluid phases it takes in principle the form of the model for single phase flow presented in the previous Section 3.1.2. However, at the interface additional collision operators describe the molecular interactions between different phases. First, a perturbation step is introduced to capture the surface tension between the two fluids and afterwards the local 'color gradient' between the two phases is used to enforce phase separation (recoloring operator). The model was later on improved by Grunau *et al.* [177] to handle flexible density and viscosity ratios. However, due to numerical difficulties it was still restricted to rather small values. This is a serious problem common to all Lattice-Boltzmann multiphase models and obviates the usage of LBM in many technically relevant applications, including air-water flow. This topic will be discussed in Section 3.2.4.

Although, considerable improvements have been made, this issue is a topic of active research in the LBM community. One of the reasons for these numerical problems is the occurrence of spurious velocities at the interface between the two fluids. Inamuro *et al.* [178, 179] succeeded in simulating density ratios in the order of 1000 by using a modified FEM approach. However, in his method he solves the Poisson equation in every time step to achieve a divergence-free velocity field which causes a tremendous computational cost. The method was improved by Zheng *et al.* who circumvented the time consuming solution

of the Poisson equation, still, demonstrating good accuracy of the model for important test cases like a stationary bubble [173].

Recently, several authors proposed improvements for the RK type models [180–185]. Revisions of the perturbation operator were proposed [184, 185] which ensure the conservation of mass and recover the Navier-Stokes Equations in the macroscopic limit. The authors use the concept of a continuum surface force [184, 186] to describe the effect of interfacial tension. In this concept the perturbation operator can be seen as an additional forcing term which ensures the correct capillary pressure across the interface. The magnitude of the force can be calculated from the surface normal and curvature following Laplace law. The color gradient determining the surface normal in the two-phase region is approximated by higher-order isotropic discretization schemes which significantly reduce spurious velocities [180, 184, 187]. Another topic is the so-called 'lattice-pinning' where the lattice discretization is reported to suppresses a motion of phase boundaries. Tölke [188] and Latva-Koko *et al.* [189] proposed modified recoloring operators to circumvent this problem. The latter allows a moderate mixing of the two phases at the interface which additionally reduces spurious currents. These improvements allow the simulation of density ratios up to 10,000 [180] and are important contributions for further developments of the Lattice-Boltzmann method.

The model presented in this work is based on the publications of Tölke *et al.* [161, 188] and various improvements proposed by Leclaire and Liu *et al.* [180–182, 184]. The algorithm of the previous section is extended to incorporate collisions of the two-phase system. Each phase k has its own distribution function $f^k(\mathbf{x}, t)$ and the operators are applied individually.

1. Single-phase collision (SRT-BGK)

$$f_i^k(\mathbf{x}, t^*) = f_i^k(\mathbf{x}, t) + \Omega_i^{k,1} \left(f_i^k(\mathbf{x}, t) \right) \quad (3.13)$$

2. Two-phase collision (Perturbation)

$$f_i^k(\mathbf{x}, t^{**}) = f_i^k(\mathbf{x}, t^*) + \Omega_i^{k,2} \left(f_i^k(\mathbf{x}, t^*) \right) \quad (3.14)$$

3. Two-phase collision (Recoloring)

$$f_i^k(\mathbf{x}, t^{***}) = \Omega_i^{k,3} \left(f_i^k(\mathbf{x}, t^{**}) \right) \quad (3.15)$$

4. Streaming

$$f_i^k(\mathbf{x} + \mathbf{e}_i, t + 1) = f_i^k(\mathbf{x}, t^{***}) \quad (3.16)$$

3.1.4. Boundary conditions

In the description of the Lattice-Boltzmann model a discussion of boundary conditions was omitted so far. There are two types of boundaries in micro-structure resolved simulations of porous media: boundaries at the borders of the computational domain and boundaries at the fluid-solid interface. For the first type, periodic boundary conditions represent the most convenient approach. Still, in many cases reasonable results can be obtained, e.g., equilibrium distributions of multiphase flow. In this approach the computational domain is surrounded by its periodic images and e.g. the top of the simulation box interacts with the bottom of its periodic image (essentially itself). It is important that the simulation box is chosen large enough to avoid a correlation of the whole domain due to the periodic boundary conditions. This could cause considerable systematic errors and the formation of unphysical fluid geometries (cf. formation of a slab in Figure 3.8). Pressure or velocity boundary conditions are also possible in the LBM framework. Their implementation is slightly more difficult since unknown probability distributions have to be constructed at the boundary of the lattice [122, 161].

The solid-fluid boundaries are typically described by a no-slip boundary condition. In LBM this is commonly modeled using a simple bounce-back scheme. Figure 3.2 shows the probability distribution at a lattice node next to a solid wall before and after the collision process. The basic idea of the bounce-back scheme is that a particle is moving in the opposite direction after the collision process

$$f_i^k = f_{\tilde{i}}^k. \quad (3.17)$$

The opposite lattice direction in Eq. (3.17) is indicated by \tilde{i} . In the simplest bounce-back scheme it is assumed that the wall is half-way between two lattice nodes. If the distance between the nodes and the interface is different, interpolation schemes can be used [122]. In the algorithm the bounce-back operator is applied after the particle collision operators and before the streaming step.

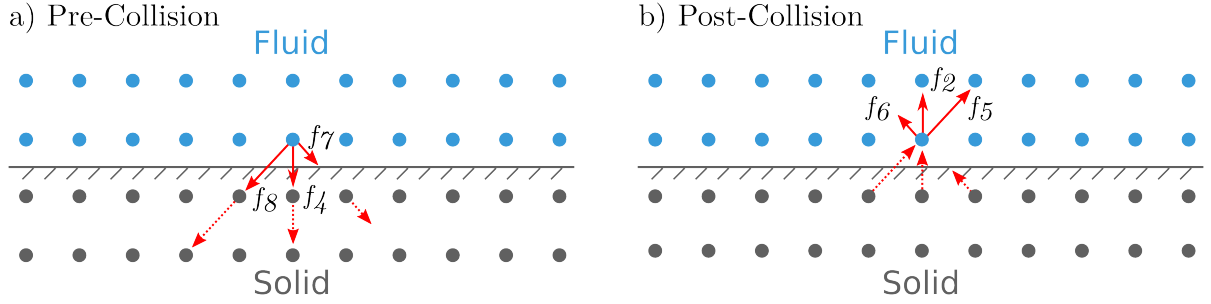


Figure 3.2.: Schematic illustration of bounce-back boundary conditions. The figure shows the velocity distributions of an arbitrary lattice node next to a solid wall before (left) and after (right) the collision process. After the collision the discrete probabilities i point in the opposite direction \tilde{i} .

3.2. Methodology

The LBM multiphase model introduced in this section will be used for the calculation of fluid dynamics in the porous structure of the Ag/Ag₂O electrode (Chapter 2). An important feature of this electrode is that it consists of hydrophilic Ag/Ag₂O substrate and hydrophobic binder material. This kind of structure was barely investigated in the LBM literature so far [110]. The LBM model presented here is implemented in the commercial software package Matlab. The two-phase model of Tölke provided by Prof. Volker Schulz [190] was used for preliminary investigations. The model has some deficiencies regarding numerical stability and flexibility of input parameters. During this work it was improved inspired by the recently published multiphase models of Leclaire and Liu *et al.* [182, 184].

3.2.1. Model description and parametrization

The two-phase model presented in this section is set up following the publications of Leclaire and Liu *et al.* [180, 181, 184]. Due to numerical problems in the simulation of porous media the recoloring operator proposed by Tölke *et al.* [188] is used in this work. In the derivation of model equations the phases k are named red and blue according to the nomenclature proposed by Rothman *et al.* [174].

Single-phase collision

The single-phase collision operator in the present model is given by the SRT-BGK approximation

$$\Omega_i^{k,1} = -\frac{f_i^k(\mathbf{x}, t) - f_i^{k,\text{eq}}(\mathbf{x}, t)}{\tau}, \quad (3.18)$$

where τ_k is the relaxation time of the collision process and $f_i^{k,\text{eq}}$ the local equilibrium distribution of fluid velocities. The relaxation time can be related to the kinematic viscosity ν_k of the fluid as [161]

$$\tau_k = \frac{3\nu_k}{c^2} + 0.5\Delta t. \quad (3.19)$$

In the two-phase model the same relaxation time $\tau_{\text{red}} = \tau_{\text{blue}} = \bar{\tau}$ is used for both phases. It is calculated from a density average of the kinematic viscosity

$$\bar{\nu} = \left(\sum_k \frac{\rho_k}{\rho\nu_k} \right)^{-1}. \quad (3.20)$$

In the bulk of the two phases the density average yields $\bar{\nu} = \nu_k$. Note, that in contrast to the single-phase models the average relaxation time $\bar{\nu}$ has to be updated in every iteration as the fluid density at a node might have changed.

The local equilibrium $f_i^{k,\text{eq}}$ is given by the Maxwell distributions which are known from the statistical theory of ideal gases [122]

$$f_i^{k,\text{eq}} = \rho \left(\phi_i^k + w_i \left[3 \frac{\mathbf{e}_i \mathbf{v}}{c^2} + \frac{9}{2} \frac{(\mathbf{e}_i \mathbf{v})^2}{c^4} - \frac{3 \mathbf{v}^2}{2 c^2} \right] \right), \quad (3.21)$$

where ϕ_i^k determines the compressibility of the fluid and w_i is a lattice specific weighting parameter. For the D2Q9 and D3Q19 lattices w_i is given by

$$w_i = \begin{cases} 4/9 & i = 0 \\ 1/9 & i = 1 \dots 4 \\ 1/36 & i = 5 \dots 8 \end{cases} \quad (3.22)$$

3. Lattice-Boltzmann modeling and simulation

and

$$w_i = \begin{cases} 1/3 & i = 0 \\ 1/18 & i = 1 \dots 6 \\ 1/36 & i = 7 \dots 18 \end{cases}, \quad (3.23)$$

respectively. The parameter ϕ_i^k is related to the compressibility of the fluid and, thus, to the speed of sound c_s^k and hydrostatic pressure in phase k . For the D2Q9 and D3Q19 lattice ϕ_i^k is given by [182, 184]

$$\phi_i^k = \begin{cases} \alpha_k & i = 0 \\ (1 - \alpha_k)/5 & i = 1 \dots 4 \\ (1 - \alpha_k)/20 & i = 5 \dots 8 \end{cases} \quad (3.24)$$

and

$$\phi_i^k = \begin{cases} \alpha_k & i = 0 \\ (1 - \alpha_k)/12 & i = 1 \dots 6 \\ (1 - \alpha_k)/24 & i = 7 \dots 18 \end{cases}, \quad (3.25)$$

respectively, where one of the α_k is a free parameter setting the pressure level in the system

$$\begin{aligned} p_k &= \rho_k (c_s^k)^2 = \frac{3}{5} \rho_k (1 - \alpha_k) \quad (\text{D2Q9}) \\ p_k &= \rho_k (c_s^k)^2 = \frac{1}{2} \rho_k (1 - \alpha_k) \quad (\text{D3Q19}). \end{aligned} \quad (3.26)$$

The values of α_k are related by

$$\gamma = \frac{\rho_{\text{red}}}{\rho_{\text{blue}}} = \frac{1 - \alpha_{\text{blue}}}{1 - \alpha_{\text{red}}} \quad (3.27)$$

in order to guarantee a stable interface ($p_{\text{red}} = p_{\text{blue}}$).

In analogy to the standard single phase model the density of each phase is calculated according to Eq. (3.5). For the calculation of fluid velocity the total density of the two-phase system $\rho = \rho_{\text{red}} + \rho_{\text{blue}}$ has to be used (Eq. (3.6)).

Perturbation

At this point it is convenient to introduce a color-field $\psi(\mathbf{x}, t)$ in order to distinguish the two phases

$$\psi(\mathbf{x}, t) = \frac{\rho_{\text{red}} - \rho_{\text{blue}}}{\rho_{\text{red}} + \rho_{\text{blue}}}. \quad (3.28)$$

Regions of red and blue phase are marked by values of ψ around 1 and -1, respectively. At the interface the color-field takes values inbetween. The influence of surface tension in RK type models is described by the perturbation operator. In the present work it is chosen to take the form [185]

$$\Omega_i^{k,2} (f_i^k(\mathbf{x}, t^*)) = \frac{A_k}{2} |\nabla\psi| \left[w_i \frac{(\mathbf{e}_i \nabla\psi)^2}{|\nabla\psi|^2} - B_i \right], \quad (3.29)$$

where A_k is a free parameter controlling the surface tension, $\nabla\psi$ is the color gradient in the two-phase region, and B_i is a parameter which has to be chosen in order to recover the Navier-Stokes Equations [184, 185]. In the present model it is assumed that [184]

$$A_{\text{red}} = A_{\text{blue}} = A = \frac{9}{4} \sigma \bar{\tau}, \quad (3.30)$$

where σ is the surface tension and $\bar{\tau}$ the density averaged relaxation time. The color gradient $\nabla\psi$ is in the present model calculated by higher-order isotropic numerical discretization schemes [180, 184, 187]. This causes a higher computational effort, however, reduces the spurious velocities at the interface. In the 2D case a sixth-order isotropic color gradient is calculated according to

$$\nabla\psi = \sum_{i=1}^{25} \omega_i \mathbf{d}_i \psi(\mathbf{x} + \mathbf{d}_i), \quad (3.31)$$

where \mathbf{d}_i are the coordinates of a pseudo-D2Q25 lattice with corresponding weights ω_i . The Cartesian coordinates of the pseudo-lattice are given by

$$\mathbf{d} = \begin{pmatrix} 0 & 0 & 1 & 0 & -1 & 1 & -1 & -1 & 1 & 0 & 0 & 2 & -2 & 2 & -2 & 2 & -2 & 1 & -1 & -1 & 1 & 2 & 2 & -2 & -2 \\ 0 & 1 & 0 & -1 & 0 & 1 & -1 & 1 & -1 & 2 & -2 & 0 & 0 & 1 & 1 & -1 & -1 & 2 & 2 & -2 & -2 & 2 & -2 & 2 & -2 \end{pmatrix} \quad (3.32)$$

3. Lattice-Boltzmann modeling and simulation

and the corresponding weights follow as [187]

$$\omega_i = \frac{1}{5040} \cdot \begin{cases} 0 & i = 0 \\ 448 & i = 1 \dots 4 \\ 960 & i = 5 \dots 8 \\ 84 & i = 9 \dots 12 \\ 32 & i = 13 \dots 20 \\ 1 & i = 21 \dots 24 \end{cases} . \quad (3.33)$$

In the 3D case only a fourth-order isotropic approximation is used in order to decrease the computational load [184]

$$\nabla\psi = 3 \sum_{i=1}^{19} w_i \mathbf{e}_i \psi(\mathbf{x} + \mathbf{e}_i) . \quad (3.34)$$

The parameters B_i depend on the lattice and have to be chosen in order to ensure the conservation of mass in the perturbation step

$$\sum_i \Omega_i^{k,2} = 0 . \quad (3.35)$$

For the D2Q9 and D3Q19 lattice the parameters are given by [184, 185]

$$B_i = \begin{cases} -4/27 & i = 0 \\ 2/27 & i = 1 \dots 4 \\ 5/108 & i = 5 \dots 8 \end{cases} \quad (3.36)$$

and

$$B_i = \begin{cases} -1/3 & i = 0 \\ 1/18 & i = 1 \dots 6 \\ 1/36 & i = 7 \dots 18 \end{cases} , \quad (3.37)$$

respectively.

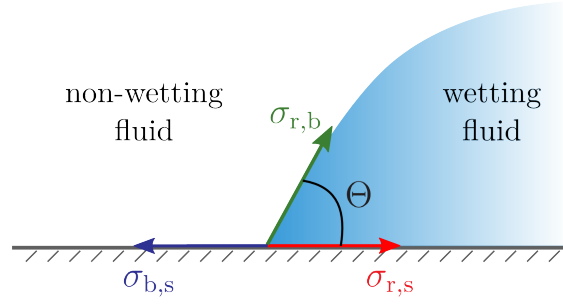


Figure 3.3.: Force balance at the contact line of red (r), blue (b), and solid (s) phase. Arrows indicate the forces induced by the surface tensions σ between the phases.

Recoloring

The perturbation operator alone is not sufficient to get a separation of the two phases. This is achieved in the subsequent recoloring step. In this work the recoloring operator of Tölke [188] is implemented which is simpler than other operators proposed in the literature, however, also avoids the problem of lattice pinning. Additionally, it does not allow a partial mixing of the two phases and, therefore, gives a very sharp interface. Drawback of the operator is the occurrence of spurious currents which limits the algorithm to simulations with low density and viscosity ratios. This constraint, however, does not prevent the application of the model for the problem discussed in this work as it is explained in more detail in Section 3.2.4. The combination of the perturbation operators proposed by Leclaire and Liu *et al.* [182, 184] and the recoloring operator of Tölke [188] also introduces some numerical artifacts in the simulation of porous media. In some situations this leads to unphysical negative probabilities. This issue will be discussed in more detail in Section 3.3.2. The algorithm of the recoloring operator $\Omega_i^{k,3}$ for the red and blue phase can be written as

$$\begin{aligned} f_i^{\text{red}}(t^{***}) &= f_i^{\text{red}}(t^{**}) + \cos(\theta_i) \min(f_i^{\text{red}}(t^{**}), f_i^{\text{blue}}(t^{**}), f_{\tilde{i}}^{\text{red}}(t^{**}), f_{\tilde{i}}^{\text{blue}}(t^{**})) \\ f_i^{\text{blue}}(t^{***}) &= f_i^{\text{blue}}(t^{**}) - \cos(\theta_i) \min(f_i^{\text{red}}(t^{**}), f_i^{\text{blue}}(t^{**}), f_{\tilde{i}}^{\text{red}}(t^{**}), f_{\tilde{i}}^{\text{blue}}(t^{**})), \end{aligned} \quad (3.38)$$

where \tilde{i} again indicates the direction opposite to i and θ_i is the angle between $\nabla\psi$ and \mathbf{e}_i . It can be calculated by the normalized inner product of the two vectors

$$\cos(\theta_i) = \frac{\mathbf{e}_i \cdot \nabla\psi}{|\mathbf{e}_i| |\nabla\psi|}. \quad (3.39)$$

Contact angles

In a multiphase system the wettability of the surface is determined by the interactions between the solid and the fluid phases. The situation at the three-phase contact line of a liquid droplet on a solid surface is schematically shown in Figure 3.3. The arrows indicate surface forces induced by the surface tensions between the phases. In RK-type Lattice-Boltzmann models the surface tension is proportional to the absolute value of the color gradient $|\nabla\psi|$ (see Eq. (3.29)). It is, therefore, a common approach to assign a certain density to the fluid phases at the position of solid nodes [161, 191]. The magnitude of the density determines if the surface is wetting or non-wetting. If the densities at solid nodes are larger than densities in the bulk this will result in a wetting surface and densities smaller than the bulk density will give a non-wetting behavior. A quantitative description for the density of the fluids with respect to the contact angle can be obtained from a force balance at the three phase contact line (see Figure 3.3)

$$\sigma_{\text{red,blue}} \cdot \cos(\Theta) = \sigma_{\text{blue,solid}} - \sigma_{\text{red,solid}} . \quad (3.40)$$

The relation to fluid density is given by the proportionality of the surface tension to the absolute value of the color gradient. For fluids with a density ratio of unity ($\rho_{\text{red}} = \rho_{\text{blue}} = \rho$) the density of the fluids at solid nodes can be calculated according to [161, 191]

$$\begin{aligned} \rho_{\text{red}}^s &= \rho + 0.5 \rho \cos(\Theta) \\ \rho_{\text{blue}}^s &= \rho + 0.5 \rho \cos(180 - \Theta) , \end{aligned} \quad (3.41)$$

where Θ is per definition the contact angle of the red phase. This approach allows to introduce several materials in the solid phase, each having a different contact angle or fluid density, respectively. This is an important step in simulating the heterogeneous structure of the GDE consisting of hydrophilic Ag particles and hydrophobic binder material.

3.2.2. Structure generation

The imaging [141] and reconstruction process of Ag/Ag₂O GDEs is described in detail in Chapter 2. The reconstructions are mirrored at the $x - y$ plane in order to increase the simulation domain in the direction of FIB sampling (z -direction). This step is necessary in

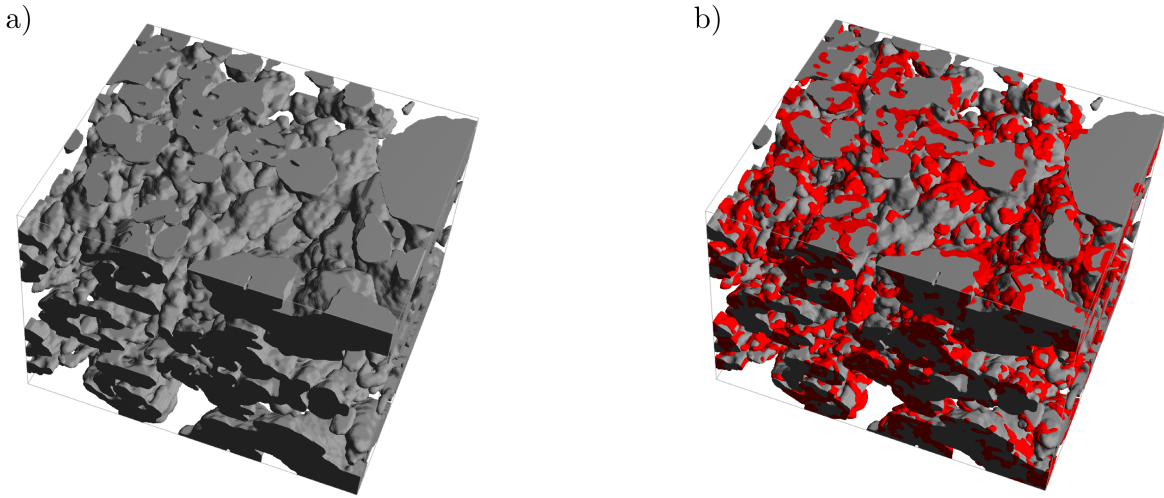


Figure 3.4.: Initial structure of the reduced high-porosity GDE (left) and including the reconstructed binder phase (right). The reconstruction is mirrored in the $x - y$ plane and coarsened for computational reasons.

order to avoid systematic errors due to the periodic boundary conditions (Section 3.1.4). The number of voxels in the resulting geometries is far too large for numerical studies in a feasible amount of time. Thus, the reconstructions are coarsened in GeoDict [143] which reduces the number of voxels by a factor of 64. The final number of voxels in the 2D and 3D cases are around $1.6 \cdot 10^4$ and $1.5 \cdot 10^6$, respectively (cf. dimensions in Table 2.1).

An important feature of the Ag/Ag₂O GDEs is the hydrophobic binder material. Unfortunately, the binder distribution is lost in the imaging and reconstruction process (see Section 2.3.1). For the two-phase simulations in the heterogeneous structure it is, however, important to model the hydrophobic binder fibers as they ensure the coexistence of gas and liquid phase. Therefore, the binder is distributed in a stochastic process on the surface of the reconstructed electrode. Starting at an arbitrary position on the electrode surface the algorithm performs a random walk on the particles until a pre-defined fiber length is reached. This process is repeated until the binder volume fraction in the reconstruction corresponds to the weight fraction in the substrate of the production process. Binder fibers crossing the void space between electrode particles are not modeled in this approach. Figure 3.4 shows images of the reduced high-porosity electrode before (left) and after (right) the binder phase reconstruction step. Electrode particles and binder fibers are displayed in gray and red color, respectively.

Similar to the electron microscope image shown in Figure 2.14 the binder forms at some places an almost dense film of hydrophobic material. The resolution in the coarsened

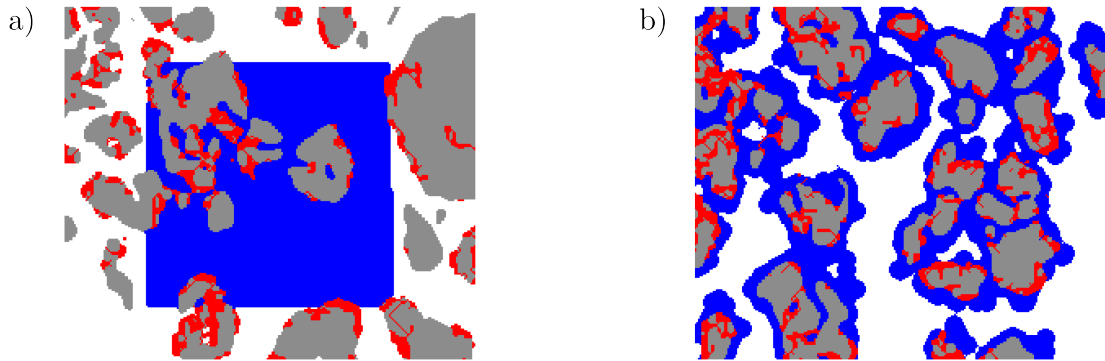


Figure 3.5.: Initial conditions for the simulation of $p_c - s$ curves. Left: Liquid phase is introduced as one solid block (imbibition). Right: Liquid phase is dispersed on wetting surfaces (drainage).

reconstruction is ~ 200 nm which is about a factor of 4 higher than the actual diameter of the fibers as determined from the electron microscope image. This discrepancy might introduce an error in the simulation of electrolyte distributions but is necessary for reasonable computation times.

3.2.3. Initial conditions

The $p_c - s$ curves of porous media are typically determined in so-called imbibition and drainage experiments [102–105, 107]. After filling the porous medium to a defined saturation level the corresponding average capillary pressure follows as difference between the pressure in the gas and the liquid phase. This experimental approach gives rise to two different scenarios [107]:

1. Imbibition of the liquid phase

Initially, the pore space of the GDE is empty or rather, say, completely filled with the gas phase. The liquid phase is pressed into the porous medium at a low flow rate. Once a pre-defined saturation is reached the imbibition is stopped and the system is put at rest until a constant pressure is measured. Successively, several saturations on the $p_c - s$ curve are screened until the electrode is completely filled. This is indicated by a strong increase in the pressure signal.

2. Drainage of the liquid phase

In the so-called drainage process, the measurements are basically repeated in reversed

direction. Starting with an electrode completely filled with the liquid phase more and more electrolyte is withdrawn from the sample in a step-wise process.

In the LBM model presented in this work periodic boundary conditions are implemented. Hence, an exact reproduction of the experiments described above is not possible as this would require Neumann type boundary conditions. However, the two processes can be mimicked by a suitable choice of initial conditions. Figure 3.5 shows the two types of initial conditions as implemented in the current model for a representative saturation of 50%. In the case of the imbibition process the liquid phase is introduced in the pore space as one solid block (Figure 3.5 a)). This is comparable to the experimental setup as the electrolyte is also pushed into the porous structure at one side of the electrode. The initial configuration displayed in Figure 3.5 b) corresponds to the drainage process. During drainage the electrolyte will remain preferentially on the hydrophilic electrode particles. In the simulation this initial configuration is generated by randomly placing liquid droplets on the electrode surface or, if all surface sites are occupied, in contact with another liquid droplet.

3.2.4. Simulation of Ag/Ag₂O electrodes

2D and 3D simulations are conducted on the reconstructed electrodes presented in Chapter 2. The 2D simulations are aiming at the calculation of the characteristic pressure-saturation ($p_c - s$) curves of the porous medium. This is an important input parameter for the continuum model presented in Chapter 4 and could not be determined in the experimental part. Similar information could also be retrieved from the 3D simulations, however, a much longer computation time is needed. 3D simulations are rather performed for selected saturations of the pore space in order to determine the distribution of liquid electrolyte in fluid mechanical equilibrium. In a subsequent step these distributions can be used to obtain effective transport parameters and active surface areas.

For the simulations the LBM model presented in the previous section is employed. The lattice-specific parameters were given in the course of model derivation. In order to obtain comparable results the same set of physical parameters is used for both, 2D and 3D simulations. The values are summarized in Table 3.1.

3. Lattice-Boltzmann modeling and simulation

	$\rho / \text{kg/m}^3$		$\nu / \text{m}^2/\text{s}$		$\sigma / \text{N/m}$	$\Theta / ^\circ$		$\alpha / -$
	Gas	Liquid	Gas	Liquid	Gas-Liquid	Ag/Ag ₂ O	Binder	Gas
LBM	1	1	1/6	1/6	0.1	60	175	4/9
Physical	1.18	997	$1.58 \cdot 10^{-5}$	$8.93 \cdot 10^{-7}$	$7.28 \cdot 10^{-2}$	-	-	-

Table 3.1.: Input parameters of the LBM simulations and corresponding physical parameters of the electrolyte-O₂ system.

Physical parameters of the fluid system

As explained in Section 3.1.3, high density and viscosity ratios are difficult to simulate using the Lattice-Boltzmann method. Unfortunately, the electrolyte-O₂ system of the aqueous Li-O₂ battery falls into this class (see 3.1). In the present model numerical instabilities obviate a simulation of high density and viscosity ratios. Still, under some circumstances the error of assuming ratios of unity is negligible. An analysis of dimensionless numbers can be helpful to evaluate the relevant forces of the problem. Fluid flow in porous media is mainly determined by four different forces, namely, gravitational, viscous, inertial, and surface forces. The dimensionless numbers describing the ratio between these forces are

- Bond number

$$Bo = \frac{\text{gravitational forces}}{\text{surface forces}} = \frac{\rho g l^2}{\sigma} \sim 4 \cdot 10^{-7} \quad (3.42)$$

- Capillary number

$$Ca = \frac{\text{viscous forces}}{\text{surface forces}} = \frac{\mu \mathbf{v}}{\sigma} \sim 1 \cdot 10^{-8} \quad (3.43)$$

- Reynolds number

$$Re = \frac{\text{inertial forces}}{\text{viscous forces}} = \frac{\rho \mathbf{v} l}{\mu} \sim 2 \cdot 10^{-6} \quad (3.44)$$

The characteristic length in the analysis of dimensionless numbers is approximately given by the mean pore diameter d_{50} of the reduced Ag electrode (Table 2.2). For the flow velocity \mathbf{v} a value of $1 \cdot 10^{-6}$ m/s is assumed which corresponds to the maximum velocity observed in the simulation of permeability (see Figure 2.13). However, in the limit of

fluid mechanical equilibrium the flow velocity will tend to zero. The small values of the dimensionless numbers demonstrate that gravitational and viscous forces are negligible compared to the strong influence of surface forces in the porous structure studied in this work. Therefore, the error which is introduced by assuming unity density and viscosity ratios will be rather small.

The physical input parameters of the simulations are summarized in Table 3.1. 2D and 3D simulations are parametrized using the same fluid parameters in order to obtain comparable results. Lattice specific parameters were given during the derivation of the model in Section 3.2.1. The physical parameters of the fluids are chosen to ensure the numerical stability of the simulations. The density and kinematic viscosity of the gas and liquid phase are 1 kg/m^3 and $1/6 \text{ m}^2/\text{s}$, respectively. The surface tension is given a value of 0.1 N/m and the parameter α determining the compressibility is $4/9$ for the liquid and gaseous phase. The contact angle of the liquid phase is 60° in the case of the hydrophilic electrode particles and 175° for hydrophobic binder fibers [192]. The same contact angle is assigned to the pristine and reduced state of the electrode.

This choice of parameters will of course initially lead to results in arbitrary lattice units. However, suitable scaling rules can be applied to the output of the simulations in order to retrieve physically meaningful predictions. As determined in the analysis of dimensionless numbers the surface forces determine to a large extent the fluid dynamical behavior and, thus, the hydrostatic pressure in the two phases. These are in turn related by the Laplace law for capillary pressure

$$\Delta p_c = \frac{2\sigma}{r} . \quad (3.45)$$

The Laplace law can be used as relation between capillary pressure of the real and simulated system. The ratio between the two is determined by the length scales and surface tensions. The length scale for r of the physical system is given by the resolution of the reconstruction Δx which corresponds to one lattice unit (lu). An equation for the capillary pressure of the physical system can then be deduced as

$$\Delta p_c = \frac{\sigma}{\sigma^{\text{LBM}}} \frac{1 \text{ (} lu \text{)}}{\Delta x} \Delta p_c^{\text{LBM}} . \quad (3.46)$$

3. Lattice-Boltzmann modeling and simulation

In a similar approach the time scale of the simulation can be obtained by relating the kinematic viscosity of the LBM simulation and physical system [193]

$$\Delta t = \frac{\nu^{\text{LBM}}}{\nu} \frac{(\Delta x)^2}{(1(lu))^2}, \quad (3.47)$$

where Δt is the time step in one iteration.

2D simulations

Main goal of the 2D simulations is the determination of characteristic $p_c - s$ curves of the reconstructed Ag/Ag₂O electrodes. Therefore, 2D simulations were run at saturations of the liquid phase between 2 and 98 %. At each saturation 10 independent simulations were performed in order to obtain statistically relevant results. Randomly chosen two-dimensional slices of the reconstructions were used as input for lattice generation. The simulations were conducted for the scenarios imbibition and drainage as introduced in Section 3.2.3.

Similar to the experimental approach the capillary pressure in the LBM simulations is calculated as difference between the pressure in the liquid and gas phase $\Delta p_c = p^{\text{liquid}} - p^{\text{gas}}$. The local pressure in the two phases is calculated according to Eq. (3.26) where the density is taken as average of all nodes residing in the bulk of the respective phases ($\psi = \pm 1$). The capillary pressure can be calculated as an average of the 10 simulations and is rescaled according to Eq. (3.46) in order to obtain physically meaningful units. The number of iterations per simulation was chosen to $1 \cdot 10^6$ (10 ms) which was sufficient to achieve fluid mechanical equilibrium.

Pressure saturation curves are in the literature often formulated in the dimensionless form of the Leverett function [194, 195]

$$J(s) = \frac{\Delta p_c}{\sigma |\cos(\Theta)|} \sqrt{\frac{B_0}{\varepsilon_0}}, \quad (3.48)$$

where B_0 is the permeability and ε_0 the porosity of the porous media. This standard approach explicitly assumes a homogeneous wetting behavior of the fluid with contact

angle Θ . In the heterogeneous structure of the GDE this assumption is not justified and a modification of Eq. (3.48) is used [110]

$$J(s) = \frac{\Delta p_c}{\sigma} \sqrt{\frac{B_0}{\varepsilon_0}}, \quad (3.49)$$

where only the surface tension between gas and liquid phase is taken into account.

3D simulations

3D simulations of reconstructed electrodes were performed only at selected saturations of the pore space and only for the drainage scenario. Reason is the high computational effort of the simulations. $1 \cdot 10^5$ iterations (1 ms) are needed to obtain a state of fluid mechanical equilibrium (cf. capillary pressure in Figure 3.10 a)). This corresponds to a computation ('wall-clock') time of about one month on a standard desktop computer.

The resulting electrolyte distribution at the end of the simulations is used as input for the calculation of saturation-dependent effective transport parameters and effective surface areas in GeoDict [143] (see Chapter 2.2). For the calculation of effective transport in the liquid phase the voxels of the gas phase are regarded as solids and vice versa. The saturation-dependent effective transport parameters are evaluated following the Bruggeman equation as introduced in Eq. (2.41). In the case of transport in the liquid phase the relevant volume fraction follows as $\varepsilon = \varepsilon_{\text{elyte}} = s \varepsilon_0$ and the Bruggeman relation can be written as

$$D_i^{\text{eff}} = (s \varepsilon_0)^{1.5} \cdot D_i^0. \quad (3.50)$$

For transport in the gas phase ε follows as $\varepsilon_{\text{gas}} = (1 - s)\varepsilon_0$ correspondingly. The treatment of non-transporting phases as solid material introduces a systematic error in the calculation of effective transport parameters. In the case of diffusivity calculations this error will be negligible as free convection induced due to small differences in phase composition will be minor. However, for the calculation of permeability a small pressure gradient is applied in order to enforce Stokes flow in the pore space. In this case the non-transporting phase will not be rigid but pushed away by the transporting phase. While this error might still be negligible in the case of a flowing gas phase it can be significant for the permeability of the liquid phase. Therefore, the simulated permeability of the liquid phase will be smaller

than what is observed in the experiments. An extension of the Kozeny-Carman correlation (2.44) can be used [144] as a reference for the trend of permeability with saturation

$$B_{\text{elyte}} = \frac{\varepsilon_0^3 d_p^2}{72 \bar{\tau} (1 - \varepsilon_0)^2} \cdot s^{3.5}, \quad (3.51)$$

where d_p is the particle diameter and s the saturation of the liquid phase. For calculations of B_{gas} the saturation is substituted by $(1 - s)$.

3.3. Results and discussion

This section summarizes the results of the LBM simulations. First, some simple, yet important, numerical test cases are presented to demonstrate the validity of the model. Afterwards the multiphase model is applied to the simulation of $p_c - s$ curves and phase distributions in the pore space of the Ag/Ag₂O GDEs.

3.3.1. Numerical tests

There are several numerical test cases proposed in the literature to verify the correctness of multiphase models. Among these, the simulation of steady bubbles, surface wetting, and spinodal decomposition are the most important ones and thus, studied here.

Simulation of steady bubbles

2D and 3D simulations of a steady bubble can be used to see if the form of a bubble is preserved during the simulation. Furthermore, it shows if capillary pressures are predicted correctly. This test might seem to be simple, however, it is essential to see if predictions of the model in more complicated structures will be reliable. At the beginning of the simulations single liquid droplets of different sizes are consecutively inserted in the simulation box. The form of the bubble is not supposed to change since no external forces (negligence of gravity) are applied. The simulations are run for 50,000 and 10,000 thousand iterations for 2D and 3D simulations, respectively. During the simulations the

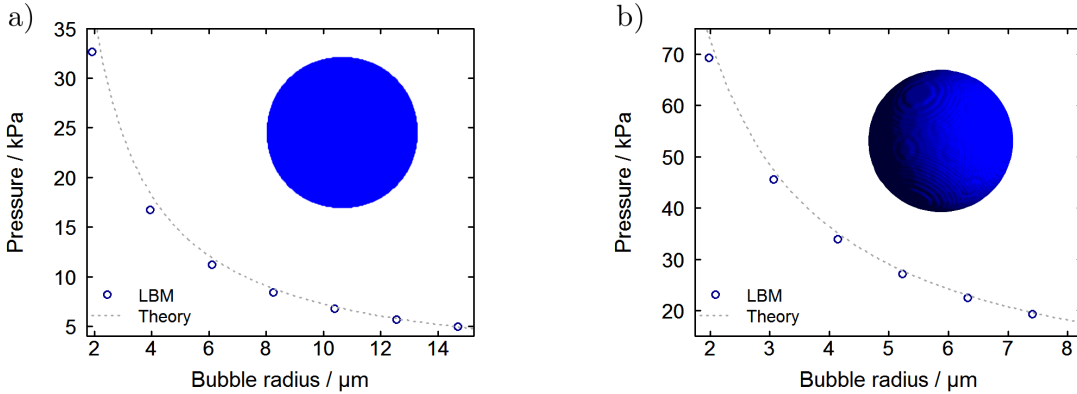


Figure 3.6.: 2D (left) and 3D (right) simulations of a steady bubble in the absence of external forces. Open symbols are results of the simulations and the dotted line represents the theoretical capillary pressure predicted by the Laplace law (Eq. (3.45)). The inset on the upper-right shows a bubble at the end of the simulation and demonstrates that its form is preserved.

form and capillary pressure are monitored. Figure 3.6 shows simulation results for steady bubbles with diameters ranging from 20 to 140 lu in the 2D case (a)) and 20 to 70 lu in the 3D case (b)). In accordance to the simulations of the reconstruction the voxel size Δx is chosen to 216 nm for the evaluation of capillary pressures. Representative bubbles at the end of the simulation are presented as insets on the upper right-hand corner of the plots.

The graphs show the relation between capillary pressure and bubble radius which is given by the Laplace law (see Eq. (3.45)). The radius of the simulated bubbles is calculated from their surface area and volume, respectively. The simulated capillary pressures are in good agreement with the theoretical predictions of Laplace's law. Especially for large bubble radii the relative errors are less than 1%. For smaller bubbles some deviation is observed which can be attributed to an increase in the share of interface area compared to the bulk volume. At the interface the color-field parameter ψ smoothly varies between 1 (liquid) and -1 (gas) and contributions to capillary pressure are not considered in this area.

The depicted bubbles demonstrate that the original form is preserved. This trivial observation indicates that the problem of lattice pinning can be overcome by the current model and that the effects of spurious currents are negligible.

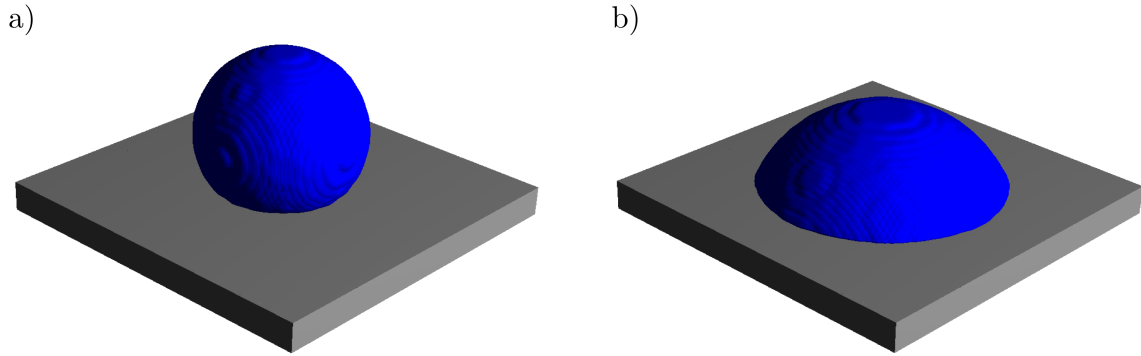


Figure 3.7.: 3D simulations of the wetting behavior on a solid surface. The contact angle Θ is set to 175° (left) and 60° (right) to represent the cases of a hydrophobic and hydrophilic surface in the heterogeneous GDE.

Simulation of surface wetting

As shown by the analysis of dimensionless numbers in Section 3.2.4 the flow in the reconstructed porous media is dominated by capillary forces. Therefore, this test is particularly important to prove the capabilities of the model. Figure 3.7 shows results of 3D simulations for a non-wetting (a)) and wetting (b)) surface. The contact angles Θ of the simulations are set to 60° and 175° which corresponds to the parameters in the simulation of the Ag/Ag₂O electrodes. The simulations demonstrate that the general wetting behavior is predicted correctly by the simulations. At $\Theta = 60^\circ$ the resulting simulated contact angle is in good agreement with the input parameter. At the high contact angle there is obviously some deviation between the input and simulation results. However, the angle of $\Theta = 175^\circ$ was already chosen slightly larger than what is commonly assumed as contact angle of the pure binder surface. The resulting contact angle of the simulation of around 145° reflects the wetting behavior of binder material quite well. Similar to the bubble test in the previous section the spherical bubble segment can be used for a calculation of capillary pressure according to Laplace law. The simulated capillary pressures of the droplets are in excellent agreement with the theoretical predictions.

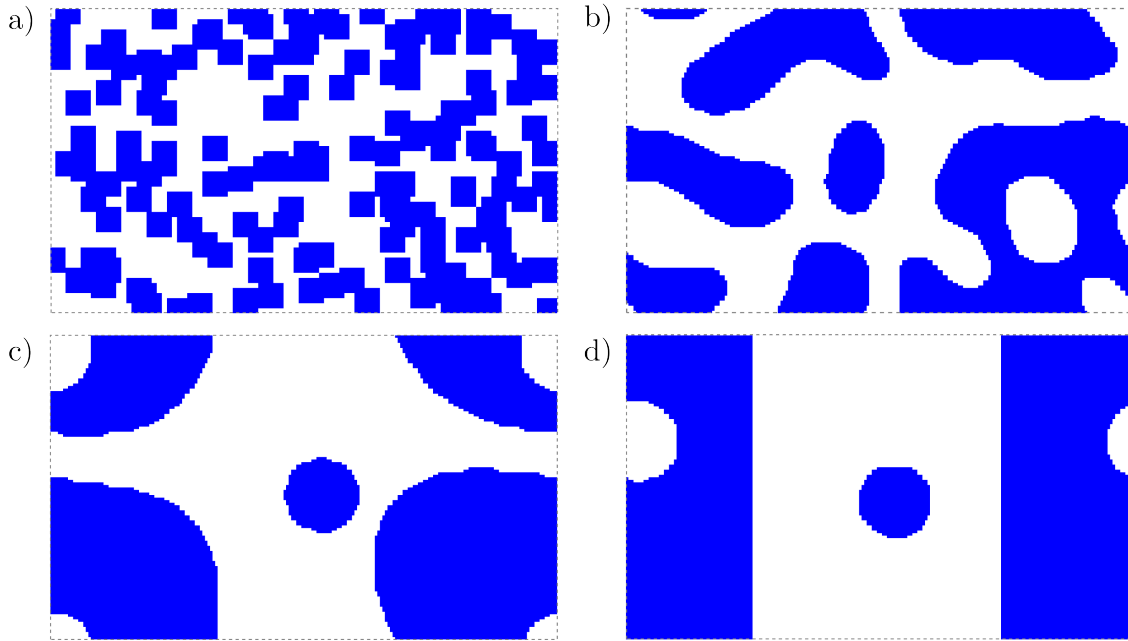


Figure 3.8.: Snapshots of 2D simulations representing the process of spinodal decomposition. Panel a) represents the initial configuration of the computational domain and simulation time increases from a) to d).

Simulation of spinodal decomposition

Spinodal decomposition describes the rapid process of phase separation and e.g. occurs if a mixture at super-critical conditions is cooled down. If the new state of the system favors a coexistence of the two phases already small fluctuations are able to initiate a nucleation process. After the nucleation larger regions consisting of the pure components start to form rapidly. This scenario is an important test case to demonstrate the immiscibility of the fluids and stability of the algorithm.

Figure 3.8 shows the phase distributions of a system during a simulation of spinodal decomposition in which the simulation time increases from a) to d). At the beginning the liquid phase is dispersed in the gas phase and the small squares can be seen as nucleation sites of the decomposition process. After a short simulation time larger bubbles and clusters start to form (b) and c)). The driving force of this process is the minimization of the surface free energy by reducing the interfacial area. At the end of the simulation (d)) the two phases are separated almost completely and only two small bubbles of the gas and liquid phase remain in the bulk of the other phase. The simulations nicely illustrate the influence of periodic boundary conditions if the computational domain is not sufficiently

large. In the final state the bulk part of the two phases are connected to their own periodic images in the neighboring simulation domains. As a result the formation of slabs is energetically favored over the formation of bubbles.

It is also important to note, that the volume fractions stay rather constant during the simulations. Since the two fluids are almost incompressible this indicates that the conservation of mass is obeyed in these simulations.

3.3.2. Simulation of $p_c - s$ curves

Capillary pressure-saturation curves were determined for the pristine and reduced high-porosity electrodes as well as for the reduced low-porosity electrode. In the two-dimensional simulations the complete $p_c - s$ curves were screened during an imbibition and drainage process. In the 3D simulations only electrolyte distributions of the drainage process were simulated.

Figure 3.9 displays snapshots of the 2D electrolyte distributions during imbibition (left) and drainage (right) simulations for the reduced high-porosity electrode at a saturation of 50%. The corresponding initial conditions were shown in Figure 3.5. In the drainage process the liquid phase is distributed more uniformly in the porous structure. In the case of imbibition most of the electrolyte is still in the center of the simulation box even after $1 \cdot 10^6$ iterations. Note, that the liquid electrolyte is preferentially in contact with the hydrophilic electrode surface.

In both simulations isolated regions of the two fluids can be observed. In the drainage simulation most of these regions can be related to the the initial condition. In the case of imbibition some areas were originally not in contact to their bulk fluid phases. In the equilibration process the gas and liquid phase distributions undergo considerable reconfigurations and parts of these isolated areas might have been reached. Another possibility is that these areas were results of spurious velocities and numerical problems. In narrow and confined pores unphysical negative probabilities and even negative densities were observed during the simulation. This might cause the formation of 'ghost fluids' at solid surfaces. An example is the air bubble which forms in the center of the simulation domain during the imbibition simulation. However, since the pressure in the two phases is calculated as average of the whole computational domain it can be expected that the error due to this local phenomenon is not very large, especially taking into account that this issue did not occur in all simulations. Still, this is a serious problem of the model and

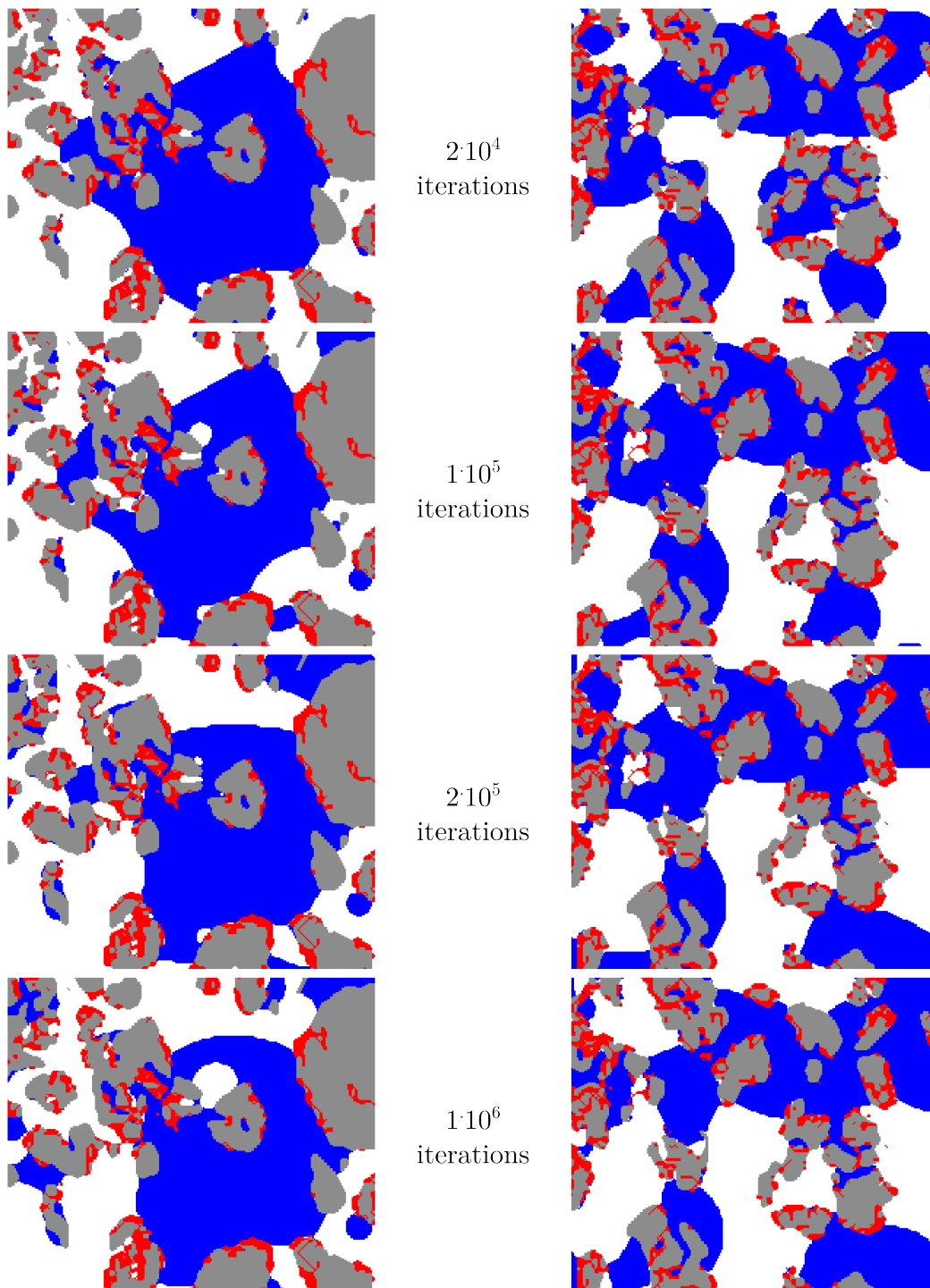


Figure 3.9.: Snapshots of the temporal evolution during 2D simulations of the imbibition (left) and drainage (right) process in different randomly chosen slices of the reduced high-porosity electrode. The saturation of the pore space is in both cases around 50%.

will require further analysis.

Figure 3.10 shows simulated capillary pressures in the pristine high-porosity electrode during simulation of the drainage process. In Figure 3.10 a) p_c is plotted as function of number of iterations for 3D simulations with varying saturation. The graph demonstrates that after $1 \cdot 10^5$ iterations the 3D simulations essentially have reached fluid mechanical equilibrium. It is interesting to note that according to Eq. (3.47) this corresponds to only 1 ms of physical time. This time scale seems to be rather small and probably a time scaling according to viscosity is not justified if the system is dominated by capillary forces (Section 3.2.4). In general, the capillary pressure in the pore space consistently increases with saturation. This is expected as at higher saturations the fluid is forced to penetrate areas of the pore space which are energetically unfavorable, such as surfaces with a high binder content or very narrow pores.

Figure 3.10 b) shows the $p_c - s$ curves corresponding to the 3D simulations of the reduced high-porosity electrode. The simulation results of 2D simulations are also included and the error bars represent the standard deviation calculated from 10 independent simulations. The dashed line represents data obtained by the pore-morphology approach implemented in GeoDict for a homogeneous electrode with an average contact angle of $\Theta = 110^\circ$ [196, 197]. At low and high saturation the error bar in the 2D simulations is higher compared to saturations in the intermediate range. A possible reason is that at these conditions the liquid droplets or gas bubbles are more or less isolated in the simulation regime and larger reconfigurations are suppressed. Thus, the resulting pressure strongly depends on the choice of the initial configurations. Due to their random generation the configurations can be more or less energetically favorable. At intermediate saturations areas of liquid and gas phase are connected throughout the pore space and reconfigurations are facile. Therefore, the phases are able to relax towards configurations which have a similar energy and capillary pressure, respectively. The results of the 3D simulations agree favorably with the 2D data and calculated capillary pressures are in almost all cases within the standard deviation. This demonstrates that the computationally less expensive 2D simulations are an efficient tool for the calculation of $p_c - s$ curves.

The $p_c - s$ curve simulated in GeoDict predicts a fundamentally different wetting behavior compared to the curve determined by the LBM simulations. During operation of the GDE in the electrochemical measurements the pressure difference between gas and liquid phase is ~ 0 kPa. While the curve calculated in GeoDict predicts a negligible saturation of the porous structure the predicted saturation of the LBM simulations is about 50%.

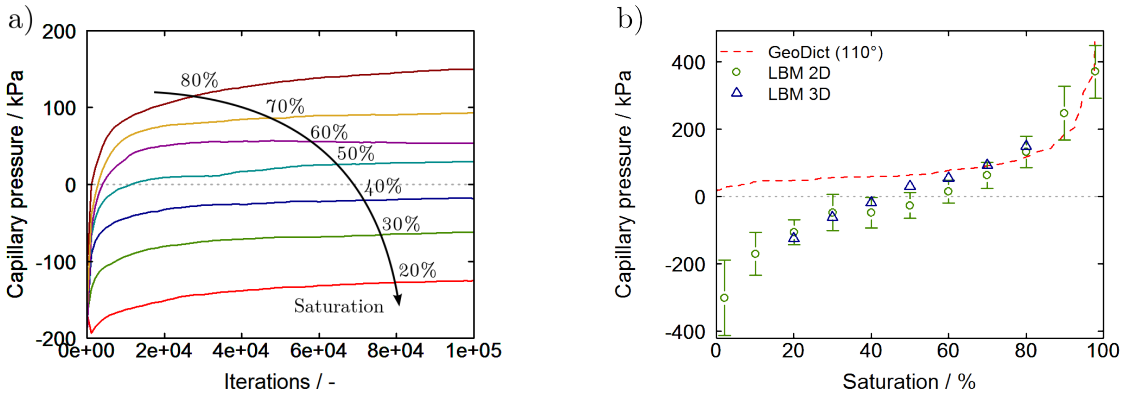


Figure 3.10.: Capillary pressures in the pristine high-porosity electrode during simulation of the drainage process. Left: Graph of p_c against number of iterations for 3D simulations at varying saturation. Right: Corresponding $p_c - s$ curves determined from 2D (green) and 3D (blue) LBM simulations. Error bars represent the standard deviation determined from 10 independent 2D simulations. The dashed red line represents results of simulations in GeoDict following the pore-morphology approach in a homogeneous electrode.

This demonstrates the importance of taking into account the heterogeneity in the wetting properties of the porous medium. As the two methods are entirely different the shape of the two curves is not really comparable. For intermediate saturations the transition from negative to positive capillary pressure is rather smooth in LBM whereas a plateau can be observed in the pore-morphology approach. However, in the limit of a fully flooded electrode the predicted pressures should be in the same order of magnitude as a similar force will be needed to fill pores with small diameter. The good agreement at least indicates that the values calculated in the LBM approach are reliable.

As mentioned in Section 3.2.4 it is common practice to represent $p_c - s$ curves in the form of the dimensionless Leverett function $J(s)$. The Leverett functions resulting from the 2D simulations are shown in Figure 3.11. In Figure 3.11 a) the imbibition-drainage behavior is depicted for the reduced electrodes of the low- and high-porosity case. The values of the Leverett function of the electrode with smaller porosity are generally higher compared to the electrode with higher porosity. This can be explained on the one hand by the generally smaller pore diameter and on the other hand by the higher volumetric binder content. In practice this implicates a smaller saturation of the pore space at the same pressure difference between gas and liquid phase in the low-porosity case. The graph also

3. Lattice-Boltzmann modeling and simulation

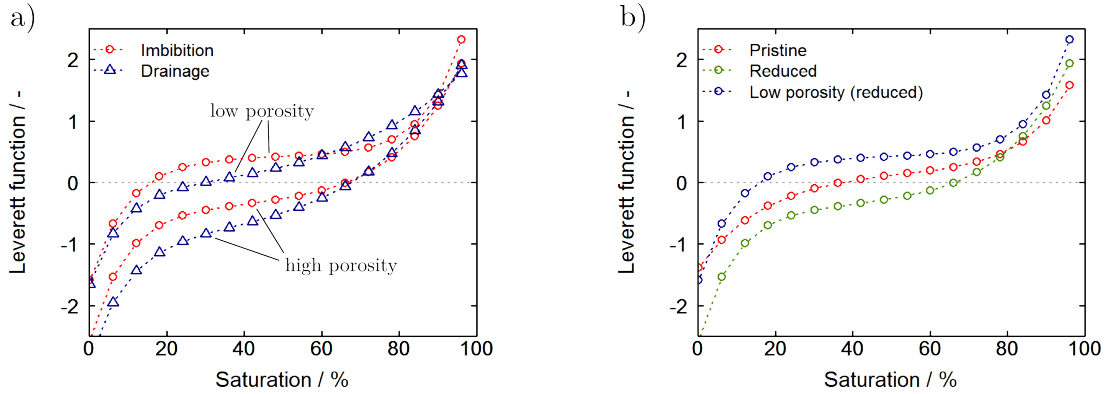


Figure 3.11.: a) Leverett functions for the imbibition and drainage process simulated on the reduced low- and high-porosity electrodes. b) Leverett functions for the imbibition process on the pristine (red) and reduced (green) high-porosity electrode as well as on the reduced low-porosity electrode (blue).

nicely shows the hysteresis between the imbibition and drainage process. This behavior can be regarded as a result of micro-structural effects. During the imbibition of liquid electrolyte some areas of the pore space are only accessible through narrow pores. If the pressure is slowly increased they are filled with liquid electrolyte only at pressure differences high enough to overcome this barrier. As a first guess this pressure barrier can be approximated by the Laplace law. In this case it is implicitly assumed that only droplets with diameters smaller than the diameter of the bottle neck are able to access the 'blocked' pore space. In the drainage process in turn these areas are longer filled with the liquid phase as higher negative pressure differences are needed to withdraw the electrolyte. Especially at moderate saturations there is a distinctive gap between the two curves. At low and high saturation the Leverett functions collapse onto a single line. This indicates that in these regions the initial condition, or better say, the direction of the process (imbibition or drainage) is not relevant which is in line with experimental observations [107].

Figure 3.11 b) shows Leverett functions of the imbibition process for the pristine and reduced high-porosity electrode as well as for the reduced low-porosity electrode. The relevant pressure level in this graph is given at $J(s) = 0$ as most of the experimental studies were done at zero pressure difference between gas and liquid phase (see Section 2.2.2). The highest saturation is predicted in the case of the reduced high-porosity electrode, followed by the pristine high-porosity electrode and finally the reduced electrode with low porosity.

These results are in qualitative agreement with Eq. (3.48) in which the saturation is proportional to the porosity of the electrode (ε_0) and the wetting behavior of the solid ($\cos(\Theta)$). The reduced high-porosity electrode possesses the highest porosity of the three electrodes. The porosity of the pristine high-porosity and reduced low-porosity electrode is approximately the same (see Table 2.2). However, due to the higher compression in the production process the low-porosity electrode has a higher volumetric binder content. As a result the effective contact angle is higher and, thus, the saturation at the same pressure level is lower compared to the pristine high-porosity electrode.

The resulting saturation of the pore space has a tremendous effect on transport and also effective surface area. This topic will be addressed in the following section.

3.3.3. Determination of transport parameters and active surface area

The determination of saturation-dependent transport parameters is not very accurate in 2D simulations. Therefore, 3D simulations are performed in order to obtain the electrolyte distributions in fluid mechanical equilibrium. Only one initial configuration is simulated at each saturation as these studies are computationally very demanding. From the observations in the 2D simulations it can be expected that the initial configuration will have an impact on the final electrolyte distribution, especially, at low and high saturation (cf. error bars in Figure 3.10 b)). However, the relevant saturation range is in the present case given by the moderate capillary pressures which are studied experimentally. Therefore, simulations are conducted within a saturation range between 20 and 80%.

The electrolyte equilibrium distributions in the pore space of the reduced high-porosity electrode are shown exemplary in Figure 3.12 a)-d) for saturations of 20, 40, 60, and 80%. Parts of the electrode are clipped to allow a better view of the liquid phase distribution inside the GDE. In agreement to the 2D simulations the hydrophilic pore space is wetted preferentially. The larger pores in the upper right part of the clipping are filled only at high pressure and saturation, respectively. This behavior is due to the initial conditions of the drainage process.

The electrolyte distributions at the end of the simulations are used to determine effective transport parameters and specific surface areas in GeoDict. Figure 3.13 shows diffusivity D^{eff}/D^0 and Bruggeman coefficient β of the liquid phase as function of electrolyte saturation. Effective parameters for diffusive transport in the gas phase are not shown here as

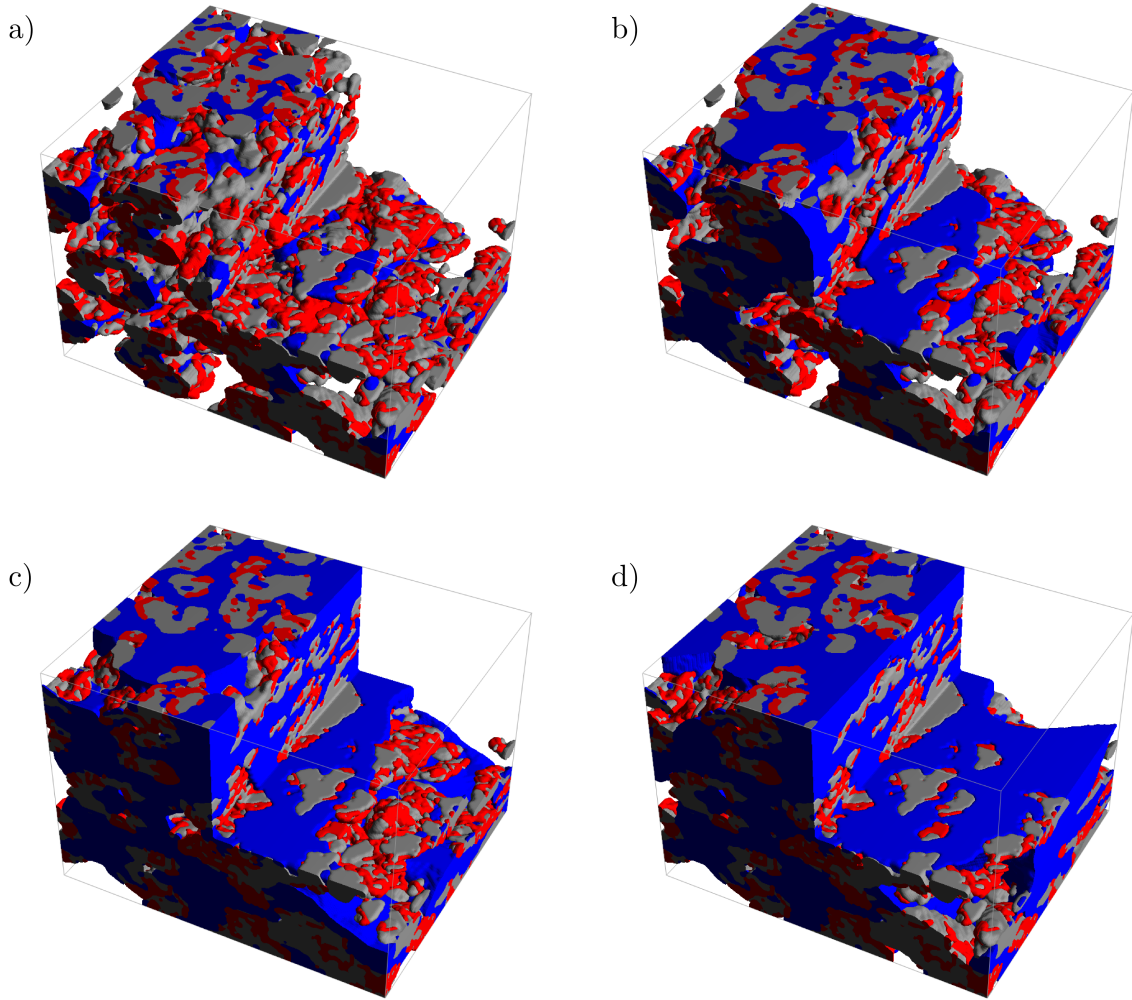


Figure 3.12.: Distributions of the liquid electrolyte in the reduced high-porosity electrode at the end of the simulations ($1 \cdot 10^5$ iterations). The initial saturation of the pore space with electrolyte in figures a) to d) is 20, 40, 60, and 80%.

they do not limit the performance of the GDE since bulk diffusion coefficients are orders of magnitude larger.

The diffusivity in the liquid phase of the three electrodes increases non-linearly with the saturation of the pore space. From Eq. (2.39) it can be expected that the diffusivity at the same saturation strongly depends on the porosity of the electrode. This trend is well reflected in Figure 3.13 a). The reduced high-porosity electrode has the highest diffusivity and also porosity of the three electrodes investigated here. The pristine high-porosity and reduced low-porosity electrode both have a similar porosity (see Table 2.2). In agreement

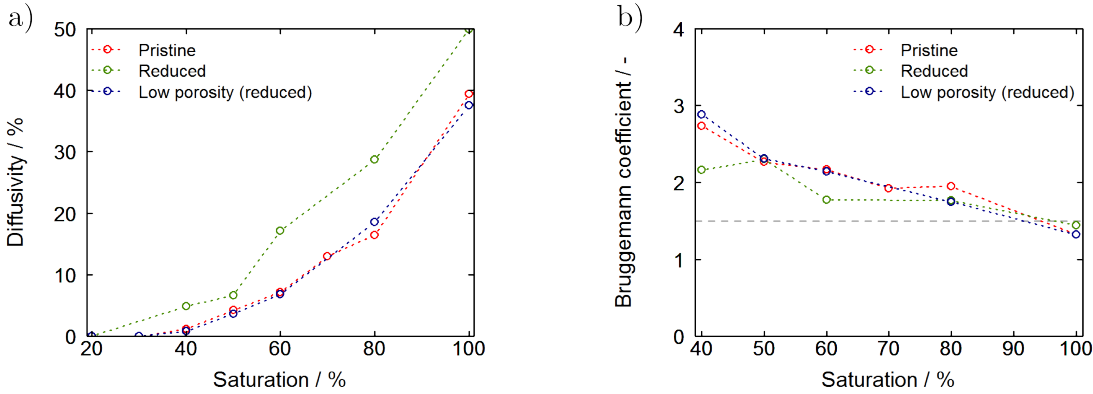


Figure 3.13.: Effective diffusivity and Bruggeman coefficient of the liquid phase as function of saturation for the pristine (red) and reduced (green) high-porosity electrode as well as for the reduced low-porosity electrode (blue). The Bruggeman coefficients follow from the simulations in GeoDict by evaluating Eq. (3.50). The dashed line indicates the standard value of 1.5.

to theory also the effective diffusivities are almost exactly the same.

The Bruggeman coefficients of the liquid phase as shown in Figure 3.13 b) are calculated according to Eq. (3.50). In general the Bruggeman coefficients determined in the simulations are slightly higher compared to the standard value of 1.5 and even increase towards lower saturations. This indicates an exponential rise of the tortuosity factor or diffusion length due to interrupted transport pathways. The Bruggeman coefficients of the three electrodes do have comparable values in the saturation range studied here. It is however important to note, that the points of operation at the same capillary pressure are different. While in the high-porosity case the reduced electrode operates at a saturation of around 60%, the saturation in the pristine electrode is only around 50% and even less in the low-porosity electrode.

Figure 3.14 displays the permeability of the electrode samples for the liquid (left) and gas phase (right) at various saturations. The empty circles represent the permeability determined from the LBM simulations and the dashed line gives the Kozeny-Carman correlation (Eq. (3.51)). The effective particle diameter in the correlation is adjusted to meet the permeability in the case of $s = 100\%$ and $s = 0\%$, respectively. In the liquid phase the trend which is predicted by the correlation agrees fairly well with the simulated permeability. In the case of gas phase permeability the reduced high-porosity electrode shows significant deviation from the expected behavior. This can be explained with the help of the electrolyte distributions displayed in Figure 3.12. The larger pore space in the

3. Lattice-Boltzmann modeling and simulation

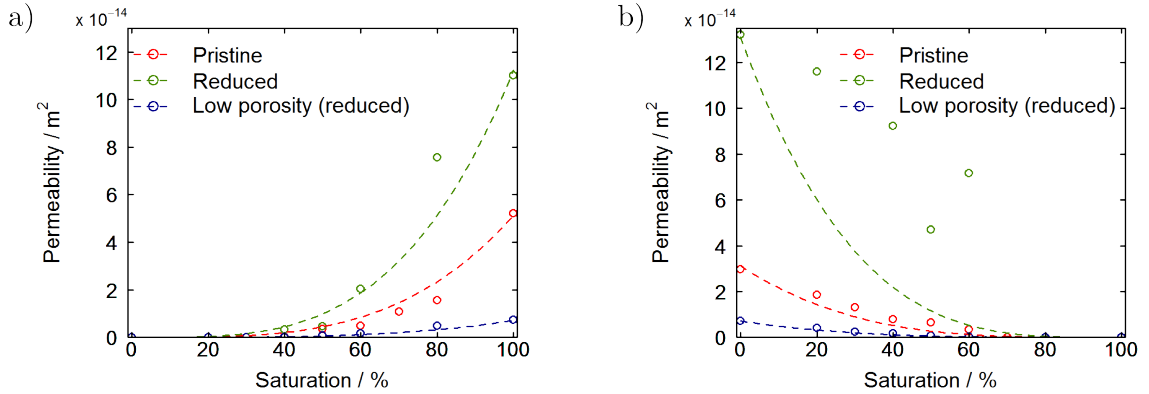


Figure 3.14.: Permeability of liquid phase (left) and gas phase (right) as function of saturation for the pristine (red) and reduced (green) high-porosity electrode as well as for the reduced low-porosity electrode (blue). The dashed line represents the Kozeny-Carman correlation (Eq. (3.51)) in which the effective particle diameter is adjusted to meet the permeability in the case of $s = 100\%$ and $s = 0\%$, respectively.

upper-right corner of the reconstruction (Figure 3.12) is filled only at very high pressures and saturations, respectively. Thus, the electrolyte is distributed non-uniformly in the porous structure and this area can be seen as a preferred transport route for the gas phase (cf. red areas in Figure 2.13 b)). This in turn leads to high values of permeability also at relatively high saturations.

The saturation of the pore space does not only determine effective transport parameters but also the surface areas which are available for (electro-)chemical reactions. In the porous GDE two reactions are important, namely, the dissolution and reduction of oxygen. Dissolution can of course occur only at the interface between the gas phase and liquid electrolyte. The situation for the ORR is more complicated since in principle three phases can be involved (gas, electrolyte, solid). In such cases the highest reactivity is usually found at the triple-phase boundary where liquid, gas, and solid phase are in contact. In the modeling approach presented here (Chapter 4) it is assumed that only dissolved O_2 is participating in the ORR. Therefore, the relevant surface is taken as the interface between the liquid electrolyte and the solid electrode. For the sake of simplicity binder and electrode phase are not distinguished in the determination of active surface area.

Figure 3.15 displays the active surface areas for O_2 reduction (left) and dissolution (right) as function of saturation. In general the specific surface areas in the low-porosity electrode are higher compared to the high-porosity samples. The active surface area of the ORR

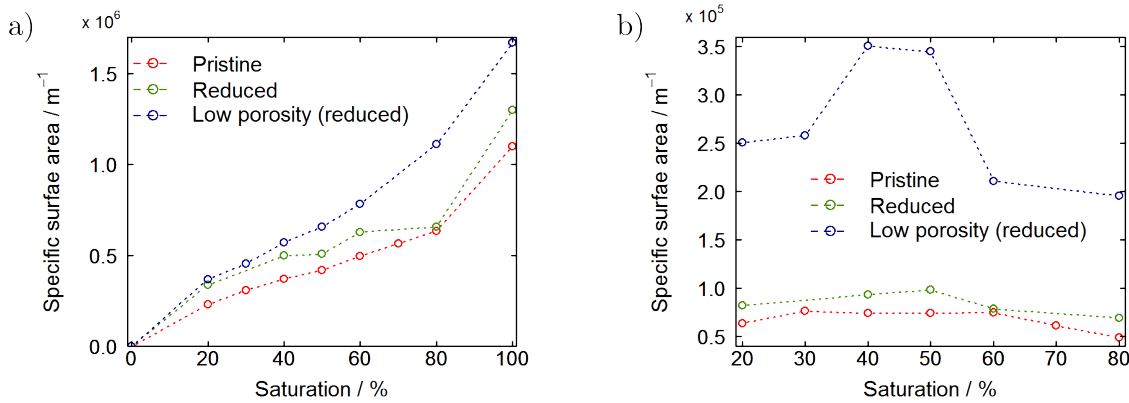


Figure 3.15.: Specific surface areas as function of the liquid phase saturation for O_2 reduction (solid-electrolyte interface, left panel) and dissolution (gas-electrolyte interface, right panel) in the case of the pristine (red) and reduced (green) high-porosity electrode as well as for the reduced low-porosity electrode (blue).

continuously increases with saturation. This is not very surprising since ever larger parts of the electrode are filled with electrolyte. The specific surface area for O_2 dissolution first increases as more electrolyte is dispersed everywhere in the pore space. At higher saturations the electrolyte is able to form clusters in order to minimize its surface and the interfacial area stops to increase. A small plateau in the values of specific surface area can be observed at saturations between around 40 and 60%. At high saturation large areas of the pore space are not accessible for the gas phase and as a consequence the specific surface area for O_2 dissolution starts to decrease.

3.4. Conclusions

In Chapter 3 a RK type SRT-BGK Lattice-Boltzmann model for the simulation of two-phase flow in porous media was introduced. A preliminary version of the model was provided by Prof. Volker Schulz from the DHBW Mannheim [190] which basically represents a reimplementation of Tölke's D3Q15 model in the software package Matlab. As part of this work it was improved taking into consideration the work of Leclaire *et al.* (D2Q9) and Hao *et al.* (D3Q19) which in principle allow the handling of high density and viscosity ratios. The models were extended for the simulation of porous media with

multiple contact angles. Problems with the recoloring operator made it necessary to keep the one proposed by Tölke *et al.*. This operator avoids the problem of lattice pinning and offers the advantage of very sharp interfaces. However, it was found to introduce a systematic error which in some cases manifests in unphysical negative probabilities.

The final model was validated on simple test problems like a steady bubble, a wetting/non-wetting surface, and spinodal decomposition. The simulations demonstrate that despite the numerical deficiencies the model is capable of simulating multiphase flow in porous media including a correct prediction of capillary pressure.

In order to reduce the computational load a coarsening of the experimentally determined micro-structure was necessary. Furthermore, the binder phase which was lost in the imaging process was reconstructed successfully by a stochastic algorithm. Due to the coarse lattice it was not possible to fully resolve the very thin binder fibers in the simulations.

The ultimate goal of this modeling study is the determination of $p_c - s$ curves, effective transport parameters, and active surface areas of the reconstructed electrode samples presented in Chapter 2. A series of 2D simulations of randomly chosen electrode slices was used to calculate the $p_c - s$ characteristics of the samples for the cases imbibition and drainage. These simulations predict saturations of the samples between 25 and 65 % at the pressure difference of 0 kPa which was used in the electrochemical characterization (Section 2.3.2). These large saturations are significantly different from the small saturations predicted by the pore-morphology approach for homogeneous structures in GeoDict. The hysteresis in the capillary pressure which was observed between the imbibition and drainage process is in good agreement to experiments in the literature. The capillary pressures of the 2D simulations agree favorably with the pressures calculated in the more time-consuming 3D simulations. This demonstrates that a series of 2D simulations can be an efficient tool for the calculation of $p_c - s$ curves.

3D simulations mimicking the drainage process were conducted at selected saturations of the pore space. The electrolyte distributions in fluid mechanical equilibrium were used to calculate effective transport parameters and active surface areas in the software GeoDict. As expected, the effective transport parameters depend strongly on the saturation of the pore space and increase towards higher volume fractions of the transporting phase. Values of the Bruggeman coefficient were found to be generally higher than the standard value of 1.5. The calculated permeability followed the trends given by the Kozeny-Carman correlation. Deviations in the case of the reduced high-porosity electrode can be explained by an inhomogeneous distribution of the electrolyte in the reconstructed pore volume.

The $p_c - s$ characteristics, effective transport parameters, and active surface areas are important input parameters for the transport model in the continuum approach presented in Chapter 4. The combination of LBM and continuum modeling in a framework of multiscale simulations is able to offer the opportunity of an efficient optimization of electrode properties in order to improve the performance of electrochemical systems.

4. Continuum modeling and simulation

Main goal of this thesis is the development of a predictive continuum model for reaction and transport in porous GDEs for application in aqueous Li-O₂ batteries. The continuum model presented in this work is explained in detail in Sections 4.1 and 4.2. The current version of the model allows the simulation half-cell and full-cell setups. This is an important step in order to couple the experimental data of half-cell measurements to the performance of the final battery cell.

A requirement for every predictive model is a sound parametrization of the relevant physical parameters. The foundation for this approach is laid in Chapters 2 and 3 and parameters of the model will be discussed in detail in Section 4.3.1. The model is validated for experimental data measured on Ag/Ag₂O electrodes over a large range of electrolyte concentrations and temperatures. The validated model is used to extract the most important parameters for electrode design and extensive parameter variations are performed in order to determine an improved electrode structure. Furthermore, the model of the GDE can be coupled to simulations of virtual battery cells in order to evaluate the electrode and cell design of future Li-O₂ batteries.

Results of the continuum model were published in references [78] and [198] and presented on several conferences. A detailed list of publications and conference contributions can be found on page 199.

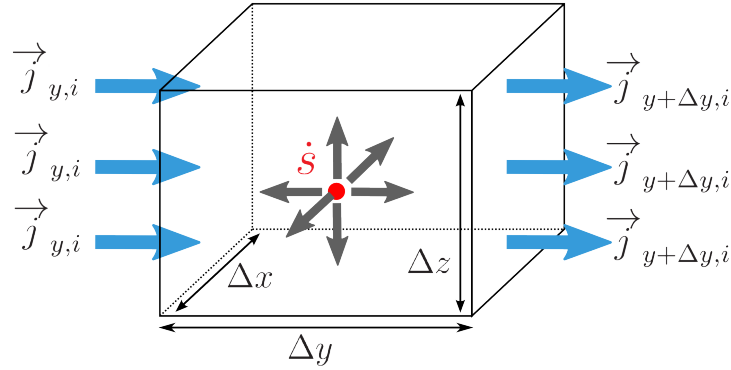


Figure 4.1.: Control volume for the derivation of the equations for mass and charge conservation. Blue arrows indicate area-specific fluxes describing diffusion, migration and convection into/out of the control volume and the red dot represents a volume-specific source term due to (electro)chemical reactions or double layer currents.

4.1. Background

The continuum modeling of electrochemical systems and batteries in particular was pioneered by the works of John Newman [62, 125]. Many of the concepts which he developed can also be found in this work such as the theory of transport in concentrated solutions or porous electrode theory.

Continuum models on the electrode and cell level are typically based on the conservation equations for mass, momentum, energy, and charge. In order to reduce the complexity of the model, it is often assumed that either the system is isothermal and/or convection in the electrolyte is very slow. Therefore, it is not necessary to solve the energy and momentum equations and the system reduces to the conservation equations for mass and charge. Furthermore, the structure of the porous electrodes is not resolved in detail and mathematical theorems can be used to derive a volume-averaged model. Above mentioned steps are explained in more detail in the following sections.

Conservation equations for mass and charge in the liquid phase

Typically, the conservation equations of mass and charge have the form of partial differential equations. Analytical solutions can be found only for very special cases and usually the equations are solved numerically. The numerical solution requires a spatial and temporal discretization of the equations. In this type of simulation commonly finite volume schemes are employed for the spatial resolution. Figure 4.1 shows a representative control volume in the bulk of the simulation domain. For the sake of simplicity only transport in y -direction is discussed here. The derivation in other directions of the coordinate system is straightforward.

Let us first consider the conservation equation of an arbitrary species i in the liquid electrolyte. The change of the amount N_i of species i with time t due to fluxes across the boundaries of the control volume j_i and (electro)chemical source terms \dot{S}_i is given by

$$\frac{\partial N_i}{\partial t} = \left(j_{y,i}^{\text{tot}} - j_{y+\Delta y,i}^{\text{tot}} \right) \Delta x \Delta z + \dot{S}_i, \quad (4.1)$$

where $j_{y,i}^{\text{tot}}$ is the sum of diffusive, migrative, and convective fluxes. A first-order Taylor series expansion of $j_{y+\Delta y,i}^{\text{tot}}$ gives

$$j_{y+\Delta y,i}^{\text{tot}} = j_{y,i}^{\text{tot}} + \frac{\partial j_{y,i}^{\text{tot}}}{\partial y} \Delta y \quad (4.2)$$

and insertion into Eq. (4.1) results in

$$\frac{\partial N_i}{\partial t} = -\frac{\partial j_{y,i}^{\text{tot}}}{\partial y} \Delta x \Delta y \Delta z + \dot{S}_i. \quad (4.3)$$

At this point it is convenient to introduce the concentration $c_i = N_i/\Delta V$ and a division of Eq. (4.3) through the incremental control volume $\Delta V = \Delta x \Delta y \Delta z$ yields

$$\frac{\partial c_i}{\partial t} = -\frac{\partial j_{y,i}^{\text{tot}}}{\partial y} + \dot{s}_i, \quad (4.4)$$

where \dot{s}_i is now a volume-specific source term. As it can be seen from Eq. 4.4 the conservation equation of species i allows the calculation of spatially resolved concentration distributions in the liquid electrolyte.

The equations for the calculation of potential profiles is given by the conservation of

4. Continuum modeling and simulation

charge. The charge Q in the control volume of the liquid electrolyte can be calculated as sum over the amount of all charged species residing in ΔV . In a similar approach the change of $q = Q/\Delta V$ over time due to fluxes across the boundaries and electrochemical source terms can be derived as

$$\frac{\partial q}{\partial t} = \sum_i z_i F \left[-\frac{\partial j_{y,i}^{\text{tot}}}{\partial y} + \dot{s}_i \right], \quad (4.5)$$

where z_i is the charge of species i . On the macroscopic scale it can be safely assumed that the electrolyte solution is electro-neutral, meaning the sum over all charged species is zero ($q = 0$). Therefore, the equation for charge conservation in the liquid electrolyte follows as

$$0 = \sum_i z_i F \left[-\frac{\partial j_{y,i}^{\text{tot}}}{\partial y} + \dot{s}_i \right]. \quad (4.6)$$

Note, that although this equation will be used to determine the potential distribution in the liquid electrolyte ϕ_{elyte} this variable does not even appear in Eq. (4.6). It will be introduced during the description of area-specific fluxes $j_{y,i}$ and volume-specific source terms \dot{s} .

The (electro)chemical source term can be modeled by a general expression according to the law of mass action. The rate expression of an (electro)chemical reaction m is in the present case given by

$$r_m = \left[k_{f,m} \prod_{educts} a_j^{-\nu_{j,m}} e^{\left(\frac{-\beta n F}{RT} \Delta\phi\right)} - k_{r,m} \prod_{products} a_j^{\nu_{j,m}} e^{\left(\frac{(1-\beta)n F}{RT} \Delta\phi\right)} \right], \quad (4.7)$$

where a_j and $\nu_{j,m}$ are the activity and the stoichiometric coefficient of species j , β the symmetry factor of the reaction, $\Delta\phi = \phi_{\text{elode}} - \phi_{\text{elyte}}$ the potential difference between electrode and electrolyte, and $k_{f,m}$ and $k_{r,m}$ the reaction rate constants of the forward and reverse reaction, respectively. The forward rate constant is modeled by an Arrhenius type approach according to

$$k_{f,m} = k_{f,m}^0 e^{-\frac{E_m^a}{RT}}, \quad (4.8)$$

where $k_{f,m}^0$ and E_m^a are the frequency factor and activation energy of the reaction. The relation between $k_{f,m}$ and $k_{r,m}$ is given by the thermodynamics of the reaction according to

$$\frac{k_{f,m}}{k_{r,m}} = e^{-\frac{\Delta G_{r,m}}{RT}}, \quad (4.9)$$

where $\Delta G_{r,m}$ is the molar Gibbs reaction enthalpy calculated from the chemical potentials. The source term \dot{s}_i is given as sum over all reactions in which species i is involved

$$\dot{s}_i = \sum_m \nu_{i,m} r_m. \quad (4.10)$$

In the charge conservation equation the source term is multiplied with a factor of $z_i F$ which gives the relation for the Faradaic current i_F (compare Eq. (2.26)).

In a macroscopic model the electric double layer requires a special treatment as the length scale of the layer is typically not resolved. Therefore, a second volumetric source term is included in the charge conservation equation according to Eq. (2.30)

$$i_{\text{dl}} = C_{\text{dl}} \frac{\partial \Delta \phi}{\partial t}$$

and Eq. (4.6) can be rewritten as

$$C_{\text{dl}} \frac{\partial \Delta \phi}{\partial t} = \sum_i z_i F \frac{\partial j_{y,i}^{\text{tot}}}{\partial y} - i_F. \quad (4.11)$$

In the species mass balance a contribution of the double layer current is included as

$$\frac{\partial c_i}{\partial t} = -\frac{\partial j_{y,i}}{\partial y} + \dot{s}_i + \frac{i_{\text{dl}}}{z_i F}, \quad (4.12)$$

taking into account a specific adsorption of cations and anions at the anode and cathode, respectively.

In a dilute solution the contributions to the transport of species i can be split up linearly into diffusive, migrative, and convective fluxes

$$j_{y,i}^{\text{tot}} = j_{y,i}^{\text{diff}} + j_{y,i}^{\text{migr}} + j_{y,i}^{\text{conv}}. \quad (4.13)$$

4. Continuum modeling and simulation

Transport by diffusion is commonly described by Fick's law

$$j_{y,i}^{\text{diff}} = -D_i \frac{\partial c_i}{\partial y}, \quad (4.14)$$

where D_i is the so-called self-diffusion coefficient of species i in the solution. In a similar way charged species will move if exposed to a gradient in potential (migration)

$$j_{y,i}^{\text{migr}} = -D_i^{\text{migr}} \frac{\partial \phi_{\text{elyte}}}{\partial y}, \quad (4.15)$$

where the migration coefficient $D_i^{\text{migr}} = D_i \frac{z_i F c_i}{RT}$ is often referred to as the mobility of the ionic species in the electrolyte. It is a measure for the ionic conductivity of the electrolyte solution. The contribution of convection in the liquid electrolyte can be expressed as

$$j_{y,i}^{\text{conv}} = \mathbf{v}_y c_i, \quad (4.16)$$

where \mathbf{v}_y is the average convection velocity. Finally, the continuity equation of species i in a dilute electrolyte solution follows as

$$\frac{\partial c_i}{\partial t} + \frac{\partial}{\partial y} (\mathbf{v}_y c_i) = \frac{\partial}{\partial y} \left(D_i \frac{\partial c_i}{\partial y} + D_i \frac{z_i F c_i}{RT} \frac{\partial \phi_{\text{elyte}}}{\partial y} \right) + \dot{s}_i + \frac{i_{\text{dl}}}{z_i F}. \quad (4.17)$$

Eq. (4.17) is also known as the Nernst-Planck equation. In this approach it is implicitly assumed that the different species in the liquid electrolyte do not interact during transport. While this is a justified approximation in the case of dilute solutions there will certainly be some interaction in the case of concentrated solutions, especially taking into account the long-range electrostatic interactions of the ionic species. A more detailed model for transport in concentrated electrolyte solutions will be discussed in the next paragraph.

Transport in concentrated electrolyte solutions

Transport in concentrated electrolyte solutions [62] can be derived based on the theory of multicomponent mass transport as e.g. proposed by Krishna and Wesselingh [199, 200]. As key point of this approach an interaction between the different species is taken into account in the calculation of 'dispersive' fluxes (diffusion and migration).

The driving force of the dispersive transport is a gradient in the electrochemical potential

$\bar{\mu}_i$. It is balanced by friction (interactions) between the molecules which also causes a drag on component i due to a gradient in electrochemical potential of component j . A general ansatz for transport in a system of n components can therefore be written as [200]

$$\frac{d\bar{\mu}_i}{dy} = RT \sum_{j=1}^n \frac{c_j(\mathbf{v}_{y,j} - \mathbf{v}_{y,i})}{c_{\text{tot}} D_{ij}}, \quad (4.18)$$

where D_{ij} is the 'binary diffusion coefficient' describing the friction between the molecules, c_{tot} the total concentration of the solution, and \mathbf{v}_i and \mathbf{v}_j are the component velocities of species i and j , respectively. The component velocities are given as sum of the average convection velocity of the solution and the dispersive velocity of the individual species $\mathbf{v}_{y,i} = \mathbf{v}_y + \mathbf{v}_{y,i}^{\text{disp}}$. Multiplication of Eq. (4.18) with c_i and introduction of the dispersive fluxes as $j_{y,i}^{\text{disp}} = c_i \mathbf{v}_{y,i}^{\text{disp}}$ yields

$$c_i \frac{d\bar{\mu}_i}{dy} = RT \sum_{j=1}^n \frac{c_i j_{y,j}^{\text{disp}} - c_j j_{y,i}^{\text{disp}}}{c_{\text{tot}} D_{ij}}. \quad (4.19)$$

The relations give the dispersive fluxes $j_{y,i}^{\text{disp}}$ in an implicit form. In the case of a binary electrolyte solution explicit formulations of dispersive fluxes can be derived as [62]

$$\begin{aligned} j_{y,+}^{\text{disp}} &= -\frac{\nu_+ \mathfrak{D}_e}{\nu RT} \frac{c_{\text{tot}}}{c_0} c_e \frac{d\mu_e}{dy} + \frac{it_+}{z_+ F} \\ j_{y,-}^{\text{disp}} &= -\frac{\nu_- \mathfrak{D}_e}{\nu RT} \frac{c_{\text{tot}}}{c_0} c_e \frac{d\mu_e}{dy} + \frac{it_-}{z_- F}, \end{aligned} \quad (4.20)$$

where ν_{\pm} is the number of cations/anions after the dissociation of one electrolyte molecule, \mathfrak{D}_e a thermodynamic definition of the diffusion coefficient, $\mu_e = \nu_+ \mu_+ + \nu_- \mu_-$ is the chemical potential of the electrolyte, c_0 the concentration of the solvent, and $t_+ = 1 - t_-$ the transference number with respect to the average solution velocity. In more complicated cases Eqs. (4.19) need to be solved iteratively.

Based on Eqs. (4.20) a more common form of the continuity equation for the electrolyte salt can be derived as [61, 62, 201]

$$\frac{\partial c_e}{\partial t} = \frac{\partial}{\partial y} \left(D_e \frac{\partial c_e}{\partial y} - \frac{i_e(1 - t_+)}{F} \right), \quad (4.21)$$

4. Continuum modeling and simulation

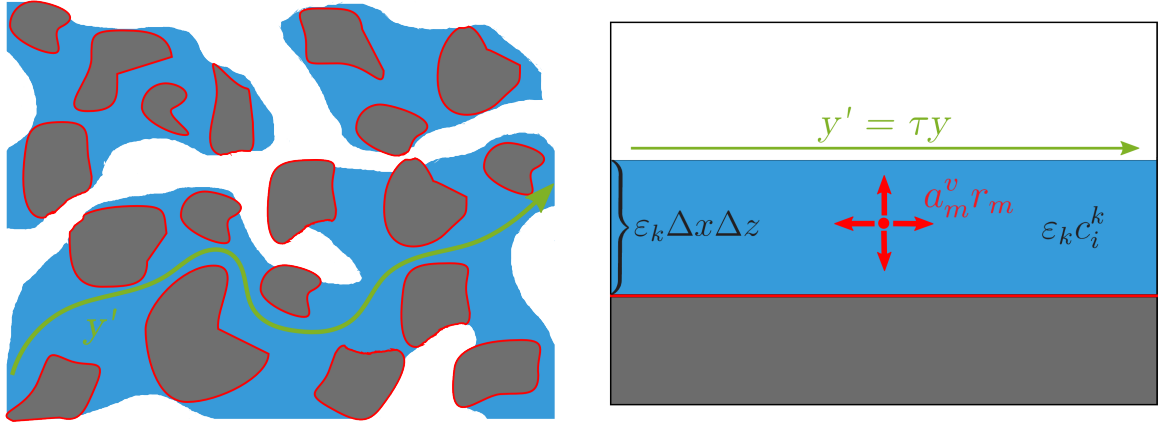


Figure 4.2.: Schematic of a porous electrode (left) and its volume-averaged representation in the modeling approach (right).

where i_e is the ionic current in the electrolyte solution which can be described by a liquid-phase version of Ohm's law

$$i_e = -\sigma_{\text{elyte}} \frac{\partial \phi_{\text{elyte}}}{\partial y} - \frac{\sigma_D}{c_e} \frac{\partial c_e}{\partial y}. \quad (4.22)$$

σ_{elyte} is the ionic conductivity of the electrolyte and σ_D is a diffusional conductivity which follows as [78]

$$\sigma_D = \frac{2\sigma_{\text{elyte}}c_+(t_+ - 1)}{z_+F} \frac{\partial \mu_+}{\partial c_+}. \quad (4.23)$$

For an univalent binary salt (such as LiOH) the electrolyte concentration is $c_e = c_+ = c_-$. In this simple case it is in fact possible to derive consistent diffusion and migration coefficients for the Nernst-Planck equation (Eq. (4.17)) from Eqs. (4.21) and (4.22) [78]

$$D_{\pm} = D_{\pm}^0 + \frac{t_{\pm}}{z_{\pm}F} \frac{\sigma_D}{c_{\pm}} \quad \text{and} \quad D_{\pm}^{\text{migr}} = \frac{t_{\pm}}{z_{\pm}F} \sigma_{\text{elyte}}, \quad (4.24)$$

where D_{\pm}^0 is the self-diffusion coefficient of the electrolyte salt. It is an advantage of this description that all parameters are readily available in suitable experiments [202–204]. The parameters of the LiOH solution are summarized in Section 4.3.1.

Transport in porous electrodes

The porous nature of GDEs is up to this point not taken into account. In simulations resolving the micro-structure of the GDE the equations derived in the previous paragraphs are sufficient to describe the transport in the liquid electrolyte. These simulations are a valuable tool for the detailed investigation of transport processes, however, they are often computationally very demanding and render intensive design studies of whole battery cells or systems impossible. Volume averaged formulations of the conservation equations can be derived mathematically. In this approach the geometric detail of the electrode is disregarded and characteristic material properties such as porosity and specific surface area are introduced [125].

Figure 4.2 shows schematic images of a GDE micro-structure (left) and the representation which is solved in the averaged model (right). Each control volume consists of k phases which are described by their volume fraction ε_k [$\text{m}_{\text{phase}}^3/\text{m}_{\text{tot}}^3$] with

$$\sum_k \varepsilon_k = 1 . \quad (4.25)$$

Therefore, the concentration in the control volume [$\text{mol}/\text{m}_{\text{tot}}^3$] is given by $\varepsilon_k c_i^k$ and fluxes across the boundary of the control volume are related to the cross-sectional area of the phase by $\varepsilon_k \Delta x \Delta z$.

The electrochemical reactions occur at the interface between the liquid and solid phases and the reaction rate is typically related to the surface area of the solid. In the continuum approach the heterogeneous reactions are treated as volume-specific source terms by introducing a specific surface area available for reaction a_m^v . The resulting continuity equation for the transport in the porous electrode can be written as

$$\frac{\partial \varepsilon_k c_{k,i}}{\partial t} = -\frac{\partial \varepsilon_k j_{y,i}}{\partial y'} + \dot{s}_i + \frac{i_{\text{dl}}}{z_i F} . \quad (4.26)$$

In the definition of the two source terms the specific surface area is introduced as

$$\dot{s}_i = \sum_m \nu_{m,i} a_m^v r_m \quad \text{and} \quad i_{\text{dl}} = a_{\text{dl}}^v c_{\text{dl}} \frac{\partial \Delta \phi}{\partial t} . \quad (4.27)$$

Furthermore, the transport pathways in porous media are tortuous and, therefore, longer compared to the transport in the bulk phase. A representative transport pathway in the porous GDE along the coordinate y' is illustrated by the green line in the left panel of

4. Continuum modeling and simulation

Figure 4.2. The tortuosity of the media is taken into account by the tortuosity factor $\bar{\tau}$ with $y' = \bar{\tau}y$. In battery modeling very often the Bruggeman correlation (Eq. (2.41)) is used to model the porosity-tortuosity relationship

$$\varepsilon/\bar{\tau} = \varepsilon^\beta . \quad (4.28)$$

As explained in the previous Chapter this relation is employed in the calculation of effective transport parameters which are used in the volume-averaged model instead of the transport coefficients of the bulk phase

$$D_i^{\text{eff}} = D_i^0 \varepsilon_k^{\beta_k} , \quad D_i^{\text{migr,eff}} = D_i^{\text{migr},0} \varepsilon_k^{\beta_k} \quad \text{and} \quad \sigma_k^{\text{eff}} = \sigma_k^0 \varepsilon_k^{\beta_k} . \quad (4.29)$$

4.2. Methodology

The models presented in this section were developed in a close collaboration with Dr. Birger Horstmann in the context of the LuLi project [6]. They allow the simulation of full battery cells (Section 4.2.1) as well as experimental half-cell measurements (4.2.2). The parametrization of model parameters is summarized in Section 4.3.1. Details on the model implementation and simulation methodology are given in Section 4.2.3.

4.2.1. Half-cell model

Modeling domain

Figure 4.3 schematically depicts the modeling domain describing the experimental setup as explained in Chapter 2.2. In the 1D continuum model the temporal evolution of concentrations and potentials is determined based on conservation equations for mass and charge, respectively. The system is assumed to be isothermal and convection in gas and liquid phase is characterized by low Reynolds numbers (Stokes flow). During discharge pure oxygen gas enters the GDE at constant temperature and pressure. Transport in the gas phase is described by

$$\frac{\partial(\varepsilon_{\text{gas}} c^{\text{tot,gas}} X_i)}{\partial t} = - \frac{\partial j_{y,i}^{\text{diff,gas}}}{\partial y} - \frac{\partial j_{y,i}^{\text{conv,gas}}}{\partial y} + \dot{s}_{i,m} , \quad (4.30)$$

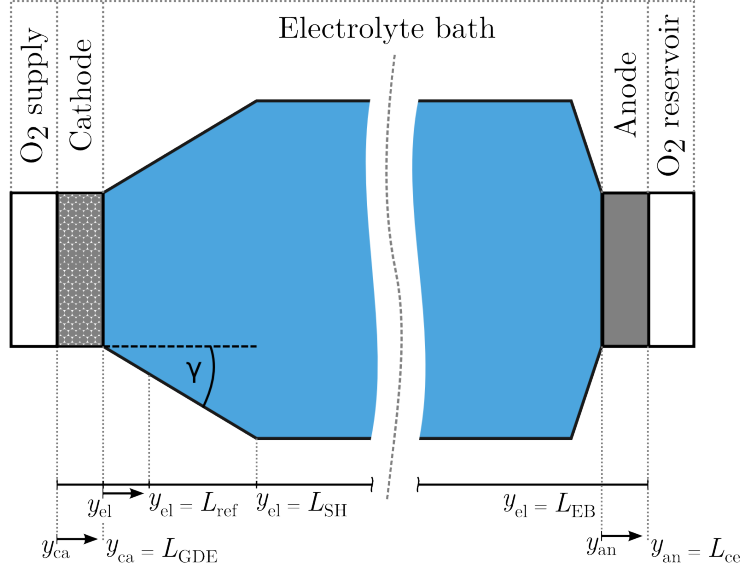


Figure 4.3.: Schematic depiction of the modeling domain. The geometry represents the experimental half-cell setup introduced in Section 2.2. In the 1D continuum model transport of reactants in cathode, electrolyte bath and anode is considered. During discharge oxygen is consumed in the cathode (ORR) and released by the reverse reaction (OER) at the anode.

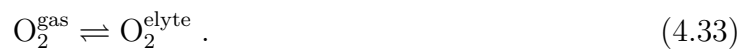
where X_i is the mole fraction of species i . The diffusive transport in the gas phase is modeled by the Stefan-Maxwell equation which takes a similar form to Eq. (4.19)

$$\frac{\partial(c^{\text{tot,gas}} X_i)}{\partial y} = - \sum_{j \in S_g} \frac{X_i j_{y,j}^{\text{diff,gas}} - X_j j_{y,i}^{\text{diff,gas}}}{D_{ij}^{\text{eff}}} . \quad (4.31)$$

At low Reynolds numbers the convection velocity can be calculated according to Darcy's law (Eq. (2.42)) and the convection term follows as

$$j_{y,i}^{\text{conv}} = \frac{B_{\text{gas}}}{\mu_{\text{gas}}} \frac{\partial p_{\text{gas}}}{\partial y} X_i c^{\text{tot,gas}} , \quad (4.32)$$

where B_{gas} , μ_{gas} , and p_{gas} are the permeability, viscosity, and pressure of the gas phase, respectively. The gaseous oxygen subsequently dissolves in the liquid electrolyte. In the approach presented here the dissolution process is modeled as chemical reaction



4. Continuum modeling and simulation

The kinetics of the dissolution reaction follow from the Hertz-Knudsen equation. It is assumed that 1% of the molecules hitting the gas-liquid interface are absorbed in the electrolyte [78]. The dissolved oxygen is transported in the liquid electrolyte assuming negligible interactions with other species (Eq. (4.17))

$$\frac{\partial \varepsilon_{\text{elyte}} c_{\text{O}_2}}{\partial t} + \frac{\partial}{\partial y} (\mathbf{v}_{y,\text{elyte}} c_{\text{O}_2}) = \frac{\partial}{\partial y} \left(D_{\text{O}_2}^{\text{eff}} \frac{\partial c_{\text{O}_2}}{\partial y} \right) + \dot{s}_{\text{O}_2} . \quad (4.34)$$

Finally, the dissolved oxygen reacts in the ORR (Eq. (1.11)) with water and electrons forming hydroxide ions. Transport of the electrolyte species (Li^+ , OH^-) is modeled by concentrated solution theory

$$\frac{\partial \varepsilon_{\text{elyte}} c_{\pm}}{\partial t} + \frac{\partial}{\partial y} (\mathbf{v}_{y,\text{elyte}} c_{\pm}) = \frac{\partial}{\partial y} \left(D_{\pm}^{\text{eff}} \frac{\partial c_{\pm}}{\partial y} + D_{\pm}^{\text{migr,eff}} \frac{\partial \phi_{\text{elyte}}}{\partial y} \right) + \dot{s}_{\text{O}_2} , \quad (4.35)$$

with the diffusion and migration coefficients as defined in Eq. (4.24). Again Darcy's law can be used to describe the convective transport in the pore space of the GDE

$$\mathbf{v}_{y,\text{elyte}} = \frac{B_{\text{elyte}}}{\mu_{\text{elyte}}} \frac{\partial p_{\text{elyte}}}{\partial y} . \quad (4.36)$$

The assumption of electro-neutrality is employed to determine the potential distribution in the liquid electrolyte (Eq. (4.11)). The electronic resistivity of the GDE can be safely neglected due to the high conductivity of silver [152].

In the porous structure of the GDE, gas phase and liquid electrolyte are in mechanical equilibrium. The electrolyte saturation s is determined by the capillary pressure p_c

$$p_c = \Delta p = p_{\text{gas}} - p_{\text{elyte}} = \sigma \sqrt{\frac{\varepsilon_0}{B_{\text{elyte}}}} J(s) , \quad (4.37)$$

where $J(s)$ is the Leverett function as introduced in Chapter 3. The pressure level in the liquid phase at the electrode boundary is determined by the hydrostatic pressure of the electrolyte bath. In the experiments the liquid pressure is usually adjusted to meet the pressure of the gas phase ($\Delta p = 0$). The volume fractions of the gas and the liquid phases need to be determined from their respective equations of state. In the gas phase

the relation between pressure and density or partial molar volume is given by the ideal gas law

$$\rho_{\text{gas}} = \frac{p_{\text{gas}}}{RT} \overline{MW}_{\text{gas}} , \quad (4.38)$$

where $\overline{MW}_{\text{gas}}$ is the mean molecular weight of the gas phase. In the electrolyte the volume fraction is determined by the partial molar volumes of the components as

$$\sum_i \left[V_i + (p_{\text{elyte}} - p^\ominus) \kappa_i \right] \varepsilon_{\text{elyte}} c_i = \varepsilon_{\text{elyte}} , \quad (4.39)$$

where V_i and κ_i are the partial molar volume and compressibility of species i at the standard pressure p^\ominus . The transport model of a GDE with generic structure was developed by Dr. Birger Horstmann [78] and was adopted for the Ag/Ag₂O electrode presented in this work.

In the experiments the concentration of LiOH in the electrolyte bath is kept well below the solubility limit ($c_s = 5.23$ mol/l). Thus, the formation of LiOH·H₂O (Eq. (1.12)) is neglected in the simulation of half-cell experiments.

Changes in the cross-sectional area of the experimental setup are taken into account by a modification of the mass balances according to

$$\frac{\partial(\varepsilon_{\text{elyte}} c_i)}{\partial t} = -\frac{1}{A} \frac{\partial(A (j_i^{\text{tot}}))}{\partial y} . \quad (4.40)$$

At high discharge currents the formation of gas bubbles can be observed at the counter electrode of the experimental setup which consists of a platinum sheet. This is attributed to the OER according to Eq. (1.11). In the model the evolved oxygen is assumed to stay dissolved in the electrolyte and is in equilibrium with the surrounding O₂ atmosphere (Eq. (4.33)).

The reference electrode is not explicitly modeled in the current approach as the electrolyte potential at the position of the reference electrode ($y_{\text{ref}} = 5$ mm) directly constitutes the potential of a standard hydrogen electrode (SHE).

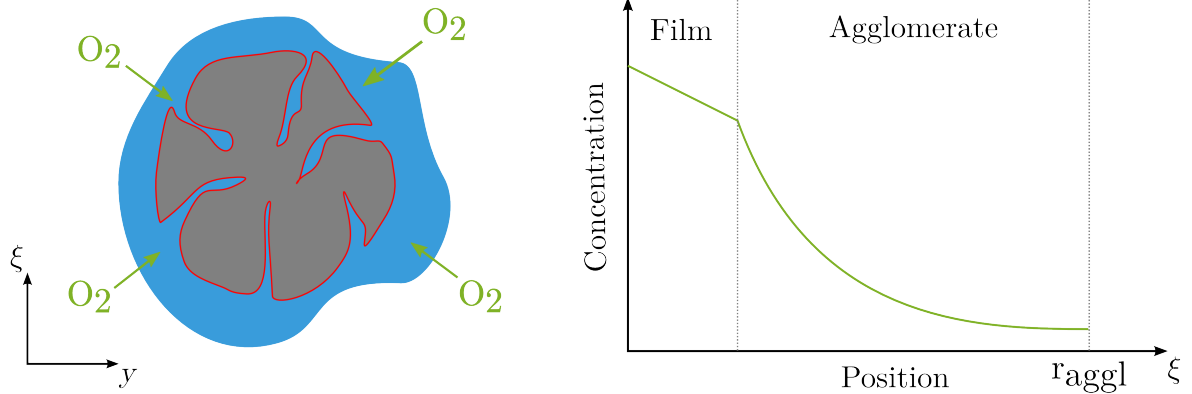


Figure 4.4.: Schematic depiction of a model agglomerate. The electrode particle is surrounded and filled by the liquid electrolyte. O_2 dissolves at the gas/electrolyte interface and dissolves to the active sites on the agglomerate surface. The right panel shows an exemplary distribution of O_2 concentration through the electrolyte film and in the mesoporous agglomerate.

Fllooded agglomerate model

In the standard 1D continuum model described above the main transport direction denoted by y is given by the transport of ions between anode and cathode. Transport perpendicular to the y direction is not taken into account in this simple model. The situation in the agglomerate is schematically shown in Figure 4.4. During the reduction process of the Ag_2O electrode a considerable amount of meso- and micropores is formed (cf. particle morphology in Figure 2.8). The small pores increase the surface area available for the electrochemical reaction but the transport within these pores is relatively slow. The right panel of Figure 4.4 shows an exemplary concentration profile for diffusive transport through the electrolyte film on the agglomerate surface and reaction and transport in the porous agglomerate itself. Due to transport limitations the resulting reaction rate in the agglomerate will be smaller than at bulk conditions.

A 1+1D model could be used to resolve reaction and transport in the agglomerate, however, this approach would be computationally much more demanding. In chemical engineering the concept of the effectiveness factor was proposed to model transport limitations in porous media such as catalyst pellets. In this approach the reaction rate is corrected

with a factor implicitly taking into account diffusive transport in the agglomerate. The effectiveness factor is defined as

$$\eta_m^{\text{aggl}} = \frac{\text{real reaction rate}}{\text{reaction rate at bulk conditions}} = \frac{1/V_{\text{aggl}} \int_0^{V_{\text{aggl}}} r_m dV_{\text{aggl}}}{r_m^{\text{bulk}}}, \quad (4.41)$$

where V_{aggl} is the volume of the agglomerate and r_m the rate of reaction. The real reaction rate in the agglomerate can be calculated based on the analytical solution of the component mass balance [200, 205, 206]. On the assumption of a first order reversible reaction in a flat geometry the reaction-diffusion equation of a quasi-stationary system can be used to determine three dimensionless parameters

- inner Thiele modulus

$$\Phi_1^2 = \frac{\text{Forward reaction rate}}{\text{Diffusion in agglomerate}} = \frac{k_f}{D^{\text{eff}}/r_{\text{aggl}}^2} \quad (4.42)$$

- outer Thiele modulus

$$\Phi_2^2 = \frac{\text{Backward reaction rate}}{\text{Diffusion in agglomerate}} = \frac{k_b/c}{D^{\text{eff}}/r_{\text{aggl}}^2} \quad (4.43)$$

- Sherwood number

$$Sh = \frac{\text{Diffusion in film}}{\text{Diffusion in agglomerate}} = \frac{D/\delta_F}{D^{\text{eff}}/r_{\text{aggl}}} \quad (4.44)$$

where r_{aggl} is the agglomerate radius and δ_F the thickness of the electrolyte film on the agglomerate surface. The Thiele moduli give the relation between reaction and diffusion velocity in the agglomerate. Therefore, a high Thiele modulus indicates a diffusion limitation of the reaction. The Sherwood number relates the diffusion velocity in the surface film to the diffusion velocity in the particle itself. Usually, the thickness of the surface film is rather small such that the influence of the outer mass transfer can be neglected.

A general solution of Eq. (4.41) is quite lengthy [200] even for this simple case. It can be further reduced on the assumption of an irreversible reaction ($\Phi_2 = 0$) and fast transport in the surface film ($Sh \rightarrow \infty$). These are reasonable assumptions, especially, taking into account that the system is usually operated at high overpotentials (Taylor approximation).

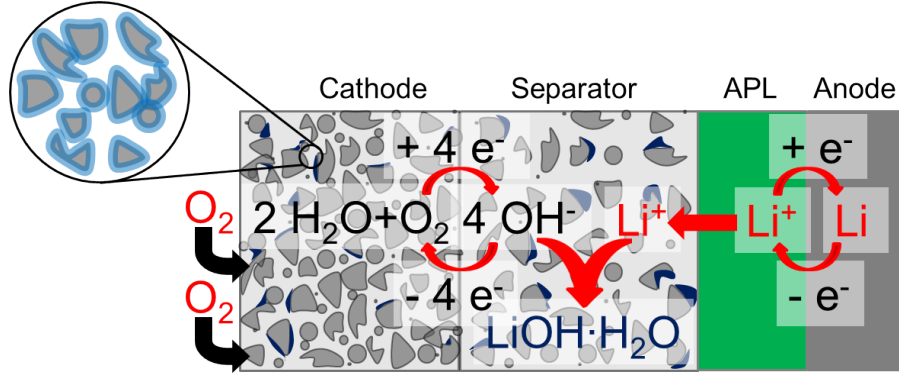


Figure 4.5.: Schematic depiction of the modeling domain representing a full-cell setup with a Li metal anode. The Li metal is protected from the aqueous electrolyte by a Li ion conducting APL. During discharge oxygen is consumed in the cathode (ORR) and Li dissolves at the anode. At LiOH concentrations above the solubility limit $LiOH \cdot H_2O$ precipitates on the surfaces in the porous separator and cathode.

In this case the effectiveness factor follows as function of the inner Thiele modulus Φ_1 to

$$\eta_m^{\text{aggl}} = \frac{\tanh(\Phi_1)}{\Phi_1}. \quad (4.45)$$

Strictly speaking, this concept is only valid for isothermal and potentiostatic simulations [200]. However, the potential scan rate in the simulations presented below is usually very slow such that the system is assumed to be quasi-stationary.

The agglomerate model can be regarded as an extension to the standard model already presented in [198]. Results of this approach demonstrating the significant influence of transport in the agglomerates of a dense electrode structure are presented in Section 4.3.3.

4.2.2. Full-cell model

Modeling domain

Figure 4.5 shows a schematic representation of the modeling domain for full-cell simulations. The model can be seen as an extension to the half-cell model presented in the previous section. Instead of the Pt sheet a lithium metal electrode is employed at the anode.

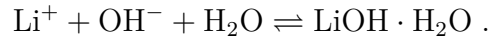
Therefore, an additional protective layer (APL) is needed to prevent contact of the lithium metal with the aqueous electrolyte. Li dissolves at the anode and migrates through the APL. In the present approach it is modeled as solid electrolyte with an ionic conductivity σ_{APL} and a transference number $t_+ = 1$. During discharge the concentration of LiOH in the separator and cathode increases until the solubility limit (c_{LiOH}^s) is reached. At prolonged discharge a precipitation of solid $\text{LiOH}\cdot\text{H}_2\text{O}$ occurs on the surface of the porous materials. A detailed description of the kinetics of $\text{LiOH}\cdot\text{H}_2\text{O}$ precipitation and growth will be presented below. The discharge product blocks the transport pathways and passivates the electrochemically active surface area. This has of course a negative feedback on transport and electrochemical reactions in GDE and separator. Transport restraints are intrinsically taken into account by the Bruggeman-Ansatz ((2.41)). Passivation of the electrode surface due to discharge products is modeled by a correction of the specific surface area which is also described in the following paragraph. Changes in volume fraction due to the formation or dissolution of solid products is modeled by [64]

$$\frac{\partial \varepsilon_k}{\partial t} = \bar{V}_k \sum_m (a_m^v r_{k,m}) = \bar{V}_k \dot{s}_k , \quad (4.46)$$

where \bar{V}_k is the molar volume of phase k . Convective or diffusive transport of solid phases is not considered in the current model.

Kinetics of precipitation and growth

The formation of the solid discharge product $\text{LiOH}\cdot\text{H}_2\text{O}$ is critical for a quantitative evaluation of the performance of aqueous Li-O₂ batteries as it limits the capacity of the cell. In the approach presented here the classical theory of nucleation and growth (CNG) is employed to derive expressions for the kinetics of the precipitation process [78]



The kinetic model was developed by Dr. Birger Horstmann in the context of the LuLi project [6] and parameters were adjusted in order to represent the conditions in the Ag/Ag₂O electrode. In the phenomenological approach it is assumed that the reaction

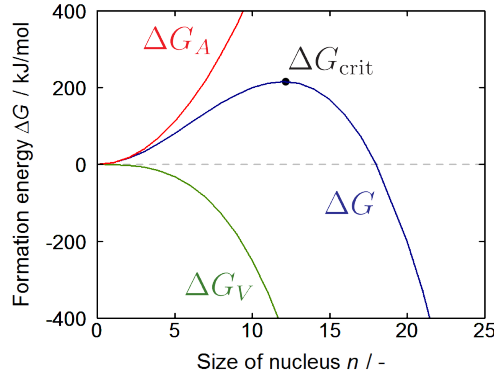


Figure 4.6.: Enthalpy for the formation of a single crystal nucleus of size n depending on a bulk (ΔG_V) and surface term (ΔG_A). The bulk term decreases with nucleus size and the surface term increases with nucleus size. As a result the combined formation enthalpy reaches a maximum at ΔG_{crit} .

enthalpy for the formation of a single crystal nucleus of size n depends on a bulk and a surface term

$$\Delta G = \Delta G_V + \Delta G_A = -2nk_B T \ln S + A(n)\gamma_A, \quad (4.47)$$

where γ_A is the macroscopic surface energy and the factor of 2 results from LiOH being a binary salt. The supersaturation of the solution S is the main driving force of the nucleation process. It is defined as the ratio between the concentration in the bulk and at the solubility limit $S = c_{\text{LiOH}}/c_{\text{LiOH}}^s$. At high supersaturation the reaction enthalpy of formation becomes increasingly negative and, thus, the formation of nuclei is favored.

Figure 4.6 shows the enthalpies of nucleus formation as function of nucleus size. The surface energy increases exponentially with nucleus size, while the bulk energy is decreasing. The latter is dominating at higher nucleus sizes, therefore, the enthalpy for nucleus formation goes through a maximum at the critical nucleus size n_{crit} with

$$\Delta G_{\text{crit}} = \frac{\pi\gamma_A^2 a^4}{2k_B T \ln S}. \quad (4.48)$$

The parameter $a = \bar{V}_{\text{cryst}}^{-1/3} N_A^{-1}$ is the typical length scale of the critical nucleus which is modeled as a disc-shaped particle.

The rate of the nucleation process is calculated according to

$$\dot{s}_N = D_{\text{LiOH}}^0 a_{\text{LiOH}}^{-2} Z N_0 e^{-\frac{\Delta G_{\text{crit}}}{k_B T}}, \quad (4.49)$$

where $D_{\text{LiOH}}^0 a_{\text{LiOH}}^{-2}$ describes the diffusion limitation of the nucleation process,

$$Z = \sqrt{\Delta G_{\text{crit}} / (3\pi k_B T) / n_{\text{crit}}}$$

is the so-called Zeldovich factor taking into account a disintegration of critical nuclei, N_0 is the number of nucleation sites, and the last term characterizes the activation of a critical complex due to thermal fluctuations. In the present configuration the precipitation on the surface of the electrode and separator will be dominant in comparison to a precipitation in the bulk of the solution [78]. In this case N_0 can be calculated from the initial specific surface area $a^{v,0}$ according to

$$N_0 = (a^{v,0} - a_{\text{cryst}}^v) a^{-2}, \quad (4.50)$$

where a_{cryst}^v is the specific surface area occupied by stable nuclei. As the actual growth mode of LiOH·H₂O on the electrode surface is not known a formation of disc-shaped nuclei is assumed. The specific surface area a_{cryst}^v follows by

$$\frac{\partial a_{\text{cryst}}^v}{\partial t} = \pi r_{\text{crit}}^2 \dot{s}_N(N_0). \quad (4.51)$$

Note, that N_0 is not constant during the nucleation process (Eq. (4.50)).

After the formation of the nucleus the crystals start to grow. In the simplest case the reaction rate of crystal growth is modeled by a linear term which is determined by the rate of diffusion to the nucleation site

$$r_{\text{cryst}} = \frac{D_{\text{LiOH}}^0}{\delta_{\text{cryst}}} (c_{\text{LiOH}} - c_{\text{LiOH}}^s), \quad (4.52)$$

4. Continuum modeling and simulation

where δ_{cryst} is the diffusion layer thickness. Although this model is relatively simple it is reported to give excellent results at high supersaturations which can be generally found in the case of the LiOH|H₂O system. The source term

$$\dot{s}_{\text{cryst}} = a_{\text{cryst}}^v r_{\text{cryst}} \quad (4.53)$$

can be inserted in Eq. (4.46) for the calculation of the volume fraction of the crystal phase.

4.2.3. Simulation methodology

For the numerical simulations outlined below the electrochemical modeling software DENIS [64, 207] is employed. Originally developed for the simulation of fuel cells [153, 207, 208] its ability to model the processes in Li-O₂ batteries [64, 78] was shown only recently. DENIS is coupled to the software package Cantera [209] for the calculation of (electro)chemical source terms and the DAE solver LIMEX [210] for time-integration of the set of equations. For the numerical simulation, all transport equations are discretized using a finite-volume approach in one dimension (denoted by y). The GDE is discretized with 30 non-uniform compartments. The smallest FV-compartments are located at the boundary to the electrolyte bath. Their width is chosen to 0.56 μm in order to resolve the penetration depth of the ac signal during impedance simulations (Eq. (2.45)). The electrolyte bath and separator are discretized with 10 and 20 equally-spaced FV-compartments, respectively. The coarse discretization of the electrolyte bath is justified by small gradients in electrolyte concentration and potential in the bath the discretization of the different layers and designs is summarized in Table 4.2.

In the experimental part electrochemical impedance spectra are recorded based on a sinusoidal excitation of the reference electrode potential at different frequencies. The same approach could also be used in the numerical simulation of impedance spectra. However, it is much more efficient to simulate the impedance spectra by a step excitation of potential and numerical integration of the current response instead of simulating each signal frequency separately [153]. The step function includes all relevant frequencies and resulting potential and current traces can be Fourier transformed to obtain the impedance spectra in the frequency domain. The lower and upper limit of the frequency range are in this approach given by the simulation time and sharpness of the excitation step,

respectively. In the present simulations the step in potential is conducted in $1 \cdot 10^{-5}s$ and the total integration time varies with the temperature of the solution. The minimum simulation time at 55 °C is $1 \cdot 10^3s$. Therefore, the accessible frequencies range from 100 kHz down to 1 mHz.

Impedance spectra are simulated at various potentials of the system. In accordance to the experimental procedure the system is polarized for 300 seconds at the potential of the upcoming measurement before the actual impedance simulation starts.

4.3. Results and discussion

4.3.1. Model parametrization

The model formulation as presented in Section 4.2 has already been parametrized and validated in previous publications of our group [78, 198]. The findings of the LBM simulations were not included at that time. Therefore, the model of the GDE in this work is re-parametrized based on the results presented in Chapter 3.3 regarding pore space saturation, effective transport, and active surface area.

The experimental data of the half-cell measurements is used for a parametrization of the kinetics of charge-transfer reactions and is also an excellent basis for model validation. The thermodynamic and transport parameters of the system are obtained from the literature on aqueous electrolytes.

Structural parameters of electrodes

The structural parameters of the half- and full-cell models are summarized in Table 4.2. The volume fractions and surface areas are initial values and might change during the simulations due to the formation of solid discharge product. The active surface areas in the GDE were determined in the LBM simulations in Section 3.3.3.

The initial saturation of the pore space is chosen in order to meet the condition of zero pressure difference between the bulk phases. The Leverett function is parametrized based

4. Continuum modeling and simulation

			A	B	C	D	E
High porosity	pristine	imbibition	0.1872	0.02523	8.707	0.09515	5.622
		drainage	-0.727	0.5577	2.995	0.01142	8.729
	reduced	imbibition	-0.4153	0.1609	5.814	0.009717	10.84
		drainage	-0.9794	0.4986	3.805	0.01159	10.3
Low porosity	reduced	imbibition	0.357	0.01127	10.75	0.01085	10.13
		drainage	-0.178	0.3996	3.101	0.003013	12.16

Table 4.1.: Parameters of the Leverett function according to Eq. (4.54).

on the LBM simulations presented in the previous chapter. An expression as proposed by Hao *et al.* [110] was shown to give a good representation of $J(s)$

$$J(s) = A + Be^{C(s-0.5)} - De^{-E(s-0.5)}. \quad (4.54)$$

The parameters of the different electrodes for the imbibition and drainage process are summarized in Table 4.1. In the continuum simulations the drainage curves are employed for the reduced low and high porosity electrodes. A temperature and concentration dependence of the Leverett function is implicitly taken into account by the surface tension [N/m] of LiOH solution [mol/l] against air [211, 212]

$$\begin{aligned} \sigma = & \left[235.8 \cdot 10^{-3} \left[\frac{\text{N}}{\text{m}} \right] \left(\frac{T_c - T}{T_c} \right)^{1.256} \left(1 - 0.625 \frac{T_c - T}{T_c} \right) \right] \\ & + 1.8 \cdot 10^{-3} \left[\frac{\text{N l}}{\text{m mol}} \right] c_{\text{LiOH}}, \end{aligned} \quad (4.55)$$

where $T_c = 647.15$ K is the critical temperature of water. The changes in surface tension are relatively small and the saturation stays almost constant at all temperatures and concentrations. Kumbur *et al.* [104] report a significant dependence on temperature. This is most likely a result of changes in the wetting properties (contact angle) which are not taken into account in the LBM simulations.

Transport in the liquid electrolyte

Transport in the liquid electrolyte is modeled by Eqs. (4.24), (4.23), and (4.17). The relevant parameters can be found in the extensive literature on aqueous electrolytes. In the correlations below the concentration c_i and molality m_i of species i have to be inserted

4.3. Results and discussion

		Half-cell		Full-cell
		High porosity	Low porosity	High porosity
Channel	Phases	Volume fraction	Volume fraction	Volume fraction
	Gas (O_2^g)	1	1	1
	Pressure	101 325 Pa	101 325 Pa	101 325 Pa
Cathode	Thickness	560 μm	480 μm	560 μm
	Compartments	30	30	30
	Surface area			
	O_2 dissolution	$7.5 \cdot 10^4 \text{ m}^{-1}$	$2.6 \cdot 10^5 \text{ m}^{-1}$	$7.5 \cdot 10^4 \text{ m}^{-1}$
	O_2 reduction	$6.4 \cdot 10^5 \text{ m}^{-1}$	$4.6 \cdot 10^5 \text{ m}^{-1}$	$6.4 \cdot 10^5 \text{ m}^{-1}$
	LiOH precipitation	-	-	$6.4 \cdot 10^5 \text{ m}^{-1}$
	Bruggeman coefficient	1.8	2.75	1.8
	Phases	Volume fraction / Pressure	Volume fraction / Pressure	Volume fraction / Pressure
	Gas (O_2^g)	0.199 / 101 325 Pa	0.299 / 101 325 Pa	0.199 / 101 325 Pa
	Electrolyte (H_2O , Li^+ , OH^- , O_2^{aq})	0.418 / 101 325 Pa	0.177 / 101 325 Pa	0.418 / 101 325 Pa
	LiOH· H_2O	0	0	0
Ag	0.383	0.524	0.383	
Separator	Thickness	10 cm	10 cm	100 μm
	Reference (L_{ref})	5 mm	5 mm	-
	Sample holder (L_{SH})	2 cm ($\gamma = 30^\circ$)	2 cm ($\gamma = 30^\circ$)	-
	Compartments	10	10	20
	Surface area			
	LiOH precipitation	-	-	$3 \cdot 10^5 \text{ m}^{-1}$
	Bruggeman coefficient	-	-	1.8
	Phases	Volume fraction	Volume fraction	Volume fraction
	Electrolyte (H_2O , Li^+ , OH^- , O_2^{aq})	1	1	0.8
	LiOH· H_2O	0	0	0
Polymer	0	0	0.2	
APL	Thickness	-	-	100 μm
	Compartments	-	-	10
	Phases	Volume fraction	Volume fraction	Volume fraction
	Li glass ceramic	0	0	1
Anode	Thickness	100 μm	100 μm	1 μm
	Compartments	1	1	1
	Phases	Volume fraction	Volume fraction	Volume fraction
	Pt metal	1	1	0
	Li metal	0	0	1
	Surface area			
	Li dissolution	-	-	$1 \cdot 10^6 \text{ m}^{-1}$
	O_2 dissolution	$1 \cdot 10^2 \text{ m}^{-1}$	$1 \cdot 10^2 \text{ m}^{-1}$	-
O_2 evolution	$2 \cdot 10^4 \text{ m}^{-1}$	$2 \cdot 10^4 \text{ m}^{-1}$	-	

Table 4.2.: Structural parameters of the geometries studied in this work. In the case of volume fractions and surface areas initial values are given which are subject to changes during the simulations.

4. Continuum modeling and simulation

in the units mol/l and mol/kg, respectively. The temperature T has to be given in K. The diffusion coefficients of OH^- in dilute solutions were measured by Littauer *et al.*. The range of concentrations and temperatures is extended by using the Stokes-Einstein relation which predicts a scaling of diffusion coefficients according to viscosity μ [213]. It is assumed that Li^+ and OH^- diffuse with the same velocity in the solvent due to electro-neutrality. The expression for the diffusion coefficient [m²/s] is given by

$$\begin{aligned}
 D_{\pm} &= 6.8 \cdot 10^{-9} \left[\frac{\text{m}^2}{\text{s}} \right] \frac{\mu_{\text{H}_2\text{O}}}{\mu_{\text{elyte}}} \frac{T}{298.15} (8.90466 \cdot 10^{-4} \left[\left(\frac{\text{kg}}{\text{mol}} \right)^4 \right] m_{\text{LiOH}}^4 \\
 &- 1.27732 \cdot 10^{-2} \left[\left(\frac{\text{kg}}{\text{mol}} \right)^3 \right] m_{\text{LiOH}}^3 + 5.38298 \cdot 10^{-2} \left[\left(\frac{\text{kg}}{\text{mol}} \right)^2 \right] m_{\text{LiOH}}^2 \\
 &- 3.81098 \cdot 10^{-2} \left[\frac{\text{kg}}{\text{mol}} \right] m_{\text{LiOH}} + 8.56882 \cdot 10^{-1} , \tag{4.56}
 \end{aligned}$$

where $\mu_{\text{H}_2\text{O}}$ and μ_{elyte} are the viscosities of pure water and electrolyte solution, respectively [213]. Similarly the diffusion coefficient of O_2 [m²/s] in pure water [214] is extended to LiOH solutions at various concentrations according to

$$D_{\text{O}_2} = 1.693 \cdot 10^{-6} \left[\frac{\text{m}^2}{\text{s}} \right] \frac{\mu_{\text{H}_2\text{O}}}{\mu_{\text{elyte}}} \exp \left(- \frac{16739[\text{J/mol}]}{RT} \right) . \tag{4.57}$$

The ionic conductivity [S/m] of the aqueous electrolyte is obtained from a fit to data published in the literature and the measurements presented in Chapter 2.3.2

$$\begin{aligned}
 \sigma_{\text{elyte}} &= (-3.83584 \left[\frac{\text{S}}{\text{m}} \right] + 0.01363 \left[\frac{\text{S}}{\text{m K}} \right] T) \\
 &+ (-49.6837 \left[\frac{\text{S l}}{\text{m mol}} \right] + 0.2193 \left[\frac{\text{S l}}{\text{m mol K}} \right] T) c_{\text{LiOH}} \\
 &+ (1.54934 \left[\frac{\text{S l}^2}{\text{m mol}^2} \right] - 0.01038 \left[\frac{\text{S l}^2}{\text{m mol}^2 \text{K}} \right] T) c_{\text{LiOH}}^2 . \tag{4.58}
 \end{aligned}$$

The conductivity in the Li ion conducting glass ceramic is taken from Ref. [79] to $\sigma_{\text{APL}} = 2.5 \cdot 10^{-2}$ S/m. Last unknown transport parameter is the transference number t_+ of Li^+ . For an infinitely dilute solution t_+ can be calculated as

$$t_+ = (1 - t_-) = \frac{\lambda_{\text{Li}^+}^0}{\lambda_{\text{Li}^+}^0 + \lambda_{\text{OH}^-}^0} = 0.1637 , \tag{4.59}$$

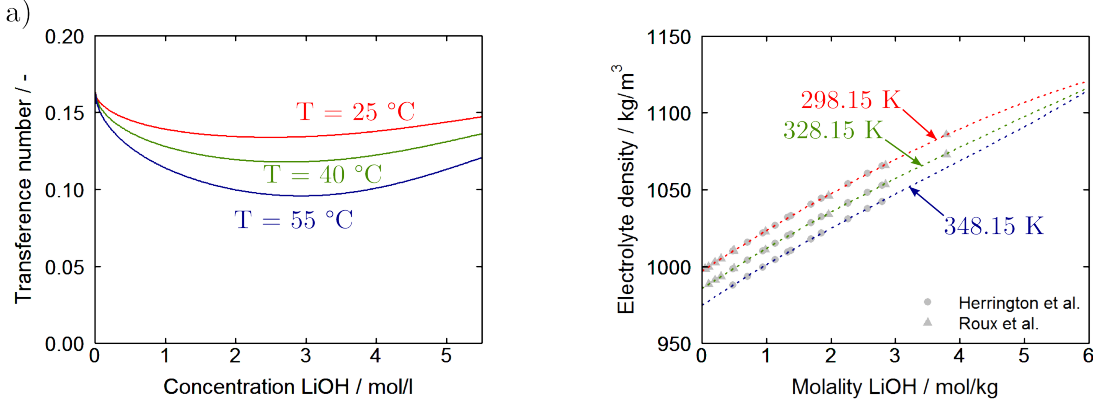


Figure 4.7.: Transference number (left) and electrolyte density (right) as function of c_{LiOH} and T . Transference numbers are calculated according to Eq. (4.60) and consistently reach a limit of 0.1637 in infinite dilution. The electrolyte density is calculated from the partial molar volumes with the coefficients as summarized in Table 4.3.

where λ_i^0 is the limiting molar conductivity of Li^+ and OH^- [62] at standard conditions. Transference numbers at other temperatures and concentrations can be derived based on Debye-Hückel theory [215, 216]. For an univalent electrolyte the transference number is calculated according to

$$t_+ = \frac{\lambda_{\text{Li}^+} - 0.5A\sqrt{c/(\kappa r_{\text{hd}})}}{\lambda_{\text{Li}^+} + \lambda_{\text{OH}^-} - A\sqrt{c/(\kappa r_{\text{hd}})}}, \quad (4.60)$$

where $\kappa = \sqrt{c_{\text{LiOH}} \frac{8\pi z^2 F^2}{\epsilon RT}}$ is the inverse Debye length, $A = 82.5/(\mu_{\text{elyte}} \sqrt{\epsilon_{\text{LiOH}} T})$, and $r_{\text{hd}} = k_{\text{B}}T/(6\pi\mu_{\text{elyte}}D_{\pm})$ the hydrodynamic radius. The dependence of transference number on c_{LiOH} and T is shown in Figure 4.7 a). At infinite dilution the transference number reaches the value of 0.1637. It decreases towards higher concentrations and then slightly increases again due to an increase in the solution viscosity μ_{elyte} and permittivity ϵ_{LiOH} .

The derivative of the chemical potential with respect to concentration which is needed in the calculation of the diffusional conductivity can be calculated using the expressions for LiOH activity presented in the following sections.

Convective transport in the liquid electrolyte depends on the pressure gradient as described by Darcy's law (Eq. (2.42)). The pressure gradient is caused by changes in the electrode porosity and electrolyte density. The density of the liquid electrolyte is calculated from the

4. Continuum modeling and simulation

partial molar volumes of its components (Eq. (4.39)). The partial molar volumes of H_2O , Li^+ , and OH^- were fitted to experimental data [217, 218] by Dr. Birger Horstmann using the so-called Pitzer formalism [78, 219]. This is possible since the partial molar volume is given by $V_i = \partial\mu_i/\partial p$. The parameters of the temperature dependent polynomials are summarized in Table 4.3 and more detailed information about the Pitzer formalism can be found in appendix A. The partial molar compressibility of LiOH is parametrized for data of NaOH solution according to Millero *et al.* [220]. In the limit of infinite dilution the partial molar compressibility is exchanged with data from measurements of Roux *et al.* [218]. The resulting correlations [$\text{m}^3/\text{mol}/\text{Pa}$] are given by

$$\begin{aligned}
 \kappa_{\text{LiOH}} &= -6.89 \cdot 10^{-14} \left[\frac{\text{m}^3}{\text{mol Pa}} \right] + 1.5\sqrt{m_{\text{LiOH}}} 6.63 \cdot 10^{-15} \left[\frac{\text{m}^3 \text{kg}^{0.5}}{\text{mol}^{1.5} \text{Pa}} \right] \\
 &+ 2m_{\text{LiOH}} 7.16 \cdot 10^{-15} \left[\frac{\text{m}^3 \text{kg}}{\text{mol}^2 \text{Pa}} \right] \\
 \kappa_{\text{H}_2\text{O}} &= -4.4773 \cdot 10^{-10} \left[\frac{1}{\text{Pa}} \right] V_{\text{H}_2\text{O}}^0 \\
 &- 0.0180 \cdot (3.315 \cdot 10^{-15} \left[\frac{\text{m}^3 \text{kg}^{1.5}}{\text{mol}^{2.5} \text{Pa}} \right] m_{\text{LiOH}}^{1.5} \\
 &- 7.16 \cdot 10^{-15} \left[\frac{\text{m}^3 \text{kg}^2}{\text{mol}^3 \text{Pa}} \right] m_{\text{LiOH}}^2) .
 \end{aligned} \tag{4.61}$$

Figure 4.7 b) shows the density of the electrolyte solution as function of LiOH concentration. The symbols represent the experimental data which is scarce at higher concentrations and some deviation can be expected. As the concentration of O_2 in the electrolyte is very low its contribution to the electrolyte density is neglected.

Another important parameter for the convective transport in porous media is the permeability. In the LBM simulations the permeability of the GDE has been determined as function of electrolyte saturation. It was found to be in good agreement with the predictions of the Kozeny-Carman correlation (Eq. (3.51)). Therefore, this correlation is employed for the calculation of saturation dependent permeability and the effective particle diameter d_p is adjusted to match the permeability at full saturation. In the case of the reduced high- and low-porosity electrode the diameter is found to be 3.225 and 1.25 μm , respectively. In the porous separator of the full-cell setup the effective diameter is set to 7.35 μm .

n	$V_{\text{Li}^+}^0$	$MW_{\text{H}_2\text{O}}/V_{\text{H}_2\text{O}}^0$	$\partial A^\phi/\partial p$	$\partial\beta_0^\phi/\partial p$	$\partial\beta_1^\phi/\partial p$	$\partial C^\phi/\partial p$
-1	0	0	$-2.4374\cdot 10^{-7}$	0	0	0
0	$7.3146\cdot 10^{-5}$	$-5.5855\cdot 10^3$	$3.7765\cdot 10^{-9}$	$-7.2178\cdot 10^{-10}$	$-5.4432\cdot 10^{-9}$	$4.3352\cdot 10^{-10}$
1	$-7.5328\cdot 10^{-7}$	$9.3239\cdot 10^1$	$-2.3333\cdot 10^{-9}$	$2.8338\cdot 10^{-12}$	$4.3584\cdot 10^{-11}$	$-1.4049\cdot 10^{-12}$
2	$2.5245\cdot 10^{-9}$	$-5.2950\cdot 10^{-1}$	$6.3087\cdot 10^{-14}$	0	$-8.3883\cdot 10^{-14}$	0
3	$-2.8374\cdot 10^{-12}$	$1.5138\cdot 10^{-3}$	$-6.7886\cdot 10^{-17}$	0	0	0
4	0	$-2.1816\cdot 10^{-6}$	0	0	0	0
5	0	$1.2614\cdot 10^{-9}$	0	0	0	0

Table 4.3.: Pitzer parameters for the electrolyte volume, fitted to polynoms $g = \sum_n g_n(T/[K])^n$ [78].

Electrochemical reactions

The kinetic parameters of the ORR follow from the Tafel analysis as presented in Section 2.3.2. Following the law of mass action kinetics (Eq. (4.7)) the rate expression for the ORR is in the present framework given by

$$r_{\text{ORR}} = k_f c_{\text{O}_2} c_{\text{H}_2\text{O}}^2 \exp\left(-\frac{\beta_{\text{ORR}} z F}{RT} \Delta\Phi\right) - k_r c_{\text{OH}^-}^4 \exp\left(\frac{(1 - \beta_{\text{ORR}}) z F}{RT} \Delta\Phi\right). \quad (4.62)$$

The equation for the Faradaic current follows after multiplication with nF as

$$i_{\text{F}} = 4F \left(k_f c_{\text{O}_2} c_{\text{H}_2\text{O}}^2 \exp\left(-\frac{\beta_{\text{ORR}} z F}{RT} \Delta\Phi\right) - k_r c_{\text{OH}^-}^4 \exp\left(\frac{(1 - \beta_{\text{ORR}}) z F}{RT} \Delta\Phi\right) \right). \quad (4.63)$$

In the limit of high overpotentials (Tafel analysis) the back-most part of Eq. (4.63) can be neglected

$$i_{\text{F}} = 4F k_f(T) c_{\text{O}_2} c_{\text{H}_2\text{O}}^2 \exp\left(-\frac{\beta_{\text{ORR}} z F}{RT} \Delta\Phi\right) \quad (4.64)$$

and the exchange current density i_0 is defined by

$$i_0 = 4F k_f(T) c_{\text{O}_2} c_{\text{H}_2\text{O}}^2. \quad (4.65)$$

Values for i_0 and β_{ORR} at 25, 40, and 55 °C are summarized in Table 2.5. The rate constant $k_f(T)$ can be determined from Eq. (4.65). An Arrhenius plot (Figure 4.8 a)) of k_f over $1/RT$ yields the pre-exponential factor $k_{f,\text{ORR}}^0 = 4.955 \cdot 10^{-3} \text{ m}^6/\text{kmol}^2/\text{s}$ and activation energy $E_{\text{ORR}}^a = 21.755 \text{ kJ/mol}$. For the simulations a temperature average

4. Continuum modeling and simulation

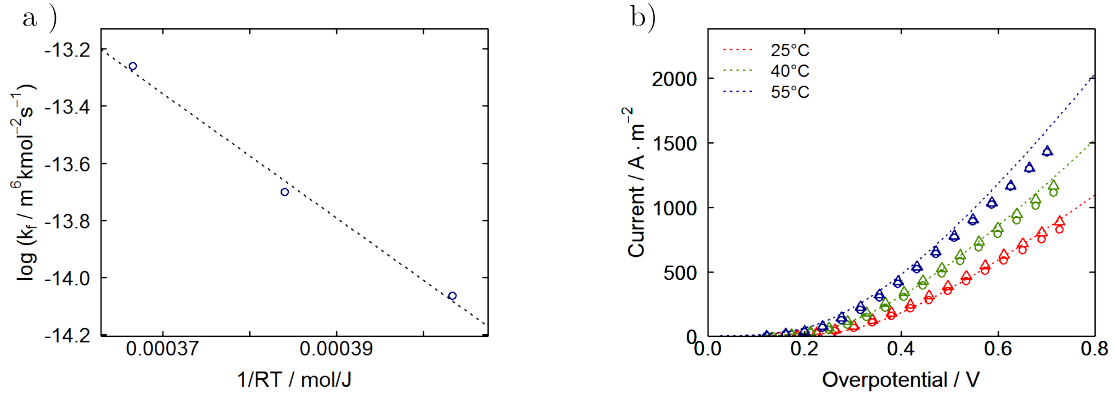


Figure 4.8.: a) Arrhenius plot of the rate constants of the ORR as determined in the Tafel analysis. b) IV curves of the reduced Ag electrode in 1M LiOH solution. Symbols represent the experimental data and dashed lines are results of the simulations with kinetic parameters as determined from the Arrhenius plot.

value of $\beta_{\text{ORR}} = 0.1495$ is employed. The thermodynamic data presented in the following sections is used to determine the rate constant of the backward reaction k_b according to Eq. (4.9). The same set of parameters is used for the calculation of O_2 evolution rates at the Pt anode of the half-cell setup.

The dissolution kinetics of Li at the anode of the full battery cell are chosen to $k_{f,\text{Li}}^0 = 3.84 \cdot 10^{15} \text{ mol/m}^2/\text{s}$ with $\beta_{\text{Li}}=0.5$. As an approximation the same rate constant is used at all temperatures ($E_{\text{Li}}^a=0$).

Figure 4.8 b) shows simulated (dashed line) and experimental (symbols) IV curves in 1M LiOH solution. The excellent quantitative agreement between simulation and experiment demonstrates that the results obtained in the Tafel analysis are relatively accurate. This shows that an iR -correction (Eq. (2.50)) of the experimental data for mass transport losses compensates potential systematic errors.

Double layer capacitance

Upon characterization under transient conditions (CV, EIS), the electric double layer at the electrode-electrolyte interface leads to additional capacitive currents. In the data obtained from the fit to the equivalent circuit model the double layer capacitance decreases continuously with overpotential and approaches a constant value at high overpotentials. This is explained by taking into account the structure of the double layer which becomes

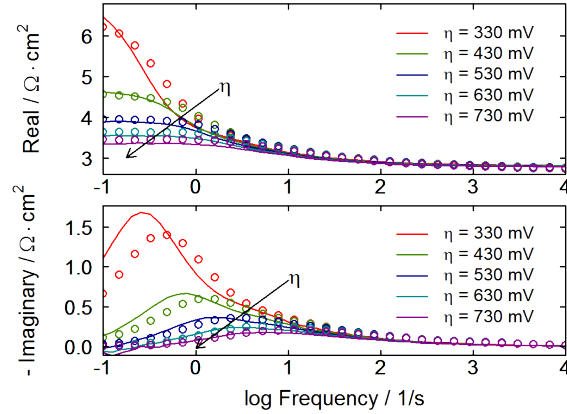


Figure 4.9.: Bode plots of impedance spectra in 1 M LiOH solution at 40 °C and various overpotentials. Symbols represent the experimental data and dashed lines show the results of the continuum simulations. The graph demonstrates the validity of the model of the electric double layer.

more compact at high polarization (cf. capacitance in Figure 2.19). In the limit of high overpotentials the double layer is assumed to behave similar to a parallel-plate capacitor. The area-specific capacitance c_{dl} of an ideal parallel-plate capacitor was introduced in Eq. (2.28) according to

$$c_{dl} = \frac{\epsilon^0 \epsilon_{\text{elyte}}}{\delta_{dl}},$$

where ϵ_{elyte} is the dielectric constant of the solution, $\epsilon^0 = 8.85 \cdot 10^{-12}$ F/m the permittivity of vacuum and δ_{dl} the thickness of the double layer. In lack of experimental data for LiOH the dielectric constant is parametrized for data on NaOH solution [221, 222]. The double layer thickness δ_{dl} is the only remaining parameter of the capacitance model. It can be determined by a fit to the experimental impedance spectra at high overpotential (cf. dotted line in Figure 2.19 b)). Figure 4.9 shows a Bode plot of simulated and experimental impedance spectra [198] in 1 M LiOH solution at 40 °C. In a Bode plot, the relaxation time $\tau = R_{ct} c_{dl}$ of the charge-transfer process corresponds to the frequency at the maximum of the imaginary part (cf. maximum in Figure 2.15). The position of the simulated maxima in Figure 4.9 agrees fairly well with the experiments. The corresponding double layer thickness δ_{dl} was previously [198] determined to 5.0 Å. In the present model which uses a revised set of structural parameters δ_{dl} is adjusted for the change in specific surface area of the electrode-electrolyte interface. A change of a_{ORR}^v from $3.3 \cdot 10^6$ to $5.4 \cdot 10^5$ m⁻¹

4. Continuum modeling and simulation

	Species	h^\ominus / kJ/mol	s^\ominus / J/mol/K	c_p^\ominus / J/mol/K
Ag/Ag ₂ O ($\rho = 10490/7140$ kg/m ³)	Ag	0.0	42.55	25.351
	Ag ₂ O	-31.05	121.3	65.86
Electrolyte (ρ from Table 4.4)	H ₂ O	-285.83	69.91	75.291
	Li ⁺	-278.49	13.4	68.6
	OH ⁻	-229.99	-10.75	-148.5
	O ₂ ^{aq}	-12.033	166.95	209.35
LiOH·H ₂ O ($\rho = 1510$ kg/m ³)	LiOH·H ₂ O	-787.07	83.352	9.7674
APL ($\rho = 3044$ kg/m ³ [223])	-	-	-	-
Li ($\rho = 534$ kg/m ³)	Li	0.0	29.12	0.0

Table 4.4.: Thermodynamic data of phases and contained species in the standard state. The data is either taken from Ref. [224] or determined by a fit to experimental data.

gives a modified thickness of 0.97 \AA which corresponds to the radius of an OH⁻ molecule and, thus, to the IHP. c_{dl} can be extrapolated to other salt concentrations by using the correlations for ϵ_{elyte} given in Refs. [221, 222].

LiOH precipitation

During discharge of a full battery cell the concentration of LiOH in the liquid electrolyte rises until it reaches its solubility limit. Monnin *et al.* [225] present a review of thermodynamic data [226] and solubility [227, 228] for the LiOH|H₂O system. The authors employ the Pitzer formalism [219] for a temperature and concentration dependent description of LiOH activity coefficients as shown in Figure 4.10 a). The data can be utilized in order to determine h^\ominus , s^\ominus , and c_p^\ominus of the precipitation product LiOH·H₂O by fitting the solubility of LiOH at varying temperature. The mathematical fitting criterion is given by the minimum of the Gibbs enthalpy in thermodynamic equilibrium as introduced in Chapter 2.1. As the temperature range of the battery during operation is relatively small the heat capacity is assumed to be constant. Figure 4.10 b) shows the LiOH solubility as function of concentration. Symbols present the experimental data from the literature [227, 228] and the solid line is the result of the fit of the thermodynamic parameters of LiOH·H₂O. Thermodynamic parameters are summarized in Table 4.4.

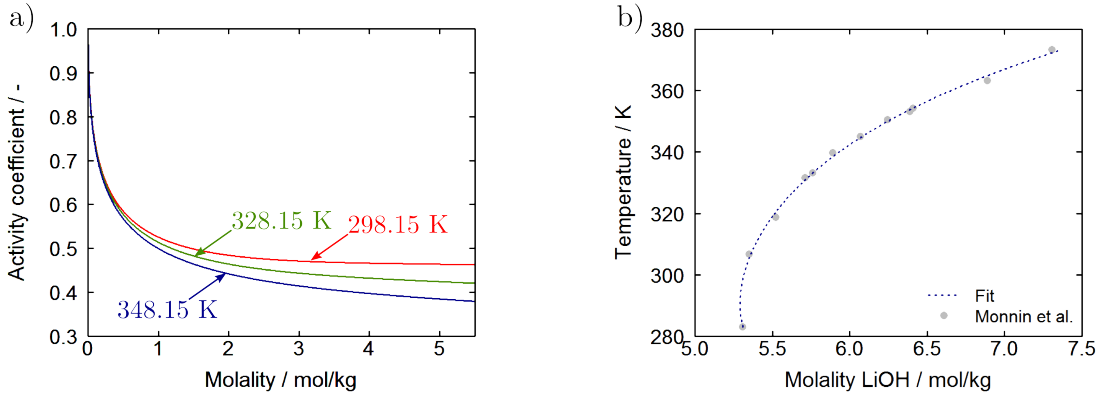


Figure 4.10.: a) Activity coefficient [225] as function of concentration. b) Solubility limit of LiOH in water at temperatures between 280 and 370 K. Symbols represent experimental data [225, 227, 228] and the solid line is the result of the fit of thermodynamic data for $\text{LiOH}\cdot\text{H}_2\text{O}$.

The kinetics of the precipitation process are derived in Section 4.2. Remaining parameters of the model are the surface energy of $\text{LiOH}\cdot\text{H}_2\text{O}$ and the thickness of the diffusion layer δ_{crystal} . The surface free energy is taken from the theoretical work of Mersmann *et al.* [229]

$$\gamma_A = -0.414 \frac{k_B T}{a^2} \ln(c_{\text{LiOH}}^s V_{\text{LiOH}\cdot\text{H}_2\text{O}}^M). \quad (4.66)$$

It is in good agreement with the data of Nielsen *et al.* fitted to experiments [230]. The typical diffusion layer thickness δ_{crystal} is chosen to 10 μm .

Solubility of O_2

Experimental studies show that the solubility of O_2 decreases with increasing salt concentration. This is an effect also known as salting-out [231, 232]. Commonly, the solubility of gases is given by the Henry coefficient. In the approach presented here, the dissolution process is modeled as a chemical reaction (Eq. (4.33)) in which the condition of chemical equilibrium is given by

$$\mu_{\text{O}_2}^g = \mu_{\text{O}_2}^{\text{aq}}. \quad (4.67)$$

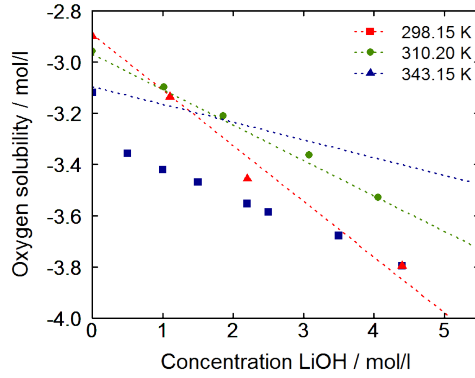


Figure 4.11.: O_2 solubility as function of LiOH concentration. Symbols present experimental data [231, 232] from the literature and the solid lines represent a fit via the empirical Setchenov relation.

The chemical potential of O_2 in the gas phase is calculated with a 7 coefficient NASA polynomial [233]. The data of O_2 in the solution has to be determined by a fit to experimental data from the literature. First, the thermodynamic data in pure water at standard conditions is parametrized based on the data reviewed by Tromans [234] (Table 4.4). In a second step the activity of O_2 as function of salt concentration and temperature is obtained from the solubility data of Elliot and Lang *et al.* [231, 232]. It is described by

$$a_{O_2}^{\text{aq}} = \gamma_{O_2} c_{O_2} = e^{\left(\frac{0.01057}{T-277}\right) c_{\text{LiOH}})} c_{O_2}, \quad (4.68)$$

where γ_{O_2} is the activity coefficient of O_2 which is modeled by the empirical Setchenov relation.

Figure 4.11 shows O_2 solubility as function of LiOH concentration at temperatures of 25, 37, and 70 °C. The data of Elliot agrees well with the Setchenov relation, however, there is some deviation to the data of Lang at high temperatures. Still, the trends are described correctly by the relation proposed above.

The kinetics of the dissolution process are modeled by the Hertz-Knudsen equation

$$k_{f,O_2} = 0.01 \frac{1}{\sqrt{2\pi M_{O_2} RT}}, \quad (4.69)$$

where the pre-factor of 0.01 takes into account that only 1% of all molecules colliding with the phase boundary are actually absorbed in the liquid electrolyte.

4.3.2. Model validation

The model for transport in a porous GDE as presented above is validated against electrochemical measurements in the half-cell setup. The model in its current mathematical form was already validated in a previous publication [198]. Compared to this previous work the structural parameters are adjusted to take into account the findings of the LBM simulations.

Cyclic Voltammetry

Similar to the experiments a potential sweep is simulated at a scan rate of 1 mV/s. Both experiments and simulations show a stationary behavior at these low scan rates, therefore, results are presented as IV curves. In Figure 4.12 IV curves of measurements and simulations for various temperatures are compared. The kinetic data was extracted at a concentration of 1M. The good quantitative agreement with the experimental data at other concentrations proves the validity of the model.

The model slightly overpredicts current densities at high overpotentials as already seen in Section 4.3.1. This indicates that relevant rate-limiting processes at high overpotentials and currents are not fully represented in the current model. Pinnow *et al.* [74] report a change in the apparent Tafel slope of their experiments on silver GDEs in NaOH solution. They explain it with a possible change in the adsorption isotherm of reaction intermediates and use a second Tafel slope at high overpotentials. Similar observations for Pt catalysts in alkaline media [131, 235] support this assumption. In the present model one single-step charge-transfer reaction is used to describe the kinetics at all concentrations, temperatures and overpotentials. A more rigorous elementary kinetic description of the ORR could give some additional insights on this topic [75, 208, 236]. However, such a detailed treatment of kinetics is out of the scope of this work which mainly investigates transport phenomena of porous electrodes.

Similar changes in the slope of the IV curve are also reported for PEMFCs [237, 238]. This effect is attributed to a limited supply of O₂ through a thin film of ionomer on

4. Continuum modeling and simulation

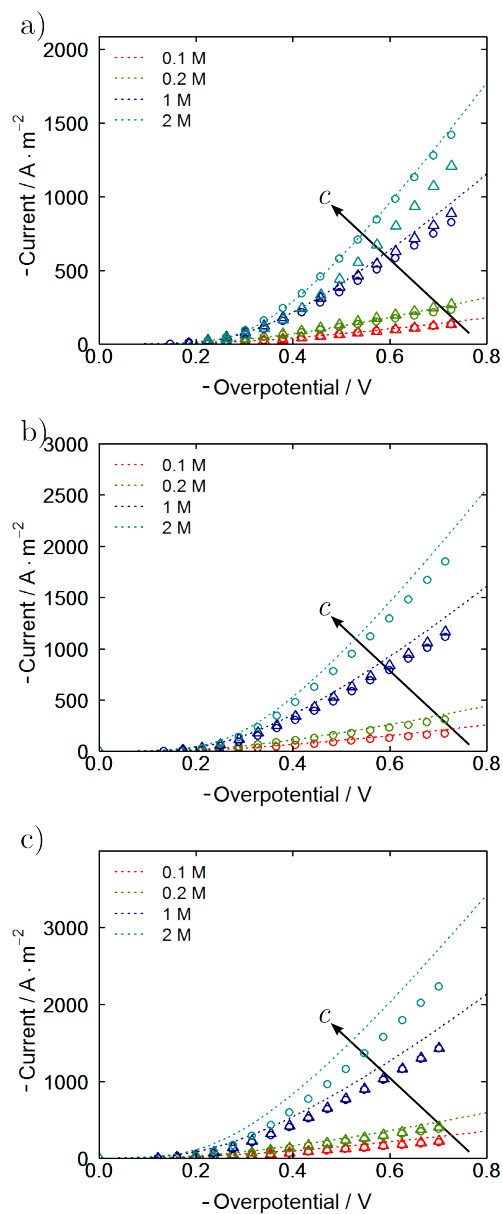


Figure 4.12.: IV curves in aqueous LiOH solution. The concentration of electrolyte solution was varied between 0.1 and 2 M. Graphs a) to c) show a comparison between simulation (dashed lines) and experiment (symbols) at 25, 40 and 55 °C, respectively. Two sets of experiments at the same conditions were conducted as a check for reproducibility (open circles and triangles).

the electrode surface. The nature of this additional transport resistance is not yet fully understood and subject of ongoing research. Suzuki *et al.* show that the dissolution of O₂ in the ionomer might be the rate-limiting step [238]. However, this observation could not be confirmed for the aqueous system (cf. sensitivity analysis in Section 4.3.3).

In the case of a limiting transport of O₂ smaller deviations of the IV curves should be expected at low concentrations as the solubility and diffusivity of O₂ in the electrolyte are generally higher in this regime [78, 231, 232]. However, also here the same discrepancy to the experiments is observed. This suggests that a resistance affecting all transport processes is more likely. A possible explanation is an over-prediction of the GDE saturation. This effect is investigated in more detail in the following paragraphs.

Still, the transport of O₂ might be limiting at high overpotentials and currents. In the literature, flooded agglomerate models are suggested to include the transport of O₂ in the agglomerate and electrolyte film [74, 238] (cf. Figure 4.4). This approach will be pursued in a following section. However, it requires an additional parametrization of the model with structural quantities of the agglomerate.

Electrochemical impedance spectroscopy

Although an excellent agreement could be reported for IV curves in the previous paragraph, there is some deviation between simulation and experiment for electrochemical impedance spectra. Impedance spectra from simulation and experiment are shown in Figure 4.13 for various conditions. Overall, simulations and experiments are in a good qualitative agreement and all trends described in the experimental part (Section 2.3.2) can also be found in the simulated spectra. It has to be stressed that only one set of physical parameters is used for the simulations at all experimental conditions. This is an important difference to equivalent circuit models, where each spectrum is fitted individually.

The continuum model reproduces the characteristic shape of impedance spectra of porous electrodes in the complex plane. Its features are described in detail in Section 2.3.2. The intersection with the real axis is in good agreement for experiments and simulations at high concentrations. At lower concentrations minor deviations of the simulated data can be observed. This is attributed to a lower accuracy of the fit of ionic conductivity in this region (cf. parametrization of σ_{elyte} in Section 4.3.1). At lower frequencies the depressed semi-circle closes into a straight line with a slope of 45°, originating from transport and reaction in the porous electrode.

4. Continuum modeling and simulation

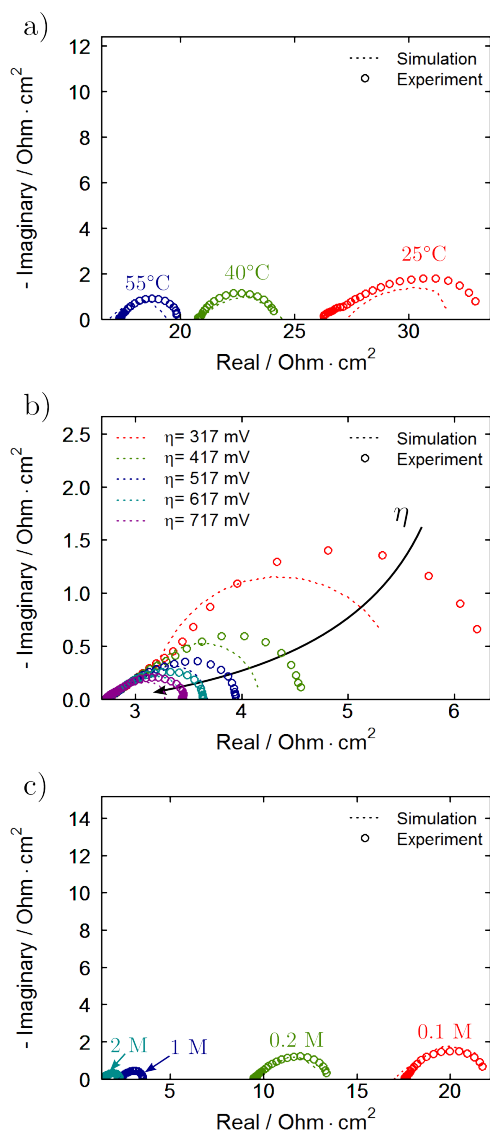


Figure 4.13.: Impedance spectra of the Ag electrode in the complex plane at various conditions. Symbols represent the experimental data and dashed lines are the results of the impedance simulations of the continuum model. a) Spectra in 0.1 M solution and a potential of 600 mV vs. RHE. b) Series of spectra at various overpotentials in 1 M solution and at a temperature of 40°C. c) Spectra at 25 °C and a potential of 800 mV vs. RHE.

The simulated polarization resistance is generally smaller than in the measurements. Only at low concentration and temperature the simulated impedance is slightly larger. This is a difference to the model presented in our previous publication [198]. In this case the polarization resistance of the GDE was under-predicted only at high temperatures and overpotentials. Since, in comparison to the previous model only structural parameters and saturation properties were changed, this suggests that the saturation in the pore space is probably too high. This topic will be revisited in Section 4.3.3.

Variation of electrode structure

In this work two different batches of Ag/Ag₂O electrodes are investigated regarding their electrochemical and structural properties, one having a slightly higher porosity compared to the second one which is prepared at a higher compression in the production process. Most of the experimental work described in Chapter 2 was done on the high-porosity GDE. Therefore, also the model parametrization and validation focuses on this batch of electrodes. It is now interesting to see if the model is also able to predict the performance of the low-porosity electrode.

For an easier comparison Figure 4.14 a) shows measurements and simulations of the high-porosity electrode at 25, 40, and 55°C in 1 M LiOH solution. Figure 4.14 b) presents IV curves of the low-porosity GDE at 25 and 50°C. The solid lines present the results of the standard model as validated in the previous sections. In the simulations of the dense electrode the structural parameters and wetting properties are adjusted according to the results of the LBM simulations. The adjusted model is able to qualitatively reproduce the experimental trends, however, the quantitative agreement is not fully satisfying. At small overpotentials the simulated currents are smaller than in the experiments whereas at high overpotentials they are over-predicted by the model. A similar trend is also observed for the high-porosity electrode, however, in the denser structure the effect is obviously amplified. The results indicate that important limiting factors are not taken into account correctly. A possible mechanism is a transport limitation in the liquid electrolyte on and in the electrode particles.

A simple model which takes into account liquid phase transport in the agglomerate is the concept of the effectiveness factor as introduced in Section 4.2. During the reduction process of the GDE from Ag₂O to Ag oxygen is evolved which leads to micro- and mesoporous electrode particles. It is assumed that the porosity of the particles is around

4. Continuum modeling and simulation

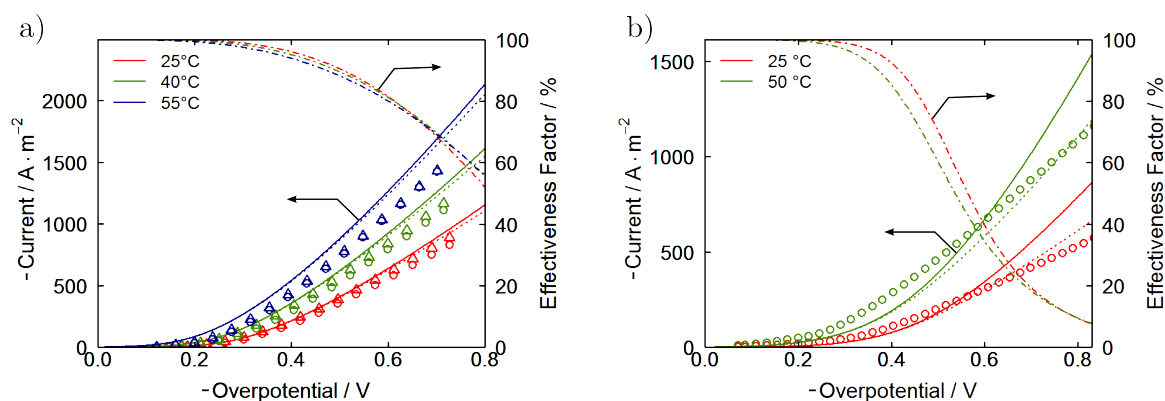


Figure 4.14.: IV curves of the high-porosity GDE (left) and low-porosity GDE (right) in 1M LiOH. Symbols represent the experimental data and dashed or solid lines are results of the simulations with and without taking into account the model for flooded agglomerates, respectively.

30% which is given by the density ratio between $\text{Ag}/\text{Ag}_2\text{O}$. Effective transport parameters are calculated with a standard Bruggeman coefficient of 1.5 and the agglomerate radius is estimated from the SEM images to around 4 μm .

Dotted lines in Figure 4.14 show results of simulations taking into account the additional transport resistance in the agglomerate. The dashed-dotted lines present the average effectiveness factor in the cathode. In the case of the high-porosity electrode (Figure 4.14 a)) the impact of the agglomerate model is rather small. Transport effects become prominent only at overpotentials larger than 0.4 V and the average effectiveness factor is still more than 50% even at the highest overpotential and temperature.

However, in the low-porosity GDE the effect is more pronounced and the inclusion of transport limitations in the agglomerate improves the agreement with the experiments considerably. The average effectiveness factor is less than 10 % at high overpotentials. It is generally lower at the interface of the GDE and the electrolyte bath which causes an enlargement of the ORR reaction zone towards the gas inlet.

Still, the additional transport resistance in the agglomerate is not able to explain the deviations in electrochemical impedance spectra reported in the previous paragraph. Figure 4.15 presents spectra of the high-porosity electrode in 1M LiOH solution at a temperature of 40 °C and potentials between 900 and 500 mV vs. RHE. Only a small increase in polarization resistance can be observed in simulations using the flooded agglomerate model

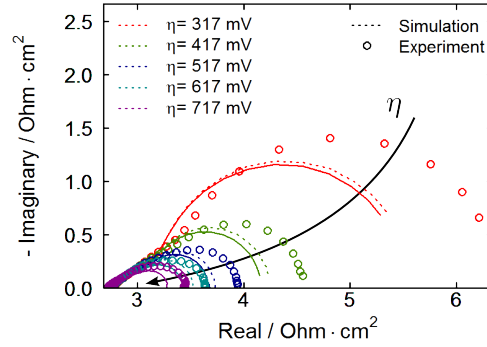


Figure 4.15.: Impedance spectra of the high-porosity GDE in 1M LiOH at 40 °C. Symbols represent the experimental data and dashed or solid lines are results of the simulations with and without taking into account the model for flooded agglomerates, respectively.

(dashed lines). This result indicates that additional rate-limiting effects are responsible for the deviations in the frequency domain.

4.3.3. Electrode design

The detailed physical model of the GDE is in excellent qualitative agreement with the experimental data which allows a determination of important design parameters. In a first step a sensitivity analysis is performed which is able to identify the rate-limiting electrode parameters at different overpotentials. The most important parameters will be discussed in more detail in the following paragraphs.

Sensitivity analysis

A sensitivity analysis of the validated continuum model is performed in order to identify the most important physico-chemical processes. The relative sensitivity s_{ζ} of the current density i on the change of parameter ζ is given by

$$s_{\zeta} = \frac{(i - i^0)/i^0}{(\zeta - \zeta^0)/\zeta^0} . \quad (4.70)$$

The parameters are varied individually by 5% of their original value (indicated by superscript 0). Sensitivities are calculated at 300, 500 and 700 mV overpotential. A sensitivity

4. Continuum modeling and simulation

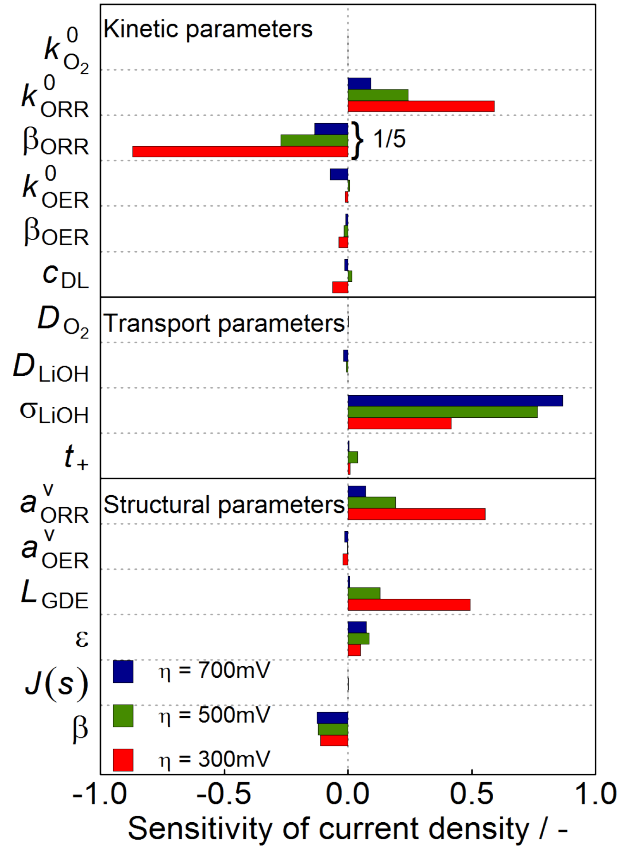


Figure 4.16.: Sensitivity analysis (Eq. (4.70)) at 300, 500, and 700 mV overpotential. Upper part: kinetic parameters, middle part: transport parameters, bottom part: geometrical parameters. The sensitivity of β_{ORR} is divided by a factor 5 for convenience.

close to zero indicates parameters with only a small impact, whereas a high sensitivity reveals a limiting influence on the system performance. A sensitivity of unity means direct proportionality between the varied parameter and the current.

Results of the sensitivity analysis in 1 M LiOH at 25 °C are shown in Figure 4.16. The parameters are grouped according to their effect on physical processes. The first part shows kinetic parameters, the second part transport parameters and the third part geometrical parameters. In the following discussion an emphasis is put on the structural parameters, which are important design variables for the future development of GDEs.

The **kinetic parameters** of the GDE show the highest impact on the system performance. This highlights the need for the development of novel catalysts [76, 86–88]. Especially the symmetry factor of the ORR exhibits the highest sensitivity of all parameters. Kinetic

parameters of the anode show a negligible sensitivity. This is expected in the simulated three-electrode setup and confirms the model assumptions at the counter electrode (Section 4.2). The dynamics of the O_2 dissolution at the cathode are represented by the rate constant of the reaction $k_{\text{O}_2}^0$. Even at high overpotentials and currents no limiting effect of the O_2 dissolution could be observed in the present reaction model based on the Hertz-Knudsen equation (see Section 4.3.2). The kinetics of the system will not be discussed here in more detail as the focus of this work is on transport phenomena in the porous structure of the GDE.

The sensitivity of **transport parameters** is comparatively small. Even at high overpotentials the diffusion coefficient of O_2 in the liquid phase shows only a small influence on the performance. This is due to the excellent transport of O_2 in the gas phase of the GDE. Additionally, the transport resistance in the agglomerate is neglected in the standard model. Thus, a slightly higher sensitivity can be expected in the real system (cf. Section 4.3.2). This is also indicated by the results of the agglomerate model presented in the previous section. The sensitivities of the transference number t_+ and the diffusion coefficient of LiOH D_{LiOH} are quite small. However, these parameters are very important during deep discharge of the battery as they determine the local precipitation of solid $\text{LiOH}\cdot\text{H}_2\text{O}$. The low sensitivity of transport parameters is beneficial for the validity of the continuum model. They are calculated with some uncertainty based on several assumptions from the literature (see Section 4.3.1). An exception is the ionic conductivity of the electrolyte σ_{elyte} . Its significance is due to the comparatively large electrolyte region between the GDE and the reference electrode. Here, a comparatively large drop in the electrolyte potential occurs. This decreases the potential step which drives the electrochemical reaction in the GDE. In a real battery this distance is much smaller. Still, the importance of this parameter for the transport of ions will be significant.

The **structural parameters** of the GDE show a high influence on the system performance. Porosity ε_0 and tortuosity τ are important parameters for the transport of reactants (see Eq. (2.39)). In the present model, the tortuosity is determined by the Bruggeman coefficient β (Eq.(3.50)). High porosities improve the supply of reactants to the active sites on the electrode surface. In contrast, a high Bruggeman coefficient decreases effective transport properties which causes a negative sensitivity. The specific surface areas at the cathode a_{ORR}^v and anode a_{OER}^v are multiplicative factors in the rate expression of the electrochemical source term (Eq. (4.27)). Thus, their sensitivity is the same as k_{ORR}^0 and k_{OER}^0 , respectively.

4. Continuum modeling and simulation

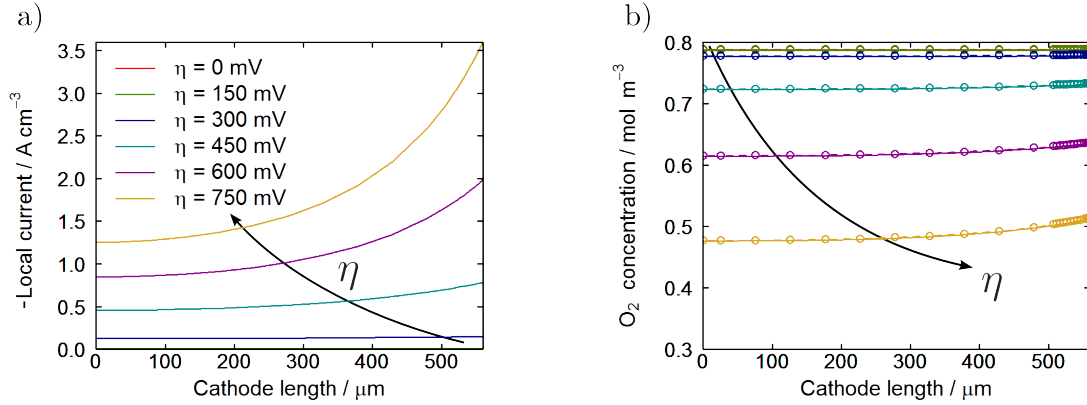


Figure 4.17.: Spatial profiles of Faradaic current a) and concentration of dissolved O₂ b) in the cathode at various overpotentials. Simulations are run at a temperature of 25 °C and a LiOH concentration of 1 M. Symbols in graph b) indicate the O₂ concentration in thermodynamic equilibrium. The gas inlet is at $y = 0$, the electrolyte bath at $y = 560 \mu\text{m}$

The thickness of the electrode is an important parameter regarding the power density of the GDE. The sensitivity strongly depends on the applied overpotential. Figure 4.17 a) shows the local Faradaic current along the y direction of the GDE. At low overpotentials the ORR proceeds in the whole GDE at almost the same rate. At high overpotentials the current strongly increases from the gas inlet towards the porous electrode/electrolyte bath interface. This gradient is caused by the ohmic resistance of the electrolyte and is enhanced by a gradient of dissolved O₂ as shown in Figure 4.17 b) (solid lines, discussed below). If the gradient in the local Faradaic current is small, a change in thickness causes a higher sensitivity compared to higher gradients.

The open symbols in Figure 4.17 b) represent the solubility of O₂ (i.e., the concentration in the limit of thermodynamic equilibrium). The solubility of O₂ depends on the local concentration of LiOH (salting-out). During oxygen reduction the local concentration of LiOH in the electrode increases in an inhomogeneous way such that higher concentrations are present close to the gas channel. Figure 4.17 shows that for all overpotentials the simulated concentrations (which includes transport limitations and salting-out) are very close to the solubility limit (which includes only salting-out). Thus, the decrease in O₂ concentration towards the electrolyte ($y_{\text{ca}} = L_{\text{GDE}}$) is only due to salting-out and not mass transport limitations. This demonstrates the good supply of O₂ even at high overpotentials.

The sensitivity of the saturation is presented in the form of the Leverett function $J(s)$. Its

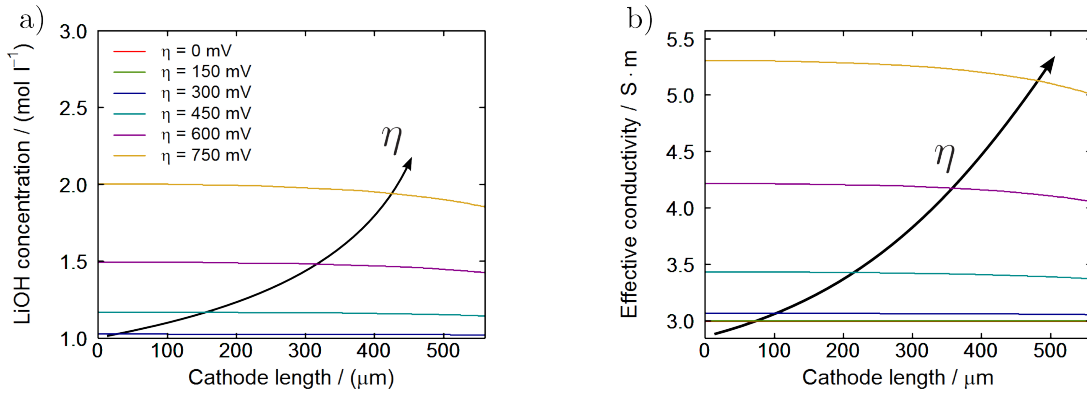


Figure 4.18.: Spatial profiles of LiOH concentration a) and local effective conductivity b) in the cathode at various overpotentials. Simulations are run at a temperature of 25 °C and an initial LiOH concentration of 1 M. The gas inlet is at $y = 0$, the electrolyte bath at $y = 560 \mu\text{m}$

small sensitivity indicates that in the studied parameter range the saturation is not limiting the performance of the electrode. Still, it is a crucial parameter for mass transport in the pore space and electrode performance in general. The findings during model validation indicate that the saturation in the standard model is probably larger than in the real system. This will be analyzed in more detail in the next paragraph.

Influence of saturation management

The saturation of the GDE with liquid electrolyte determines the transport of mass and charge. In the experiments discussed in Chapter 2.3.2 a decrease of the transport resistance Z_{pore} (cf. equivalent circuit model in Section 2.2.2) with rising potential was observed. Possible explanations were a change in local conductivity and in the effective length for ionic conduction. The spatial profiles of the Faradaic current (Figure 4.17) show an inhomogeneous distribution at high overpotentials. Therefore, the length for ionic conduction effectively decreases. Figure 4.18 presents LiOH concentration and local conductivity profiles in the GDE. At higher overpotentials the concentration of LiOH in the pore space increases which causes also an increase in local conductivity as shown in Figure 4.18 b). The simulated distributions of effective conductivity and ionic current can be used to calculate the transport resistance of the GDE. Figure 4.19 presents the pore transport resistance as function of overpotential in 0.1, 0.2, 1, and 2 M LiOH solution at

4. Continuum modeling and simulation

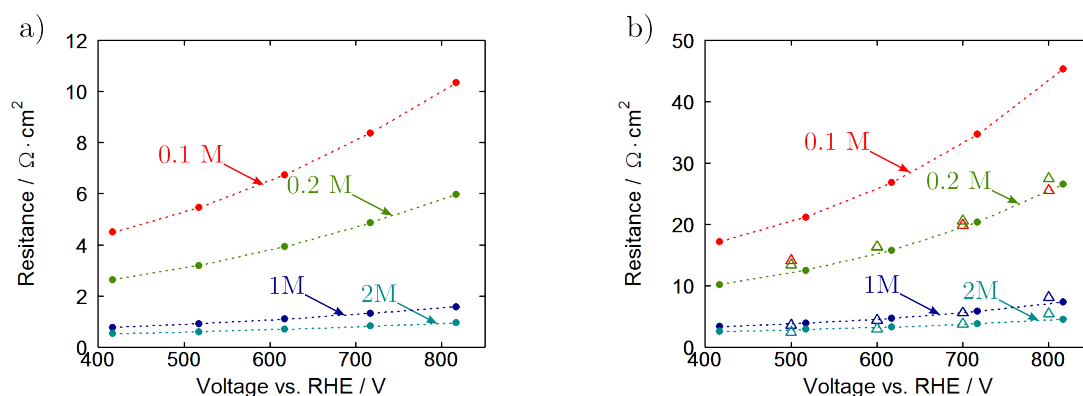


Figure 4.19.: Pore transport resistance as function of overpotential in 0.1, 0.2, 1, and 2 M LiOH solution at a temperature of 40 °C. a) Solid dots and connecting dashed lines represent simulations at standard saturation (67%). b) Solid dots and connecting dashed lines are results of simulations with 37% saturation. Open triangles represent experimental data.

a temperature of 40 °C. The left panel shows the values as calculated in the simulations at standard conditions (saturation of 67%). The trend of Z_{pore} reflects the experimental observations from Chapter 2.3.2. Therefore, the trend which is observed experimentally can be attributed to both a change in the effective length for ionic conduction and a local increase in conductivity.

However, quantitatively the simulated pore transport resistance is about a factor of 5 smaller than the experimental value. This corresponds to the results of the impedance simulations which are also found to give a generally smaller polarization resistance. A scaling of the simulated transport resistance with saturation predicts a real saturation of the GDE of $\sim 40\%$. This is significantly smaller compared to the saturation of the standard model which is initially around 67%. Figure 4.19 b) shows the experimental pore transport resistance (open symbols) along with a resistance obtained from simulations (dashed line) with 37% saturation which are in good general agreement. This finding is a further indication that the saturation of the pore space with liquid electrolyte as determined in the LBM simulations of the drainage process probably overpredicts the real saturation of the GDE. Moreover, it demonstrates that the wetting properties of the active materials require a suitable engineering.

Figure 4.20 a) compares Leverett functions from the literature with the data obtained in this work. In the correlations of Kumbur *et. al* [104] the contribution of the micro-porous layer (MPL) is neglected. The other Leverett functions are taken from Hao *et al.* [110]

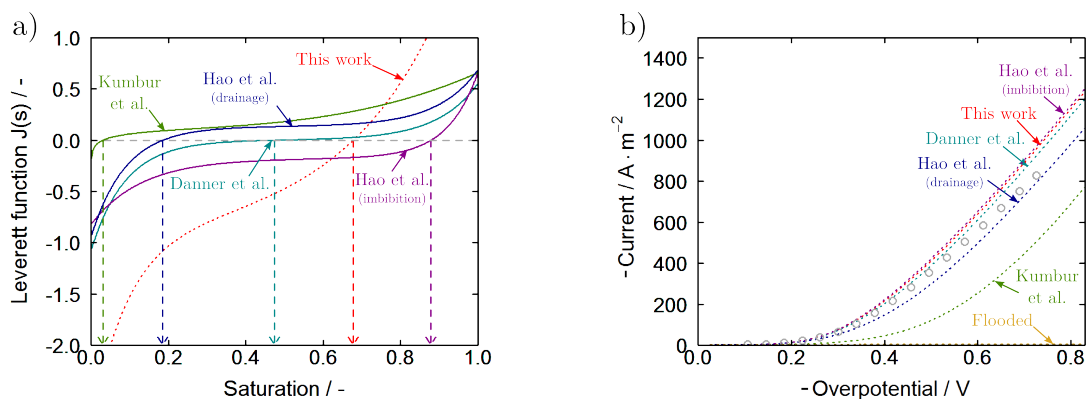


Figure 4.20.: a) Comparison of different Leverett functions from this work (dashed line) and the literature (Kumbur *et al.* [104], Hao *et al.*[110], Danner *et al.* [198]). Arrows indicate the resulting saturation in the pore space of the GDE. b) Simulations of IV curves at 25 °C in 1M LiOH solution based on the parametrizations of the Leverett function shown in Figure 4.20 a). Symbols represent the experimental data and dashed lines are results of the simulations.

and are the basis for the correlation proposed in our previous publication [198]. The correlations of Kumbur and Hao *et al.* are determined from GDLs of PEMFCs and do, therefore, have a different form compared to the correlations of the Ag/Ag₂O GDE. Still, they are indicative for the different levels of saturation which can be adjusted in porous media. Note, that the measured and simulated saturations for the same or very similar diffusion media range from 5% (Kumbur *et. al*) to 88% (Hao *et. al* for imbibition).

In Figure 4.20 b) the performance of the system presented in this work is compared to several Leverett functions from the literature (see Figure 4.20 a)). All other parameters such as the Bruggeman coefficient and active surface area are constant. The Leverett function of Hao *et al.* for imbibition gives the highest saturation (compare Figure 4.20 a)) and also the simulated electrode shows the best performance in terms of current density. The IV curves of other $J(s)$ are shifted towards higher overpotentials, i.e., the resulting current density is lower. The reason is a slower transport of reactants which is due to smaller effective transport coefficients in the liquid electrolyte (see Eq. (3.50)). Thus, a larger part of the overpotential is needed to sustain the transport of reactants and less can be used to drive the electrochemical reaction. The yellow line at the bottom of the graph represents simulation results for an electrode where the pore space is completely filled or 'flooded' with electrolyte. Although the transport parameters in the liquid phase

4. Continuum modeling and simulation

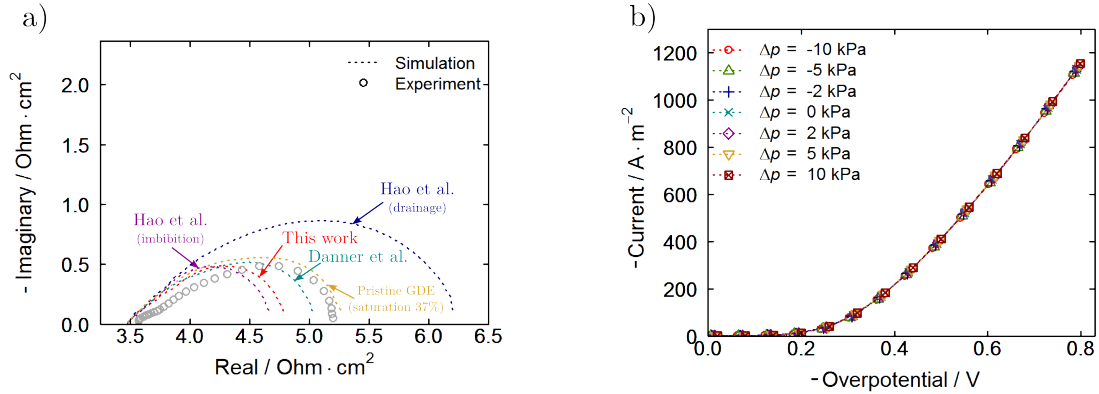


Figure 4.21.: a) Simulation of impedance spectra at 25 °C in 1M LiOH based on the parametrizations of the Leverett function shown in Figure 4.20 a). Symbols represent the experimental data and dashed lines are results of the simulations. b) Simulations of pressure differences between gas and liquid phase ranging from -10 to +10 kPa at 25 °C in 1M LiOH solution.

are the highest for this case the performance of the GDE is limited by the supply of O_2 to the active sites. This highlights the importance of a coexistence of gas and liquid phase in the porous electrode. The current density of the flooded electrode is already at an overpotential of ~ 100 mV limited by the rate of diffusion in the liquid electrolyte.

Figure 4.21 a) displays impedance spectra in 1M LiOH solution at 25 °C and a potential of 600 mV vs. RHE for the Leverett functions depicted in Figure 4.20 a). The spectra confirm the trend of the IV curves shown in Figure 4.20 b). The best agreement to the experimental data can be found by the spectrum which is simulated with the Leverett function of the pristine electrode obtained from the imbibition process. The resulting saturation of this Leverett function is 37%. This is consistent with the observations presented above (cf. pore resistance in Figure 4.19)

Figure 4.21 b) shows IV curves for pressure differences between the gas and liquid phase ranging from -10 to +10 kPa. In agreement to the experimental observations (Figure 2.24 b)) small variations in the pressure do not change the performance of the GDE. Bearing in mind the $p_c - s$ curves of the previous Chapter 3.3.2 this is not very surprising as much larger pressure difference are needed to change the saturation and, thus, performance of the GDE.

Structural design

The two most important parameters which can be investigated in this continuum approach are the thickness and porosity of the electrode. The sensitivity analysis of the previous paragraph indicates that the GDE thickness has a limiting effect only at small overpotentials. The spatial profiles of Faradaic current (Figure 4.17) confirm that at high overpotentials only a small part of the electrode is really electrochemically active. This leaves some room for a structural optimization in terms of energy and power density.

Figure 4.22 a) presents the current density as function of electrode thickness in 1M LiOH solution at 25 °C. Varying parameter is the applied overpotential and current density relationships are shown between 200 and 800 mV. The graph confirms that at high overpotentials the current which can be drawn from the system is almost constant down to an electrode thickness of 200 μm . This is an important finding because as it can be seen in Figure 4.22 b) the power density based on the mass of active particles increases exponentially towards smaller electrode thickness. Even thinner electrodes will be very challenging to prepare and also the current density will strongly decrease.

The second important parameter for electrode design is the porosity of the GDE. It is not straight forward to modify this parameter as the porosity is directly related to the surface area of the electrode. Furthermore, as seen in Chapter 3, a change in porosity will cause a fundamentally different wetting and, thus, transport behavior of the porous electrode. Still, some qualitative trends can be deduced from the calculations.

In the simulations a packing of spherical particles is assumed for the relation between porosity and specific surface area. All other parameters are kept constant. Figure 4.23 a) shows the current density as a function of porosity. The curves at different overpotentials exhibit a slight maximum at intermediate porosity. This can be explained by a change in the rate-limiting process. At low porosity the effective transport parameters are small (cf. Bruggeman correlation Eq. (4.29)) and the supply of reactants becomes limiting. At high porosity the surface area available for the electrochemical reaction is the limiting factor. The maximum shifts to lower porosity with decreasing overpotential as transport limitations will not be significant at low currents.

Figure 4.23 b) shows a plot of power density as function of current density for electrodes consisting of two layers with high and low porosity. This type of electrode could be manufactured by producing the first layer with a high pressure load and the second one with a more moderate one. In the simulations the influence of layer thickness and position

4. Continuum modeling and simulation

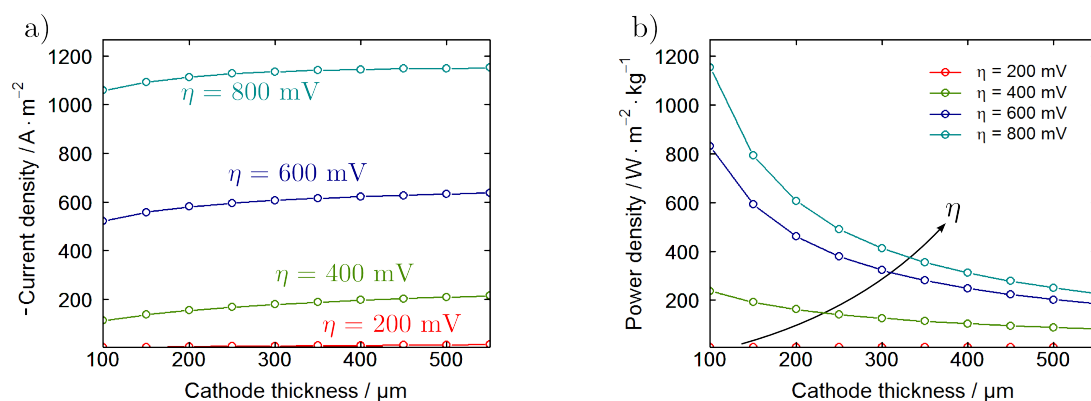


Figure 4.22.: Influence of cathode thickness on electrode performance in 1M LiOH at 25 °C and 200, 400, 600, and 800 mV overpotential. a) Current density as function of cathode thickness. b) Power density based on the mass of electrode material (Ag) as function of cathode thickness.

is investigated in detail. The overall thickness of the electrodes stays constant. The red (open circle) and green graphs (open triangle) represent electrodes consisting of a single layer with high and low porosity, respectively. They frame all other simulations indicating that a layering of the electrodes will most likely not be able to improve the overall performance of the GDE.

Yellow (reverse triangle) and brown (crossed rectangle) graphs represent electrodes consisting of 25% low-porosity material facing the gas inlet and electrolyte bath, respectively. While the configuration with the high-porosity case at the gas inlet gives a comparable performance to the full high-porosity electrode the power and current density in the electrode with opposite configuration are considerably smaller. This demonstrates that it is advantageous to place the high-porosity layer towards the interface with the electrolyte bath as transport processes in the liquid phase are more facile here. Although the designs with a low-porosity layer show a minor performance they might be a helpful tool in the engineering of the saturation management in the high-porosity part. The configuration could allow an operation at elevated pressures in the liquid phase while preventing a flooding of the gas inlet.

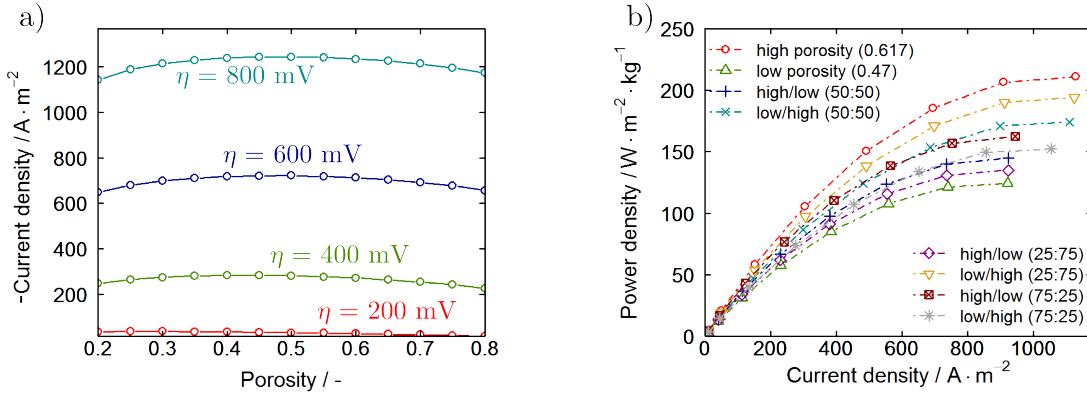


Figure 4.23.: Influence of porosity on electrode performance in 1 M LiOH. a) Current density at various overpotentials for a simultaneous variation of GDE porosity and active surface area. For the relation between porosity and surface area a packing of spherical particles is assumed. b) Simulations of a GDE with constant thickness consisting of layers with high and low porosity.

4.3.4. Full cell simulations

An advantage of the modeling approach is that it allows to study systems which are not easily accessible in experiments. One of the challenges of the aqueous Li-O₂ battery is the need for a stable Li ion conducting material which prevents contact of the Li metal anode with the aqueous electrolyte. Several authors dedicated their efforts to this task and demonstrated stable operation for a reasonable number of cycles [70, 79, 83]. Still, experimental studies on aqueous Li-O₂ full-cells are cumbersome.

In this section results of a full-cell Li-O₂ battery model are presented. This virtual battery cell employs the validated model of the GDE at the cathode. Moreover, it includes an APL which was not modeled in the previous publications [78]. Although the model is parametrized for a large temperature range the cell is operated at 25 °C and under pure O₂ atmosphere.

Discharge characteristics of aqueous Li-O₂ batteries

The discharge of an aqueous Li-O₂ battery is characterized by a two-stage process (compare Chapter 1.2.2). First, the concentration of LiOH in the solution rises until the solubility

4. Continuum modeling and simulation

limit is reached. Afterwards, the nucleation and growth process of $\text{LiOH}\cdot\text{H}_2\text{O}$ crystals sets in and the concentration stays approximately constant. This leads to a plateau in the cell voltage until the transport of reactants in the porous electrode is blocked by the precipitate. This causes a sudden drop in voltage and limits the discharge of the battery. Figure 4.24 shows the discharge process for a constant discharge current of 10 A/m^2 . The green curve displays the cell potential and red and blue lines show the average LiOH concentration and $\text{LiOH}\cdot\text{H}_2\text{O}$ volume fraction in the separator. The discharge capacity is based on the total mass of the battery neglecting the contributions of housing and peripheral devices. Dashed vertical lines numbered from a) to d) indicate time points at increasing depth of discharge (DOD). Corresponding spatial profiles of LiOH concentration and $\text{LiOH}\cdot\text{H}_2\text{O}$ volume fraction in the cathode and separator are shown below.

In the first period of discharge the LiOH concentration increases. Still, it is below the solubility limit and no precipitation of $\text{LiOH}\cdot\text{H}_2\text{O}$ crystals is observed (compare Figure 4.24 a)). The LiOH concentration is higher close to the APL. This is caused by the low transference number of Li^+ ions in the solution. At point b) the LiOH concentration reaches its solubility limit and the nucleation process slowly kicks in. This is characterized by a small overshoot in LiOH concentration before it is again reduced by the nucleation process. The precipitation of $\text{LiOH}\cdot\text{H}_2\text{O}$ crystals also diminishes the concentration gradients in the battery (cf. y -axis scales in Figure 4.24). Still, the concentration is higher close to the APL and anode causing a preferential growth of crystals in this area. At the end of discharge (Figure 4.24 d)) the solid reaction products block the pore space of the separator and cause a steep voltage drop until the cut-off voltage of 1 V is reached. This behavior is an important finding of the current model which has not been reported in other modeling work. It demonstrates a fundamentally different mode of operation compared to the aprotic Li-O_2 battery where the capacity of the cell is limited by solid discharge products at the gas inlet.

Comparison of oxygen electrode design

In Section 4.3.3 the benefits of GDEs in terms of rate capability are discussed in detail. In this paragraph a full battery cell using a GDE at the cathode is compared to a cell design using an electrode which is completely flooded with liquid electrolyte. Figure 4.25 displays discharge curves of Li-O_2 battery cells employing a GDE (left) or flooded electrode (right) as cathode. The capacity of the batteries strongly depends on the applied discharge

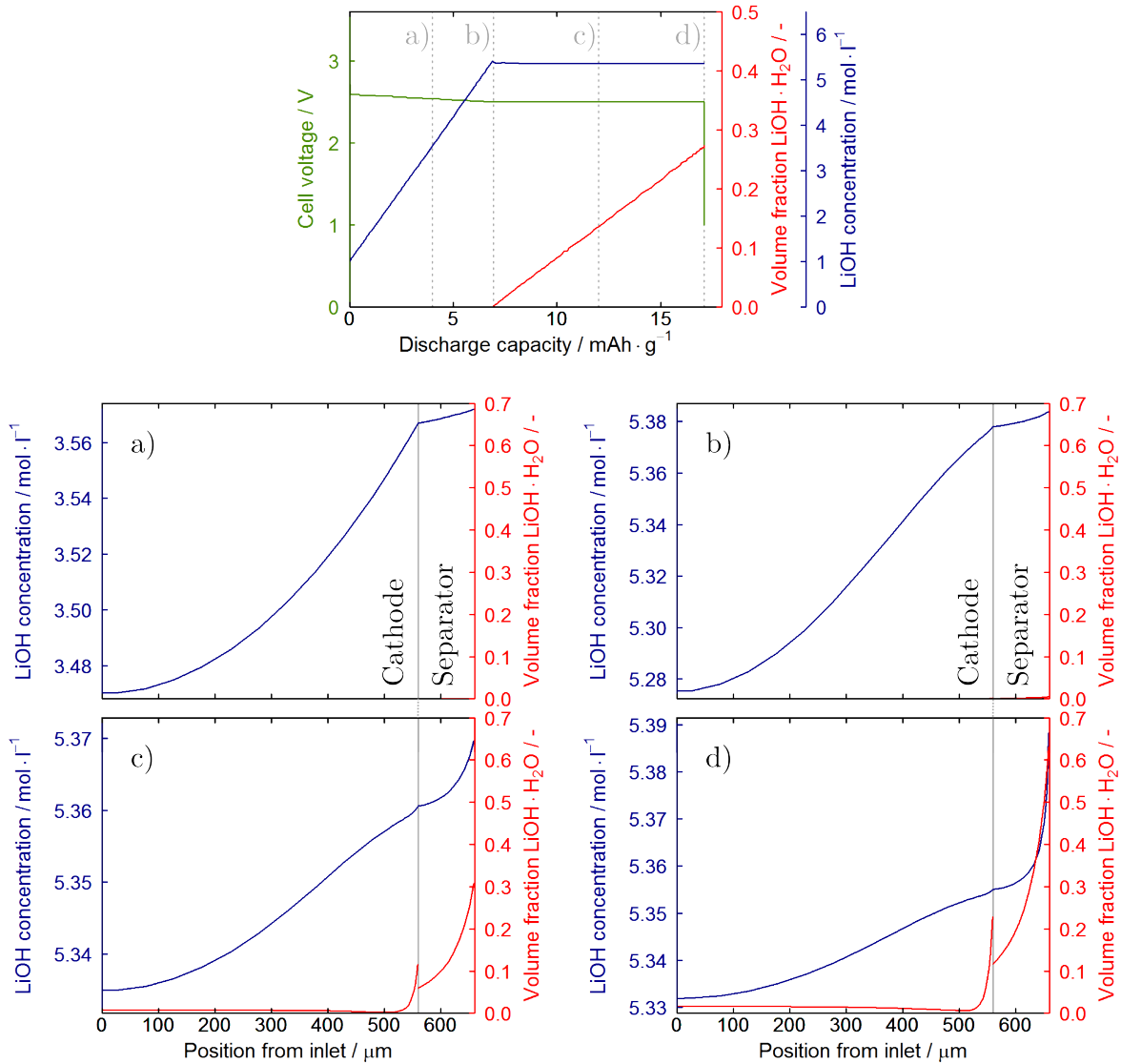


Figure 4.24.: Discharge curve of a Li-O_2 full cell at a constant current of 10 Am^{-2} . Green line represents the cell potential and red and blue lines show the average LiOH concentration and $\text{LiOH} \cdot \text{H}_2\text{O}$ volume fraction in the separator. Dashed vertical lines indicate time points at which spatial profiles are shown in graphs a) to d) for an increasing DOD.

4. Continuum modeling and simulation

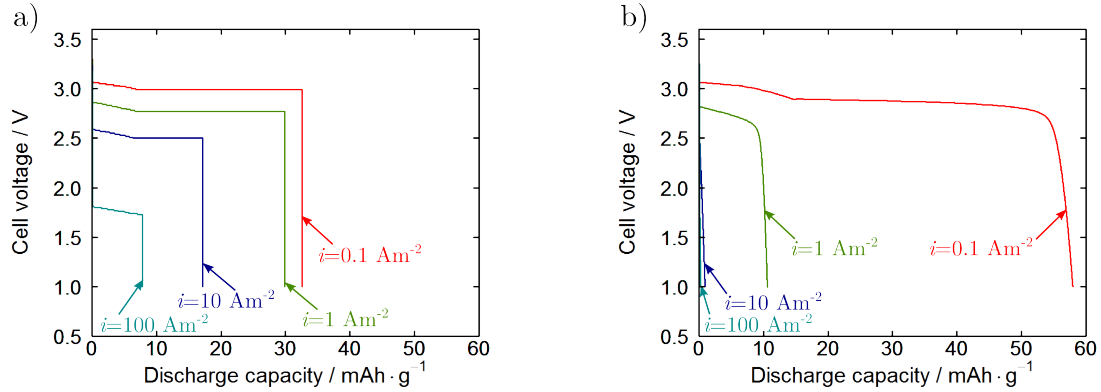


Figure 4.25.: Discharge curves of a Li-O₂ battery cell with a GDE (left) or flooded electrode (right) as cathode. Batteries are discharged at constant currents between 0.1 and 100 A/m².

current. At low current densities the specific capacity is generally better compared to high discharge rates. The decrease in capacity is caused by an inhomogeneous precipitation of LiOH·H₂O crystals which is more pronounced at high discharge currents. For the battery design using a GDE this is illustrated in Figure 4.26 which displays spatial profiles of i_F , c_{LiOH} , $\varepsilon_{\text{elyte}}$, and c_{O_2} at 90 % DOD. The profiles at 0.1, 1, and 10 A/m² are depicted by solid, dashed, and dotted lines, respectively. In the GDE the Faradaic current (Figure 4.26 a)) is distributed uniformly over its whole length which again demonstrates the good supply of O₂ as shown in Figure 4.26 b). The LiOH concentration in the cathode is slightly higher at increased discharge currents as the rate of the electrochemical reactions ('production of LiOH') is faster compared to the consumption of LiOH in the precipitation process. The most important information in Figure 4.26 is given by the spatial profiles of LiOH·H₂O volume fraction. At high currents LiOH·H₂O mainly precipitates in the separator (cf. LiOH·H₂O volume fraction in Figure 4.24). However, at lower currents the gradient in LiOH concentration is less pronounced which causes a shift of the main precipitation zone to the cathode where the number of nucleation sites is higher. Moreover, the distribution of $\varepsilon_{\text{elyte}}$ is more homogeneous at low rates. In this regime the overall capacity of the battery is determined by the total amount of precipitate. Thus, an efficient utilization of the available pore space will increase the specific capacity. At very high rates ohmic losses and activation overpotentials in the battery might cause a premature end of discharge as the cell potential drops below the cut-off voltage. This effect will be discussed in more detail later.

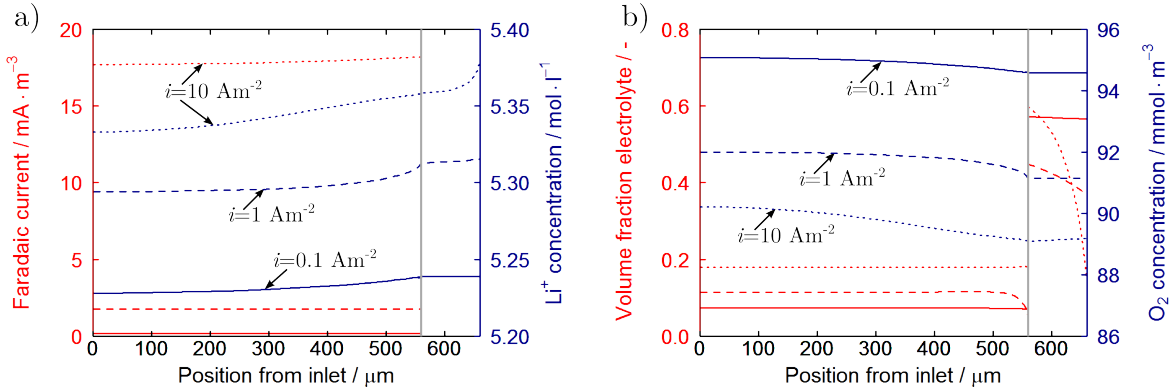


Figure 4.26.: Spatial profiles of i_F , c_{LiOH} , $\varepsilon_{\text{elyte}}$, and c_{O_2} in cathode and separator of a full cell using the concept of a GDE. The profiles at 0.1, 1, and 10 A/m² are depicted by solid, dashed, and dotted lines at 90 % DOD, respectively.

In Section 4.3.3 the superior rate capability of GDEs was already demonstrated. However, as it can be seen in Figure 4.24 b) the capacity of a battery concept using a flooded electrode might at low current density be even higher than in the GDE design. Yet, it strongly decreases towards higher discharge currents where again the GDE gives superior performance. While for the GDE the plateau in the discharge curves is essentially horizontal, the cell voltage of batteries with a flooded electrode decreases constantly. This can be explained by the current, concentration, and volume fraction profiles in cathode and separator shown in Figure 4.27. Due to an insufficient supply of O₂ in the liquid electrolyte the reaction zone of the ORR is limited to regions close to the gas inlet. Still, the LiOH concentration in cathode and separator is almost homogeneous and very similar to the distributions observed in the GDE. However, the length for ionic conduction in the liquid electrolyte is considerably longer in the case of a flooded electrode. During discharge the volume fraction of the liquid electrolyte decreases continuously due to the precipitation of LiOH·H₂O crystals (Figure 4.27 b)). This causes an increase in transport resistance which in turn results in additional ohmic losses. At high currents this effect is more pronounced and the cut-off voltage is reached although transport pathways are not fully blocked.

These investigations demonstrate the complexity of the interactions between transport, precipitation, and electrochemistry in aqueous Li-O₂ batteries. Parameter studies can be a helpful tool to develop a better understanding of the system in order to find optimal structural properties for certain conditions.

4. Continuum modeling and simulation

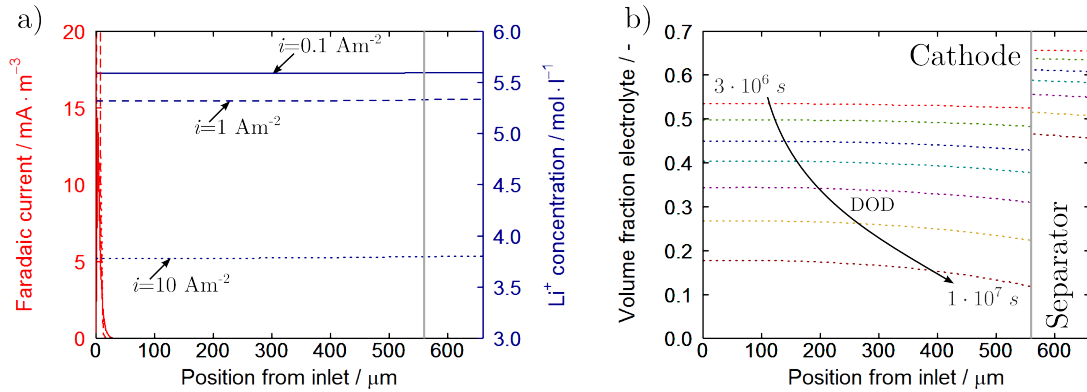


Figure 4.27.: Spatial profiles in cathode and separator of a Li-O₂ battery employing a flooded electrode at the cathode. a) Faradaic current and O₂ concentration at 90 % DOD for constant discharge currents of 0.1, 1, and 10 A/m² indicated by solid, dashed, and dotted lines, respectively. b) Volume fraction of the electrolyte phase at increasing DOD for a discharge current of 0.1 A/m².

Sensitivity analysis of cell performance

As already demonstrated in the design studies of GDEs a sensitivity analysis can be helpful to identify rate-limiting structural parameters. Important specifications of a battery cell are its specific power and capacity. Therefore, they will be used in this paragraph instead of current density (compare Eq. (4.70)). The focus of this study is on the structural parameters of the GDE, separator, and APL.

Figure 4.28 shows the sensitivity of specific capacity and power on structural parameters. Generally, parameters which increase the weight of the battery tend to decrease the mass-specific quantities. However, often the analysis is not this simple. Taking the thickness of the cathode it can be seen that at higher currents an increase will indeed lower the specific capacity. However, at low currents the capacity is predicted to effectively increase. This can be explained by the observations of the previous paragraph. At high currents the battery capacity is limited by the preferential precipitation in the separator. Therefore, an increase in cathode thickness will decrease the specific capacity. At low currents also larger parts of the cathode are utilized for a precipitation of LiOH · H₂O and an increase in available pore volume improves the specific capacity. Similar conclusions can be drawn for the porosity of the cathode and the corresponding parameters of the separator.

The specific surface areas in cathode and separator do have opposite effects at low and

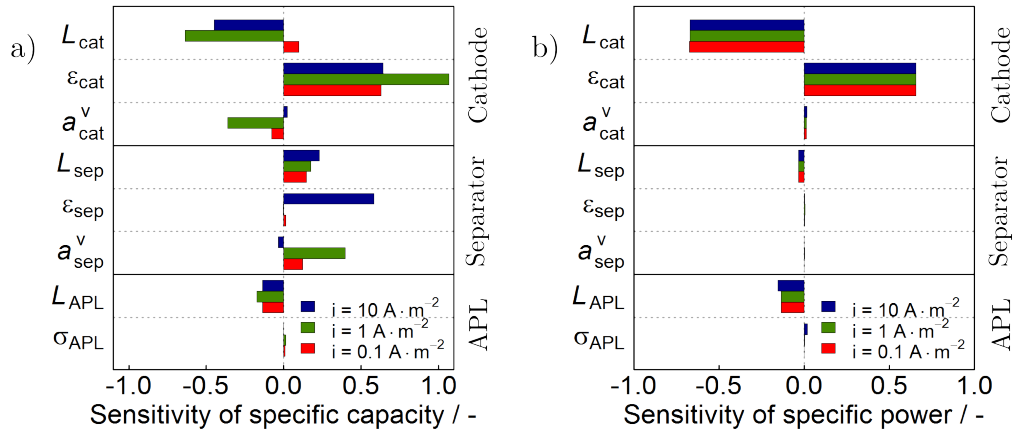


Figure 4.28.: Sensitivity analysis of an aqueous Li-O₂ battery. Target variables of the analysis are the specific capacity (left) and power (right) of the battery cells. The focus of this study is on the structural parameters of GDE, separator, and APL.

high currents. Again this can be explained by a preferential precipitation in cathode and separator at low and high currents, respectively. The available surface area for nucleation of seed crystals balances the precipitation process between cathode and separator. At high discharge currents an increase in cathode surface area favors the precipitation in the cathode and, thus, improves the total capacity. In contrast, high surface areas in the separator will improve the utilization of separator pore space at low currents. In the end the key aspect for an optimal cell design regarding its capacity is to maximize the volume available for the solid discharge products, either by increasing the physical volume of the cell or by improving the utilization of the pore space.

The parameters of the APL do not have a strong effect on battery capacity. The decrease of the specific capacity with APL thickness can be assigned to the increase in battery mass. However, the properties of the APL can be expected to have some influence on the specific power of the system. The APL consists of a Li ion conducting glass ceramic which has a low ionic conductivity compared to the aqueous electrolyte. The additional transport resistance will be visible in the battery performance, especially at high current density. Figure 4.28 b) presents the sensitivity of specific power on structural parameters. The thickness of GDE, separator, and APL show a negative sensitivity as the additional mass reduces the specific power. The sensitivity of cathode and separator thickness is comparable for all three discharge currents. This indicates that additional effects due to ionic conduction in the liquid electrolyte are negligible. The sensitivity of APL thickness

4. Continuum modeling and simulation

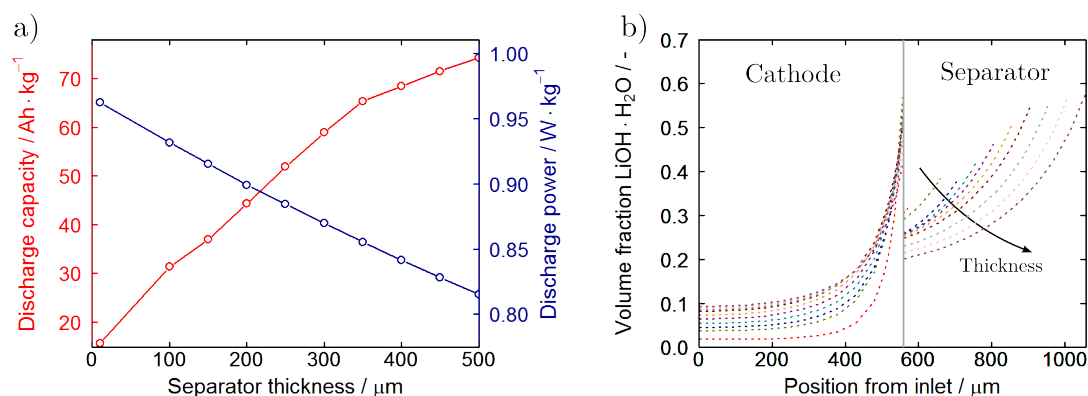


Figure 4.29.: Variation of separator thickness at a discharge current of 1 A/m^2 . a) Effect on specific capacity and power. b) Spatial profiles of $\text{LiOH} \cdot \text{H}_2\text{O}$ volume fraction in the cathode and separator at the end of discharge.

is slightly larger at the highest discharge current. A similar effect can be observed for the APL conductivity. This reveals a limiting impact of the protective layer at elevated discharge currents.

Another important parameter for the specific battery power is the porosity of the cathode. On the one hand a higher porosity reduces the mass of the battery and on the other hand the transport resistance in the liquid electrolyte is reduced even further. Therefore, a similar effect would be expected for the separator porosity. Yet, the sensitivity of this parameter on the specific power is negligible. This issue will be discussed in more detail in the next paragraph.

Parameter variations and cell design

The importance of the structural parameters of the cathode was discussed in detail in Section 4.3.3. The focus in this paragraph will be on the structural and material parameters of the separator and APL. Figure 4.29 a) shows a plot of specific capacity and power at a discharge current of 1 A/m^2 for separator thicknesses ranging from 10 to 500 μm . The specific power of the battery decreases linearly with thickness which can be primarily assigned to the higher mass of the system. Additionally, an increase of the transport resistance in the liquid electrolyte might contribute to some extent. The specific capacity in turn rises continuously and increases almost by a factor of 5. This highlights the importance of a suitable design of the separator which in the aqueous Li-O_2 battery

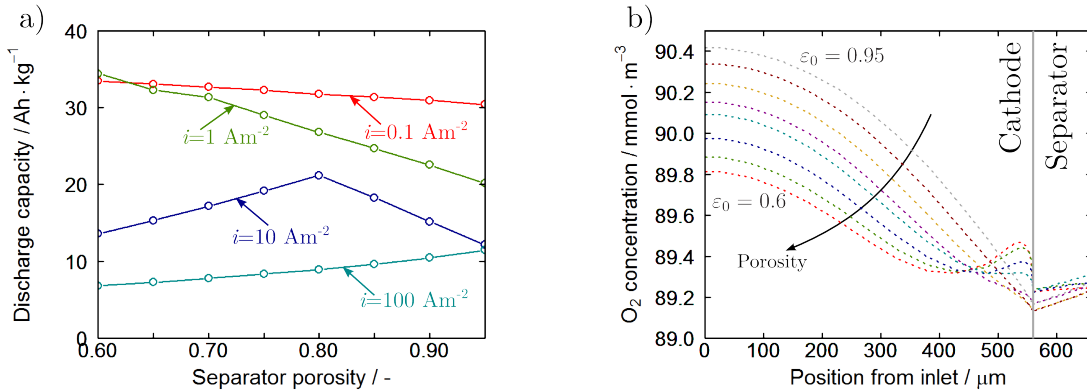


Figure 4.30.: a) Influence of separator porosity on discharge capacity at discharge currents of 0.1, 1, 10, and 100 A/m². b) Concentration of dissolved O₂ in cathode and separator for varying separator porosity at a discharge current of 10 A/m².

serves as a reservoir for solid discharge products.

Figure 4.29 b) displays the distribution of LiOH·H₂O volume fraction in cathode and separator at the end of discharge. As discussed before the capacity of the battery is more or less given by the amount of precipitated discharge product. In the current graph it is proportional to the area under the profiles of LiOH·H₂O volume fraction. It is interesting to see that an increase in separator thickness not only improves the amount of LiOH·H₂O which can be stored in the separator but also in the cathode.

In the sensitivity analysis the separator porosity and surface area are varied independently. However, in reality these two structural properties are correlated. Again a packing of spherical particles is assumed to model this relationship. Figure 4.30 a) presents specific capacities as function of separator porosity for discharge currents between 0.1 and 100 A/m². The graph illustrates the change in the preferred area for precipitation discussed previously. At high currents precipitation predominantly occurs in the separator and increasing porosity favors larger battery capacities. At low currents the capacity is limited by precipitation in the cathode and slower precipitation kinetics due to a smaller surface area in the separator will cause a minor utilization of the pore space. A discharge current of 10 A/m² resides right between these two regimes and the specific capacity goes through a distinct maximum. The model predicts that a separator porosity of around 80% yields the best balance between precipitation in cathode and separator and optimizes the utilization of the available pore space.

4. Continuum modeling and simulation

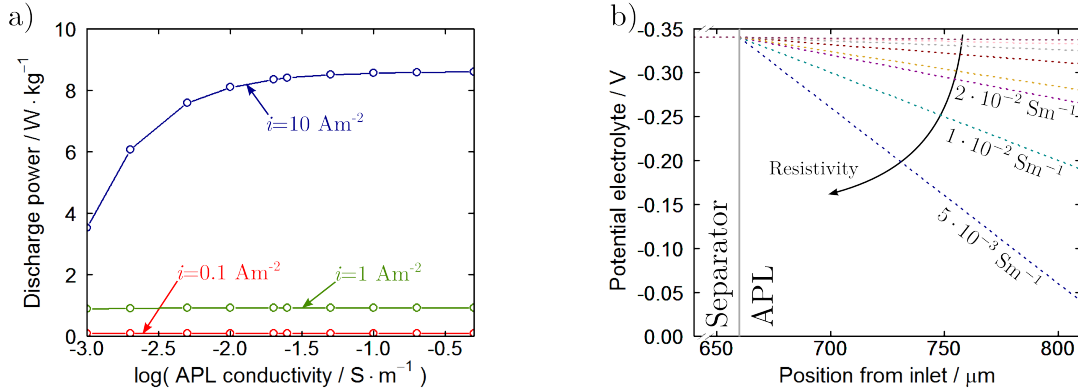


Figure 4.31.: Influence of APL conductivity on specific battery power (left) and profiles of electrolyte potential (right). Profiles are reported at the end of discharge at a current density of 10 A/m^2 .

Figure 4.30 b) shows the concentration of oxygen in the cathode and separator for varying separator porosity at a discharge current of 10 A/m^2 . The profiles exhibit some interesting features. At high porosity the precipitation occurs in the cathode close to the separator. This causes a drop in the LiOH concentration which results in a higher O_2 concentration in this confined area (salting-out). At low porosity a slow mass transport in the separator causes a larger LiOH concentration gradient which eventually initiates the precipitation in the separator. This reduces the LiOH concentration in large parts of the cathode which in turn favors higher oxygen concentration and improves the kinetics of the ORR. This effect balances to some extent the negative impact of a higher separator mass and might be responsible for the negligible sensitivity of separator porosity on specific power reported in the previous paragraph.

Figure 4.31 a) presents the specific discharge power as function of APL conductivity for current densities of 0.1 , 1 , and 10 A/m^2 . At low currents the influence of conductivity on battery power is small. Even at conductivities which are an order of magnitude smaller than values reported in the literature [79] the reduction of specific power is negligible. However, at high discharge currents the effect becomes more prominent and a strong decrease in specific power can be observed. In the pristine state ($\sigma_{\text{APL}} = 2.5 \cdot 10^{-2} \text{ S/m}$) the rate-limiting aspect of the APL is not very severe. However, if exposed to strongly alkaline solution the Li glass was shown to deteriorate which results in a loss in ionic conductivity by almost an order of magnitude. Figure 4.31 b) shows potential profiles in the APL and separator for a current density of 10 A/m^2 . The ohmic resistance of the Li

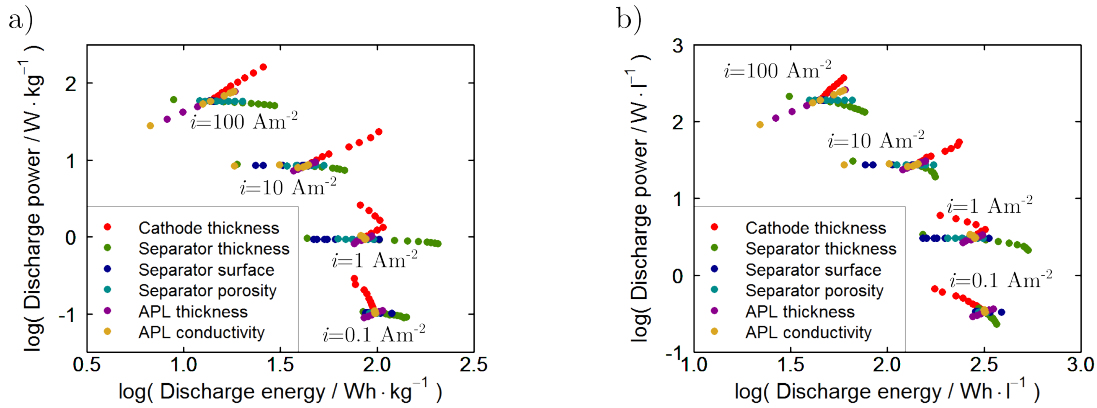


Figure 4.32.: Ragone plots for the evaluation of battery performance. Values of battery power and energy are related to the battery mass (left) and volume (right). The points of operation group according to the applied current density ranging from 0.1 to 100 A/m².

ion conducting material causes a linear drop in the electrolyte potential. At the low ionic conductivity of the aged Li glass the potential drop in the APL can be as high as 1 V. This is a serious problem regarding the long-term operation of the system.

Specific energy and power

Due to their high theoretical capacity Li-O₂ batteries are considered promising candidates for automotive applications. However, as shown above the system is very complicated and research is still in its early stages. The detailed continuum model gives the opportunity to evaluate the battery performance at the current state of research and for possible future developments. At the end of the day the specific energy and power of the battery which are commonly used as a benchmark are decisive for the successful evaluation of the developments.

Figure 4.32 shows so-called Ragone plots of battery power vs. energy and represent a possibility to evaluate the battery performance in a very condensed form. In Figure 4.32 a) the values are related to the battery mass while in 4.32 b) they are based on its volume which is equally important for some applications. Colored dots represent different sets of parameters as given in the legend. The observed trends are similar in both graphs and depict the typical trade-off between battery power and energy. The parameter sets group according to the applied discharge current which is high at the top and small at the

bottom of the graphs. The most prominent parameters for cell design are the thickness of the cathode and separator which are able to cover a large range of specific power and energy. The highest specific energy is obtained at low discharge currents and reaches values of around 200 Wh/kg and 500 Wh/l, respectively.

It is now interesting to compare the performance of the current cell design to state-of-the-art Li-ion batteries. The specific power of commercially available cylindrical cells is as high as 2600 W/kg [239] still retaining a specific energy of 100-200 Wh/kg [240, 241]. This benchmark can not be reached with the aqueous Li-O₂ battery in its present design and demonstrates that it will be a long way for commercialization, especially taking into account that battery housing and other additional equipment is not included in the calculations of battery mass and volume. However, at least at low current densities the system is already able to deliver a comparable or even superior specific energy which gives some hope that with appropriate improvements the technology will become competitive.

4.4. Conclusions

This chapter presented a detailed continuum model for reaction and transport in porous gas diffusion electrodes for application in aqueous Li-O₂ batteries. In the first part of the chapter the fundamental equations for transport in porous electrodes were derived. The model is implemented in the software DENIS (Detailed Electrochemistry and Numerical Impedance Spectroscopy) [64, 207] developed by Wolfgang Bessler and co-workers. It can be used for the simulation of full battery cells as well as for experimental half-cell setups. The structural and electrochemical parameters of the model were adjusted according to the results presented in Chapters 2 and 3. Thermodynamic and transport properties of the LiOH | H₂O system were parametrized based on the extensive literature on aqueous electrolytes.

Half-cell simulations of IV curves compare favorably with the experimental data for oxygen reduction over a large range of parameters and demonstrate the validity of the model. The agreement to the data of electrochemical impedance spectra is only qualitative which could be related to an underestimation of the pore transport resistance. This indicates that the saturation of the electrode as taken from the LBM simulations is slightly too high. In the case of the low-porosity electrode it could be shown that the transport in the meso- and micropores of reduced electrode particles becomes limiting for the performance

of the system.

The validated model was used to identify the most important parameters for electrode design by means of a sensitivity analysis. The kinetics of the electrode material show the highest sensitivity of all parameters which highlights the need for a development of efficient catalysts [86]. Structural parameters of the electrode exhibit an almost comparable impact on electrode performance. The saturation of the electrode plays a central role in the transport of reactants. A high saturation improves the transport in the liquid phase. However, the inferior rate capability of a flooded electrode demonstrated that a coexistence of the gas and liquid phases is absolutely mandatory for a sufficient supply of O_2 at high currents. Parameter variations of electrode thickness and porosity were performed in order to determine an improved structure for advanced battery electrodes.

The validated model of the GDE was inserted as cathode into a virtual battery cell. During discharge of the battery the LiOH concentration in the electrolyte increases until the solubility limit is reached. At prolonged operation the formation of the solid discharge product $LiOH \cdot H_2O$ is observed. The detailed model of an aqueous Li- O_2 battery was used for an analysis of rate- and capacity-limiting processes. It was found that the formation of $LiOH \cdot H_2O$ crystals blocks the transport pathways in the porous separator and cathode, thereby, limiting the capacity of the battery. In contrast to the aprotic design it was shown that precipitation is favored in regions close to the APL and anode. This is caused by the low transference number of Li^+ in the solution. However, the position depends strongly on the applied discharge current and structural parameters.

The interplay between structural parameters, electrochemistry, and $LiOH \cdot H_2O$ precipitation is rather complex. It was found that the capacity of the battery can be improved by either increasing the physical volume (porosity, thickness) or the utilization of the pore space (surface area modifications). The conductivity and thickness of the APL have a detrimental effect on the battery power at high rates. While the effect is relatively moderate in the pristine state a deterioration of the APL and a resulting lower conductivity will massively limit the discharge performance.

Finally, the specific energy and power of the different sets of parameters was calculated. These properties are the most important benchmarks for a comparison of battery cells. Although the specific power and energy of the aqueous cells are relatively high they cannot compete with state-of-the-art Li-ion technology. This is a disappointing finding as the Li- O_2 battery is considered a promising candidate for the automotive sector. However,

4. Continuum modeling and simulation

suitable modifications and new developments might be able to further improve the energy density.

5. Summary and outlook

5.1. Summary

Li-air batteries are considered as potential candidates for automotive and mobile applications as they possess the highest theoretical energy density of all Li batteries. However, the Li-O₂ system is very complex and the number of remaining challenges which obviate a successful commercialization is large.

Several designs of Li-air batteries are proposed in the literature, mainly differing in the choice of electrolyte. Aprotic Li-air batteries recently received the most attention. However, most of these organic electrolytes were found to rapidly decompose under the conditions in Li-O₂ cells. The aqueous Li-air battery discussed in this work is an interesting alternative as it offers a comparable theoretical energy density and reversible electrochemistry. At the cathode the concept of gas diffusion electrodes (GDEs) can be employed which ensures a fast transport of O₂ and an excellent rate capability. The structure and composition of these porous electrodes has a strong influence on transport processes and, thus, the performance of the system.

Aim of this work is the development of a methodology which allows a systematic improvement of GDEs for application in aqueous Li-air batteries. The interplay of (electro)chemistry and multiphase transport in the porous structure of the electrode is rather complex. Therefore, experimental studies are combined with multiscale modeling in order to generate a fundamental understanding of relevant processes. Comparable studies at the same level of detail could not be found in the literature. Therefore, this work closes a fundamental gap and is an important contribution for the development of future aqueous Li-air battery concepts.

The methodology and the most important results are summarized in the following paragraphs.

Experiments

Experimental studies were conducted on commercial GDEs provided by Bayer Material Science. The electrode substrate consisted of Ag, Ag₂O and a polymeric binder material. The hydrophobic binder improves the mechanical stability of the electrode and additionally ensures the coexistence of gas and liquid phase in the pore network. Two different batches of GDEs with the same composition but varying porosity were characterized both structurally and electrochemically which gives a direct link between electrode structure and performance.

The electrochemical characterization was performed using cyclic voltammetry (CV) and electrochemical impedance spectroscopy (EIS) in a three-electrode setup. The focus of the measurements was on the oxygen reduction reaction (ORR) as the measurements during oxygen evolution (OER) led to a degradation of the electrode. Transport processes during O₂ evolution can be expected to be rather similar as long as a formation of gas bubbles is avoided.

CVs and impedance spectra were recorded for various temperatures (25, 40, 55 °C) and LiOH concentrations (0.1, 0.2, 1, 2 M) of the electrolyte bath. In general the performance of the electrodes was found to improve towards higher temperature, LiOH concentration, and overpotential. A limiting current due to mass transport limitations of reactants was not observed even at high current densities. This underlines the superior rate capability of the GDE concept.

For a quantitative investigation of ORR kinetics a Tafel analysis was performed using the data of CV measurements in 1 M LiOH solution. The resulting Tafel slope (100 mV/decade) was found to be in line with values reported in the literature for similar catalyst systems. Moreover, measurements at different temperatures allowed a calculation of the pre-exponential factor ($4.96 \cdot 10^{-3} \text{ m}^6/\text{kmol}^2/\text{s}$) and activation energy (21.8 kJ/mol) of the ORR.

The data of EIS measurements was fitted by an equivalent circuit model describing reaction and transport in porous electrodes. The parameters of the equivalent circuit represent important processes in the electrochemical system like the capacitance of the electric double layer, the transport resistance of the pore space, and the specific conductivity of

the electrolyte solution. The latter was in good agreement with data published in the literature.

A comparison of measurements which were recorded on the electrodes with low and high porosity demonstrated the influence of structure on performance. In the low-porosity case current densities were substantially smaller compared to the high-porosity electrode. The effect of electrode geometry was investigated in more detail during the structural characterization of electrode samples. 3D reconstructions of the GDEs were provided by Dr. Santhana Eswara-Moorthy (Group Prof. Ute Kaiser, University of Ulm) via FIB-SEM tomography. The geometries were imported in the commercial software package GeoDict for a detailed evaluation of structural and transport parameters (Tables 2.2, 2.4, and 2.3). The porosity of the GDE has a strong influence on the transport of reactants in the porous network. The effective diffusivity and permeability were found to be generally smaller in the low-porosity electrode. This is in line with the decrease in performance which was observed in the electrochemical measurements and highlights the importance of a suitable electrode design.

Lattice-Boltzmann simulations

The Lattice-Boltzmann method (LBM) is an efficient tool for the calculation of multiphase flow in complex geometries. In this work LBM simulations were employed to access the saturation behavior of the reconstructed electrode samples with liquid electrolyte. The saturation of the porous media and corresponding effective transport parameters are central for the functionality of the GDE concept.

A multiphase LBM model of the RK-type was developed in collaboration with Prof. Volker Schulz (DHBW Mannheim). Prominent feature of the model is the handling of multiple solid materials with different wetting behavior such as Ag substrate and hydrophobic binder. The reconstructed geometries obtained from FIB-SEM tomography were employed for the generation of the computational lattice of the LBM simulations.

3D simulations of the micro-structure allow the determination of liquid phase distributions in the state of fluid mechanical equilibrium. In a subsequent step the distributions were used as input for the calculation of effective transport parameters in the commercial software package GeoDict. The porosity and saturation of the GDEs had a strong influence on diffusivity, permeability, and active surface areas. Generally, effective transport parameters were found to decrease with saturation. Results of the 3D LBM simulations in principal

allow the calculation of pressure-saturation characteristics of the porous media. However, the large computational effort makes efficient calculations practically impossible.

In the present study it was suggested to employ a more time-efficient series of 2D simulations to obtain an estimate of $p_c - s$ curves. The average capillary pressure was in good agreement with the results of the 3D simulations which proves the validity of the approach. This is an important finding as the proposed method allows for an efficient screening of the wetting properties of porous media.

In the present case the method was employed to obtain the $p_c - s$ characteristics of the low- and high-porosity electrode samples. The simulations demonstrate the strong influence of the electrode structure on the saturation behavior for both imbibition and drainage of liquid electrolyte. In the low-porosity case the capillary pressures has to be orders of magnitude larger in order to obtain a significant saturation of the pore space. An observed hysteresis in capillary pressure between the imbibition and drainage process of liquid electrolyte is in good agreement with experimental $p_c - s$ curves reported in the literature.

The saturation and transport behavior of the GDE is important input for the continuum model presented in the following paragraph. The direct link between the microscopic transport behavior of the porous media (LBM) and the macroscopic electrode performance (continuum modeling) is a unique strength of the multiscale modeling approach presented in this work.

Continuum modeling

In this work a detailed continuum model describing multiphase transport in porous GDEs for application in aqueous Li-air batteries was developed. The model was implemented in the in-house modeling software DENIS developed by Prof. Wolfgang Bessler and co-workers [64, 78, 207]. In its current implementation the model allows the simulation of the experimental half-cell setup as well as full aqueous Li-O₂ battery cells. This is an important feature of this physical model as it enables a coupling of electrode performance to the behavior of a full battery cell. All model parameters were either determined in the experiments and microscale simulations described in the previous paragraphs or extracted from the extensive literature on aqueous electrolytes.

The continuum simulations of the half-cell setup were found to be in good qualitative agreement with the data of CV and EIS measurements over the whole range of experimental

conditions. Moreover, it could be shown that the model was able to reproduce the effect of structural parameters on electrode performance.

It has to be pointed out that all simulations were performed with one set of physical parameters which is an important difference to the class of equivalent circuit models where each impedance spectrum is fitted individually. This is a tremendous advantage of the physics-based modeling approach and allows a target-oriented improvement of electrode design.

A sensitivity analysis of selected model parameters revealed the prominent influence of the kinetic and structural parameters of the GDE. This underlines that a suitable engineering of the electrode structure is almost equally important as the development of novel catalyst materials.

The GDE model was included as cathode in a virtual battery cell. The full cell model allows conclusive insights in the operation of aqueous Li-O₂ batteries. During discharge the concentration of LiOH in the liquid electrolyte rose until it reached the solubility limit. After further discharge of the cell the formation of solid LiOH·H₂O was observed. At the end of discharge the transport pathways were blocked by the precipitate which limits the capacity of the cell. At high current densities the LiOH·H₂O crystals preferentially precipitated close to the anode. This is caused by the low transference number of Li⁺ in the solution. This effect is in agreement with experimental evidence and could not be described by other theoretical work published in the literature [96].

The discharge capacity was found to strongly depend on operating conditions. In the simulations it could be demonstrated that the thickness and porosity of the GDE and separator can be adjusted to maximize the battery capacity. However, an evaluation of the virtual cells regarding specific energy and power showed that the aqueous Li-O₂ battery at the current state of research is not competitive to state-of-the-art Li-ion batteries.

Suitable improvements and smart engineering might help to overcome some limitations of the aqueous Li-air battery concept. The multiscale methodology presented in this work bridges the gap between electrode structure and final battery performance. The thorough investigation of transport and capacity-limiting processes presented in this thesis contributes to the development of improved high-rate and high-energy density aqueous Li-O₂ batteries.

5.2. Outlook

The low utilization of the theoretical capacity by the aqueous Li-air battery designs presented in this work shows that there is considerable room for improvement of battery performance. In the following paragraphs some recommendations for future research are given.

Experiments

In the experimental part of this thesis the focus of the research was set on the analysis of GDE performance during O₂ reduction (ORR) which corresponds to the discharge process of the full battery cell. In order to evaluate the performance of the electrode during charging detailed investigations of O₂ evolution (OER) will be necessary.

The Ag electrodes studied in this work were found to dissolve under the conditions during O₂ evolution. Intense material research will be needed for a successful development of suitable bi-functional catalysts. Measurements on composite electrodes consisting of Ag and Co₃O₄ showed a good cycling stability in the half-cell setup and even an improved kinetic activity [95]. However, the high density of Ag reduces the specific energy of the system and materials with a lower density would be preferable. Still, the synergistic effect of the composite metal-oxide material is a good starting point for future research on suitable catalyst systems.

The second and, admittedly, more severe issue is the stability of the anode protective layer (APL). In this work all measurements were conducted in a half-cell setup. Eventually, it will of course be necessary to evaluate the performance of a full battery cell. As intermediate solution some intercalation material (e.g. LiV₃O₈ [242]) could be used at the anode in order to improve the cycling stability and to reduce the security risk. This approach will also give the opportunity to validate the capacity predictions of the continuum model. However, in the long run the application of a Li metal electrode will be absolutely mandatory for the competitiveness of the aqueous Li-air battery concept.

Lattice-Boltzmann simulations

The Lattice-Boltzmann model presented in this work was shown to be a valuable tool for the investigation of multiphase flow in complex geometries. Still, the model in its current form suffers from several shortcomings which need to be addressed.

The most important point is the occurrence of unphysical negative probabilities during the simulations. This issue can be resolved by a modification of the recoloring operator. Preliminary results of simulations with a revised recoloring scheme showed artifact-free phase distributions. Moreover, the revised model resolves numerical instabilities in the simulation of multiphase flow with high density and viscosity ratios.

In the present version of the Lattice-Boltzmann model only periodic boundary conditions can be simulated. The implementation of flux boundary conditions at the border of the computational domain will help to study the transport behavior also at dynamic operating conditions. This allows the direct simulation of imbibition and drainage experiments and improves the predictive capabilities of the model.

LBM offers the opportunity to study all kinds of transport problems in complex geometries and the simulation of multiphase flow is only one application of the method. The current model could be extended to include reaction and transport of multiple components within the phases. This will give the possibility to study local phenomena such as the formation or dissolution of solid discharge products ($\text{LiOH}\cdot\text{H}_2\text{O}$ or Li_2O_2).

Moreover, the developed model is not limited to the simulation of multiphase flow in Li-air batteries. Other applications are, e.g. the simulation of transport processes in catalyst or gas diffusion layers of fuel cells.

Continuum modeling

The theoretical studies of this work exclusively treat the oxygen reduction reaction (ORR). During the validation of the continuum model minor deviations between the experimental data and the simulations were observed. Several physical and chemical processes were proposed to explain these deviations.

In structures with a low porosity the results of the agglomerate model indicate the influence of transport limitations of O_2 . The concept of the effectiveness factor gives a reasonable first approximation of rate limiting effects. For a thorough analysis a 1+1D model could be developed which will give more insights in the transport processes within

the agglomerate.

The focus of the current model is on the description of transport phenomena within the porous structure of the GDE. Electrochemical reactions were treated in a simple Butler-Volmer type global reaction scheme. However, the mechanism of the ORR is known to be very complex. Elementary kinetic models could be used to describe the reaction mechanism in more detail. This will help to improve the understanding of the electrochemical behavior of the electrode and might resolve some of the remaining deviations to the experimental data.

Also for a theoretical investigation of rechargeable Li-air batteries the evolution of O_2 will need to be studied in more detail. As mentioned in the first paragraph this will require reliable experimental data for the validation of the kinetic mechanism. The extended model will allow to study the cycling behavior of full aqueous Li-air battery cells. This gives the opportunity to evaluate possible design concepts under more realistic conditions.

This work demonstrates the complexity of physical and chemical processes within the Li-air battery and the list of remaining challenges is long. A successful development of Li-air battery cells will require a continuous close collaboration of theoretical and experimental groups.

Bibliography

- (1) U.S. Energy Information Administration, *International Energy Outlook*, 2013 (cit. on p. 1).
- (2) Bundesregierung. Energiewende - Gesetzespaket im Überblick., <http://www.bundesregierung.de/ContentArchiv/DE/Archiv17/Artikel/2012/06/2012-06-04-artikel-hintergrund-energiewende-gesetzespaket.html> (accessed 03/18/2014) (cit. on p. 1).
- (3) Bundesnetzagentur, *First Monitoring Report - Energy of the future*, 2013 (cit. on p. 1).
- (4) Bundesregierung. Energiewende - Maßnahmen im Überblick., <http://www.bundesregierung.de/Content/DE/StatischeSeiten/Breg/Energiekonzept/0-Buehne/ma\ssnahmen-im-ueberblick.html> (accessed 03/18/2014) (cit. on p. 2).
- (5) Kraftfahrt-Bundesamtes. Bestand an Personenkraftwagen in den Jahren 2006 bis 2014 nach ausgewählten Kraftstoffarten., http://www.kba.de/DE/Statistik/Fahrzeuge/Bestand/Umwelt/b_umwelt_z_teil_2.html?nn=663524 (accessed 06/04/2014) (cit. on p. 2).
- (6) Verbundprojekt. Strom aus Luft und Lithium., <http://www.chemie.uni-bonn.de/forschung/luli> (accessed 04/18/2014) (cit. on pp. 2, 114, 121).
- (7) Reddy, Thomas B., *Linden's Handbook of Batteries*, 4th ed.; McGraw-Hill: 2011 (cit. on p. 3).
- (8) Girishkumar, G.; McCloskey, B.; Luntz, A. C.; Swanson, S.; Wilcke, W. Lithium - Air Battery: Promise and Challenges. *Journal of Physical Chemistry Letters* **2010**, *1*, 2193–2203 (cit. on pp. 4, 6, 18).
- (9) Bruce, P. G.; Freunberger, S. A.; Hardwick, L. J.; Tarascon, J.-M. Li-O₂ and Li-S batteries with high energy storage. *Nature Materials* **2012**, *11*, 19–29 (cit. on pp. 4, 18).
- (10) Nissan. Design and specs of the Nissan Leaf battery electric vehicle., <http://www.nissanusa.com/electric-cars/leaf/versions-specs/> (accessed 03/18/2014) (cit. on p. 4).

- (11) Toyota. Ni-MH battery in the 3rd generation Toyota Prius., <http://www.toyota.com/esq/vehicles/batteries/nickel-metal-hydride.html> (accessed 03/18/2014) (cit. on p. 4).
- (12) Scrosati, Bruno and Abraham, K.M. and van Schalkwijk, Walter A. and Hassoun, Jusef, *Lithium Batteries: Advanced Technologies and Applications*; John Wiley & Sons: 2013; Vol. 58 (cit. on pp. 4, 7).
- (13) Scrosati, B.; Garche, J. Lithium batteries: Status, prospects and future. *Journal of Power Sources* **2010**, *195*, 2419–2430 (cit. on p. 4).
- (14) Kraytsberg, A.; Ein-Eli, Y. Higher, Stronger, Better. . . A Review of 5 Volt Cathode Materials for Advanced Lithium-Ion Batteries. *Advanced Energy Materials* **2012**, *2*, 922–939 (cit. on p. 4).
- (15) Palomares, V.; Serras, P.; Villaluenga, I.; Hueso, K. B.; Carretero-González, J.; Rojo, T. Na-ion batteries, recent advances and present challenges to become low cost energy storage systems. *Energy & Environmental Science* **2012**, *5*, 5884 (cit. on p. 5).
- (16) Slater, M. D.; Kim, D.; Lee, E.; Johnson, C. S. Sodium-Ion Batteries. *Advanced Functional Materials* **2013**, *23*, 947–958 (cit. on p. 5).
- (17) Rahman, M. A.; Wang, X.; Wen, C. High Energy Density Metal-Air Batteries: A Review. *Journal of The Electrochemical Society* **2013**, *160*, A1759–A1771 (cit. on p. 5).
- (18) Kim, H.; Jeong, G.; Kim, Y.-U.; Kim, J.-H.; Park, C.-M.; Sohn, H.-J. Metallic anodes for next generation secondary batteries. *Chemical Society Reviews* **2013**, *42*, 9011–34 (cit. on p. 5).
- (19) Egan, D.; Ponce de León, C.; Wood, R.; Jones, R.; Stokes, K.; Walsh, F. Developments in electrode materials and electrolytes for aluminium–air batteries. *Journal of Power Sources* **2013**, *236*, 293–310 (cit. on p. 5).
- (20) Park, M.; Sun, H.; Lee, H.; Lee, J.; Cho, J. Lithium-Air Batteries: Survey on the Current Status and Perspectives Towards Automotive Applications from a Battery Industry Standpoint. *Advanced Energy Materials* **2012**, *2*, 780–800 (cit. on p. 6).
- (21) Kraytsberg, A.; Ein-Eli, Y. Review on Li-air batteries–Opportunities, limitations and perspective. *Journal of Power Sources* **2010**, *196*, 886–893 (cit. on p. 6).
- (22) Christensen, J.; Albertus, P.; Sanchez-Carrera, R. S.; Lohmann, T.; Kozinsky, B.; Liedtke, R.; Ahmed, J.; Kojic, A. A Critical Review of Li/Air Batteries. *Journal of The Electrochemical Society* **2012**, *159*, R1–R30 (cit. on pp. 6, 11).
- (23) Li, F.; Kitaura, H.; Zhou, H. The pursuit of rechargeable solid-state Li–air batteries. *Energy & Environmental Science* **2013**, *6*, 2302 (cit. on p. 6).
- (24) Wang, J.; Li, Y.; Sun, X. Challenges and opportunities of nanostructured materials for aprotic rechargeable lithium–air batteries. *Nano Energy* **2013**, *2*, 443–467 (cit. on pp. 6, 9).

-
- (25) Shao, Y.; Park, S.; Xiao, J.; Zhang, J.-G.; Wang, Y.; Liu, J. Electrocatalysts for Nonaqueous Lithium–Air Batteries: Status, Challenges, and Perspective. *ACS Catalysis* **2012**, *2*, 844–857 (cit. on p. 6).
- (26) Shao, Y.; Ding, F.; Xiao, J.; Zhang, J.; Xu, W.; Park, S.; Zhang, J.-G.; Wang, Y.; Liu, J. Making Li-Air Batteries Rechargeable: Material Challenges. *Advanced Functional Materials* **2013**, *23*, 987–1004 (cit. on p. 6).
- (27) Black, R.; Adams, B.; Nazar, L. F. Non-Aqueous and Hybrid Li-O₂ Batteries. *Advanced Energy Materials* **2012**, *2*, 801–815 (cit. on p. 6).
- (28) Garcia-Araez, N.; Novák, P. Critical aspects in the development of lithium–air batteries. *Journal of Solid State Electrochemistry* **2013**, *17*, 1793–1807 (cit. on p. 6).
- (29) Abraham, K. M.; Jiang, Z. A Polymer Electrolyte-Based Rechargeable Lithium/Oxygen Battery. *Journal of The Electrochemical Society* **1996**, *143*, 1–5 (cit. on p. 6).
- (30) Meini, S.; Piana, M.; Beyer, H.; Schwaemmlein, J.; Gasteiger, H. A. Effect of Carbon Surface Area on First Discharge Capacity of Li-O₂ Cathodes and Cycle-Life Behavior in Ether-Based Electrolytes. *Journal of The Electrochemical Society* **2012**, *159*, A2135–A2142 (cit. on p. 6).
- (31) Franco, A. A.; Xue, K.-H. Carbon-Based Electrodes for Lithium Air Batteries: Scientific and Technological Challenges from a Modeling Perspective. *ECS Journal of Solid State Science and Technology* **2013**, *2*, M3084–M3100 (cit. on p. 6).
- (32) Marinaro, M.; Theil, S.; Jörissen, L.; Wohlfahrt-Mehrens, M. New insights about the stability of lithium bis(trifluoromethane)sulfonimide-tetraglyme as electrolyte for Li-O₂ batteries. *Electrochimica Acta* **2013**, *108*, 795–800 (cit. on pp. 6, 9).
- (33) Laoire, C. O.; Mukerjee, S.; Abraham, K. M.; Plichta, E. J.; Hendrickson, M. A. Elucidating the Mechanism of Oxygen Reduction for Lithium-Air Battery Applications. *Journal of Physical Chemistry C* **2009**, *113*, 20127–20134 (cit. on p. 7).
- (34) Laoire, C. O.; Mukerjee, S.; Abraham, K. M.; Plichta, E. J.; Hendrickson, M. A. Influence of Nonaqueous Solvents on the Electrochemistry of Oxygen in the Rechargeable Lithium-Air Battery. *Journal of Physical Chemistry C* **2010**, *114*, 9178–9186 (cit. on p. 7).
- (35) Meini, S.; Tsiouvaras, N.; Schwenke, K. U.; Piana, M.; Beyer, H.; Lange, L.; Gasteiger, H. A. Rechargeability of Li-air cathodes pre-filled with discharge products using an ether-based electrolyte solution: implications for cycle-life of Li-air cells. *Physical Chemistry Chemical Physics* **2013**, *15*, 11478–11493 (cit. on p. 7).

- (36) Lu, Y.-C.; Gallant, B. M.; Kwabi, D. G.; Harding, J. R.; Mitchell, R. R.; Whittingham, M. S.; Shao-Horn, Y. Lithium-oxygen batteries: bridging mechanistic understanding and battery performance. *Energy & Environmental Science* **2013**, *6*, 750–768 (cit. on pp. 7, 9, 10).
- (37) Read, J. Characterization of the lithium/oxygen organic electrolyte battery. *Journal of The Electrochemical Society* **2002**, *149*, A1190–A1195 (cit. on p. 8).
- (38) Trahan, M. J.; Mukerjee, S.; Plichta, E. J.; Hendrickson, M. A.; Abraham, K. M. Studies of Li-Air Cells Utilizing Dimethyl Sulfoxide-Based Electrolyte. *Journal of The Electrochemical Society* **2013**, *160*, A259–A267 (cit. on p. 8).
- (39) Xu, W.; Xiao, J.; Zhang, J.; Wang, D. Y.; Zhang, J. G. Optimization of Nonaqueous Electrolytes for Primary Lithium/Air Batteries Operated in Ambient Environment. *Journal of The Electrochemical Society* **2009**, *156*, A773–A779 (cit. on p. 8).
- (40) Laoire, C. O.; Mukerjee, S.; Plichta, E. J.; Hendrickson, M. A.; Abraham, K. M. Rechargeable Lithium/TEGDME-LiPF₆/O₂ Battery. *Journal of The Electrochemical Society* **2011**, *158*, A302–A308 (cit. on pp. 8, 9).
- (41) Bryantsev, V. S.; Uddin, J.; Giordani, V.; Walker, W.; Addison, D.; Chase, G. V. The Identification of Stable Solvents for Nonaqueous Rechargeable Li-Air Batteries. *Journal of The Electrochemical Society* **2012**, *160*, A160–A171 (cit. on pp. 8, 10).
- (42) McCloskey, B. D.; Bethune, D. S.; Shelby, R. M.; Girishkumar, G.; Luntz, A. C. Solvents' Critical Role in Nonaqueous Lithium–Oxygen Battery Electrochemistry. *The Journal of Physical Chemistry Letters* **2011**, *2*, 1161–1166 (cit. on p. 9).
- (43) McCloskey, B. D. and Speidel, A. and Scheffler, R. and Miller, D. C. and Viswanathan, V. and Hummelshøj, J. S. and Nørskov, J. K. and Luntz, A. C. Twin Problems of Interfacial Carbonate Formation in Nonaqueous Li-O₂ Batteries. *The Journal of Physical Chemistry Letters* **2012**, *8*, 997–1001 (cit. on p. 9).
- (44) Freunberger, S. A.; Chen, Y. H.; Peng, Z. Q.; Griffin, J. M.; Hardwick, L. J.; Barde, F.; Novak, P.; Bruce, P. G. Reactions in the Rechargeable Lithium-O₂ Battery with Alkyl Carbonate Electrolytes. *Journal of the American Chemical Society* **2011**, *133*, 8040–8047 (cit. on p. 9).
- (45) Bryantsev, V.; Blanco, M. Computational study of the mechanisms of superoxide-induced decomposition of organic carbonate-based electrolytes. *The Journal of Physical Chemistry Letters* **2011**, *2*, 379–383 (cit. on p. 9).
- (46) Peng, Z.; Freunberger, S. A.; Chen, Y.; Bruce, P. G. A Reversible and Higher-Rate Li-O₂ Battery. *Science* **2012**, *337*, 563–566 (cit. on p. 9).
- (47) Lewandowski, A.; Świdarska-Mocek, A. Ionic liquids as electrolytes for Li-ion batteries—An overview of electrochemical studies. *Journal of Power Sources* **2009**, *194*, 601–609 (cit. on p. 9).

- (48) Allen, C. J.; Mukerjee, S.; Plichta, E. J.; Hendrickson, M. A.; Abraham, K. M. Oxygen Electrode Rechargeability in an Ionic Liquid for the Li–Air Battery. *The Journal of Physical Chemistry Letters* **2011**, *2*, 2420–2424 (cit. on p. 9).
- (49) Kowaluk, I.; Read, J.; Salomon, M. Li-air batteries: A classic example of limitations owing to solubilities. *Pure and Applied Chemistry* **2007**, *79*, 851–860 (cit. on p. 9).
- (50) Sandhu, S. S.; Brutchen, G. W.; Fellner, J. P. Lithium/air cell: Preliminary mathematical formulation and analysis. *Journal of Power Sources* **2007**, *170*, 196–209 (cit. on pp. 9, 10).
- (51) Lu, Y. C.; Gasteiger, H. A.; Parent, M. C.; Chiloyan, V.; Shao-Horn, Y. The Influence of Catalysts on Discharge and Charge Voltages of Rechargeable Li–Oxygen Batteries. *Electrochemical and Solid State Letters* **2010**, *13*, A69–A72 (cit. on p. 9).
- (52) Lu, Y.; Gasteiger, H.; Shao-Horn, Y. Catalytic activity trends of oxygen reduction reaction for nonaqueous Li-air batteries. *Journal of the American Chemical Society* **2011**, *133*, 19048–19051 (cit. on p. 9).
- (53) Débart, A. and Bao, J. and Armstrong, G. and Bruce, P. G. An O₂ cathode for rechargeable lithium batteries: The effect of a catalyst. *Journal of Power Sources* **2007**, *174*, 13th International Meeting on Lithium Batteries, 1177–1182 (cit. on p. 9).
- (54) Débart, A. and Paterson, A. J. and Bao, J. and Bruce, P. G. α -MnO₂ nanowires: a catalyst for the O₂ electrode in rechargeable lithium batteries. *Angewandte Chemie (International ed. in English)* **2008**, *47*, 4521–4 (cit. on p. 9).
- (55) Kim, K. S.; Park, Y. J. Catalytic properties of Co₃O₄ nanoparticles for rechargeable Li/air batteries. *Nanoscale Research Letters* **2012**, *7*, 47 (cit. on pp. 9, 14).
- (56) Hummelshøj, J. S.; Blomqvist, J.; Datta, S.; Vegge, T.; Rossmeisl, J.; Thygesen, K. S.; Luntz, A. C.; Jacobsen, K. W.; Nørskov, J. K. Communications: Elementary oxygen electrode reactions in the aprotic Li-air battery. *The Journal of Chemical Physics* **2010**, *132* 071101, 071101 (cit. on p. 9).
- (57) Viswanathan, V.; Thygesen, K. S.; Hummelshøj, J. S.; Nørskov, J. K.; Girishkumar, G.; McCloskey, B. D.; Luntz, A. C. Electrical conductivity in Li₂O₂ and its role in determining capacity limitations in non-aqueous Li - O₂ batteries. *The Journal of Chemical Physics* **2011**, *135* 214704, 214704 (cit. on p. 9).
- (58) Ong, S. P.; Mo, Y.; Ceder, G. Low hole polaron migration barrier in lithium peroxide. *Physical Reviews B* **2012**, *85*, 081105 (cit. on pp. 9, 16).
- (59) Hou, J.; Yang, M.; Ellis, M. W.; Moore, R. B.; Yi, B. Lithium oxides precipitation in nonaqueous Li-air batteries. *Physical Chemistry Chemical Physics* **2012**, *14*, 13487–501 (cit. on p. 10).

- (60) Andrei, P.; Zheng, J. P.; Hendrickson, M.; Plichta, E. J. Some Possible Approaches for Improving the Energy Density of Li-Air Batteries. *Journal of The Electrochemical Society* **2010**, *157*, A1287–A1295 (cit. on p. 10).
- (61) Albertus, P.; Girishkumar, G.; McCloskey, B.; Sanchez-Carrera, R. S.; Kozinsky, B.; Christensen, J.; Luntz, A. C. Identifying Capacity Limitations in the Li/Oxygen Battery Using Experiments and Modeling. *Journal of The Electrochemical Society* **2011**, *158*, A343–A351 (cit. on pp. 10, 111).
- (62) Newman, J.; Thomas-Alyea, K. E., *Electrochemical Systems*, 3rd ed.; John Wiley & Sons: 2004 (cit. on pp. 10, 17, 106, 110, 111, 129).
- (63) Wang, Y.; Cho, S. C. Analysis of Air Cathode Performance for Lithium-Air Batteries. *Journal of The Electrochemical Society* **2013**, *160*, A1847–A1855 (cit. on p. 10).
- (64) Neidhardt, J. P.; Fronczek, D. N.; Jahnke, T.; Danner, T.; Horstmann, B.; Bessler, W. G. A Flexible Framework for Modeling Multiple Solid, Liquid and Gaseous Phases in Batteries and Fuel Cells. *Journal of The Electrochemical Society* **2012**, *159*, A1528–A1542 (cit. on pp. 10, 11, 17, 121, 124, 164, 170).
- (65) Hartmann, P.; Grübl, D.; Sommer, H.; Janek, J.; Bessler, W. G.; Adelhelm, P. Pressure Dynamics in Metal–Oxygen (Metal–Air) Batteries: A Case Study on Sodium Superoxide Cells. *The Journal of Physical Chemistry C* **2014**, *118*, 1461–1471 (cit. on p. 10).
- (66) Sahapatombut, U.; Cheng, H.; Scott, K. Modelling the micro-macro homogeneous cycling behaviour of a lithium-air battery. *Journal of Power Sources* **2013**, *227*, 243–253 (cit. on p. 10).
- (67) Sahapatombut, U.; Cheng, H.; Scott, K. Modelling of electrolyte degradation and cycling behaviour in a lithium-air battery. *Journal of Power Sources* **2013**, *243*, 409–418 (cit. on p. 10).
- (68) Sahapatombut, U.; Cheng, H.; Scott, K. Modelling of operation of a lithium-air battery with ambient air and oxygen-selective membrane. *Journal of Power Sources* **2014**, *249*, 418–430 (cit. on p. 10).
- (69) Bryantsev, V. S.; Giordani, V.; Walker, W.; Blanco, M.; Zecevic, S.; Sasaki, K.; Uddin, J.; Addison, D.; Chase, G. V. Predicting solvent stability in aprotic electrolyte Li-air batteries: nucleophilic substitution by the superoxide anion radical ($O_2(\bullet-)$). *The Journal of Physical Chemistry A* **2011**, *115*, 12399–409 (cit. on p. 10).
- (70) Zhang, T.; Imanishi, N.; Shimonishi, Y.; Hirano, A.; Takeda, Y.; Yamamoto, O.; Sammes, N. A novel high energy density rechargeable lithium-air battery. *Chemical communications (Cambridge, England)* **2010**, *46*, 1661–3 (cit. on pp. 11, 153).
- (71) Zhang, T.; Imanishi, N.; Takeda, Y.; Yamamoto, O. Aqueous Lithium/Air Rechargeable Batteries. *Chemistry Letters* **2011**, *40*, 668–673 (cit. on pp. 11, 12).

- (72) Wang, Y.; Zhou, H. A lithium-air battery with a potential to continuously reduce O₂ from air for delivering energy. *Journal of Power Sources* **2010**, *195*, 358–361 (cit. on p. 11).
- (73) Bidault, F.; Brett, D. J. L.; Middleton, P. H.; Brandon, N. P. Review of gas diffusion cathodes for alkaline fuel cells. *Journal of Power Sources* **2009**, *187*, 39–48 (cit. on pp. 11, 14).
- (74) Pinnow, S.; Chavan, N.; Turek, T. Thin-film flooded agglomerate model for silver-based oxygen depolarized cathodes. *Journal of Applied Electrochemistry* **2011**, *1053*, 1–12 (cit. on pp. 11, 14, 31, 137, 139).
- (75) Spendelow, J. S.; Wieckowski, A. Electrocatalysis of oxygen reduction and small alcohol oxidation in alkaline media. *Physical Chemistry Chemical Physics* **2007**, *9*, 2654–2675 (cit. on pp. 11, 13, 31, 54, 59, 137).
- (76) Jörissen, L. Bifunctional oxygen/air electrodes. *Journal of Power Sources* **2006**, *155*, 23–32 (cit. on pp. 11, 13, 32, 144).
- (77) Stevens, P.; Toussaint, G.; Caillon, G.; Viaud, P.; Vinatier, P.; Cantau, C.; Fichet, O.; Sarrazin, C.; Mallouki, M. Development of a lithium air rechargeable battery. *ECS Transactions* **2010**, *28*, 1–12 (cit. on pp. 12–14).
- (78) Horstmann, B.; Danner, T.; Bessler, W. G. Precipitation in aqueous lithium–oxygen batteries: a model-based analysis. *Energy & Environmental Science* **2013**, *6*, 1299–1314 (cit. on pp. 12, 14, 17, 105, 112, 116, 117, 121, 123–125, 130, 131, 139, 153, 170).
- (79) Shimonishi, Y.; Zhang, T.; Imanishi, N.; Im, D.; Lee, D. J.; Hirano, A.; Takeda, Y.; Yamamoto, O.; Sammes, N. A study on lithium/air secondary batteries-Stability of the NASICON-type lithium ion conducting solid electrolyte in alkaline aqueous solutions. *Journal of Power Sources* **2011**, *196*, 5128–5132 (cit. on pp. 12, 13, 128, 153, 162).
- (80) Wolfenstine, J. Stability predictions of solid Li-ion conducting membranes in aqueous solutions. *Journal of Materials Science* **2010**, *45*, 3954–3956 (cit. on p. 13).
- (81) Zhang, T.; Imanishi, N.; Hasegawa, S.; Hirano, A.; Xie, J.; Takeda, Y.; Yamamoto, O.; Sammes, N. Li-Polymer Electrolyte-Water Stable Lithium-Conducting Glass Ceramics Composite for Lithium-air Secondary Batteries with an Aqueous Electrolyte. *Journal of The Electrochemical Society* **2008**, *155*, A965 (cit. on p. 13).
- (82) Visco, S.; Nimon, E.; Katz, B. In *Honolulu PRiME*, ECS: 2012, p 1156 (cit. on p. 13).
- (83) Imanishi, N.; Takeda, Y.; Yamamoto, O. Aqueous Lithium-air Rechargeable Batteries. *Electrochemistry* **2012**, *80*, 706–715 (cit. on pp. 13, 153).
- (84) Sun, Y. Lithium ion conducting membranes for lithium-air batteries. *Nano Energy* **2013**, *2*, 801–816 (cit. on p. 13).

- (85) Demarconnay, L.; Coutanceau, C.; Léger, J.-M. Electroreduction of dioxygen (ORR) in alkaline medium on Ag/C and Pt/C nanostructured catalysts—effect of the presence of methanol. *Electrochimica Acta* **2004**, *49*, 4513–4521 (cit. on p. 13).
- (86) Wittmaier, D.; Danner, T.; Wagner, N.; Friedrich, K. A. Screening and further investigations on promising bi-functional catalysts for metal-air batteries with an aqueous alkaline electrolyte. *Journal of Applied Electrochemistry* **2013**, *44*, 73–85 (cit. on pp. 13, 31, 56, 144, 165).
- (87) Koninck, M. D.; Marsan, B. $Mn_xCu_{(1-x)}Co_2O_4$ used as bifunctional electrocatalyst in alkaline medium. *Electrochimica Acta* **2008**, *53*, 7012–7021 (cit. on pp. 13, 144).
- (88) Hamdani, M.; Singh, R. N.; Chartier, P. Co_3O_4 and Co- Based Spinel Oxides Bifunctional Oxygen Electrodes. *International Journal of Electrochemical Science* **2010**, *5*, 556–577 (cit. on pp. 13, 32, 144).
- (89) Cheng, F.; Shen, J.; Peng, B.; Pan, Y.; Tao, Z.; Chen, J. Rapid room-temperature synthesis of nanocrystalline spinels as oxygen reduction and evolution electrocatalysts. *Nature Chemistry* **2011**, *3*, 79–84 (cit. on p. 13).
- (90) Ross, P. N.; Sokol, H. The Corrosion of Carbon Black Anodes in Alkaline Electrolyte. *Journal of The Electrochemical Society* **1984**, *131*, 1742–1750 (cit. on p. 13).
- (91) Staud, N.; Ross, P. N. The Corrosion of Carbon Black Anodes in Alkaline Electrolyte. *Journal of The Electrochemical Society* **1986**, *133*, 1079–1084 (cit. on p. 13).
- (92) Ross, P. N.; Sattler, M. The Corrosion of Carbon Black Anodes in Alkaline Electrolyte. *Journal of The Electrochemical Society* **1988**, *135*, 1464–1470 (cit. on p. 13).
- (93) Staud, N.; Sokol, H.; Ross, J. P. N. The Corrosion of Carbon Black Anodes in Alkaline Electrolyte. *Journal of The Electrochemical Society* **1989**, *136*, 3570–3576 (cit. on p. 13).
- (94) Wagner, N.; Schulze, M.; Gülzow, E. Long term investigations of silver cathodes for alkaline fuel cells. *Journal of Power Sources* **2004**, *127*, 264–272 (cit. on pp. 13, 39).
- (95) Wittmaier, D.; Wagner, N.; Friedrich, K. A.; Amin, H. M.; Baltruschat, H. Modified carbon-free silver electrodes for the use as cathodes in lithium-air batteries with an aqueous alkaline electrolyte. *Journal of Power Sources* **2014**, accepted (cit. on pp. 13, 172).
- (96) Andrei, P.; Zheng, J. P.; Hendrickson, M.; Plichta, E. J. Modeling of Li-Air Batteries with Dual Electrolyte. *Journal of The Electrochemical Society* **2012**, *159*, A770 (cit. on pp. 14, 171).
- (97) Jo, J.-H.; Yi, S.-C. A computational simulation of an alkaline fuel cell. *Journal of Power Sources* **1999**, *84*, 87–106 (cit. on p. 14).

-
- (98) Shah, A.; Luo, K.; Ralph, T.; Walsh, F. Recent trends and developments in polymer electrolyte membrane fuel cell modelling. *Electrochimica Acta* **2011**, *56*, 3731–3757 (cit. on p. 14).
- (99) Srinivasan, S.; Hurwitz, H. Theory of a thin film model of porous gas-diffusion electrodes. *Electrochimica Acta* **1967**, *12*, 495–512 (cit. on p. 14).
- (100) Giner, J.; Hunter, C. The Mechanism of Operation of the Teflon-Bonded Gas Diffusion Electrode: A Mathematical Model. *Journal of The Electrochemical Society* **1969**, *116*, 1124 (cit. on p. 14).
- (101) Wang, X.; Nguyen, T. V. Modeling the Effects of Capillary Property of Porous Media on the Performance of the Cathode of a PEMFC. *Journal of The Electrochemical Society* **2008**, *155*, B1085–B1092 (cit. on p. 14).
- (102) Kumbur, E. C.; Sharp, K. V.; Mench, M. M. Validated Leverett Approach for Multiphase Flow in PEFC Diffusion Media - I. Hydrophobicity Effect. *Journal of The Electrochemical Society* **2007**, *154*, B1295 –B1304 (cit. on pp. 15, 82).
- (103) Kumbur, E. C.; Sharp, K. V.; Mench, M. M. Validated Leverett Approach for Multiphase Flow in PEFC Diffusion Media - II. Compression Effect. *Journal of The Electrochemical Society* **2007**, *154*, B1305 –B1314 (cit. on pp. 15, 82).
- (104) Kumbur, E. C.; Sharp, K. V.; Mench, M. M. Validated Leverett Approach for Multiphase Flow in PEFC Diffusion Media - III. Temperature Effect and Unified Approach. *Journal of The Electrochemical Society* **2007**, *154*, B1315 –B1324 (cit. on pp. 15, 82, 126, 148, 149).
- (105) Gostick, J. T.; Fowler, M. W.; Ioannidis, M. A.; Pritzker, M. D.; Volfkovich, Y.; Sakars, A. Capillary pressure and hydrophilic porosity in gas diffusion layers for polymer electrolyte fuel cells. *Journal of Power Sources* **2006**, *156*, 375–387 (cit. on pp. 15, 82).
- (106) Nguyen, T. V.; Lin, G.; Ohn, H.; Wang, X. Measurement of Capillary Pressure Property of Gas Diffusion Media Used in Proton Exchange Membrane Fuel Cells. *Electrochemical and Solid-State Letters* **2008**, *11*, B127–B131 (cit. on p. 15).
- (107) Dwenger, S.; Eigenberger, G.; Nieken, U. Measurement of Capillary Pressure–Saturation Relationships Under Defined Compression Levels for Gas Diffusion Media of PEM Fuel Cells. *Transport in Porous Media* **2011**, *91*, 281–294 (cit. on pp. 15, 82, 96).
- (108) Fairweather, J. D.; Cheung, P.; St-Pierre, J.; Schwartz, D. T. A microfluidic approach for measuring capillary pressure in PEMFC gas diffusion layers. *Electrochemistry Communications* **2007**, *9*, 2340–2345 (cit. on p. 15).
- (109) Niu, X.; Munekata, T.; Hyodo, S.; Suga, K. An investigation of water-gas transport processes in the gas-diffusion-layer of a PEM fuel cell by a multiphase multiple-relaxation-time lattice Boltzmann model. *Journal of Power Sources* **2007** (cit. on pp. 15, 65).

- (110) Hao, L.; Cheng, P. Capillary pressures in carbon paper gas diffusion layers having hydrophilic and hydrophobic pores. *International Journal of Heat and Mass Transfer* **2012**, *55*, 133–139 (cit. on pp. 15, 17, 65, 74, 87, 126, 148, 149).
- (111) Park, J.; Li, X. Multi-phase micro-scale flow simulation in the electrodes of a PEM fuel cell by lattice Boltzmann method. *Journal of Power Sources* **2008**, *178*, 248–257 (cit. on pp. 15, 65).
- (112) Karplus, M.; Levitt, M.; Warshel, A. Noble prize in chemistry "for the development of multiscale models for complex chemical systems"., http://www.nobelprize.org/nobel_prizes/chemistry/laureates/2013/ (accessed 03/18/2014) (cit. on p. 15).
- (113) Grew, K. N.; Chiu, W. K. S. A review of modeling and simulation techniques across the length scales for the solid oxide fuel cell. *Journal of Power Sources* **2012**, *199*, 1–13 (cit. on p. 16).
- (114) Burke, K. The ABC of DFT., <http://www.chem.uci.edu/~kieron/dftold2/materials/bookABCDFT/gamma/g1.pdf> (accessed 03/18/2014) (cit. on p. 15).
- (115) Jacob, T. The mechanism of forming H₂O from H-2 and O-2 over a Pt catalyst via direct oxygen reduction. *Fuel Cells* **2006**, *6*, 159–181 (cit. on p. 16).
- (116) Nørskov, J.; Rossmeisl, J.; Logadottir, A.; Lindqvist, L.; Kitchin, J.; Bligaard, T.; Jonsson, H. Origin of the overpotential for oxygen reduction at a fuel-cell cathode. *Journal of Physical Chemistry B* **2004**, *108*, 17886–17892 (cit. on p. 16).
- (117) Frenkel, D.; Smit, B., *Understanding Molecular Simulation: From Algorithms to Applications*, 2nd ed.; Academic Press: 2001 (cit. on p. 16).
- (118) Pathria, R. K., *Statistical Mechanics*, 2nd ed.; Butterworth-Heinemann: 1996 (cit. on pp. 16, 66).
- (119) Castillo-Sanchez, J. M.; Danner, T.; Gross, J. Grand canonical Monte Carlo simulations of vapor-liquid equilibria using a bias potential from an analytic equation of state. *The Journal of Chemical Physics* **2013**, *138* 234106, – (cit. on p. 16).
- (120) Provatas, N.; Elder, K., *Phase-Field Methods in Materials Science and Engineering*, 1st ed.; Butterworth-Heinemann: 2010 (cit. on p. 17).
- (121) Horstmann, B.; Gallant, B.; Mitchell, R.; Bessler, W. G.; Shao-Horn, Y.; Bazant, M. Z. Rate-dependent morphology of Li₂O₂ growth in Li-O₂ batteries. *The Journal of Physical Chemistry Letters* **2013**, *4*, 4217–4222 (cit. on p. 17).
- (122) Sukop, M. C.; Thorne, D. T., *Lattice Boltzmann Modeling: An Introduction for Geoscientists and Engineers*, 1st ed.; Springer Berlin Heidelberg: 2006 (cit. on pp. 17, 65, 69, 73, 75).
- (123) Schütz, S.; Kissling, K.; Schilling, M.; Seyfert, C. In *Multiphase Flow Research*, Martin, S., Williams, J., Eds., 2009, 3–146 (cit. on pp. 17, 70).

- (124) Bernnat, J.; Rink, M.; Tuttlies, U.; Danner, T.; Nieken, U.; Eigenberger, G. Heat-Integrated Concepts for Automotive Exhaust Purification. *Topics in Catalysis* **2009**, *52*, 2052–2057 (cit. on p. 17).
- (125) Newman, J.; Tiedemann, W. Porous-electrode theory with battery applications. *AIChE Journal* **1975**, *21*, 25–41 (cit. on pp. 17, 38, 106, 113).
- (126) Remmlinger, J.; Tippmann, S.; Buchholz, M.; Dietmayer, K. Low-temperature charging of lithium-ion cells Part II: Model reduction and application. *Journal of Power Sources* **2014**, *254*, 268–276 (cit. on p. 17).
- (127) Bulan, A. A process for producing gas diffusion electrodes., DE Patent App. DE102005023615A1, 2006 (cit. on pp. 21, 33, 60).
- (128) Bard, A.; Faulkner, L., *Electrochemical Methods: Fundamentals and Applications*; Wiley: 2000 (cit. on pp. 21, 28, 39, 59).
- (129) Bagotsky, V., *Fundamentals of Electrochemistry*; The ECS Series of Texts and Monographs; Wiley: 2005 (cit. on p. 21).
- (130) Hamann, C.; Vielstich, W., *Elektrochemie*; John Wiley & Sons Australia, Limited: 2005 (cit. on pp. 24, 25).
- (131) Šepa, D.; Vojnovic, M.; Vracar, L.; Damjanovic, A. Apparent enthalpies of activation of electrodic oxygen reduction at platinum in different current density regions - II. Alkaline solution. *Electrochimica Acta* **1986**, *31*, 97–101 (cit. on pp. 29, 31, 137).
- (132) Abd El Rehim, S. S.; Hassan, H. H.; Ibrahim, M. A. M.; Amin, M. A. Electrochemical Behaviour of a Silver Electrode in NaOH Solutions. *Monatshefte fuer Chemie/Chemical Monthly* **1998**, *129*, 1103–1117 (cit. on pp. 29, 30, 57).
- (133) Stonehart, P. Potentiodynamic determination of electrode kinetics for chemisorbed reactants: The Ag/Ag₂O/OH⁻ system. *Electrochimica Acta* **1968**, *13*, 1789–1803 (cit. on p. 29).
- (134) Droog, J. M. M.; Huisman, F. Electrochemical formation and reduction of silver oxides in alkaline media. **1980**, *115*, 211–224 (cit. on p. 29).
- (135) Hampson, N.; Lee, J.; Morley, J. The electrochemistry of oxides of silver - a short review. *Electrochimica Acta* **1971**, *11*, 637–642 (cit. on pp. 29, 47).
- (136) Šepa, D.; Vojnovic, M.; Damjanovic, A. Oxygen reduction at silver electrodes in alkaline solutions. *Electrochimica Acta* **1970**, *15*, 1355–1366 (cit. on p. 31).
- (137) Lyons, M.; Brandon, M. The oxygen evolution reaction on passive oxide covered transition metal electrodes in aqueous alkaline solution. Part I - Nickel. *International Journal of Electrochemical Science* **2008**, *3*, 1386–1424 (cit. on p. 32).
- (138) Lyons, M. E. G.; Brandon, M. P. The Oxygen Evolution Reaction on Passive Oxide Covered Transition Metal Electrodes in Alkaline Solution Part II - Cobalt. **2008**, *3*, 1425–1462 (cit. on p. 32).

- (139) Lyons, M. E. G.; Floquet, S. Mechanism of oxygen reactions at porous oxide electrodes. Part 2-Oxygen evolution at RuO₂, IrO₂ and Ir_xRu_{1-x}O₂ electrodes in aqueous acid and alkaline solution. *Physical Chemistry Chemical Physics* **2011**, *13*, 5314–5335 (cit. on p. 32).
- (140) Bockris, J. O. The Electrocatalysis of Oxygen Evolution on Perovskites. *Journal of The Electrochemical Society* **1984**, *131*, 290 (cit. on p. 32).
- (141) Eswara, S., *Electron Microscopy Group of Materials Science*, <https://www.uni-ulm.de/en/einrichtungen/electron-microscopy-group-of-materials-science.html>; University of Ulm: Ulm, 2013 (cit. on pp. 32–36, 62, 80).
- (142) Boulder Laboratory IMOD - Image processing, MOdeling and Display programs., <http://bio3d.colorado.edu/imod/> (accessed 03/18/2014) (cit. on p. 36).
- (143) Math2Market GmbH - Becker, J.; Wiegmann, A. GeoDict - User Guide., <http://www.geodict.com/userguide.php?lang=en> (accessed 03/18/2014) (cit. on pp. 37, 81, 87).
- (144) Bear, J., *Dynamics of Fluids in Porous Media*; Elsevier: New York, 1972 (cit. on pp. 38, 46, 88).
- (145) Wagner, N., *Institute for Technical Thermodynamics - Electrochemical Energy Technology*, <http://www.dlr.de/tt/en/desktopdefault.aspx/tabid-7197/>; German Aerospace Center: Stuttgart, 2013 (cit. on pp. 39, 42, 48, 60).
- (146) Compton, R.; Banks, C., *Understanding Voltammetry*; Imperial College Press: 2011 (cit. on p. 40).
- (147) Barsoukov, E.; Macdonald, J., *Impedance spectroscopy: theory, experiment, and applications*, 2nd; John Wiley&Sons, Inc.: 2005 (cit. on pp. 40, 42, 49, 50).
- (148) Lasia, A. In *Modern Aspects of Electrochemistry*, Conway, B. E., Bockris, J., White, R., Eds.; Kluwer Academic/Plenum Publishers: New York, 1999; Vol. 32, pp 143–248 (cit. on pp. 40, 50).
- (149) In *THALES manual*; Zahner Elektrik GmbH: Kronach, 2013; Chapter 4 (cit. on pp. 41, 49, 55).
- (150) de Levie, R. In *Advances in electrochemistry and electrochemical engineering: Electrochemistry*, Delahay, P., Ed.; Interscience Publ.: 1967; Vol. 6, p 329 (cit. on p. 42).
- (151) Goldin, G. M.; Colclasure, A. M.; Wiedemann, A. H.; Kee, R. J. Three-dimensional particle-resolved models of Li-ion batteries to assist the evaluation of empirical parameters in one-dimensional models. *Electrochimica Acta* **2012**, *64*, 118–129 (cit. on p. 46).
- (152) Matula, R. A. Electrical Resistivity of Copper, Gold, Palladium, and Silver. *Journal of Physical and Chemical Reference Data* **1979**, *8*, 1147 (cit. on pp. 47, 50, 116).

- (153) Gewies, S.; Bessler, W. G. Physically Based Impedance Modeling of Ni/YSZ Cermet Anodes. *Journal of The Electrochemical Society* **2008**, *155*, B937–B952 (cit. on pp. 50, 124).
- (154) Gierszewski, P. J.; Finn, P. A.; Kirk, D. W. Properties of LiOH and LiNO₃ aqueous solutions. *Fusion Engineering and Design* **1990**, *13*, 59–71 (cit. on pp. 52, 53).
- (155) Maurice, V.; Klein, L. H.; Strehblow, H.-H.; Marcus, P. In Situ STM Study of the Surface Structure, Dissolution, and Early Stages of Electrochemical Oxidation of the Ag(111) Electrode. *The Journal of Physical Chemistry C* **2007**, *111*, 16351–16361 (cit. on p. 57).
- (156) Savinova, E. R.; Pettinger, B.; Doblhofer, K. In situ Raman spectroscopy studies of the interface between silver (111) electrodes and alkaline NaF electrolytes. *Journal of Electroanalytical Chemistry* **1997**, *430*, 47–56 (cit. on p. 57).
- (157) Aidun, C. K.; Clausen, J. R. Lattice-Boltzmann Method for Complex Flows. *Annual Review of Fluid Mechanics* **2010**, *42*, 439–472 (cit. on p. 65).
- (158) Freund, J. B. Numerical Simulation of Flowing Blood Cells. *Annual Review of Fluid Mechanics* **2014**, *46*, 67–95 (cit. on p. 65).
- (159) Ben Salah, Y.; Tabe, Y.; Chikahisa, T. Two phase flow simulation in a channel of a polymer electrolyte membrane fuel cell using the lattice Boltzmann method. *Journal of Power Sources* **2012**, *199*, 85–93 (cit. on p. 65).
- (160) Latz, A., *DLR - Institute for Technical Thermodynamics - Computational Electrochemistry*, <http://www.dlr.de/tt/en/desktopdefault.aspx/tabid-8172/>; Helmholtz Institute Ulm for electrochemical energy storage (HIU): Ulm, 2013 (cit. on p. 65).
- (161) Tölke, J. Gitter-Boltzmann-Verfahren zur Simulation von Zweiphasenströmungen., Ph.D. Thesis, Technische Universität München, 2001 (cit. on pp. 68, 69, 72, 73, 75, 80).
- (162) McNamara, G. R.; Zanetti, G. Use of the Boltzmann Equation to Simulate Lattice-Gas Automata. *Physical Review Letters* **1988**, *61*, 2332–2335 (cit. on p. 68).
- (163) Chen, S.; Doolen, G. D. Lattice Boltzmann Method. *Annual Reviews* **1998**, *30*, 329–364 (cit. on p. 68).
- (164) Qian, Y.; D’Humières, D.; Lallemand, P. Lattice BGK Models for Navier-Stokes Equation. *Europhysics Letters* **1992**, *17*, 479–484 (cit. on pp. 68, 69).
- (165) Bhatnagar, P. L.; Gross, E. P.; Krook, M. A Model for Collision Processes in Gases. I. Small Amplitude Processes in Charged and Neutral One-Component Systems. *Physical Reviews* **1954**, *94*, 511–525 (cit. on p. 70).
- (166) D’Humières, D.; Ginzburg, I.; Krafczyk, M.; Lallemand, P.; Luo, L.-S. Multiple-relaxation-time lattice Boltzmann models in three dimensions. *Philosophical transactions. Series A, Mathematical, physical, and engineering sciences* **2002**, *360*, 437–51 (cit. on p. 70).

- (167) Hirt, C.; Nichols, B. Volume of fluid (VOF) method for the dynamics of free boundaries. *Journal of Computational Physics* **1981**, *39*, 201–225 (cit. on p. 70).
- (168) Shan, X.; Chen, H. Lattice Boltzmann model for simulating flows with multiple phases and components. *Physical Review E* **1993**, *47*, 1815–1819 (cit. on p. 71).
- (169) Shan, X.; Chen, H. Simulation of nonideal gases and liquid-gas phase transitions by the lattice Boltzmann equation. *Physical Review E* **1994**, *49*, 2941–2948 (cit. on p. 71).
- (170) Huang, H.; Wang, L.; Lu, X.-y. Evaluation of three lattice Boltzmann models for multiphase flows in porous media. *Computers & Mathematics with Applications* **2011**, *61*, 3606–3617 (cit. on p. 71).
- (171) Swift, M. R.; Osborn, W. R.; Yeomans, J. M. Lattice Boltzmann Simulation of Nonideal Fluids. *Physical Review Letters* **1995**, *75*, 830–833 (cit. on p. 71).
- (172) Swift, M. R.; Orlandini, E.; Osborn, W. R.; Yeomans, J. M. Lattice Boltzmann simulations of liquid-gas and binary fluid systems. *Physical Review E* **1996**, *54*, 5041–5052 (cit. on p. 71).
- (173) Zheng, H.; Shu, C.; Chew, Y. A lattice Boltzmann model for multiphase flows with large density ratio. *Journal of Computational Physics* **2006**, *218*, 353–371 (cit. on pp. 71, 72).
- (174) Rothman, D. H.; Keller, J. M. Immiscible cellular-automaton fluids. *Journal of Statistical Physics* **1988**, *52*, 1119–1127 (cit. on pp. 71, 74).
- (175) Gunstensen, A. K.; Rothman, D. H.; Zaleski, S.; Zanetti, G. Lattice Boltzmann model of immiscible fluids. *Physical Review A* **1991**, *43*, 4320–4327 (cit. on p. 71).
- (176) Gunstensen, A. K.; Rothman, D. H. Microscopic Modeling of Immiscible Fluids in Three Dimensions by a Lattice Boltzmann Method. *Europhysics Letters* **1992**, *18*, 157 (cit. on p. 71).
- (177) Grunau, D.; Chen, S.; Eggert, K. A lattice Boltzmann model for multiphase fluid flows. *Physics of Fluids A: Fluid Dynamics* **1993**, *5*, 2557 (cit. on p. 71).
- (178) Inamuro, T.; Ogata, T.; Tajima, S.; Konishi, N. A lattice Boltzmann method for incompressible two-phase flows with large density differences. *Journal of Computational Physics* **2004**, *198*, 628–644 (cit. on p. 71).
- (179) Inamuro, T.; Ogata, T.; Ogino, F. Numerical simulation of bubble flows by the lattice Boltzmann method. *Future Generation Computer Systems* **2004**, *20*, 959–964 (cit. on p. 71).
- (180) Leclaire, S.; Reggio, M.; Trépanier, J.-Y. Isotropic color gradient for simulating very high-density ratios with a two-phase flow lattice Boltzmann model. *Computers & Fluids* **2011**, *48*, 98–112 (cit. on pp. 72, 74, 77).
- (181) Leclaire, S.; Reggio, M.; Trépanier, J.-Y. Numerical evaluation of two recoloring operators for an immiscible two-phase flow lattice Boltzmann model. *Applied Mathematical Modelling* **2012**, *36*, 2237–2252 (cit. on pp. 72, 74).

-
- (182) Leclaire, S.; Reggio, M.; Trépanier, J.-Y. Progress and investigation on lattice Boltzmann modeling of multiple immiscible fluids or components with variable density and viscosity ratios. *Journal of Computational Physics* **2013**, *246*, 318–342 (cit. on pp. 72, 74, 76, 79).
- (183) Leclaire, S.; Pellerin, N. Enhanced equilibrium distribution functions for simulating immiscible multiphase flows with variable density ratios in a class of lattice Boltzmann models. *Journal of Multiphase Flow* **2013** (cit. on p. 72).
- (184) Liu, H.; Valocchi, A. J.; Kang, Q. Three-dimensional lattice Boltzmann model for immiscible two-phase flow simulations. *Physical Review E* **2012**, *85*, 046309 (cit. on pp. 72, 74, 76–79).
- (185) Reis, T.; Phillips, T. N. Lattice Boltzmann model for simulating immiscible two-phase flows. *Journal of Physics A: Mathematical and Theoretical* **2007**, *40*, 4033–4053 (cit. on pp. 72, 77, 78).
- (186) Lishchuk, S. V.; Care, C. M.; Halliday, I. Lattice Boltzmann algorithm for surface tension with greatly reduced microcurrents. *Physical Review E* **2003**, *67*, 036701 (cit. on p. 72).
- (187) Sbragaglia, M.; Benzi, R.; Biferale, L.; Succi, S.; Sugiyama, K.; Toschi, F. Generalized lattice Boltzmann method with multirange pseudopotential. *Physical Review E* **2007**, *75*, 026702 (cit. on pp. 72, 77, 78).
- (188) Tölke, J.; Krafczyk, M.; Schulz, M.; Rank, E. Lattice Boltzmann simulations of binary fluid flow through porous media. *Philosophical transactions. Series A, Mathematical, physical, and engineering sciences* **2002**, *360*, 535–45 (cit. on pp. 72, 74, 79).
- (189) Latva-Kokko, M.; Rothman, D. Diffusion properties of gradient-based lattice Boltzmann models of immiscible fluids. *Physical Review E* **2005**, *71*, 056702 (cit. on p. 72).
- (190) Schulz, V., *Maschinenbau*, <http://www.mb.dhbw-mannheim.de/ansprechpartner/prof-dr-volker-schulz/>; Duale Hochschule Baden Württemberg: Mannheim, 2013 (cit. on pp. 74, 101).
- (191) Latva-Kokko, M.; Rothman, D. Static contact angle in lattice Boltzmann models of immiscible fluids. *Physical Review E* **2005**, *72*, 046701 (cit. on p. 80).
- (192) Zhao, Q; Liu, Y; Wang, C Development and evaluation of electroless Ag-PTFE composite coatings with anti-microbial and anti-corrosion properties. *Applied Surface Science* **2005**, *252*, 1620–1627 (cit. on p. 85).
- (193) Schaap, M. G.; Porter, M. L.; Christensen, B. S. B.; Wildenschild, D. Comparison of pressure-saturation characteristics derived from computed tomography and lattice Boltzmann simulations. *Water Resources Research* **2007**, *43*, W12S06 (cit. on p. 86).

- (194) Leverett, M. Capillary behavior in porous solids. *Transactions of the American Institute of Mining Engineers* **1940**, *142*, 152–169 (cit. on p. 86).
- (195) Udell, K. S. Heat transfer in porous media considering phase change and capillarity—the heat pipe effect. *International Journal of Heat and Mass Transfer* **1985**, *28*, 485–495 (cit. on p. 86).
- (196) Zamel, N.; Li, X.; Becker, J.; Wiegmann, A. Effect of liquid water on transport properties of the gas diffusion layer of polymer electrolyte membrane fuel cells. *International Journal of Hydrogen Energy* **2011**, *36*, 5466–5478 (cit. on p. 94).
- (197) Hutzenlaub, T.; Becker, J.; Zengerle, R.; Thiele, S. Modelling the water distribution within a hydrophilic and hydrophobic 3D reconstructed cathode catalyst layer of a proton exchange membrane fuel cell. *Journal of Power Sources* **2013**, *227*, 260–266 (cit. on p. 94).
- (198) Danner, T.; Horstmann, B.; Wittmaier, D.; Wagner, N.; Bessler, W. G. Reaction and transport in Ag/Ag₂O gas diffusion electrodes of aqueous Li–O₂ batteries: Experiments and modeling. *Journal of Power Sources* **2014**, *264*, 320–332 (cit. on pp. 105, 120, 125, 133, 137, 141, 149).
- (199) Taylor, R.; Krishna, R., *Multicomponent Mass Transfer*; Wiley Series in Chemical Engineering; Wiley: 1993 (cit. on p. 110).
- (200) Nieken, U., *Chemische Reaktionstechnik 2*; Skripte Universität Stuttgart; Institute for chemical process engineering (ICVT): 2007 (cit. on pp. 110, 111, 119, 120).
- (201) Doyle, M.; Fuller, T. F.; Newman, J. Modeling of Galvanostatic Charge and Discharge of the Lithium Polymer Insertion Cell. *Journal of the Electrochemical Society* **1993**, *140*, 1526–1533 (cit. on p. 111).
- (202) Stewart, S. G.; Newman, J. The Use of UV/vis Absorption to Measure Diffusion Coefficients in LiPF₆ Electrolytic Solutions. *Journal of The Electrochemical Society* **2008**, *155*, F13 (cit. on p. 112).
- (203) Stewart, S. G.; Newman, J. Measuring the Salt Activity Coefficient in Lithium-Battery Electrolytes. *Journal of The Electrochemical Society* **2008**, *155*, A458 (cit. on p. 112).
- (204) Nyman, A.; Behm, M.; Lindbergh, G. Electrochemical characterisation and modelling of the mass transport phenomena in LiPF₆-EC-EMC electrolyte. *Electrochimica Acta* **2008**, *53*, 6356–6365 (cit. on p. 112).
- (205) Bischoff, K. B. Effectiveness factors for general reaction rate forms. *AIChE Journal* **1965**, *11*, 351–355 (cit. on p. 119).
- (206) Herskowitz, M.; Smith, J. M. Trickle-bed reactors: A review. *AIChE Journal* **1983**, *29*, 1–18 (cit. on p. 119).
- (207) Bessler, W. G.; Gewies, S.; Vogler, M. A new framework for physically based modeling of solid oxide fuel cells. *Electrochimica Acta* **2007**, *53*, 1782–1800 (cit. on pp. 124, 164, 170).

- (208) Yurkiv, V.; Utz, A.; Weber, A.; Ivers-Tiffée, E.; Volpp, H.-R.; Bessler, W. G. Elementary kinetic modeling and experimental validation of electrochemical CO oxidation on Ni/YSZ pattern anodes. *Electrochimica Acta* **2012**, *59*, 573–580 (cit. on pp. 124, 137).
- (209) Goodwin, D. G. Cantera., <http://code.google.com/p/cantera> (accessed 04/07/2014) (cit. on p. 124).
- (210) Deuffhard, P.; Hairer, E.; Zugck, J. One-step and extrapolation methods for differential-algebraic systems. *Numerische Mathematik* **1987**, *51*, 501–516 (cit. on p. 124).
- (211) Vargaftik, N.; Volkov, B.; Voljak, L. International tables of the surface tension of water. *Journal of Physical and Chemical Reference Data* **1983**, *12*, 817–820 (cit. on p. 126).
- (212) Markin, V. S.; Volkov, A. G. Quantitative Theory of Surface Tension and Surface Potential of Aqueous Solutions of Electrolytes. *The Journal of Physical Chemistry B* **2002**, *106*, 11810–11817 (cit. on p. 126).
- (213) Laliberte, M. Model for Calculating the Viscosity of Aqueous Solutions - Corrected. *J. Chem. Eng. Data* **2007**, *52*, 1507–1508 (cit. on p. 128).
- (214) Han, P.; Bartels, D. M. Temperature Dependence of Oxygen Diffusion in H₂O and D₂O. *The Journal of Physical Chemistry* **1996**, *100*, 5597–5602 (cit. on p. 128).
- (215) Robinson, R.; Stokes, R., *Electrolyte Solutions: Second Revised Edition*; Dover Books on Chemistry; Dover Publications: 2002, pp 155–160 (cit. on p. 129).
- (216) Dai, H.; Zawodzinski, T. A. The dependence of lithium transference numbers on temperature, salt concentration and anion type in poly (vinylidene fluoride)–hexafluoropropylene copolymer-based gel electrolytes. *Journal of Electroanalytical Chemistry* **1998**, *459*, 111–119 (cit. on p. 129).
- (217) Herrington, T. M.; Pethybridge, A. D.; Roffey, M. Densities of Aqueous Lithium, Sodium, and Potassium Hydroxides from 25 to 75 °C at 1 atm. *Journal of Chemical & Engineering Data* **1986**, *1*, 31–34 (cit. on p. 130).
- (218) Perron, G.; Perron, J.; Desnoyer, J. E.; Roux, A. H. Capacites calorifiques, volumes, expansibilites et compressibilites des solutions aqueuses concentrees de LiOH, NaOH et KOH. *Canadian Journal of Chemistry* **1984**, *62*, 878–885 (cit. on p. 130).
- (219) Pitzer, K. S., *Activity coefficients in electrolyte solutions*, 2nd; CRC Press: 1991 (cit. on pp. 130, 134, 197).
- (220) Millero, F. J.; Ward, G. K.; Chetirkin, P. V. Relative sound velocities of sea salts at 25°C. *The Journal of the Acoustical Society of America* **1977**, *61*, 1492–1498 (cit. on p. 130).
- (221) Buchner, R.; Hefter, G.; May, P. M.; Sipos, P. Dielectric Relaxation of Dilute Aqueous NaOH, NaAl(OH)₄, and NaB(OH)₄. *Journal of Physical Chemistry B* **1999**, *103*, 11186–11190 (cit. on pp. 133, 134).

- (222) Pátek, J.; Hrubý, J.; Klomfar, J.; Součková, M.; Harvey, A. H. Reference Correlations for Thermophysical Properties of Liquid Water at 0.1 MPa. *Journal of Physical and Chemical Reference Data* **2009**, *38*, 21–29 (cit. on pp. 133, 134).
- (223) Ohara Corporation. Data sheet of the Lithium-Ion Conducting Glass-Ceramic (LIC-GC)., <http://oharacorp.com/pdf/LIC-GC.pdf> (accessed 04/28/2014) (cit. on p. 134).
- (224) Atkins, P.; De Paula, J.; Bär, M., *Physikalische Chemie*, 5th ed.; Atkins, P., Ed.; Wiley VCH Verlag GmbH: 2012 (cit. on p. 134).
- (225) Monnin, C.; Dubois, M. Thermodynamics of the LiOH + H₂O System. *Journal of Chemical & Engineering Data* **2005**, *50*, 1109–1113 (cit. on pp. 134, 135).
- (226) Corti, H.; Crovetto, R.; Fernandez-Prini, R. Aqueous solutions of lithium hydroxide at various temperatures: Conductivity and activity coefficients. *Journal of Solution Chemistry* **1979**, *8*, 897–908 (cit. on p. 134).
- (227) Pickering, S. U. The hydrates of sodium, potassium, and lithium hydroxides. *Journal of the Chemical Society, Transactions* **1893**, *63* (cit. on pp. 134, 135).
- (228) Stephen, E. F.; Miller, P. D. Solubility of Lithium Hydroxide in Water and Vapor Pressure of Solutions above 220 °F. *Journal of Chemical & Engineering Data* **1962**, *7*, 501–505 (cit. on pp. 134, 135).
- (229) Mersmann, A. Calculation of interfacial tensions. *Journal of Crystal Growth* **1990**, *102*, 841–847 (cit. on p. 135).
- (230) Nielsen, A. E.; Söhnel, O. Interfacial tensions electrolyte crystal-aqueous solution, from nucleation data. *Journal of Crystal Growth* **1971**, *11*, 233–242 (cit. on p. 135).
- (231) Elliot, A. J.; Chenier, M. P.; Ouellette, D. C. Solubilities of hydrogen and oxygen in concentrated lithium salt solutions. *Fusion Engineering and Design* **1990**, *13*, 29–31 (cit. on pp. 135, 136, 139).
- (232) Lang, W.; Zander, R. Salting-out of oxygen from aqueous electrolyte solutions: prediction and measurement. *Industrial & Engineering Chemistry Fundamentals* **1986**, *25*, 775–782 (cit. on pp. 135, 136, 139).
- (233) McBride, B., *NASA Glenn Coefficients for Calculating Thermodynamic Properties of Individual Species*; NASA technical paper; National Aeronautics and Space Administration, John H. Glenn Research Center at Lewis Field: 2002 (cit. on p. 136).
- (234) Tromans, D. Modeling oxygen solubility in water and electrolyte solutions. *Industrial & Engineering Chemistry Research* **2000**, *39*, 805–812 (cit. on p. 136).
- (235) Faure, R.; Durand, R.; Genies, L. Electrochemical reduction of oxygen on platinum nanoparticles in alkaline media. **1998**, *44*, 1317–1327 (cit. on p. 137).

-
- (236) Eberle, D.; Horstmann, B. Oxygen reduction on transition metal catalysts in aqueous electrolyte : Elementary kinetic modeling. *Electrochimica Acta* **2014**, DOI:10.1016/j.electacta.2014.05.144 (cit. on p. 137).
- (237) Greszler, T. A.; Caulk, D.; Sinha, P. The Impact of Platinum Loading on Oxygen Transport Resistance. *Journal of The Electrochemical Society* **2012**, *159*, F831–F840 (cit. on p. 137).
- (238) Suzuki, T.; Kudo, K.; Morimoto, Y. Model for investigation of oxygen transport limitation in a polymer electrolyte fuel cell. *Journal of Power Sources* **2013**, *222*, 379–389 (cit. on pp. 137, 139).
- (239) A123 systems. Data sheet of the high power ANR26650M1-B cylindrical cell., http://info.a123systems.com/Portals/133376/content/data%20sheets/a123%20datasheet_26650m1b.pdf (accessed 04/26/2014) (cit. on p. 164).
- (240) Panasonic. Data sheet of the NCR18650 cylindrical cell., <http://www.panasonic.com/industrial/includes/pdf/ACA4000CE240-NCR18650.pdf> (accessed 04/26/2014) (cit. on p. 164).
- (241) Varta MicroBattery. Data sheet of the LIC 18650-22 FC cylindrical cell., http://www.varta-microbattery.com/applications/mb_data/documents/data_sheets/DS56621.pdf (accessed 04/26/2014) (cit. on p. 164).
- (242) Tang, W.; Zhu, Y.; Hou, Y.; Liu, L.; Wu, Y.; Loh, K. P.; Zhang, H.; Zhu, K. Aqueous rechargeable lithium batteries as an energy storage system of superfast charging. *Energy Environ. Sci.* **2013**, *6*, 2093–2104 (cit. on p. 172).

Appendices

A. Pitzer formalism

The Pitzer equations are a semi-empirical formalism which was developed by Kenneth S. Pitzer [219] for an accurate prediction of thermodynamic properties of concentrated electrolyte solutions. It is based on a virial expansion of the excess Gibbs energy with terms of increasing power in molality. In the limit of infinite dilution the theory converges with the limiting Debye-Hückel law.

The activity coefficient of a binary salt i (e.g. LiOH) is in this formalism expressed as

$$\ln\gamma_i = f_\gamma + B_\gamma m_i + C_\gamma m_i^2. \quad (\text{A.1})$$

The coefficients of the virial expansion are given by

$$f_\gamma = f_\Phi - A_\Phi \frac{2}{1.2} \ln(1 + 1.2\sqrt{I}) \quad (\text{A.2})$$

$$B_\gamma = B_\Phi + \beta_\Phi^{(0)} + \beta_\Phi^{(1)} g(2\sqrt{I}) \quad (\text{A.3})$$

$$C_\gamma = 1.5C_\Phi, \quad (\text{A.4})$$

where $I = 0.5 \sum z_i^2 m_i$ is the ionic strength of the electrolyte and

$$g(x) = \frac{2[1 - (1+x)\exp(-x)]}{x^2}.$$

The coefficients f_Φ and B_Φ are in turn given by

$$f_\Phi = -\frac{A_\Phi \sqrt{I}}{(1 + 1.2\sqrt{I})} \quad (\text{A.5})$$

$$B_\Phi = \beta_\Phi^{(0)} + \beta_\Phi^{(1)} \exp(-2\sqrt{I}). \quad (\text{A.6})$$

The activity coefficient of the solvent s (e.g. H_2O) can be calculated from the osmotic coefficient Φ according to

$$\ln\gamma_s = -2RT\Phi m_i MW_s, \quad (\text{A.7})$$

where Φ is in the Pitzer formalism given by

$$\Phi = 1 + f_\Phi + B_\Phi m_i + C_\Phi m_i^2. \quad (\text{A.8})$$

In the same fashion correlations for the excess partial molar volume $V_i^{\text{ex}} = \partial\mu_i^{\text{ex}}/\partial p$ can be derived which is for the salt given by

$$V_i = V_i^0 + RT \ln \left[\left(\frac{\partial f_\gamma}{\partial p} \right) + \left(\frac{\partial B_\gamma}{\partial p} \right) m_i + \left(\frac{\partial C_\gamma}{\partial p} \right) m_i^2 \right], \quad (\text{A.9})$$

where V_i^0 is the partial molar volume at infinite dilution. The coefficients A_Φ , $\beta_\Phi^{(0)}$, $\beta_\Phi^{(1)}$, C_Φ introduced in Eqs. (A.4)-(A.6) above can be substituted by $\partial A_\Phi/\partial p$, $\partial\beta_\Phi^{(0)}/\partial p$, $\partial\beta_\Phi^{(1)}/\partial p$, $\partial C_\Phi/\partial p$ given in Table 4.3.

The partial molar volume of the solvent is given by

$$V_s = V_s^0 - 2RTm_i\Phi \quad (\text{A.10})$$

where Φ follows as

$$\Phi = \left(\frac{\partial f_\Phi}{\partial p} \right) + \left(\frac{\partial B_\Phi}{\partial p} \right) m_i + \left(\frac{\partial C_\Phi}{\partial p} \right) m_i^2.$$

List of Publications

Reviewed papers

1. Bernnat, J.; Rink, M.; Tuttlies, U.; Danner, T.; Nieken, U.; Eigenberger, G.
Heat-Integrated Concepts for Automotive Exhaust Purification.
Topics in Catalysis **2009**, 52, 2052–2057.
2. Neidhardt, J. P.; Fronczek, D. N.; Jahnke, T.; Danner, T.; Horstmann, B.; Bessler, W. G.
A Flexible Framework for Modeling Multiple Solid, Liquid and Gaseous Phases in Batteries and Fuel Cells.
Journal of The Electrochemical Society **2012**, 159, A1528–A1542.
3. Castillo-Sanchez, J. M.; Danner, T.; Gross, J.
Grand canonical Monte Carlo simulations of vapor-liquid equilibria using a bias potential from an analytic equation of state.
The Journal of Chemical Physics **2013**, 138 234106.
4. Horstmann, B.; Danner, T.; Bessler, W. G.
Precipitation in aqueous lithium–oxygen batteries: a model-based analysis.
Energy & Environmental Science **2013**, 6, 1299–1314.
5. Wittmaier, D.; Danner, T.; Wagner, N.; Friedrich, K. A.
Screening and further investigations on promising bi-functional catalysts for metal-air batteries with an aqueous alkaline electrolyte.
Journal of Applied Electrochemistry **2013**, 44, 73–85.

6. Danner, T.; Horstmann, B.; Wittmaier, D.; Wagner, N.; Bessler, W. G.
Reaction and transport in Ag/Ag₂O gas diffusion electrodes of aqueous Li-O₂
batteries: Experiments and modeling.
Journal of Power Sources **2014**, 264, 320–332.

Presentations on conferences

1. T. Danner, B. Horstmann, N. Wagner, and W.G. Bessler
Modeling of Transport Processes in the Cathode of Aqueous Lithium-Oxygen Batteries.
ISE Meeting, Prag, Czech Republic (08/2012).
2. T. Danner, B. Horstmann, N. Wagner, W.G. Bessler
Modeling electrochemistry and transport in aqueous lithium-oxygen batteries.
Electrochemistry, Munich, Germany (09/2012).
3. T. Danner, B. Horstmann, D. Wittmaier, N. Wagner, and W. G. Bessler
Mass transport in gas diffusion electrodes for aqueous Li-O₂ batteries: Modeling and experiments.
10th Symposium on fuel cell and battery modeling and experimental validation, Bad Boll/Stuttgart, Germany (03/2013).
4. T. Danner, B. Horstmann, D. Wittmaier, N. Wagner, and W. G. Bessler
Precipitation in aqueous lithium-oxygen batteries: A model-based analysis.
EnMat II, Karlsruhe, Germany (05/2013).
5. T. Danner, B. Horstmann, D. Wittmaier, N. Wagner, and W.G. Bessler
Reaction and Transport in Gas Diffusion Electrodes of Li-O₂ batteries: Experiments and Modeling.
ECS Fall Meeting, San Francisco, USA (11/2013)

Curriculum Vitae

Personal information

M.Sc. Timo Danner

Date of birth: 26th of october 1984

City of birth: Göppingen



Education and research

since 06/14 Helmholtz Institute Ulm for Electrochemical Energy Storage (HIU), Ulm, Germany
Prof. Arnulf Latz, Research group for Multiphysics Electrochemical Modeling

Conferral of Doctorate

since 06/11 Ph.D. student with Prof. Wolfgang G. Bessler:
„Modeling and experimental investigation of transport processes in the porous cathode of aqueous Li-air batteries“

04/13-05/14 University of Applied Sciences Offenburg, Offenburg, Germany
Institute for Energy Systems (INES)

06/11-01/13 University of Stuttgart, Stuttgart, Germany
Institute of Thermodynamics and Thermal Engineering (ITW)

Undergraduate studies

06/12 LEWA price for master theses in process engineering

10/08-06/11 Master of Science in Process Engineering
University of Stuttgart, Stuttgart, Germany
Master thesis with Prof. Joachim Groß (ITT):
„Advanced Monte Carlo methods for the calculation of vapor-liquid equilibria“

10/05-10/08 Bachelor of Science in Process Engineering
University of Stuttgart, Stuttgart, Germany
Bachelor thesis with Prof. Ulrich Nieken (ICVT):
„Computational investigations of systems for exhaust gas treatment using ProMoT and DIANA“

Acknowledgments

At this point I would like to thank all people who supported me during the conferral of my doctorate. Without you this work would not have been possible!

First of all, I would like to thank my doctoral advisor Prof. Wolfgang Bessler for his excellent supervision and all the productive discussions over the last three years. Without your critical comments and great suggestions this work would not be as it is.

Furthermore, I would like to thank Prof. Andreas Friedrich for accepting to co-review this thesis and his support during my time in his department in Stuttgart and the transition to the Helmholtz Institut Ulm. In this regard, I would also like to thank Prof. Arnulf Latz for welcoming me in his group and the excellent collaboration. I am looking forward to my time at the HIU.

I would also like to thank Prof. Helmut Ehrenberg for agreeing to act as additional examiner.

I thank all members of the modeling and battery groups in Stuttgart and Ulm for the great time at work, on conferences, and many other occasions. It was a pleasure to work with you.

Special thanks go to Dr. Birger Horstmann for the inspiring discussions and his constant support. I truly appreciate it!

Moreover, I thank Dr. Norbert Wagner for his support, ideas, and practical solutions during my experimental work. In this respect, I would especially like to thank Dennis Wittmaier for the great teamwork and his patience with us theorists.

I thank Dr. Santhana Eswara-Moorthy and Prasanth Balasubramanian for the extensive preparation of 3D reconstructions and Prof. Volker Schulz for the excellent starting point for the Lattice-Boltzmann model.

Eventually, I would like to thank all project partners of the LuLi project for the pleasant collaboration and the German Ministry of Education and Research (BMBF) for the funding of this work.

I thank my family for their constant support. We had a rough time and I am glad you are at my side!

Above all I would like to thank my girlfriend Nicole! Thank you for the wonderful time

A. Pitzer formalism

and for your patience during all the challenges we went through together. I am looking forward to many more to come!

Declaration of Authorship

I hereby certify that the dissertation entitled

MODELING AND EXPERIMENTAL INVESTIGATION OF TRANSPORT PROCESSES IN THE
POROUS CATHODE OF AQUEOUS LI-AIR BATTERIES

is entirely my own work except where otherwise indicated. Passages and ideas from other
sources have been clearly indicated.

Ich versichere, dass ich die vorliegende Arbeit mit dem Titel

MODELLIERUNG UND EXPERIMENTELLE UNTERSUCHUNG DER TRANSPORTPROZESSE
IN DER PORÖSEN KATHODE DER LI-LUFT BATTERIE

selbständig verfasst und keine anderen als die angegebenen Quellen und Hilfsmittel benutzt
habe; aus fremden Quellen entnommene Passagen und Gedanken sind als solche kenntlich
gemacht.

Name/Name: _____

Unterschrift/Signature: _____

Datum/Date: _____